Karlsruhe Institute of Technology

Functional Microstructures via Direct Laser Writing

Zur Erlangung des akademischen Grades eines
DOKTORS DER NATURWISSENSCHAFTEN
(Dr. rer. nat.)

Fakultät für Chemie und Biowissenschaften
Karlsruher Institut für Technologie (KIT) - Universitätsbereich

genehmigte
DISSERTATION
von

Dipl.-Chem. Alexander Simon Quick

aus
Heidelberg, Deutschland

Dekan: Prof. Dr. Peter Roesky
Referent: Prof. Dr. Christopher Barner-Kowollik
Korreferent: Prof. Dr. Michael Meier
Tag der mündlichen Prüfung: 17.07.2015

Ich erkläre hiermit Wahrheitgemäß, dass die vorliegende Doktorarbeit im Rahmen der Betreuung durch Prof. Dr. Christopher Barner-Kowollik verfasst und keine anderen als die angegebenen Quellen und Hilfsmittel verwendet wurden. Des Weiteren erkläre ich, dass ich mich derzeit in keinem laufenden Promotionsverfahren befinde, keine vorausgegangenen Promotionsversuche unternommen habe sowie die Satzung zur Sicherung guter wissenschaftlicher Praxis beachtet habe.

Karlsruhe, den 03.06.2015

Alexander Simon Quick

Die vorliegende Arbeit wurde von Februar 2012 bis Juni 2015 unter der Anleitung von Prof. Dr. Barner-Kowollik und Prof. Dr. Martin Wegener am Karlsruher Institut für Technologie – Universitätsbereich angefertigt.

Abstract

Three dimensional (3D) micro- and nanostructuring is an established route for the production of functional devices with applications ranging from microelectrochemical systems to metamaterials. A powerful tool for the production of almost arbitrary 3D micro-objects is direct laser writing (DLW), a laser-based technique that has been steadily refined over the past 15 years. The development included the improvement of obtainable resolution, an increased processing throughput, and the optimization of the employed chemical system for curing.

Within the current thesis, entirely novel chemical systems for DLW are introduced. In contrast to previous efforts, which were based on the optimization of well-established chemistry for 3D lithography, the implemented systems feature novel polymerization methodologies. Thus, the investigated approaches yield structures with finely tailored properties. A commonality of the introduced processes is polymerization by step growth, allowing for the generation of uniform, well-defined polymeric networks. Moreover, the fabricated architectures are equipped with chemically reactive residual functions, which are exploited in various covalent post-modification reactions *via* different *click* reactions. Each system exhibits unique properties ranging from the possibility for the rapid production of microresolved mesostructures to the potential of diffraction unlimited resolution.

The first described chemical system for 3D lithography is radical thiol-ene mediated DLW. Therein, a tetrafunctional thiol and a tetrafunctional allyl ether are reacted with a photoinitiator for the generation of a densely crosslinked polymer network in a radical step growth curing reaction. In this fashion, complex 3D woodpile structures with a rod spacing of down to 2 µm are fabricated at a writing speed of 100 µm s^{-1}, evidencing the successful production of fully resolved 3D micro-objects. In addition, the postulated radical thiol-ene reaction during production is verified by tracing vibrational signals of the thiol and the double bond, further revealing the existence of pending thiol moieties. In a post-modification procedure, residual thiols are reacted in a thiol-Michael addition reaction for the covalent immobilization of Michael-acceptor molecules on the structural surface. By attachment of a fluorescent molecule, the grafting density of the procedure was calculated to be approximately 200 molecules μm^{-2}.

In the second implemented radical step growth approach, radical thiol-yne mediated DLW is investigated with a tetrafunctional thiol and a tetrafunctional alkyne as key reaction components. Originating from a precise tailoring of the refractive index, the photoresist allows utilization of the Dip-in configuration. In combination with a fast writing speed of 1 cm s^{-1}, both microstructures and microresolved mesostructures are accessible. As complex 3D microstructures, woodpile photonic crystals with a rod spacing of down to 3 µm are produced, while as microresolved mesostructures, cubic unit cell architectures with a height of close to 1 mm are generated. Furthermore, the postulated radical thiol-yne reaction is verified by tracing vibrational signals of the thiol and the alkyne, verifying the existence of pending thiol and alkyne moieties due to incomplete curing conversion. In a sequential post-modification

procedure, the residual thiols and alkynes are reacted in a thiol-Michael addition reaction and a subsequent copper-catalyzed azide-alkyne cycloaddition. Thereby, a route for the orthogonal, dual post-modification in the bulk structure and on the structural surface is enabled.

As a non-radical step growth approach, photoenol mediated DLW is introduced for the production of 3D microstructures. With a tetrafunctional photoenol precursor molecule and a dodecafunctional maleimide polymer as key molecules, woodpile photonic crystals with a rod spacing of down to 500 nm are fabricated at a writing speed of 100 $\mu m\ s^{-1}$. In addition, the postulated light-induced Diels-Alder reaction is verified by tracing vibrational aldehyde and hydroxy signals. Residual photoenol precursor molecules are addressed in a subsequent photo-triggered Diels-Alder reaction, enabling a covalent post-modification of the structural surface in a spatially resolved manner. Moreover, originating from the difference in both the reactivity of enol isomers and the photoisomerization reaction, the photoenol mediated approach allows for – in principle – diffraction unlimited 3D lithography *via* photoenol depletion. Following this concept, a successful proof-of-principle as well as an improved lateral resolution are achieved, highlighting photoenol depletion as a promising diffraction unlimited DLW approach.

Zusammenfassung

Dreidimensionale Micro- und Nanostrukturierung ist ein etablierter Prozess für die Produktion funktionaler Systeme mit einem weitläufigen Anwendungsgebiet, das sowohl mikroeletromechanische Systeme als auch Metamaterialien abdeckt. Ein leistungsfähiges Verfahren für die Produktion dreidimensionaler Mikroobjekte ist das direkte Laserschreiben, ein Laser-basiertes Verfahren, welches über die letzten 15 Jahre stetig verbessert wurde. Ziele dieser stetigen Verbesserung beinhalteten das Steigern der erreichbaren Auflösung, ein erhöhter Produktionsdurchsatz sowie die Optimierung verwendeter chemischer Lacksysteme.

Die vorliegende Dissertation behandelt die Einführung vollständig neuartiger chemischer Systeme für das Verfahren des direkten Laserschreibens. Im Gegensatz zu vorherigen Ansätzen, die auf der Optimierung bereits etablierter chemischer Methoden beruhten, weisen die hier eingeführten Systeme neue Polymerisationsmethoden auf, welche neue Eigenschaften der hergestellten Strukturen mit sich bringen. Eine Gemeinsamkeit der vorgestellten chemischen Prozesse ist die Stufenwachstumspolymerisation, welche die Herstellung einheitlicher, wohldefinierter Polymernetzwerke ermöglicht. Ferner sind die produzierten Objekte mit chemisch reaktiven, verbleibenden Funktionen ausgestattet, welche für diverse kovalente Modifikationen in einem weiteren Schritt mittels *click*-Chemie Verwendung finden. Neben gemeinsamen Eigenschaften besitzt jedes System einzigartige Merkmale, unter anderem die Möglichkeit einer zügigen Herstellung von Mesostrukturen mit einer Auflösung im Mikrometerbereich sowie das Potential, Strukturen mit einer Auflösung unterhalb des Beugungslimits zu erhalten.

Das erste behandelte chemische System für dreidimensionale Lithographie ist das direkte Laserschreiben mittels radikalischer thiol-ene Reaktion. Darin reagieren ein tetrafunktionales Thiol und ein tetrafunktionaler Allylether mit einem Photoinitiator zu einem Polymernetzwerk in einem radikalischen Stufenwachstumsmechanismus. Auf diese Weise können komplexe, dreidimensionale Mikrostrukturen, sogenannte “Woodpiles”, mit einem Stababstand von 2 µm bei einer Schreibgeschwindigkeit von 100 µm s^{-1} hergestellt werden. Dadurch wird die Eignung des Systems zur Erzeugung dreidimensionaler Mikrostrukturen gezeigt. Zudem kann die postulierte radikalische thiol-ene Reaktion während der Produktion verifiziert werden indem Schwingungssignale der Thiole und der Doppelbindungen verfolgt werden. Daraus ist auch das Vorhandensein restlicher Thiolgruppen in gefertigten Strukturen ersichtlich, welche in einer anschliessenden thiol-Michael Addition zur kovalenten Anbindung funktionaler Moleküle auf der strukturellen Oberfläche genutzt werden. Durch die Nutzung eines fluoreszierenden Moleküls konnte zusätzlich eine Propfdichte von etwa 200 Molekülen µm^{-2} bestimmt werden.

Der zweite eingeführte radikalische Stufenwachstumsansatz ist das direkte Laserschreiben mittels der radikalischen thiol-yne Reaktion mit einem tetrafunktionalen Thiol und einem tetrafunktionalen Alkin als Schlüsselkomponenten. Basierend auf einem präzisen Angleichen des Brechungsindex kann dieser Photolack in Dip-in Konfiguration eingesetzt werden. Kombiniert mit einer schnellen Schreibgeschwindigkeit von 1 cm s^{-1} ist es möglich, sowohl

Mikrostrukturen als auch hochaufgelöste Mesostrukturen zu erhalten. Als komplexe dreidimensionale Mikroobjekte können Woodpiles, photonische Kristalle mit einem Stababstand von 3 μm, produziert werden. Das System ermöglicht zudem die Herstellung von Mesostrukturen, bestehend aus kubischen Einheitszellen, mit einer Höhe von etwa einem Millimeter. In Anlehnung an das radikalische thiol-ene System kann sowohl die postulierte radikalische thiol-yne Reaktion während der Produktion als auch das Vorhandensein restlicher funktionaler Gruppen verifiziert werden, indem Schwingungssignale der Thiole und der Alkine verfolgt werden. In einer sequentiellen post-Modifizierungsprozedur gehen verbliebene Thiole und Alkine eine thiol-Michael Addition bzw. eine Kupfer-katalysierte Azid-Alkin Cycloaddition ein. Dadurch wird eine orthogonale, duale chemische Immobilisierung innerhalb der Objekte und auf deren struktureller Oberfläche ermöglicht.

Als ein nichtradikalischer Stufenwachstumsansatz wird zudem das photoenol-induzierte direkte Laserschreiben zur Herstellung dreidimensionaler Strukturen behandelt. Mittels einem tetrafunktionalen Photoenolmolekül und einem dodekafunktionalen Maleimidpolymer als wichtigste Ausgangsmaterialien sind photonische Kristalle mit einem Stababstand von 500 nm bei einer Schreibgeschwindigkeit von 100 $\mu m\ s^{-1}$ zugänglich. Durch Verfolgung der aldehyd- und hydoxyspezifischen Vibrationssignale im Verlauf der Objektherstellung kann die postulierte, lichtinduzierte Diels-Alder Reaktion bestätigt werden. In einem zweiten lichtkontrollierten Prozess ist in diesem Fall eine ortsaufgelöste Oberflächenstrukturierung realisierbar. Ferner ist der Photoenolansatz prinzipiell zu einer Auflösung unterhalb des Beugungslimits befähigt, ermöglicht durch den Unterschied in Reaktivität und die kontrollierte Umwandlung beider im Prozess entstehenden Enolisomere. In einer Grundsatzstudie kann sowohl die allgemeine Tauglichkeit als auch eine daraus resultierende verbesserte Auflösung gezeigt werden, was die Wichtigkeit des hier gezeigten Konzeptes untermauert und weitere detailierte Untersuchungen erstrebenswert macht.

Publications

Publications Arising from this Thesis

- **Facile Preparation of Reactive Three-Dimensional Microstructures via Direct Laser Writing and Thiol-Ene Chemistry**
  Quick, A.S.; Fischer, F.; Richter, B.; Pauloehrl, T.; Trouillet, V.; Wegener, M.; Barner-Kowollik, C. *Macromol. Rapid Commun.* **2013**, *34*, 335-340.

- **Fabrication and Spatially Resolved Functionalization of 3D Microstructures via Multiphoton-Induced Diels-Alder Chemistry**
  Quick, A.S.; Rothfuss, H.; Welle, A.; Richter, B.; Fischer, J.; Wegener, M.; Barner-Kowollik, C. *Adv. Funct. Mater.* **2014**, *24*, 3571-3580.

- **Rapid Thiol-Yne Mediated Fabrication and Dual Post-Functionalization of Micro-Resolved Mesostructures**
  Quick, A.S.; de los Santos Pereira, A.; Bruns, M.; Bückmann, T.; Rodriguez-Emmenegger, C.; Wegener, M.; Barner-Kowollik, C. *Adv. Funct. Mater.* **2015**, *25*, 3735-3744.

Patents Arising from this Thesis

- **Hochaufgelöste Photochemie Unterhalb des Beugungslimits Mittels Schaltbarer Photoenolisierung**
  Fischer, J.; Quick, A.S.; Richter, B.; Mueller, J.B.; Bastmeyer, M.; Barner-Kowollik, C.; Wegener, M. **2015**, EP-Number to be advised.

Additional Publications[a]

- **Thermally Responsive Core-Shell Microparticles and Cross-Linked Networks Based on Nitrone Chemistry**[§]
  Barner, L.; Quick, A.S.; Vogt, A.P.; Winkler, V.; Junkers, T.; Barner-Kowollik, C. *Polym. Chem.* **2012**, *3*, 2266-2276.

- **Photo-Induced Functionalization of Spherical and Planar Surfaces via Caged Thioaldehyde End-Functional Polymers**
  Kaupp, M.; Quick, A.S.; Rodriguez-Emmenegger, C.; Welle, A.; Trouillet, V.; Pop-Georgievski, O.; Wegener, M.; Barner-Kowollik, C. *Adv. Funct. Mater.* **2014**, *24*, 5649-5661.

- **Exploring the Mechanisms in STED-Enhanced Direct Laser Writing**
  Fischer, J.; Mueller, J.B.; Quick, A.S.; Kaschke, J.; Barner-Kowollik, C.; Wegener, M. *Adv. Opt. Mater.* **2015**, *3*, 221-232.

- **Photo-Induced Surface Encoding of Gold Nanoparticles**
  Stolzer, L.; Quick, A.S.; Abt, D.; Welle, A.; Naumenko, D.; Lazzarino, M.; Wegener, M.; Barner-Kowollik, C.; Fruk, L. *Chem. Commun.* **2015**, *51*, 3363-3366.

- **Designing Molecular Printboards: A Photolithographic Platform for Recodeable Surfaces**
  Abt, D.; Schmidt, B.V.K.J.; Pop-Georgievski, O.; Quick, A.S.; Danilov, D.; Kostina, N.; Bruns, M.; Wenzel, W.; Wegener, M.; Rodriguez-Emmenegger, C.; Barner-Kowollik, C. **2015**, DOI: 10.1002/chem.201501707.

[a]Publications marked by a § were achieved during the diploma thesis of the author. All remaining publications originated during the course of the current thesis from projects where the author was involved.

Contents

1 Introduction

Micro- and nanostructures are responsible for several fascinating material properties in nature and have thus always been a focus of interest for scientists around the world.[1–3] While a very significant effort is focused on the understanding of the observed phenomena, various methodologies for the generation of micro- and nanostructured materials have continuously been established over the years. To date, a range of fabrication techniques for different materials have been investigated including the synthesis of particles,[4,5] 2D patterns[6] and even complex 3D architectures.[7] As a result, applications in chromatographic techniques,[8] transistors,[9] metamaterials[10] and many other fields have been enabled. Direct laser writing (DLW),[7,11] a powerful laser-based tool for the production of almost arbitrary 3D polymeric structures has steadily been refined over the last 15 years. Next to the improvement from a physical / engineering point-of-view, chemical improvement of existing and implementation of novel chemical resist systems is of distinct importance for the promotion of 3D lithography for different applications. While a considerable amount of effort is being invested into understanding and optimizing existent polymerization protocols for DLW, the exploration of adequate polymerization methodologies that are both novel to and advantageous for the technique is a highly promising, yet poorly investigated approach.

1.1 Aim of the Thesis

The aim of the current thesis is to establish polymerization techniques or modular ligation strategies that differ from known chain growth free radical or cationic polymerization protocols in DLW photoresists. Promising techniques should fulfill certain criteria in order to be applicable for a lithographic system: Firstly, rapid polymerization and the formation of stable, insoluble crosslinked networks must be attainable employing light as a reaction trigger. Secondly, both the availability or facile synthesis of all chemical components and a straightforward verification of the postulated reaction during fabrication or any other modification is highly desirable. Thirdly and most importantly, the resulting structures must be advantageous towards *state-of-the-art* objects regarding certain aspects such as the ability for facile, efficient, and covalent post-modification.

Throughout this thesis, step-growth approaches are implemented to DLW utilizing a different chemistry, namely the radical thiol-ene coupling reaction,[12,13] the radical thiol-yne coupling reaction,[14] and the Diels-Alder reaction.[15] In all cases the formation of crosslinked insoluble polymeric material is ensured *via* the usage of multifunctional monomeric components.

Light-triggering of the reaction is enabled by a photoinitiator in the cases of the thiol-ene and the thiol-yne reaction while for the Diels-Alder approach a photoactive precursor is employed, generating a reactive diene *in situ* by photoenolization.[16] For both radical thiol coupling approaches, all components are readily available or can be synthesized in large quantities with ease. For the photoenol approach both the diene precursor and the dienophile component is synthesized in a more complicated multistep procedure. Verification of the postulated polymerization mechanism is in all cases achieved *via* transmission Fourier-transform infrared (FTIR) spectroscopy. A variety of structures are fabricated ranging from microstructures such as single lines and simple cuboid objects over woodpile photonic crystals to complex mesostructures with an overall dimension in the millimeter range. In each case the novel procedure and structure quality is compared to *state-of-the-art* systems concerning important parameters such as resolution and overall fabrication time, among others. Analysis includes scanning electron microscopy (SEM), light microscopy, optical photography and focused ion beam milling (FIB).

In addition, each novel system exhibits features that are not present in conventional structures. Due to the different photoresist composition in each system, advantageous residual functional groups such as thiols, alkynes or photoenol precursor molecules are exhibited. Each functional group is a potent reaction partner for *click* chemistry,[17] in particular for the thiol-Michael addition reaction, the copper-catalyzed azide-alkyne cycloaddition, or the Diels-Alder reaction. Residual functional groups are exploited for efficient and facile post-functionalization in a single, dual, or spatially resolved manner throughout the structure and / or on the structural surface. Analysis for the post-functionalization includes laser scanning microscopy (LSM), X-ray photoelectron spectroscopy (XPS), FTIR, and time-of-flight secondary ion mass spectrometry (ToF SIMS). For DLW employing photoenolization, the chemical process furthermore exhibits promising features that have been investigated for diffraction unlimited lithography. While the systems presented here serve as a proof-of-concept, the possibility for straightforward covalent post-functionalization has excellent potential for future applications especially in microfluidics and lab-on-a-chip systems or for biological applications.

2
Theory and Background

Throughout this chapter, an overview of topics and theoretical background that is relevant for the understanding of the studies conducted during this thesis will be given. To begin with, a brief description of fundamental topics which constitute the basis of the entire subject area is given. These are namely electronic excitation in photochemistry, polymerization methods, the concept of *click* chemistry, and important lithographic methods. Obviously, it is challenging to exhaustively describe these general topics in such a brief manner. The reader is therefore kindly advised to refer to the literature for in-depth information. Following the fundamentals, topics that play a direct role in this thesis are described in more detail. Firstly, the lithographic method *direct laser writing* that has been employed for three-dimensional structure fabrication will be introduced . Therefore, the aim of this section is a clear description of the overall technique with an emphasis on the investigated photochemical processes and recent applications. In the following sections, different chemical reactions that have been extensively employed throughout the thesis will be described individually, namely the *radical thiol-ene* and *radical thiol-yne* reaction, the *thiol-Michael addition* reaction, the *copper-catalyzed azide-alkyne cycloaddition*, and a photoinduced *Diels-Alder* reaction based upon photoenolization. After a general description of the respective reaction, beneficial and disadvantageous aspects of the reaction, especially in the context of three-dimensional photolithography and post-functionalization, will be discussed followed by several examples of application. The choice of highlighted applications for each reaction is selective rather than exhaustive and supports the topic of this thesis.

2.1 Fundamentals

2.1.1 Photochemistry

Interaction between molecules and light is a highly important aspect in natural sciences. Regarding the possible interactions of organic molecules and electromagnetic waves, there are several ways for the molecules to absorb light that are highly dependent on the energy, *i.e.*, the wavelength of light. For low energy irradiation with a wavelength in the region of centimeters, molecules can acquire the absorbed energy in rotational modes. When going to a shorter wavelength in the region of micrometers, the so-called infrared region, energy can be acquired in vibrational modes. By further reduction of the light wavelength to nanometers, entering the range of visible light and ultraviolet light, the mode of assimilated energy is of electronic nature. Light-induced electronic transitions are the cornerstone for numerous chemical and

physical processes and are therefore omnipresent in everyday life. Absorption can be treated in a quantitative manner by Beer-Lambert's law which connects the transmitted fraction of monochromatic light and an absorbing system:

$$log(\frac{I_z}{I_0}) = -\epsilon \times c \times z \tag{2.1}$$

where I_z and I_0 are the transmitted and the incident intensities of light, respectively, and ϵ, c, and z denote the decadic absorption coefficient, the absorber concentration, and the length of the absorbing system, respectively. The law is based on the fact that bimolar collisions between photons and absorbing molecules and the rate of photon-loss are proportional.

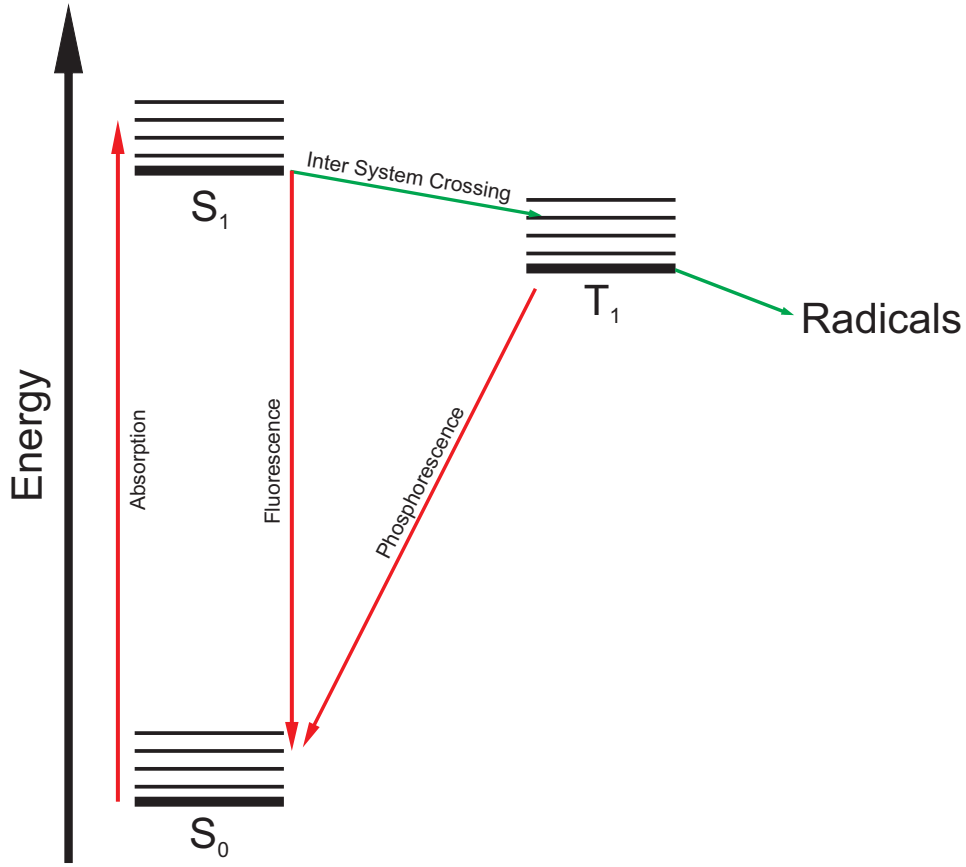

Figure 2.1: Schematic depiction of a Jablonski diagram featuring electronic excitation *via* absorption, luminescent relaxation processes such as fluorescence and phosphorescence (all red). Both inter system crossing and radical formation are processes that proceed without radiation (all green). Other common processes such as vibrational decay, internal conversion, or excited state absorption are not depicted.

After the absorption of a photon, the molecule is transferred into an excited state which possesses altered reactivity from its ground state. From the excited state several routes are possible that all lead to the loss of electronic excitation. Such pathways can be classified into

general routes such as dissociation (photolysis), inter- and intramolecular chemical reaction, isomerization, inter- and intramolecular energy transfer and emission of light. Although the overall process for any selected photochemical or photophysical process is highly complex and often vary for different systems, it is possible to qualitatively comprehend said processes *via* a so-called Jablonski diagram. In this diagram, the relative energy of possible electronic and vibrational states of a molecule and also all transitions that can occur in these states are depicted. Figure 2.1 displays common processes such as the absorption, fluorescence, inter system crossing, phosphorescence, and radical formation. It must be noted that many other existent transition processes are not depicted in this diagram. However, for a large amount of light-induced processes, a Jablonski diagram is sufficient for qualitative overall process discussions. As an example, the radical formation of numerous photoinitiators can be traced by the given Jablonski diagram. *Via* light absorption, the molecules are elevated from the ground singlet state (S_0) to the excited singlet state (S_1). After vibrational decay (not shown), the excited singlet state (S_1) undergoes inter system crossing to the excited triplet state (T_1), followed by dissociation and the generation of radical fragments.

2.1.2 Polymer Chemistry

Radical fragments that originate from above mentioned photo-excitation of initiator molecules are often efficient radicals for free radical polymerization (FRP). Being a chain polymerization technique, FRP consists of three steps: As the first step, initiation comprises the provision of radicals which is commonly light or thermally triggered and the formation of the first chain radicals. During the second step, termed propagation, the propagating radical polymer chain adds monomer units, thus increasing the molecular weight. In the final step, termed termination, propagating polymer chains are permanently deactivated *via* the recombination or disproportionation reaction of two radicals. Facile processing, among others, is a reason for the widely spread usage of FRP in science and industry. Following steady-state kinetics for an ideal homopolymerization, the average degree of polymerization (DP_n) for a FRP experiment is given by:

$$DP_N = \frac{kk_p[M]}{\sqrt{2fk_dk_t[I]}} \tag{2.2}$$

where k_p, k_d, and k_t denote the rate coefficients of propagation, dissociation, and termination, respectively, [M] and [I] denote the concentration of monomer and initiator, respectively, f is the initiator efficiency and k is the coupling constant. The termination mode in a given polymerization is described by k. However, due to the occurrence of termination events, a drawback of FRP is the large dispersion regarding the molecular weight of polymer chains.

In this context, controlled radical polymerization methodologies have been researched, namely nitroxide-mediated polymerization (NMP), atom transfer radical polymerization (ATRP), and reversible addition fragmentation chain transfer polymerization (RAFT). All the mentioned processes aim at suppressing uncontrolled, irreversible termination events. Thereby, the dispersion of obtained polymer for a given polymerization is strongly decreased. In NMP and ATRP this is achieved by an effective decrease of the radical concentration, greatly reducing

the rate of termination. While NMP is based on an equilibrium between thermally labile alkoxyamine groups and radicals, ATRP employs a Cu(I)-based catalytic system to reversibly deactivate propagating chains. A disadvantage of NMP and ATRP is the increase in reaction time that is required to reach high conversion, a side effect stemming from the reduced radical concentration. In comparison, the RAFT process is based upon another concept where the suppression of radical termination is achieved by a competitive reversible chain transfer process. Typical chain transfer agents for this process, so-called RAFT agents, are dithioesters or trithiocarbonates. Almost non-reduced radical concentration is largely beneficial for RAFT-induced polymerization compared to NMP and ATRP, allowing for reaction times that are similar to conventional FRP for a given conversion while producing narrow dispersed polymer. However, polymerization methods are not restricted to chain-type reactions.

Next to chain polymerization techniques where high molecular weight of polymer chains are produced at low conversions, step growth polymerization is an important tool throughout polymer science. Contrary to chain polymerization where the reaction is restricted to radical-radical and radical-monomer interactions, in a step growth process any species that possesses suitable functionality can react with one another in the reaction mixture (monomers, oligomers, and polymers). Consequently, following a stoichiometric consideration for bifunctional step growth monomers, the average degree of polymerization is dependent on the conversion (U) and the ratio of functional groups (q):

$$DP_N = \frac{1+q}{1+q-2qU} \tag{2.3}$$

which can be simplified to the so-called "Carothers equation", assuming equimolarity of functional groups:

$$DP_N = \frac{1}{1-U} \tag{2.4}$$

Regarding the displayed equations it becomes obvious that only high conversion leads to polymer formation. Classical step growth polymerizations are polycondensation and polyaddition. While in polycondensations the equilibrium can be altered in order to reach high conversion by removal of the released small molecule, for polyadditions it is largely beneficial to employ efficient reactions that rapidly proceed to full reaction conversion without side reactions. One collection of suitable reactions for polyadditions are therefore *click* reactions.

2.1.3 *Click* Chemistry

Conceptually, *click* chemistry evolved as an alternative strategy for natural product synthesis.[17] Contrary to traditional approaches where the desired molecule was synthesized in a sophisticated step-by-step manner, the *click* strategy is based on another synthesis strategy: The generation of all final product fragments followed by facile fragment assembly *via* high yielding, orthogonal reactions. Concerning the reactions employed for the assembly, a list of criteria, today known as the *click* criteria, was established in order to determine if a reaction was deemed suitable for assembly. A potential reaction should therefore be:

- able to reach very high yields,
- exhibit a high reaction rate,
- be applicable in a large scope,
- proceed without the formation of offensive side products,
- be stereospecific,
- possess a high thermodynamic driving force,
- require no complex purification.

It quickly became evident that the suitability of reactions that fulfill most of the mentioned criteria are not restricted to assembly reactions in natural product synthesis. In fact, reactions that fulfill the majority of the criteria can easily be adapted to various scientific fields for challenging tasks. A large benefit thereby is that, due to the stringent criteria, no significant chemical expertise is required for the conduction of click reactions. To serve as examples, biology and materials science can be mentioned as scientific fields that have employed *click* chemistry extensively. It should be noted, however, that in reality no ideal reaction exists that fulfills each criterion in every reaction to 100%. Even reactions that fulfill most criteria which are termed *click* reactions are sparse. Specific examples are the nucleophilic opening of spring-loaded rings, cycloaddition reactions, and some protecting group reactions. Naturally, for differing applications differing criteria are important.[18] To serve as a descriptive example, stereospecificity is very important for natural product synthesis whereas this criterion is non-essential in the context of polymer-polymer conjugation or lithographic approaches.

2.1.4 Lithographic Methods

Spatially resolved patterning, especially in the micro- and nanometer region, is an important cornerstone for modern technology that is becoming ever more relevant in everyday life. While the drive towards high-performance computers, based on microelectronics, has already become self-evident, expansion of the gained knowledge to chemical or even medical systems is an ongoing process with the potential to considerably enhance life quality in the near future. Perhaps the most straightforward approach for two-dimensional (2D) microlithography employs light, a photomask, and a system that is altered by exposure to light. Such an approach has the advantage of simultaneous exposure, yet for each desired pattern, a specific mask must be fabricated and the resolution is restricted to several micrometers. Another form of photolithography widely utilized in the semiconductor industry employs low wavelength laser beams (193 nm) for structuring, allowing for the fabrication of arbitrary 2D patterns. The low wavelength of light results from the fact that the resolution of a light-driven approach is limited by diffraction and is therefore linearly dependent upon the wavelength of the employed light (as will be discussed in more detail in Section 2.2). Serious drawbacks of this technique are the large cost of optical devices and the restricted number of suitable systems due to the harsh exposure conditions.

Other approaches that do not require light for structuring and display mild conditions are nanoimprint lithography,[6,19] soft lithography,[20] or dip-pen lithography (see Figure 2.2).[21] While nanoimprint lithography is based upon a molding procedure followed by etching, dip-pen lithography relies on the formation of a liquid meniscus (often water) between an atomic force microscopy tip and a substrate. The tip is coated with "inc" molecules that are deposited on substrate regions in contact. Stemming from the mild reaction conditions, a more diverse range of materials can be utilized for these techniques. An alternative, powerful technique for high resolution structuring is electron beam lithography. In this technique, a focused beam of electrons is scanned across a substrate, thereby exposing an electron-sensitive resist. Being dependent upon broadening of the electron beam, resolution of down to several nanometers can be achieved.

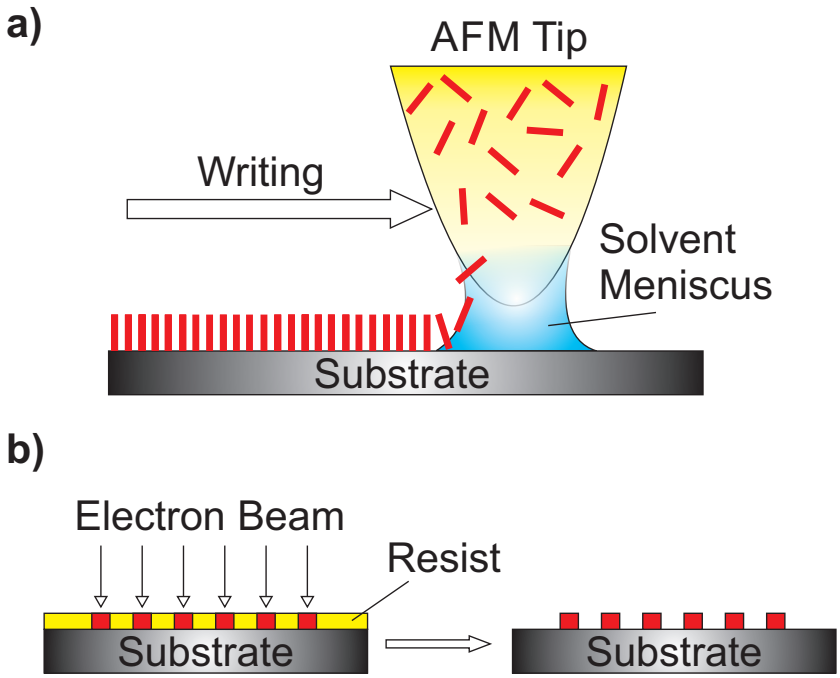

Figure 2.2: Schematic depiction of a) dip-pen lithography and b) electron beam lithography. While dip-pen lithography is based upon the deposit of "inked" molecules onto contacted area, electron beam lithography "cures" resist regions (b), left). For negative tone resists the uncured resist regions are removed *via* substrate development (b), right).

Even though the produced devices do often exhibit a significant height, in the case of nanoimprint lithography this can be several hundred nanometers, a commonality of the discussed approaches is their general restriction to planar applications. Extensions to existent techniques such as gray-tone or layer-by-layer electron beam lithography allow for the production of elevated topographies and other geometries. However, the approaches remain restricted to layered geometries, additional to being time consuming and error prone. To overcome this barrier and thereby enable the fabrication of almost arbitrary three dimensional (3D) architectures, it is

necessary to introduce multiphoton absorption into light-induced lithography approaches. The resulting technique is termed direct laser writing and will be discussed in more detail in the following section.

2.2 Direct Laser Writing

2.2.1 Brief Evolution

Chemical processing employing light is a concept that has been known to scientists for centuries. As an example, the report of an early organic photochemical reaction evoking a color change-accompanied destruction of α-santonin crystals under sunlight conditions dates back to 1834[22] and has only recently been fully understood.[23] Since then, the number of photochemical reactions has steadily been increased and the concept has gained even more importance with the emergence of laser technology.[24] From this point on, complex processes such as material deposition or surface etching have become possible and can be performed – among others – by pure photo-induced chemistry or absorption-induced thermal chemistry.[25] Such processes were generally restricted to two dimensions yet in layer-by-layer approaches, first reports of 3D microstructures *via* single-photon absorption utilizing photopolymerization were investigated and published.[26,27] The major breakthrough for the extension of such techniques to three dimensions required usage of nonlinear optical processes, specifically the multi-photon absorption process.[28] Thereby, the confinement of the photoreaction is also restricted in the vertical axis leading to a small overall reaction volume. After the mentioned prerequisites were experimentally achieved, the road was paved for the photopolymeric production of 3D micro- and nanostructures that are of significant importance for a multitude of present-day scientific research areas.

2.2.2 Working Principle

During a standard DLW procedure (see Figure 2.3) a laser beam is tightly focused into a photoactive material *via* an oil immersion objective. Laser devices commonly employed for DLW operate at a wavelength of 700-900 nm in a pulsed mode with pulse durations in the femtosecond region around 100 fs and a repetition rate of approximately 80 MHz. Such devices are usually employed as they favor the desired occurrence of a nonlinear multi-photon absorption event: While the average power of an exposure is low (there is only one 100 fs pulse every 12.5 ns for 80 MHz repetition rate) the peak intensity in the focus during a single pulse is high. The photoactive material (photoresist) which is chosen to be transparent to the utilized laser wavelength is typically deposited on top of a glass cover-slip (which is also transparent to the wavelength). Before the reaction in the focal point occurs, the laser beam passes the immersion oil and the glass substrate. On the lateral axes the absorption is automatically restricted due to the tight focus (with further contributions from the nonlinear absorption process). Additionally, due to the nonlinear nature of the absorption event the absorption is – contrary to linear processes – also restricted in the vertical axis. As a result, the absorption and thus the chemical reaction is confined to a small volume with its center in the geometrical focus for a single exposure. Curing of the photoactive material induces an efficient solubility change within the exposed volume. Complex 3D patterns are exposed by moving the substrate and the laser focus relative to each other in three dimensions. After exposure, development of the sample is performed where the soluble component of the photoresist is removed. Typically, this is achieved by immersing the entire sample in suitable solvents and thereby yielding the

targeted structure. For the overall DLW procedure, a setup is required as described in detail below.

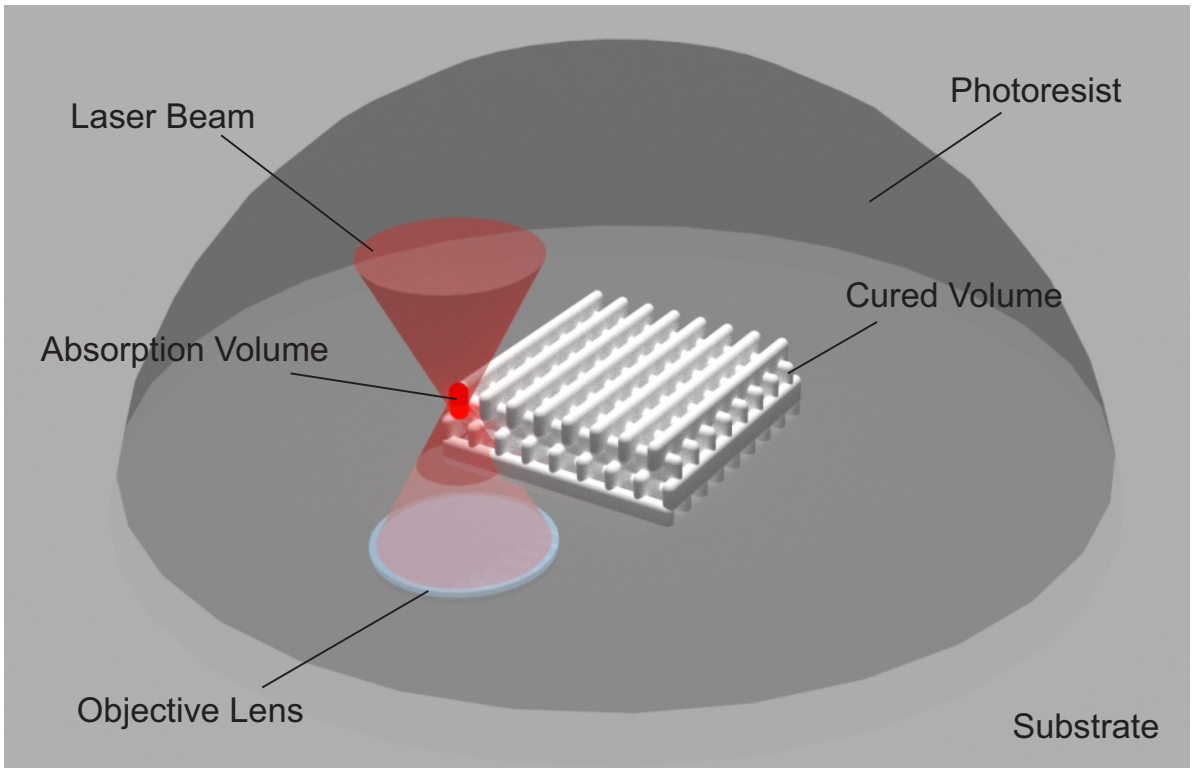

Figure 2.3: Schematic depiction of the DLW working principle. Nonlinear absorption events confine curing to a small volume around the focal point of the focused laser beam. Structures (in this case a woodpile photonic crystal) are exposed *via* respective movement of the laser focus and the substrate.

2.2.3 Common Experimental Direct Laser Writing Setups

Requirements of an experimental DLW setup allow for a certain range of choice of components. Therefore, home-built setups often differ from one another, a consequence resulting from the nature of the conducted experiments on a respective setup. Nevertheless, an identical core platform is the basis of every setup (see Figure 2.4) consisting of a laser source, a device for intensity tuning during fabrication, an objective, a device for the respective movement between substrate and focus, a computer, and a possibility for online observation of the fabrication process.[7,11] As light sources a range of systems are suitable, but due to its beneficial features concerning pulse duration and tuning of the wavelength, a mode-locked Titanium Sapphire laser is often employed. Specific examples for experimental DLW setups and their corresponding parameters are: 752 nm center wavelength with a repetition rate of 76 MHz and a pulse duration of 200 fs,[29] 793 nm with a repetition rate of 80 MHz and a pulse duration of 73 fs,[30] and 810 nm with a repetition rate of 80 MHz and a pulse duration of 100 fs.[31] Another laser source

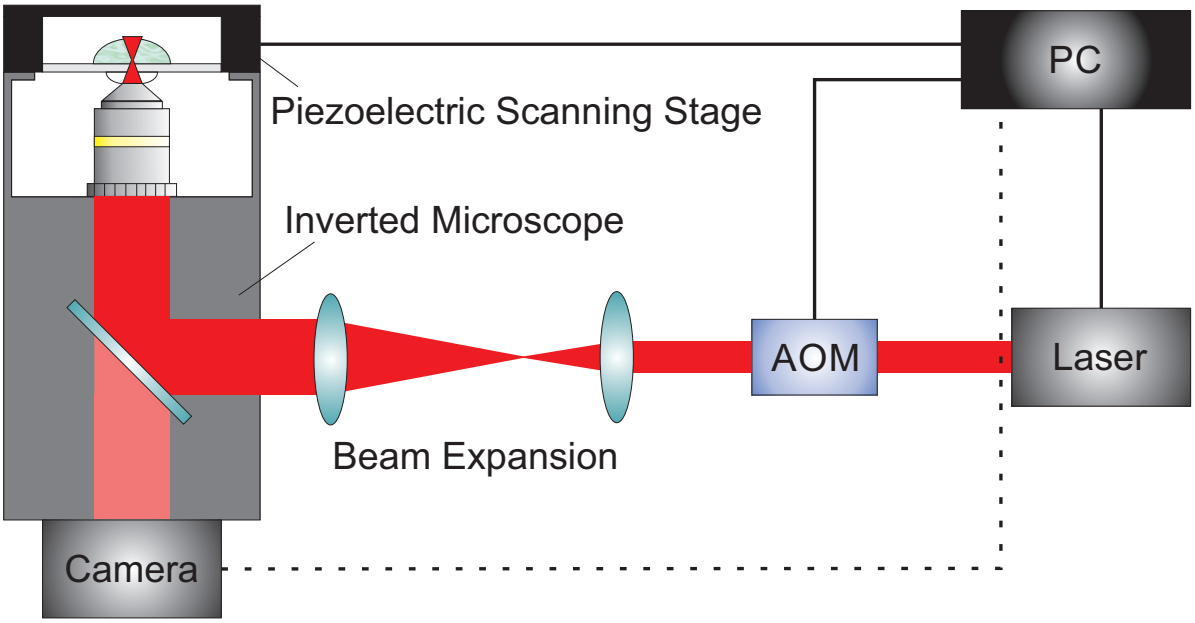

Figure 2.4: Schematic depiction of a conventional DLW setup employing a piezoelectric 3D scanning stage for movement during fabrication. Alternatively, galvanometric mirrors can be utilized for lateral movement (not shown).

can also be utilized such as the frequency-doubled Erbium fiber laser with 780 nm center wavelength, 90 fs pulse duration and a repetition rate of 80 MHz in a commercially available system.[32] Other, more sophisticated laser systems for DLW have also been employed. Two specific examples from our group are a 532 nm continuous wave solid state laser[33] or a 405 nm diode laser.[34]

Intensity tuning is usually performed by using either a shutter or, for more precise results, an acoustooptic or electrooptic modulator. A beam expansion is also implemented in order to provide adequate illumination of the objective. A high numerical aperture for employed objectives is favorable as, following the Abbe limit, it is inversely proportional to the minimal resolvable distance. Typical numerical apertures for suitable objectives lie between 1.2 and 1.4. Movement between the focus and the substrate can be achieved in two different ways. The first possibility is to keep the focus stationary while precisely moving the substrate-containing stage. In this approach piezoelectric actuators are employed allowing for nanometer scale movement. An advantage of this approach is that the stationary focus shape can easily be optimized and remains unchanged throughout the entire lithographic experiment. Therefore, this approach is preferable when fabrication of ultra precise structures is required. However, the substrate must be mechanically moved in this approach. Acceleration and deceleration issues limit the maximum achievable writing speed to approximately 100-200 µm s^{-1}. Depending on the actual sample geometry, the writing speed must be further decreased for high quality structure generation. Furthermore, depending on the employed stage, a compensation must be incorporated into the files at the mentioned writing speed to account for the incidental

piezo-induced delay which differs for each setup. Thus, it is not readily possible to utilize one set of files for fabrication of identical, complex samples on different setups. The second possibility for focus-substrate movement is by employing a set of galvanometric mirrors which enable a deflection of the laser focus on both lateral axes while the vertical movement remains stage-controlled.[35,36] Fabrication of 3D structures in this mode is usually performed in a layer-by-layer manner. Compared to the piezo-induced motion, the focus shape slightly changes due to the direction induced deflection. The movement of the galvanometric mirrors, however, can be conducted much faster than piezo-induced stage movement. Therefore, the benefit of the galvanometric mirror setup lies in a rapid accessible writing speed in the region of several cm s^{-1}, exceeding piezo-induced writing speed by a factor of about 100. Next to experimental premises, photochemical processes play an important role in DLW.

2.2.4 Absorption Process in Direct Laser Writing

As briefly described above, in DLW it is an absolute necessity to confine the excitation in both lateral and axial dimensions. Such demands can not be met by conventional one-photon absorption (1PA) and therefore another process, so-called two-photon absorption (2PA), is targeted for DLW. In 2PA the excited state is accessed by simultaneous absorption of two photons that each possess a lower energy than the corresponding photon in a one-photon transition.[37] In the case of DLW, degenerate 2PA is desired where both photons exhibit the same energy (half of the energy compared to photons in 1PA). Similar to the Beer-Lambert law for 1PA, attenuation of a beam of light for 2PA can be expressed by:

$$\frac{\partial I}{\partial z} = -N\delta F I \tag{2.5}$$

where the intensity, the distance into the medium and the number of molecules per unit volume are abbreviated by I, z and N, respectively. The photon flux F can be described as $F = I/h\nu$ (in photons $\times$ s^{-1} $\times$ cm^{-2}; hν describes the photon energy) and δ is known as the molecular 2PA cross-section which is normally reported in the unit Göppert-Mayer ($1\,\mathrm{GM} = 10^{-50}\mathrm{cm}^4 \times \mathrm{s} \times \mathrm{photons}^{-1} \times \mathrm{molecule}^{-1}$). The quality of a two-photon dye is often expressed by the δ value at a given wavelength which is also an important yet not the only parameter for two-photon initiators. Maximum δ values can be increased in molecules by employing a conjugated central region and electron-donating or electron-withdrawing groups, yet care must be taken, as these changes shift the wavelength for maximum 2PA to a lower energy.[38,39]

2.2.5 Dimensions of the Absorbing Volume in Direct Laser Writing

Different from 1PA which is linearly proportional to the light intensity, 2PA is proportional to the squared intensity. For a given wavelength ($\lambda = 800\,\mathrm{nm}$) and numerical aperture (NA, 1.4), the normalized excitation density resulting from a focused beam of monochromatic light can be plotted versus the distance from the focal point (see Figure 2.5) for 1PA and 2PA. A popular

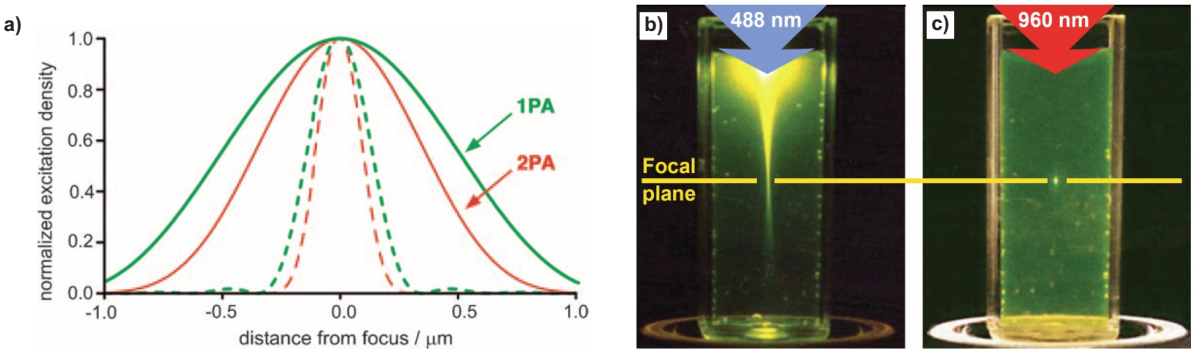

Figure 2.5: a) Normalized excitation density plotted against focus distance for 1PA (green) and 2PA (red). Dashed lines depict lateral and solid lines depict axial dimensions. b) Single-photon induced fluorescence and c) two-photon induced fluorescence of a fluorescein solution (NA = 0.16 for both cases), respectively. Figure adapted from [37] and [40] with permission from Wiley-VCH and the Nature Publishing Group.

definition for the voxel[a] for distinct numbers is the full width half max (FWHM) definition where the excitation volume is confined to regions of 50% or more of the normalized excitation density in the focal point. Transferred to lithography, where sufficient excitation leads to curing, this resembles a simple threshold model where curing occurs above a specific excitation density and does not occur below this density. In this case the voxel has a lateral width of 290 nm and an axial length of 1080 nm for 1PA and a width of 210 nm and length of 780 nm for 2PA, assuming Gaussian profiles. The aspect ratio[b] for 2PA is close to 2.5 : 1 with a given diffraction limit for a grating with a period of a_{xy} in lateral and a_z in axial direction by:[41,42]

$$a_{xy} = \frac{\lambda}{2NA} \tag{2.6}$$

$$a_z = \frac{\lambda}{n - \sqrt{n^2 - (NA)^2}} \tag{2.7}$$

where λ is the wavelength and n is the refractive index of the medium. An argument that can come to mind is that the wavelength in 1PA is usually performed with $\lambda_{2PA}/2$. Therefore, the grating period is reduced by a factor of two when comparing wavelengths for 1PA and 2PA. This deterioration is not fully compensated when going from 1PA to 2PA (the compensation factor is $\sqrt{2}$ when assuming Gaussian excitation density profiles, as will be described in Section 2.2.7) and results in larger grating periods for 2PA for a targeted excitation – a contradiction for any resolution-based conception. The reason why 2PA is still more beneficial for microscopy and lithography lies in the axial confinement as will be described below.

A good way to visualize different absorption regions for 1PA and 2PA is by considering the rate of absorption in a single transverse cross-section of a laser beam in a sample with homogeneously distributed absorbing molecules. The rate for 1PA is dependent upon the

[a]The term voxel describes the excitation volume for a single point exposure in this context
[b]In this context the aspect ratio describes the ratio between length and width of a voxel.

intensity ($\propto photons \times time^{-1} \times area^{-1}$) multiplied by the number of molecules ($\propto area$) in this transverse cross-section. As the area cancels out, no axial localization of excitation is possible, the number of excited molecules in every transverse cross-section is the same. The rate of 2PA in a given cross-section is dependent upon the squared intensity ($\propto photons^2 \times time^{-2} \times area^{-2}$) multiplied by the number of molecules ($\propto area$), resulting in an inverse dependence of the absorption rate upon the area. Thus, an axial excitation localization exists. This perception can be impressively validated in a simple experiment (see Figure 2.5).[7,37,40] Through a solution of fluorescein two laser beams are focused (NA = 0.16) at 488 nm and 960 nm targeting 1PA and 2PA, respectively. While 1PA occurs everywhere along the beam path, 2PA is confined to a small volume close to the focal point. In this volume, chemical processes take place in lithography that ultimately lead to structure formation.

2.2.6 Photoresist Chemistry

In the excitation volume, a range of photoinduced reactions or processes can be performed. For the production of stable 3D objects, however, a distinct solubility change in the exposed regions of the photoresist is crucial. One possibility is the solubilization and subsequent removal of the solid photoresist throughout the cured regions which is targeted in positive-tone photoresists.[43] Another regularly applied option for structure fabrication is the usage of negative-tone photoresists. Therein, the cured volume is solidified and thus rendered permanently insoluble. Physical conditions for negative-tone photoresists can be either solid or liquid, each condition having different advantages for applications. In solid photoresists the fabrication of free moving parts such as an interconnected chain is facilitated due to the absence of diffusion-evoked motion.[44] Liquid photoresists on the other hand are advantageous both in preparation and in handling and are therefore widespread. A high viscosity of the resist reduces undesired polymer diffusion during exposure. In fact, 3D objects with *state-of-the-art* resolution utilize liquid negative-tone photoresists by taking advantage of oxygen diffusion and thus increasing oxygen-induced radical termination at the absorption periphery.[34] Cured regions are photopolymerized in this approach leading to architectures consisting of insoluble, heavily crosslinked polymeric material. Often, a photoinitiator is utilized for the generation of active components. A beneficial attribute of the initiator is a large 2PA cross-section, yet this is but one prerequisite among others such as solubility and quantum yield of initiating species. Currently applied polymerization systems in DLW are dominated by two chain growth methods: free radical polymerization and cationic polymerization.

The most prominent cationic polymerization photoresist consists of a multiple epoxide-containing molecule (Epon SU8, average of eight epoxide groups per molecule), a solvent and a photosensitizer (see Figure 2.6).[45] Photosensitizer compounds that produce acid moieties under light exposure, so-called photo-acids, such as triaryl sulfonium salts are often employed. In an initial prebake processing step, the photoresist is placed (or spun) upon the substrate and the solvent (commonly cyclopentanone or γ-butyrolactone) is evaporated at elevated temperatures (prebake), resulting in a solid film. During the exposure, acid moieties are generated in the exposed volume. Thereupon, a postbake processing step is conducted elevating the temperature above the glass transition temperature of the film. At this point, cationic polymerization of

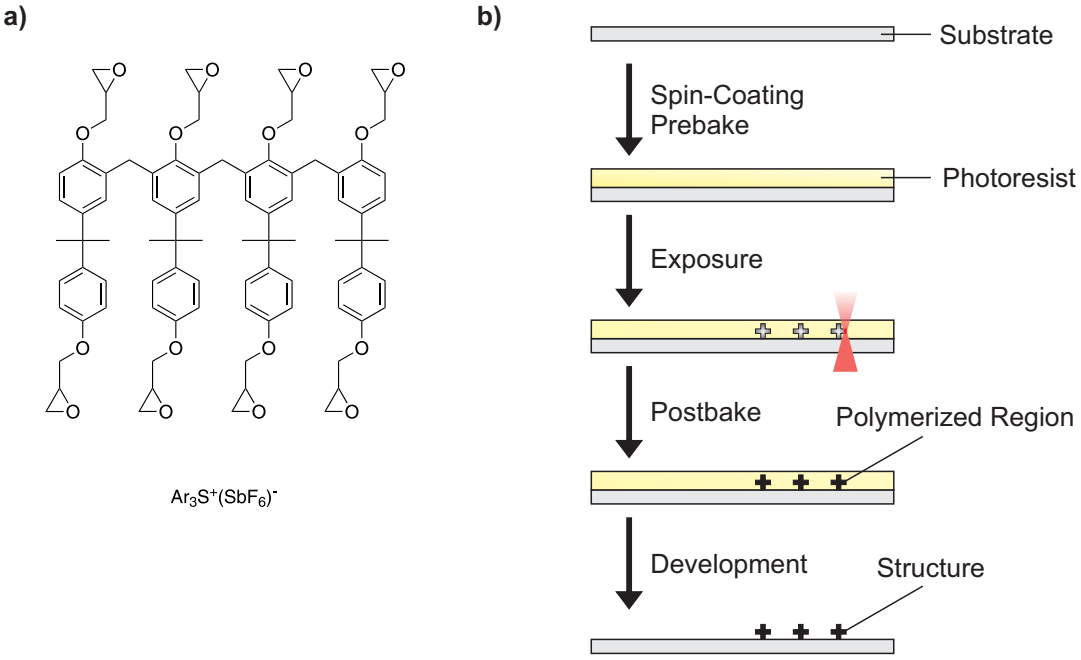

Figure 2.6: a) Typical photoresist components for DLW employing a cationic solid photoresist: An octafunctional epoxide (SU8) as a monomer and a triaryl sulfonium salt as a photoacid generator. b) Schematic depiction of consecutive process steps during DLW using SU8.

the epoxy groups is induced by the acid fragments in a ring opening manner. Due to the eight epoxy groups on each molecule the monomers are interconnected in a heavily cross-linked fashion and are hence rendered insoluble in the cured volume. Residual unpolymerized material is removed *via* development of the sample in an appropriate solvent, yielding the final structure. Investigations and applications of cationic-type photoresists include the use of different photosensitizers such as diaryl- or coumarin iodonium salts,[46,47] sensitizers with maximized 2PA cross-section values (up to 690 GM),[48] as well as different monomer systems such as Sartomer K-126 and SCR-701.[46,49] Apart from the cationic process, polymerization can also occur, as noted above, in a radical manner.

Free radical processes such as FRP have been widely established as a DLW curing reaction as they combine a simple procedure with impressive resulting 3D architectures. Typically, multifunctional acrylates are utilized as polymerization units in the monomers due to their rapid propagation coefficients, commercial availability and easy processing. Further, the resulting crosslinked polymer networks possess favorable mechanical properties, a low swelling behavior, and are inert towards harsh conditions such as different solvents and elevated temperatures. The liquid photoresist usually consists of a multifunctional monomer with a functionality between three and five and a photoinitiator. Widely used multifunctional acrylates such as pentaerythritol tetra- or triacrylate (PETTA or PETA) are viscous liquids in which small quantities of initiator are often soluble, enabling DLW in bulk material without additional, time consuming process-

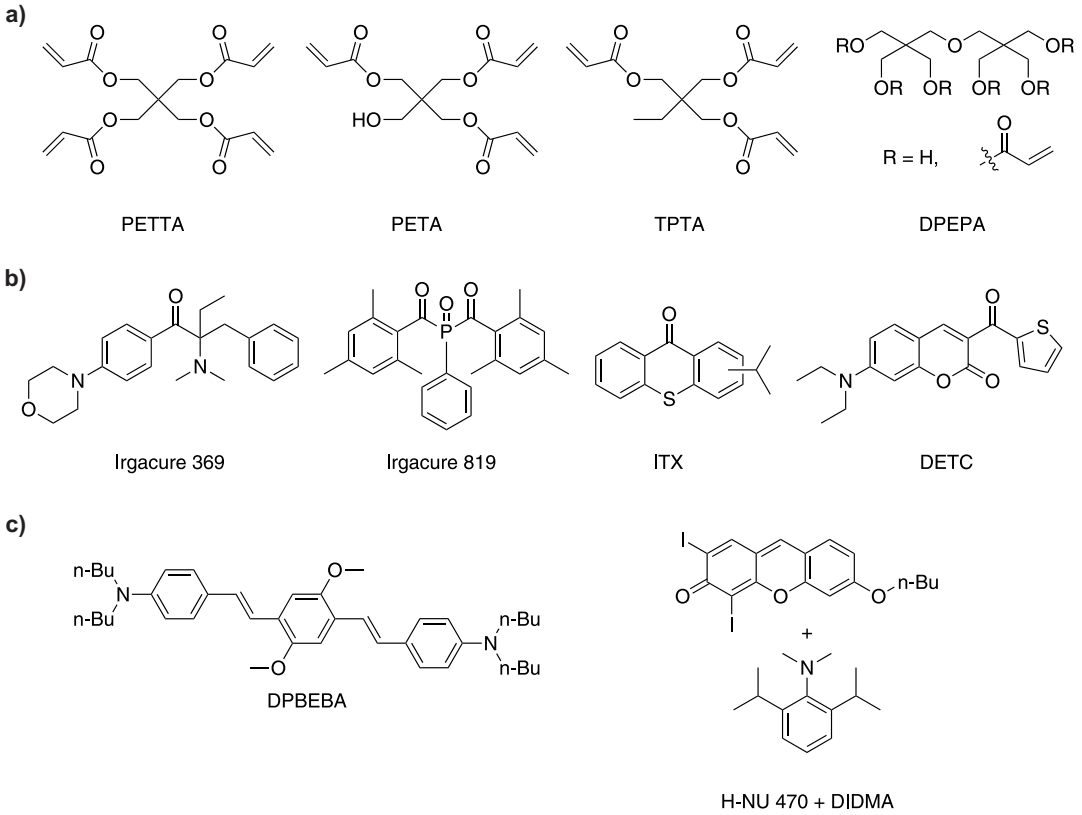

Figure 2.7: a) Commonly employed acrylate monomers for DLW based on FRP. b) Examples for commercially available Norrish type I initiators frequently utilized for DLW. c) Radical initiator exhibiting a large two-photon cross-section (left) and Norrish type II initiator with corresponding coinitiator (right).

ing steps. Extensive research has been conducted upon the investigation of initiating molecules. Examples for common monomers and initiators are given in Figure 2.7. One focus was attaining large δ values for Norrish type I initiators[c] which was achieved by symmetric charge transfer, extension of the conjugation length and implementation or variation of electron-donating and -accepting groups.[38,39] However, a high 2PA cross-section – as mentioned above – is not the sole parameter for a suitable initiator. Commercially available carbonyl compounds have been found to be suitable for 2PA microfabrication and are thus often utilized.[50] Norrish type II initiators[d] have also been applied and optimized for DLW.[46,51] An advantage is the free choice of coinitiator, facilitating an efficient overall polymerization while keeping the initiating radical fragment constant for different initiators. Apart from initiator molecule studies, an interesting and demanding topic is the in-depth investigation of the polymerization during the lithographic process. Quantification of the double bond conversion for a given acrylate system *via* FTIR measurements revealed a reaction conversion ranging from 56 % to 75 %, depending on the

[c] A Norrish type I initiator is a carbonyl-containing compound that forms radicals by cleavage of the α-carbon bond.

[d] A Norrish type II initiator is a carbonyl-containing compound that produces radicals in combination with a coinitiator by hydrogen abstraction.

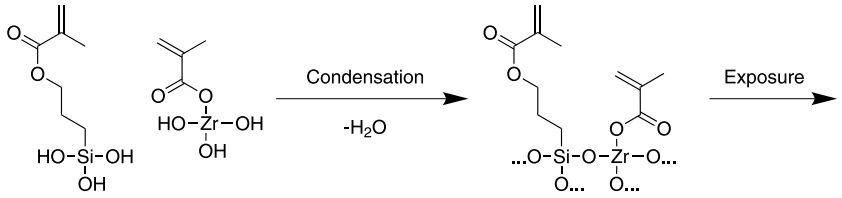

Figure 2.8: An example for DLW employing sol-gel processing. An inorganic network (with a photoinitiator, not shown) is produced prior to exposure during which FRP fixates irradiated regions. This procedure prevents structural shrinkage during exposure.

laser power.[30] Employing Raman microspectroscopy on a similar system, rather different conversions ranging from 25 % to 50 % were measured.[52] *In situ* measurements of the local temperature in the excitation volume utilizing temperature-dependent nanoparticles revealed a local heating of only a few Kelvin for optimum structural quality writing conditions.[53] Further, the influence of oxygen was investigated for acrylate-type photoresists with the result that oxygen quenching and diffusion for ambient conditions are of significant importance and are even beneficial during the lithographic experiment.[31]

Next to the widely employed acrylates described above, FRP has also been employed for the introduction of other types of material into microfabrication. One example is the photoresponsive hydrogel material utilized for the production of operational devices such as a microcantilever.[54] Here, a mixture of monomers, namely acryloylacetone, acrylamide and a bisacrylamide form the hydrogel material after curing. Motion was induced by excitation of acetylacetone at 244 nm wavelength. Another example is the fabrication of objects *via* usage of organic-inorganic hybrid materials, combining features of organic polymers with sol-gel processing.[36,55–58] Thereby, unwanted volume loss during polymerization can be reduced due to the formation of an inorganic network prior to curing (see Figure 2.8).

Other, more exotic photoresists have also been developed for production of specific 3D microstructures such as the radical initiated cross-linking of polydimethylsiloxane,[59] diazonaphtoquinonesulfonate based systems[43] or patterning of chalcogenide glass *via* multiphoton absorption.[60] However, these interesting approaches are not as universal and simple to conduct as the above mentioned techniques and are thus restricted to specific applications.

2.2.7 Limitations of and Extensions to Direct Laser Writing

One of the main benefits of DLW is the possibility of producing almost arbitrary 3D structures with high precision in a facile manner. However, in a conventional DLW setup different limitations inhibit the use of DLW for several applications. For standard oil-immersion configuration (see Figure 2.9), the choice of substrate is limited to materials that are transparent to the wavelength of the laser beam. A rather simple circumvention of this limitation is by applying a so-called “sandwich” configuration.[36,61] Herein, the substrate is placed on top of the photoresist, the laser beam is focused at the interface between the photoresist and the substrate (which is in this case not the cover slip) and fabrication is conducted in a top-down

approach. A drawback of this approach is the decreased resolution due to focus aberrations stemming from refractive index mismatches between the photoresist and the glass cover slip. Further, undesired reflection or heating near the interface originating from the non-transparent substrate can deteriorate fabrication. Finally, depending on the thickness of the photoresist film, the height of achievable structures is limited.

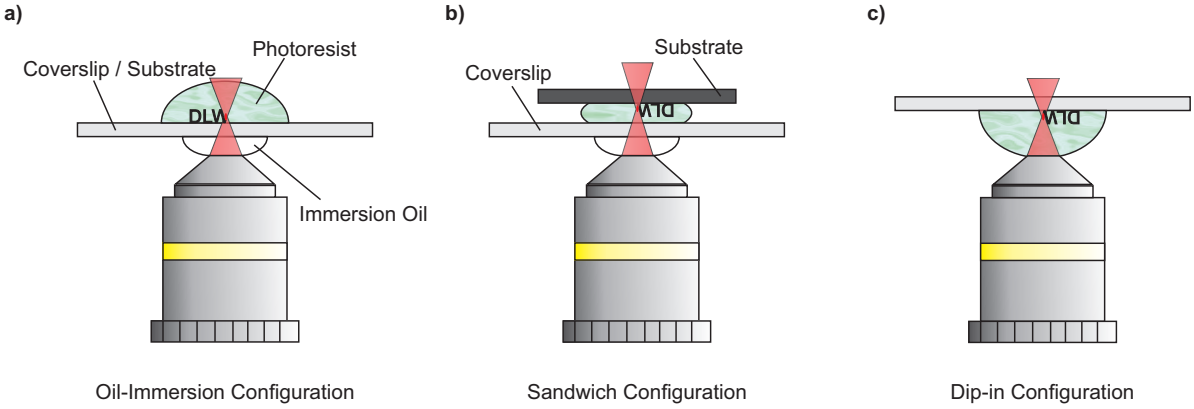

Figure 2.9: Different substrate configurations for DLW. a) Conventional oil-immersion configuration, b) Sandwich configuration enabling the usage of nontransparent substrates, and c) Dip-in configuration permitting structure fabrication without height limitation.

In fact, height limitation is a restriction that holds true for any common oil-immersion setup. During the fabrication in a conventional bottom-up approach, the focus moves away from the substrate and is thereby altered in shape and position due to refractive index mismatches of the glass substrate and the photoresist or the material of an already fabricated structural section. In addition, the height of a produced structure is fundamentally limited by the working distance[e] of the utilized objective. To overcome the height limitation, Dip-in DLW has been developed.[62] In this approach the photoresist additionally takes on the role of the immersion oil, therefore the objective is directly immersed into the photoresist and the lithographic process takes place in a top-down manner. This way the laser beam does not have to pass the glass cover slip / substrate, enabling, together with the use of galvanometric mirrors, the production of mesostructures with a height in the range of millimeters while retaining micro / nanoscale resolution.[32] An important prerequisite for Dip-in configuration is a compatible refractive index of the photoresist for high NA objectives. The laser beam must pass several hundred micrometers of photoresist before absorption occurs near the focal point and a large deflection at the interface between objective lens and photoresist would greatly impair structures fabricated in this fashion. A compatible refractive index is a constraint for the large majority of photoresists and therefore Dip-in DLW is not as universally applicable as the conventional oil-immersion configuration. Apart from limitations and extensions concerning the overall dimension of the structure, DLW also faces limitations in terms of resolution as described below.

[e]The distance between the objective lens and the focal point is termed working distance

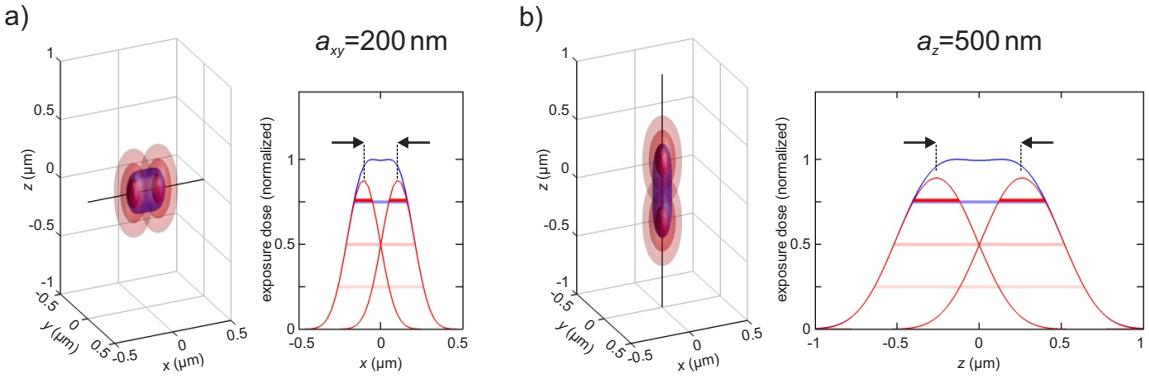

Figure 2.10: Critical distances for two-photon point exposures in a) lateral and b) axial dimension derived from numerical calculations corresponding to the Sparrow criterion. Displayed distance values are slightly larger for visualization of the local minimum. Right on each panel: Isointensity profiles where blue displays the threshold intensity (here 75%). Left on each panel: Plot of exposure dose vs distance from center with contribution of each single exposure (red) and their above threshold sum (blue). Chosen parameters are: 800 nm free-space wavelength, NA = 1.4, and circular polarization. Figure adapted from [42] with permission from the authors and Wiley-VCH.

Achievable resolution is an important parameter for each lithographic system which can be experimentally determined by fabrication of a grating with a minimum distinguishable period (for 2D).[42] For 3D resolution, structures must be produced that also exhibit periodicity in axial direction. One such structure is the woodpile photonic crystal.[63] It is important to note that line widths or feature sizes alone are no measure for grating-based resolution. In a threshold model, curing only occurs in regions where the exposure dose exceeds a certain value (the threshold value). The width of a single line can be minimized (theoretically without limitation) *via* adaption of the maximum excitation density (corresponding to an exposure dose) respective to a given threshold value (see Figure 2.5). In DLW, when writing a single line, there are additional regions that experience an exposure dose unequal to zero yet below the threshold. Being a serial process, different assumptions can be made. One possibility is that the exposed regions below the threshold "forget" the exposure dose similar to the Schwarzschild effect for photographic plates,[f] *e.g.*, due to diffusion of polymerized yet still soluble molecules. In this case, a second line could be fabricated within one line width (center-to-center), line width and minimum grating period would essentially be the same and resolution would not be fundamentally limited by diffraction. Another, more conservative assumption is that all exposed regions "remember" every exposure dose and curing occurs once the sum of all exposure doses exceeds the threshold. In this case, if a second line is written within one line width of a first line (center-to-center) the result would not be a grating but one thick line. A grating would only be possible if the sum of both exposures exhibits a minimum (see Figure 2.11). Under this

[f] The Schwarzschild effect originates from photography where no darkening of a photographic plate occurs under continuous illumination of light as long as the momentary light intensity remains below a critical value.

assumption, which is known as the "Sparrow criterion",[64] DLW is fundamentally limited by diffraction. A modified Abbe diffraction limit for the lateral (a_{xy}) and the axial (a_z) direction – adapted for DLW – has been proposed (compare to Section 2.2.5):

$$a_{xy} = \frac{\lambda}{2\sqrt{2}NA} \tag{2.8}$$

$$a_z = \frac{\lambda X}{2\sqrt{2}NA} \tag{2.9}$$

with X being the aspect ratio of the exposure volume. Naturally, being a complex field of its own, photoresist chemistry during DLW has a large influence on the achievable resolution for any given system. This fact that has not been considered in this paragraph at all. Next to the exposure "memory" of the photoresist, the stability of delicate structures is crucial for deformation of the object during the development step. Alteration of the structures induced by shrinkage due to low conversion or insufficient stability also limits the achievable solution and is thus an important parameters to consider. Therefore, for each DLW system, the achievable resolution must be determined experimentally.

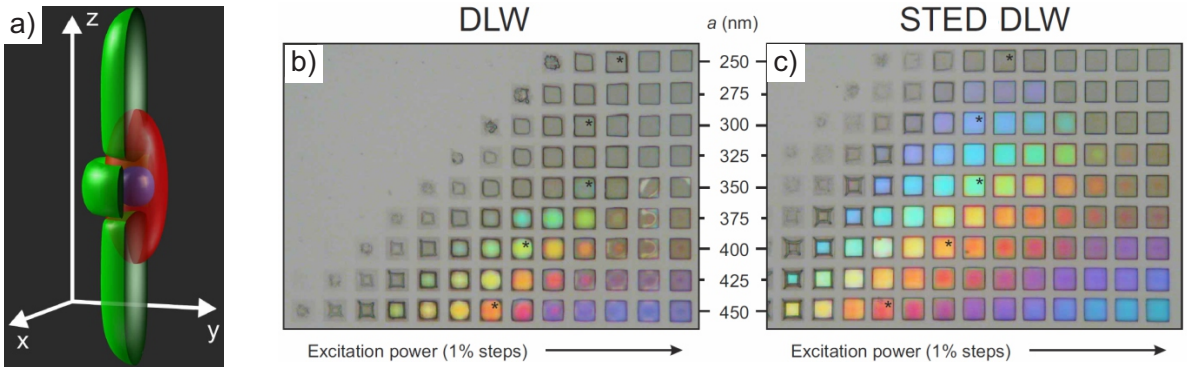

Figure 2.11: Diffraction unlimited lithography *via* STED DLW. a) Schematic depiction of the overlay of excitation (red) and depletion (green) laser foci, resulting in a smaller effective excitation volume (blue). b) Woodpile photonic crystals with different rod spacing (a) produced by conventional DLW, and c) Woodpile photonic crystals produced by STED DLW. Figure adapted from [65].

Obviously, the impetus for overcoming diffraction limitation or, more generally, increasing the achievable resolution is high and different approaches have been investigated. In one attempt the wavelength of the employed laser was reduced to 405 nm while still inducing 2PA.[34] This way woodpile photonic crystals[63] (the standard structure for determination of 3D resolution in DLW) with a photonic stop band and a lateral rod spacing of 250 nm have been fabricated. An approach to overcome the diffraction barrier employs stimulated emission depletion (STED), a technique well-known from microscopy.[66] By employing a special fluorescent photoinitiator, the excited singlet state, induced by the excitation laser, can undergo stimulated emission induced by a second "depletion" laser of a different wavelength before inter system crossing,

followed by the generation of initiating radicals, occurs. Thereby, in STED DLW the generation of radicals and thus curing only occurs in regions where an effective exposure takes place, *i.e.*, where the excited singlet state is not depleted.[42] By proficient overlap between both laser foci – which are still diffraction limited – resulting from the usage of adequate phase masks for the modulation of the focus shape, effective exposure volumes can be generated that are not limited by diffraction.[67] Woodpile photonic crystals exhibiting photonic stop band with down to 250 nm lateral rod spacing were fabricated with this technique *via* 810 nm excitation (see Figure 2.11).[65] Another approach termed resolution augmentation through photo-induced deactivation employs cationic dyes and presumably deactivates a long-lived intermediate state of the initiator molecule.[68,69] A third approach, the so-called two-color photo-initiation / inhibition lithography, makes use of an added photoinhibitor that is activated at a different wavelength than the initiator and efficiently deactivates initiating radicals and propagating chains. In this fashion the formation of an insoluble cross-linked polymer network can be prevented.[70] Both conventional and all extended DLW systems have been utilized for numerous applications, as will be described below.

2.2.8 Fields of Application for Direct Laser Writing

Facile design and fabrication of near to arbitrary 3D structures make DLW highly suitable for a large range of applications in very different scientific fields. In this section, selected applications will be described albeit there being many more reported in the literature. In microelectrochemical systems DLW has been successfully applied for the production of micromanipulators such as tweezers and needles that are optically driven.[71] Optical control allowed for the precise opening / shutting of the tweezers and the microneedle was induced to different motions such as translation and rotation. Optical waveguides have been fabricated with multiphoton lithography allowing for the coupling of optical fibers *via* straight, curved and split waveguides.[72] In fact, DLW has been applied for integrated optics combining 3D polymer structures with quasiplanar silicon nitride devices for the coupling of rib and 3D bridge waveguides, broadband mode polarization rotators and coupling between a 3D bridge waveguide and a polymer disk resonator.[73] In addition, DLW has also been introduced into microfluidics and lab-on-a-chip systems.[74] In principle it is possible to fabricate an entire microfluidic system in a DLW based approach, however, high cost and long fabrication times are currently serious drawbacks. Nevertheless, there are examples of conceptual microfluidic devices fabricated by DLW utilizing, for instance, SU8 as a photoresist (see Figure 2.12).[75] Momentarily, it is more advantageous to integrate single functional units into existing microfluidic chips *via* DLW. This way microsieves and -valves have been implemented as well as a micro overpass at the junction of a crossed microchannel.[76,77] Further, motion has been induced by the fabrication of micromixers, the salient point being the preparation and implementation of a magnetic photoresist containing Fe_3O_4 nanoparticles.[81] Finally, an integration of catalytic nanostructures partly consisting of platinum and palladium has been reported.[82] DLW has also found application for the production of biological scaffolds. Two-component polymer scaffolds fabricated *via* DLW as designer petri-dishes have been exploited for the controlled cell culture studies in three dimensions.[83] Thereby, the cells only show affinity to certain regions of the 3D structure.

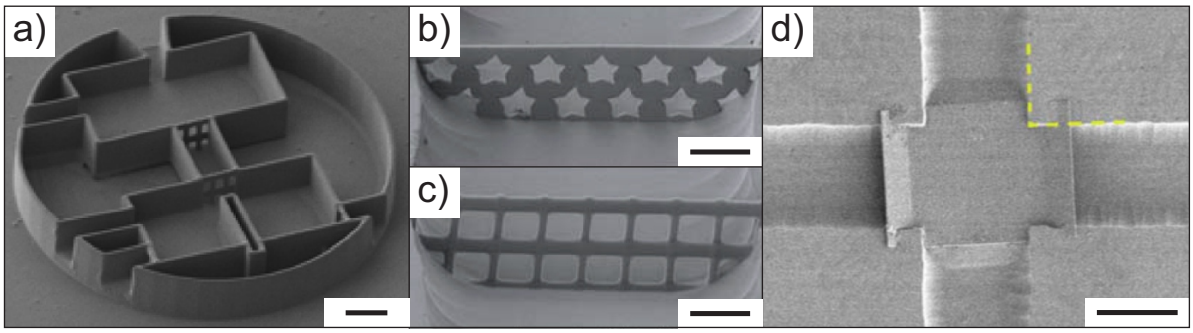

Figure 2.12: Examples for the incorporation of DLW into lab-on-a-chip systems. Depiction of a) a conceptual microfluidic device, b) and c) microsieves which differ in shape, and d) an overpass at the junction of a crossed microchannel. Scale bars are 10 µm for a), b), and c) and 50 µm for d). Figure adapted from [75–77] with permission from the Royal Society of Chemistry.

Three dimensional microscaffolds with resolved surface chemistry have also been prepared in this context where bioconjugation was employed for revelation of molecular patterns using fluorescent protein tags.[80] Uniform cell morphologies have also been achieved by precise cell-matrix adhesion of produced 3D structures.[84] By controlled deformation of the structures, stretching forces on primary fibroblasts were induced and the effects investigated for different stretching conditions.

Conventional DLW has also been exploited for the production of photonic 3D metamaterials such as gold helices as circular broadband polarizers[43] and in photonics where polymeric photonic crystals with polarization stop bands[85] and 3D chiral photonic superlattices[78] have been, among others, fabricated. An extension to the conventional DLW system such as STED DLW has further enabled the fabrication of a polarization-independent carpet invisibility cloak at visible frequencies.[79] Further, complex and highly resolved 3D structures such as N-helical metamaterials only have a chance of fabrication with diffraction unlimited lithography techniques.[86] Recent overcoming of the height limitation by Dip-in DLW has paved the way to meso-scale structures while retaining micro / nanometer resolution and has lead to applications in mechanical metamaterials with negative Poisson ratios or an elasto-mechanical unfeelability cloak (see Figure 2.13).[32,62] Apart from 3D architecture generation, a DLW setup further allows for the precise spatially resolved patterning of surfaces. In this manner, the resolved grafting of phenacylsulfide-functional polymers to polydopamine surfaces and the covalent immobilization of photoenol-modified gold nanoparticles to dienophile-containing surfaces was achieved (for more information on the mentioned chemical reactions, see Section 2.5).[87,88]

In conclusion, the working principle of DLW has been discussed along with examples of different experimental setups. The necessity of 2PA has been highlighted and the photochemistry taking place during the lithographic process has been elaborated. Limitations concerning the dimensions of objects have been addressed and extensions to the conventional DLW setup have been presented. Finally, a selected number of applications for DLW taken from different

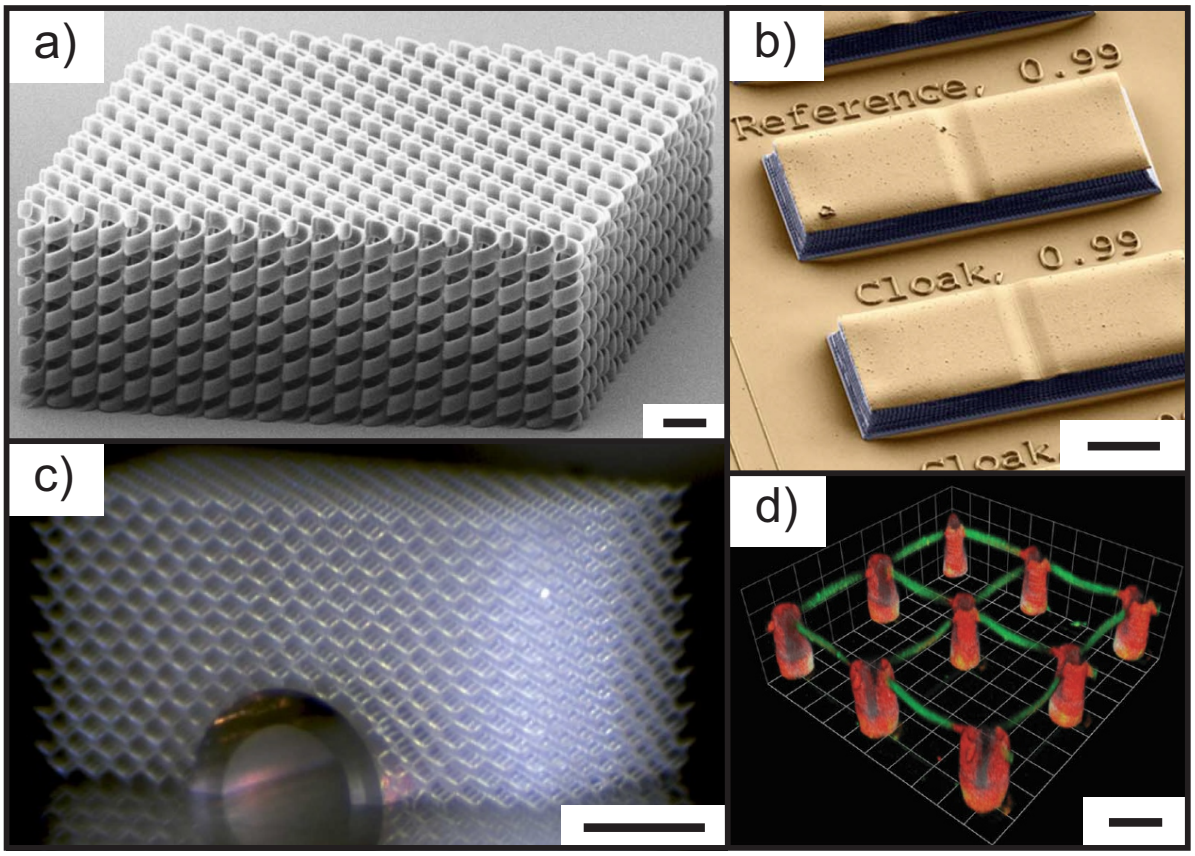

Figure 2.13: Examples for usage of DLW in photonics, metamaterials, and bioconjugation. Depiction of a) a circular spiral photonic crystal, b) an invisibility cloak at visible frequencies, c) an unfeelability cloak based on pentamode metamaterials, and d) surface-specific bioconjugation on DLW-written scaffolds. Scale bars are 5 µm for a), 10 µm for b) and d), and 0.5 mm for c). Figure adapted from [32, 78–80] with permission from the Nature Publishing Group and Wiley-VCH.

scientific fields have been introduced underpinning the fact that DLW is a powerful and versatile tool for material science. From this section, it has become clear that novel polymerization protocols featuring the possibility for covalent modification or light-induced deactivation should be implemented into DLW. The resulting structures are then of particular interest for, yet are not restricted to lab-on-a-chip systems, microfluidics, or biological applications. For this undertaking, adequate chemical systems must be found. In this context, promising chemical systems will be introduced in the following section.

2.3 Thiol Mediated Chemistry

2.3.1 Chemistry of Thiols – a Diverse Platform

Thiols can be employed as reagents for a range of potent chemical reactions and have therefore experienced a sustained interest from various scientists including chemists, biologists, and material scientists. The countless examples of thiol chemistry throughout the literature can be classified into a number of reactions in which thiols are categorized according to their role in the chemical reaction (see Figure 2.14).[89] Nucleophilic substitutions can be conducted utilizing thiols or, for increased nucleophilicity, thiolates that can readily be generated by usage of bases. Alkyl halides such as iodoalkanes, α-bromo carbonyl compounds, and pentafluorophenyl groups can be employed as efficient leaving groups. Ring-opening of epoxides can also be conducted by a base catalyzed or Lewis acid catalyzed reaction with thiols.[90,91] In all above cases a thioether is produced. Nucleophilic substitution can also occur with molecules containing electrophilic sulfur such as Bunte salts resulting in a disulfide exchange during reaction.[92] Another often utilized reaction is the oxidation of thiols to disulfides and the corresponding reduction *vice versa*. A plethora of oxidizing agents can be employed for disulfide formation such as hydrogen peroxide, iodine, or molecular oxygen. Disulfides can efficiently be reduced with mild agents such as DTT or TCEP and, therefore, this technique is widely spread in bioconjugation procedures.[93] Noble metal surfaces consisting of gold, silver, or other metals are outstanding substrates for thiol coordination and are frequently made use of for the formation of self-assembled monolayers.[94] Monolayers enable efficient chemistry on flat metallic substrates or on nanoparticles and have paved the way for a large range of applications including, among many others, surface-initiated polymerizations for anti-fouling substrates[95] or gold-silica core-shell nanoparticles coated with a self-assembled monolayer of protein resistant PEG-thiol for cancer studies.[96] In traditional FRP, thiols are added to a polymerization procedure as so-called chain transfer agents. During polymerization, a thiyl radical is generated from a thiol and a propagating chain, whereby the latter is permanently deactivated. The thiyl radical further participates in the polymerization process by initiating another propagating chain. Usage of thiols as chain transfer agents therefore reduces the overall molecular weight of the resulting polymer. In general, thiyl radicals that can also be directly generated from thiols and photoinitiators are electrophilic and thus suitable for reaction with electron-rich alkenes and alkynes. These radically mediated reactions are termed the *thiol-ene* and *thiol-yne* reaction, respectively.[12,13,97] A both scientifically and industrially important class of materials are the densely crosslinked uniform polymer networks that can be achieved *via* thiol-ene and thiol-yne mediated polymerizations. Finally, nucleophilic addition of thiols to electron deficient double bonds, termed the *thiol-Michael addition* reaction[g] is an important reaction pathway for thiols. Most commonly, electron deficiency of the double bond is provided by a conjugated carbonyl group,[98] yet other functional groups such as isocyanates

[g] In the literature scientists often employ confusing labeling for reactions between thiols and double bonds making it hard for the reader to distinguish between different types of reaction. In order to avoid confusion, the radical addition is termed *radical thiol-ene* reaction while the nucleophilic addition is termed *thiol-Michael addition* reaction in this thesis.

and corresponding derivatives are also suitable.[99] Throughout the following sections, radical thiol-ene, thiol-yne, and thiol-Michael addition will be described in more detail.

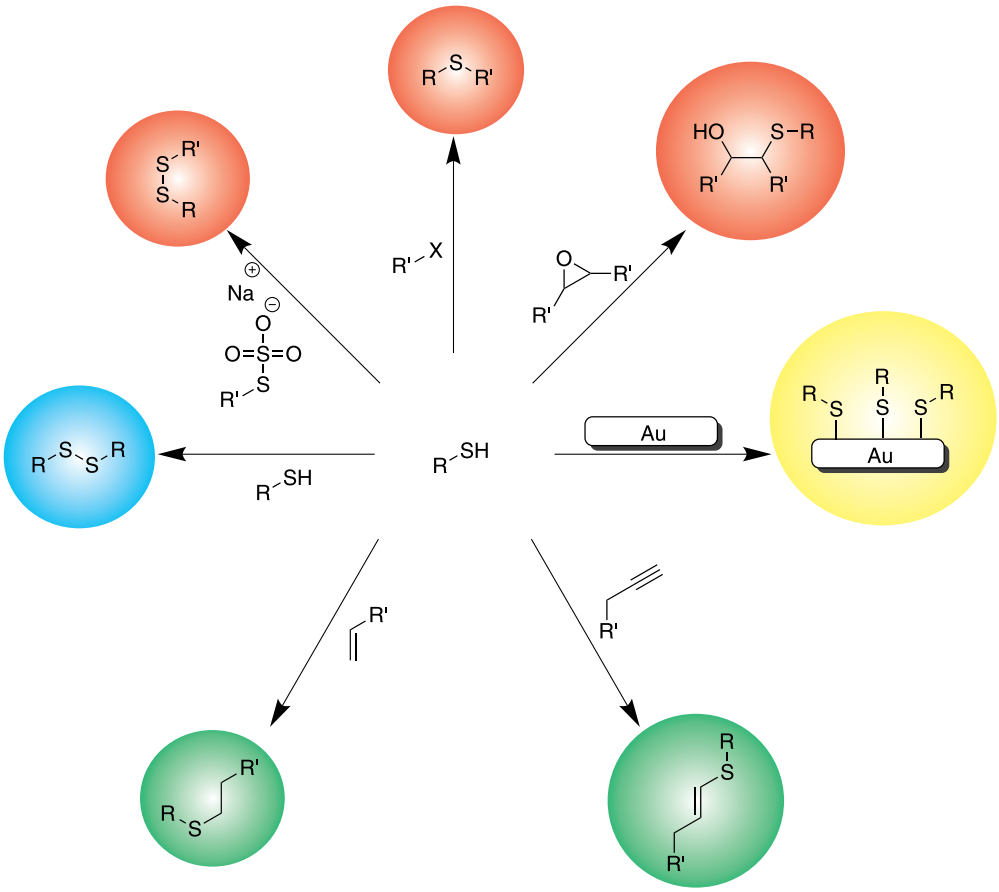

Figure 2.14: Schematic overview of reactions containing thiols as reactants. Nucleophilic substitution reaction products are highlighted in red, oxidations in blue, addition reactions in green, and coordinations in yellow.

2.3.2 Radical Thiol-Ene Reaction

As briefly mentioned above, the radical thiol-ene reaction is a radical addition reaction of a thiol to a preferably electron rich double bond, resulting in the formation of a thioether.[12,13] A mechanism for this reaction has been proposed and is displayed in Figure 2.15. A necessity for the reaction is a radical source. Typically, a photoinitiator is employed, generating radicals under exposure of light often at a wavelength between 300 and 400 nm. The radical then cleaves the relatively weak sulfur-hydrogen bond of the thiol, generating a thiyl radical *via* hydrogen abstraction. In the next step, also termed the propagation step, the thiyl radical reacts with the utilized double bond, forming a carbon-centered radical. Ideally, the carbon-centered radical does not undergo chain growth type homopolymerization with other alkenes but rather induces a chain-transfer with another thiol, resulting in the formation of a thioether and a

further thiyl radical. This newly generated thiyl radical subsequently induces a further reaction cycle. When employed as a polymerization reaction, the radical thiol-ene reaction therefore proceeds in a step growth fashion where each reaction cycle induces a further reaction. It has been demonstrated that electron rich double bonds such as allyl ethers or vinyl ethers and those with a large ring strain, *e.g.*, norbornenes polymerize faster than their electron deficient or non-strained counterparts, for instance, methacrylates or maleimides in the radical thiol-ene reaction.[100] Further, the mentioned electron rich alkenes, to be exact: their intermediate carbon-centered radicals, do not undergo homopolymerization and thus the polymerization occurs in an "ideal" manner. An interesting detail in the procedure is the rate-determining step in the reaction sequence.[101] While the overall rate of chain-transfer and propagation is equal, the slower component is the limiting factor for the overall rate. It was found that thiols with a more stable sulfur-hydrogen bond and less reactive carbon-centered radicals reduce corresponding chain-transfer- and propagation rates, respectively. By variation of the ene species and a given thiol, the reaction can thus be either chain-transfer limited (allyl ether) or propagation limited (vinyl silazane).

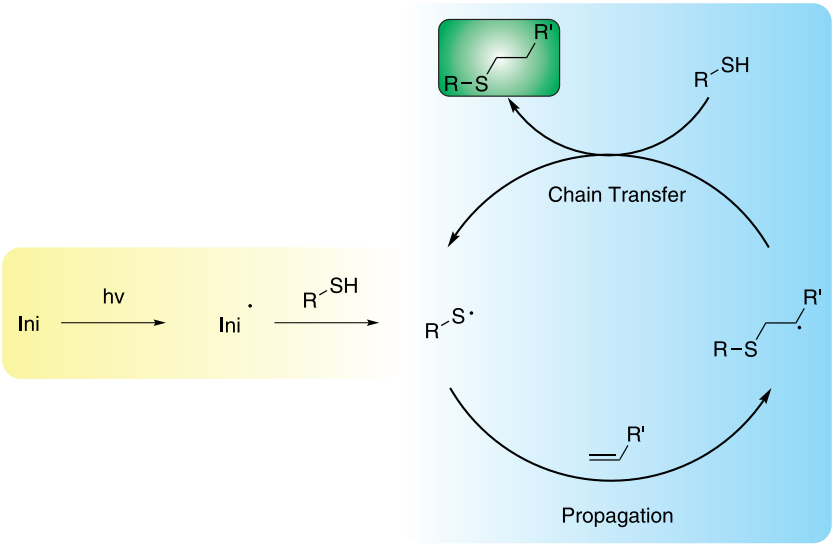

Figure 2.15: Schematic depiction of an ideal radical thiol-ene reaction. After radical initiation the process alternates between propagation and chain transfer with continuous production of a thioether as the reaction product. Initiation is emphasized in yellow while the cyclic reaction process and the reaction product are emphasized in blue and green, respectively.

If the combined number of functional groups of both thiol and ene exceeds five and each single component has a minimum functionality of two, crosslinked species can be produced *via* radical thiol-ene chemistry. In fact, an important section is the fabrication of crosslinked polymer networks *via* the radical thiol-ene reaction as it possesses several beneficial aspects when compared to traditional FRP. These aspects include rapid and near to quantitative formation of homogeneous, uniform materials, no side reactions at ambient conditions, for instance with oxygen, and optimized properties of resulting networks such as a distinct glass transition behavior.

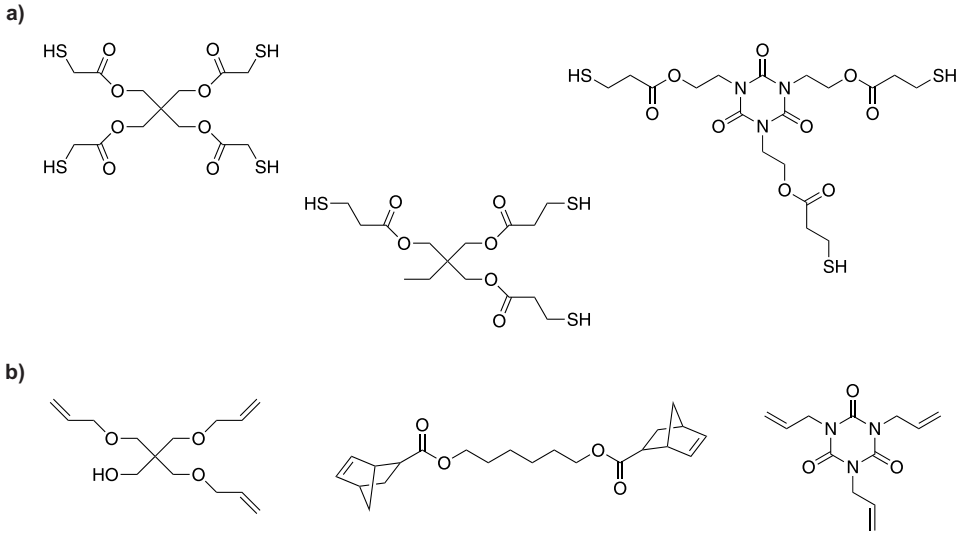

Figure 2.16: Common multifunctional monomers employed for the production of crosslinked networks by the radical thiol-ene reaction. Tri- and tetrafunctional thiols with different cores are displayed in a), corresponding molecules with electron-rich double bonds are displayed in b).

Commonly, networks are generated *via* photoinitiators that typically operate in the ultraviolet or the visible light region.[102,103] Additionally, the reaction can be conducted without the use of an initiator for large scale production of high quality materials if the monomer components and the irradiation wavelength are chosen appropriately. An advantage of this procedure is the near UV transparency of the product stemming from the dual role of the monomers as both reactants and initiators and the consequent absence of residual photoinitiator molecules in the material. During the procedure, absorbing species are bleached resulting in a polymer network with high transparency even at the 254 nm initiating wavelength.[104,105] Although often convenient, the usage of light is not a necessity for carrying out the radical thiol-ene reaction. In fact, any form of suitable radical source can be incorporated into the reaction including the introduction of thermal radical initiators.[106] A variety of different multifunctional thiols and enes is readily available. Examples of commonly employed monomers are displayed in Figure 2.16.

Next to the displayed rather common monomers, tailored molecules for applications have been synthesized and utilized for radical thiol-ene polymerization. For instance, allyl ether functionalized biodegradable polyesters,[107] thiols and enes from renewable resources,[108] highly functional dendrimers,[109] and telechelic dithiol polyesters for semicrystalline networks have been investigated.[110] Moreover, the use of monomeric components can be extended towards molecules that alter the ideal process of the radical thiol-ene reaction. Examples are the incorporation of methacrylates or acrylates into the reaction both of which can also undergo homopolymerization. Strictly speaking, acrylate or methacrylate incorporation into the radical thiol-ene reaction is identical to the usage of thiols in FRP as chain transfer agents. Nevertheless, it is interesting to observe the interplay of both competitive processes. In an example of a diacrylate and tetrathiol system, the dominance of the radical thiol-ene reaction for increasing amounts of thiol can clearly be observed in the storage modulus properties of

the resulting network.[111] It should be noted that albeit increasing the possibilities of radical thiol-ene chemistry, the simple reaction mechanism is sacrificed in such approaches which can lead to opaque material artifacts.

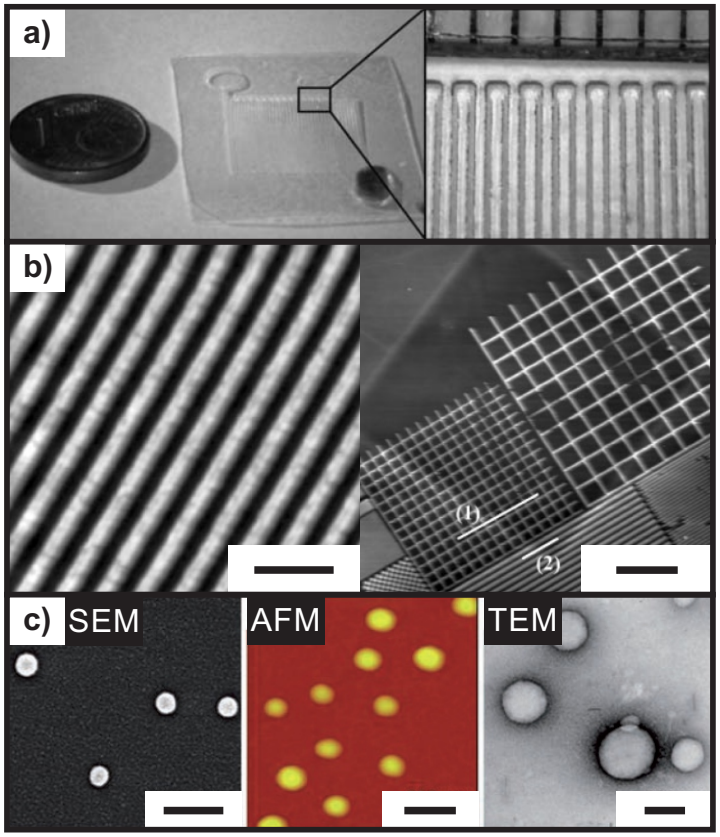

Figure 2.17: Different applications for the radical thiol-ene reaction. a) Fabrication of microfluidic devices by photopatterning in a multilayer approach. b) Step-and-flash imprint lithography for nanoscale substrate patterning (left) and subsequent modification *via* a photomask (right). Height profiles were taken along (1) and (2). The difference in height from the photomodification is close to 20 nm. c) Nanoparticle formation using flat core monomers analyzed by SEM, TEM, and AFM. Scale bars are 500 nm (left) and 10 µm (right) for b) and 200 nm (left and middle) and 100 nm (right) for c). Figure adapted from [112–114] with permission from the Royal Society of Chemistry and Wiley-VCH.

Apart from detailed investigations concerning the mechanism and general understanding of the radical thiol-ene reaction, it has been utilized in numerous applications as already mentioned above. In an interesting approach, radical thiol-ene polymerization was carried out employing thiols and vinyl silane derivatives (polyureasilazanes) as monomers, resulting in films with a thickness of up to several millimeters.[115] Subsequent pyrolysis lead to a stable 3D ceramic material. This process can be implemented when targeting microfluidic devices or optical components. Beneficial features of the radical thiol-ene reaction such as the low shrinkage and shrinkage stress, uniform network parameters and insensitivity to oxygen have also been

exploited for lithography and the fabrication of microdevices. Employing liquid thiol-ene adhesives, rapid and direct photopatterning in a multilayer masking approach can be conducted for the production of microfluidic devices with multidimensional, complex channels (see Figure 2.17).[112] Nanoimprint lithography, in particular the step-and-flash imprint technique, has also been performed using thiol-ene resists, leading to the production of substrates with nanoscale patterning.[113] Further, the nanopatterns were modified in a second dilute thiol-ene reaction enabling the grafting of crosslinked films on the nanopatterned substrates *via* a photomask. Interesting nanoparticles with a functional surface in a non-covalent manner have also been synthesized in a radical thiol-ene based process by usage of monomers with a planar core and several functional groups at the periphery. The non-destructive surface tailoring can be exploited for imaging or targeted delivery.[114] Another important and challenging yet very different field is the chemical functionalization of polymer chains that allows large range tailoring of various material parameters. A well studied example is the use of radical thiol-ene chemistry for the functionalization of residual double bonds in butadiene homo- and copolymers with a large range of monofunctional thiols.[116–118] In this approach both chemical and physical characteristics of the polymer were efficiently altered, resulting in, among others, amphiphilic behavior or pronounced chemical reactivity. One approach, the "photofixation", for 3D lithography employing a combination of the Diels-Alder and radical thiol-ene reaction was published during this thesis by another group.[44] It will be presented and compared to the work of the current thesis in Section 3.1.7.

Although the presented applications demonstrate the significant importance of the method as a powerful tool for material science, care must be taken for the implementation of the radical thiol-ene reaction for very demanding and delicate conjugations. Being a radical process, not only the aforementioned homopolymerization may occur, but also disulfide formation or radical-radical termination events. For network formation such side reactions have little influence on the final outcome and are therefore often negligible. In more demanding fields such as linear polymer chain functionalization side effects become visible, yet can be compensated, for instance by employing an excess of monofunctional thiol for the modification of polymers with pending double bonds. Highly demanding reactions such as polymer-polymer conjugation are unforgiving in terms of renunciation from an ideal reaction behavior, for instance regarding equimolarity, side product formation, and full conversion. It has been reported that for this purpose, the radical thiol-ene reaction is not suitable.[119] Thus, it is doubtful if the radical thiol-ene reaction can be termed a *click* reaction[17] as it clearly violates – in the context of polymer-polymer conjugation – important criteria in terms of byproduct formation, equimolarity of reactants, facile and straightforward reaction conditions, and high conjugation efficiencies.

2.3.3 Radical Thiol-Yne Reaction

Radical addition reactions of thiols can also be conducted with suitable carbon-carbon triple bonds, a reaction termed the thiol-yne reaction or thiol-yne coupling.[97,120] Similar to its thiol-ene counterpart, a radical source is needed to commence the reaction by abstraction of the hydrogen from the sulfur-hydrogen bond of the thiol (see Figure 2.18). The generated thiyl radical then undergoes radical addition to an alkyne resulting in formation of a vinyl

sulfide radical in the propagation step. Subsequent chain transfer occurs with another thiol, yielding a vinyl sulfide product and a thiyl radical which participates in a further reaction cycle. While it is possible to tailor reaction conditions for the generation of the vinyl sulfide as the main reaction product,[121] vinyl sulfides are in general a chemically active species in the presence of thiyl radicals. Therefore, in a second reaction cycle, radical addition of a thiyl radical to the vinyl sulfide can occur in a consecutive propagation step. A following chain transfer step with a further thiol yields a saturated bis-sulfide species as the final reaction product together with a thiyl radical that can participate in a further reaction cycle.[h] Throughout the entire reaction sequence for bis-sulfide formation one alkyne and two thiols are consumed. When comparing radical addition rate coefficients it has been shown for different thiols and alkynes that the second coupling cycle containing the vinyl sulfide as participant possesses a larger addition rate coefficient than its alkyne counterpart, indicating the possibility for efficient bis-sulfide species generation.[122,123] Again, classification of this reaction

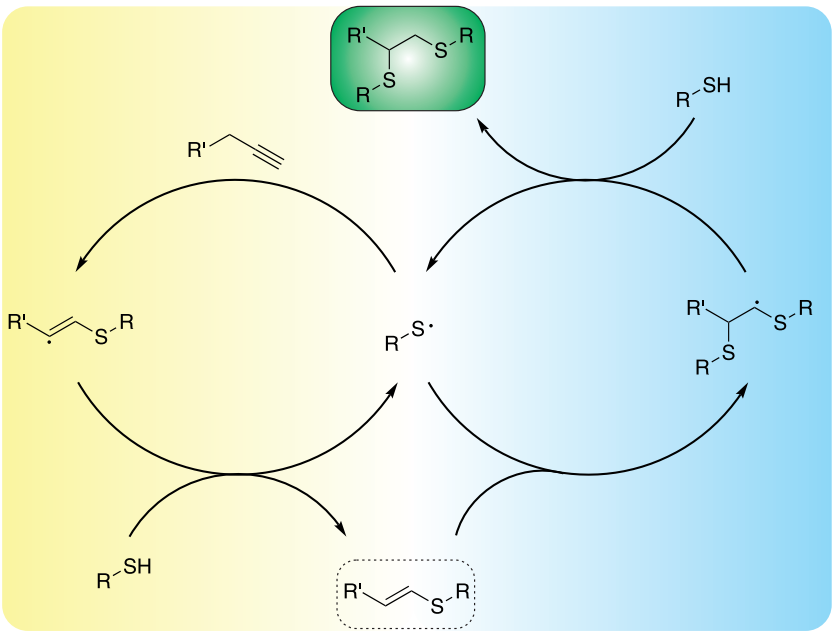

Figure 2.18: Schematic depiction of the radical thiol-yne reaction. In the first reaction cycle (yellow) a thiyl radical reacts with an alkyne to form a vinyl sulfide (hachured). Often, the vinyl sulfide reacts with another thiyl radical in a second reaction cycle (blue) yielding the bis-sulfide species (green) as the main reaction product. Throughout the complete sequence, two thiols and one alkyne are consumed.

can be debated as many articles in the literature associate the radical thiol-yne reaction with *click* chemistry.[120,124] When regarding the first reaction cycle for often employed terminal alkynes, regioselectivity in an anti-Markovnikov manner can be presumed, yet stereoselectivity is generally lost as a mixture of stereoisomers is produced. Additionally, the second

[h] In the literature different terms for the described reaction can be found. While some term the combination of both reaction cycles the radical thiol-yne reaction, others describe it as a sequence of thiol-yne and thiol-ene coupling. In this thesis the combination of both reaction cycles is termed radical thiol-yne reaction.

reaction cycle faces further disadvantages. During bis-sulfide generation new chiral centers are formed without any stereoselectivity and even regioselectivity is not generally given due to 1,1 bis-addition that can occur with several alkynes. The described drawbacks in regio- and stereoselectivity lead to the clear conclusion that the radical thiol-yne reaction is not a *click* reaction.[i]

Despite the noted drawbacks, radical thiol-yne coupling is a highly popular reaction in materials chemistry with beneficial attributes similar to those of radical thiol-ene coupling. An interesting feature of the radical thiol-yne reaction when targeting the bis-sulfide species is the possibility to straightforwardly synthesize hyperbranched architectures. In one application, a synergy of thiol-yne and hydroxy-anhydride coupling reactions was employed for dendrimer synthesis with 24 terminal functionalities which was applied for the conjugation of *cis*-platinum.[125] When performed with a photoinitiator as a radical source, photopatterning of surfaces *via* a photomask is possible and has been conducted for the production of spatially controlled, dual functional surface decoration of alkyne containing polymer brushes attached to the surface of a silicon wafer (see Figure 2.19).[126] Utilizing micro-contact printing as an alternative lithographic approach, alkyne terminated self-assembled monolayers on silicon wafers have been connected to polydimethylsiloxane stamps "inked" with a thiol- and photoinitiator containing solution. By irradiation with 365 nm light for several minutes the thiol species was efficiently immobilized throughout the areas in contact with the stamp.[127] Employing a laser, thiol-yne coupling has also been exploited for the *in situ* photocrosslinking of an aliphatic hyperbranched polyester. In this manner, patterning was achieved and patterned structures were investigated for cell adhesion experiments.[128] Thiol-yne coupling has also been employed for tailoring of polymer chains. Subsequent to RAFT polymerization, thiol-yne and hetero Diels-Alder chemistry was employed for the synthesis of a polymer with glycodendric terminal functionality that can undergo self-assembly to micelles in water.[129]

Naturally, the thiol-yne reaction itself can be employed for the production of crosslinked polymeric networks in a step growth manner.[130] Unlike the radical thiol-ene approach, the usage of bifunctional components is sufficient for the production of polysulfide networks when targeting the bis-sulfide formation as the major reaction product. Furthermore, tailoring of the network properties can easily be achieved, *e.g.*, by changing the weight percentage of sulphur throughout the network. This alteration results in a change of density and refractive index of the network, thereby expressing a linear dependence between the weight percentage of sulfur and the density or the refractive index. As expected, the crosslinking density can be increased and the resulting network parameters can be modified for elevated monomer functionality.[131] All the mentioned network formations have in common that they are easy to conduct, reach a high conversion within minutes, and exhibit defined parameters due to their uniform structure.

[i] It should be mentioned that non-radical thiol-yne reaction procedures do exist for selected alkynes employing amines or metal complexes, even with increased stereoselectivity. However, these approaches are rather specialized and not extensively applicable. Therefore they are not discussed in detail in this thesis.

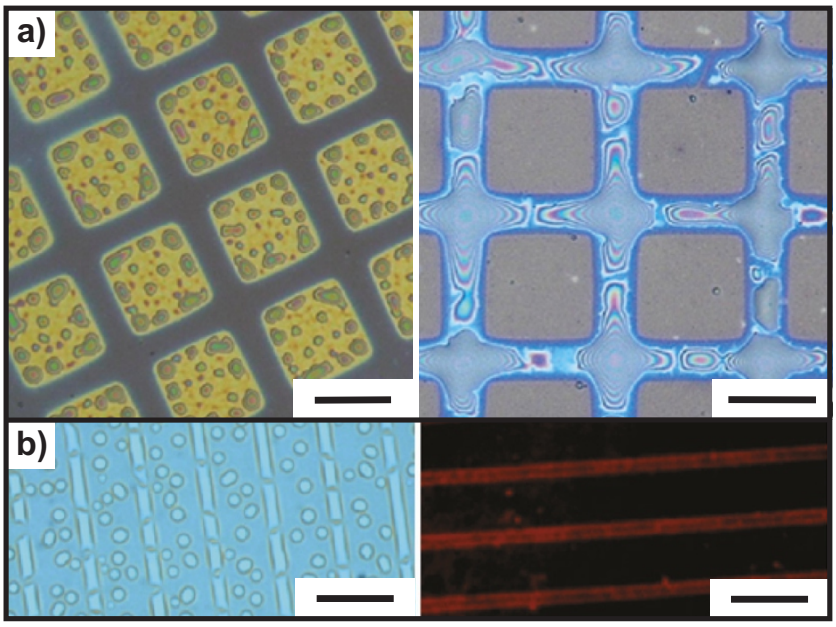

Figure 2.19: Lithographic applications of the radical thiol-yne reaction. a) Spatially resolved sequential patterning of surface-bound alkynes and two thiols (mercaptopropionic acid and DTT) using a photomask. The resulting change in hydrophilicity for different regions is observed by condensation imaging and resulting selective nucleation. Inverse reaction procedure leads to inverse hydrophilicity (compare left and right image). b) Verification of thiol-yne based micro-contact printing and resulting immobilization of galactoside-thiol on alkyne self-assembled monolayers *via* condensation imaging (left) and fluorescence microscopy (right). Scale bars are 50 µm for a) and 30 µm for b). Figure adapted from [126, 127] with permission from the American Chemical Society.

2.3.4 Thiol-Michael Addition Reaction

Apart from the above described radical additions, thiols readily undergo a non-radical addition reaction with certain double bonds as depicted in Figure 2.14, termed the thiol-Michael addition reaction.[132][j] A reaction mechanism has been proposed for this reaction which is identical to the mechanism described in Figure 2.15 when replacing all radical species with their anionic counterparts and assuming a different initiation process. In the presence of a catalyst such as a base but also a Lewis acid, a metal,[133] or even an enzyme,[134] the thiol is deprotonated to the thiolate anion. Being a potent nucleophile, the thiolate anion adds to a suitable double bond, forming a carbanion. Thereby it is important that the double bond is of electron deficient nature. Thus, maleimides, (meth)acrylates, or other $\alpha\beta$-unsaturated carbonyl molecules have proven to be potent reaction partners. The formed carbanion deprotonates another thiol in a further reaction step leading to the formation of the thioether product

[j] In the literature a plethora of names for this reaction can be found such as *thiol-based click*, *sulfa-Michael addition*, or *thiol-maleimide click*. In order to delineate from radical addition while maintaining consistency, the term *thiol-Michael addition reaction* is utilized in this thesis.

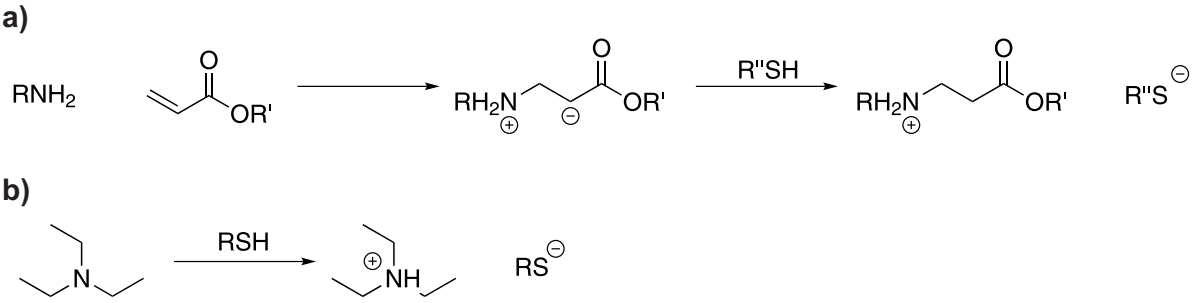

Figure 2.20: Different initiation procedures for the thiol-Michael addition reaction. a) Nucleophilic initiation *via* participation of the Michael acceptor followed by deprotonation of the thiol by the carbanion and b) direct deprotonation of the thiol by a base.

and an additional thiolate anion that participates in a further reaction cycle. Typical bases employed for the thiol-Michael addition reaction are tertiary amines such as triethylamine,[135] yet the addition of a catalyst can also be circumvented by employing adequate solvents.[136] When going to primary amines and phosphines as catalysts, the initiation mechanism is changed into a nucleophile-initiated thiol-Michael addition reaction where the catalyst adds to the Michael acceptor and formation of the thiolate results from deprotonation *via* the formed carbanion. By a convenient choice of catalysts, regioselectivity can be achieved when employing fumarate esters as Michael acceptors[137] and even enantioselective thiol-Michael additions can be performed when utilizing acrylates and methacrylates in combination with lanthanide catalysts.[138] While coupling processes in the radical thiol-ene reaction can occur, no anionic coupling reactions terminating the process in the thiol-Michael addition reaction take place, allowing for quantitative reactions. The combination of mild reaction conditions, rapid proceeding to quantitative yields, lack of side products, and other above mentioned benefits underpin the fact that the thiol-Michael addition reaction is a powerful tool for covalent bond formation. Compared to all other thiol containing reactions, the thiol-Michael addition reaction comes closest to the stringent *click* criteria that an ideal reaction should feature.

Beneficial features of the thiol-Michael addition reaction have been exploited in the organic synthesis of small molecules. Consequently, the reaction has been explored in other high-level scientific fields such as materials chemistry. In this context, the reaction has been employed as an efficient conjugation methodology for numerous modifications of polymers. One application is the endgroup modification of terminal double bond glycopolymers synthesized by cobalt-catalyzed chain transfer polymerization.[139] In the course of this study, thiol-Michael addition was orthogonal to epoxide ring-opening reactions of pending oxiranes which was subsequently performed with sodium azide, allowing for an even further post-modification *via* the CuAAC reaction. Another interesting strategy for endgroup modification of well-defined polymers is the subsequent reduction of the incorporated chain transfer agent in RAFT polymers which can be easily reduced to a thiol. Under conditions for thiol-Michael addition, thiol-containing polymer reacts efficiently with trimethylolpropane triacrylate yielding well-defined three-armed star polymers.[140] Moving from endgroup modification to the reaction of pending functional groups of a polymer chain, both thiol-Michael addition and radical thiol-ene were conducted with a

RAFT copolymer consisting of *N*,*N*-dimethylacrylamide and *N*-(2-hydroxyethyl)acrylamide. In both cases, the pending hydroxyl groups were reacted with an acrylate-containing isocyanate and the resulting acrylate groups were efficiently addressed for the addition of a large range of thiols.[141] In another approach, pending thiols equipped with a photocleavable protection group were incorporated into an ATRP-synthesized polymethacrylate. Utilizing light of 320 nm wavelength, the protection group was cleaved, resulting in the formation of thiols that efficiently reacted *in situ* with a maleimide under mild thiol-Michael reaction conditions.[142] Hydrogels can also be fabricated in a thiol-Michael approach. In one example, a hydrogel was created utilizing a multifunctional maleimide and thiol-PEG macromer.[143] By employing an excess of maleimide functionality, residual maleimides remained present after network formation and enabled a subsequent Diels-Alder reaction with a furan derivative. This application allows for the controlled release of the furan derivative from the PEG-based hydrogel for different initial maleimide concentrations or temperatures and a given span of time. Surface modification of inorganic TiO_2 nanoparticles is also possible *via* thiol-Michael addition. Activated nanoparticles were silanized with a thiol-containing silane. In a subsequent step, the anchored thiol was employed in a thiol-Michael addition for the covalent immobilization of PEG-containing double bond-terminated methacrylate polymer brushes, thereby significantly increasing the nanoparticle solubility in water.[144] In a soft lithography approach, thiol-Michael addition was conducted for a stable, hydrophilic, and microfluidic chip-on-boundless material device with a trifunctional acrylate and a trifunctional thiol as monomers. Interestingly, the initiating tertiary base was introduced in a synthetic step preceding crosslinked material formation: by an aza-Michael addition of a secondary amine to an acrylate moiety of the triacrylate monomer.[145]

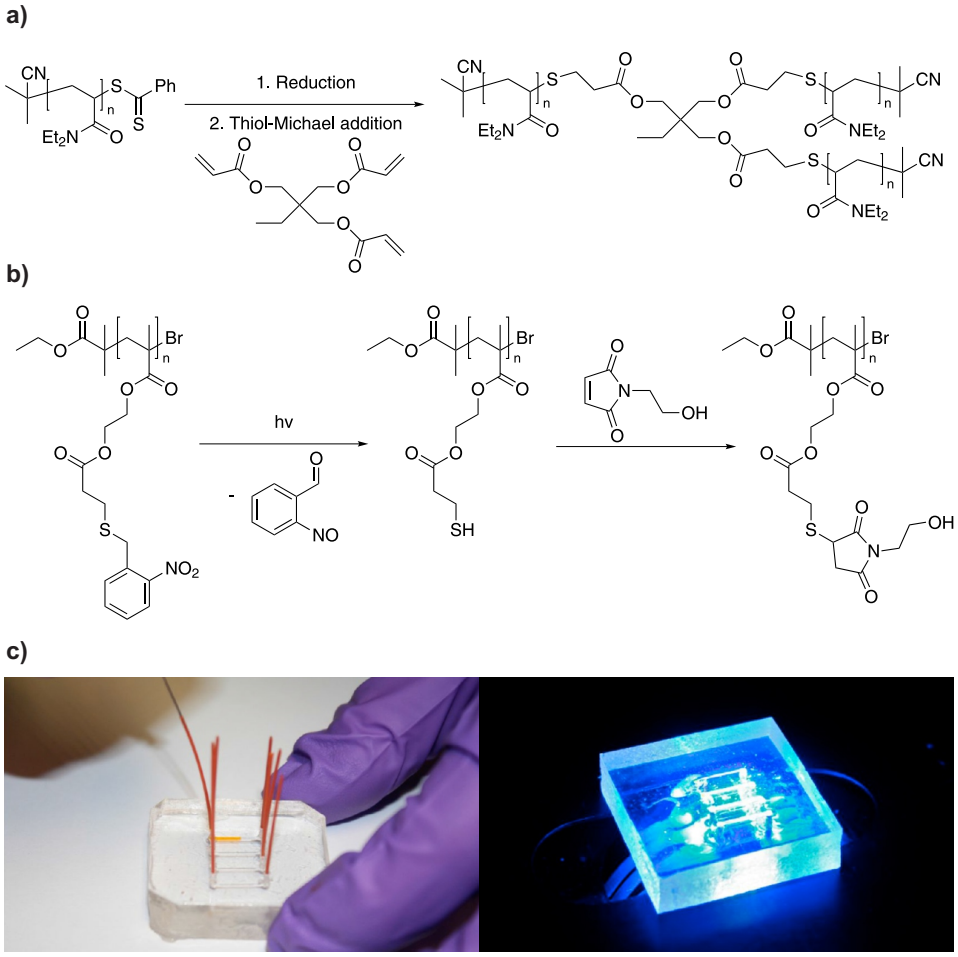

Figure 2.21: Materials applications of the thiol-Michael addition reaction. a) Synthesis of a three-armed star polymer by reduction and subsequent thiol-Michael addition of a RAFT polymer and a triacrylate core. b) Photoinduced deprotection of pending thiol moieties of a linear methacrylate polymer and subsequent thiol-Michael addition with a maleimide counterpart. c) Depiction of an operating microfluidic device fabricated by soft lithography employing the thiol-Michael reaction. c) Adapted from [145] with permission from the American Chemical Society.

When considering lithographic applications where a spatial resolution is important in two or even three dimensions, it quickly becomes apparent that the thiol-Michael addition reaction lacks a distinct advantage that its radical counterpart exhibits: The possibility for facile confinement of the reaction to a distinct area or volume. For the radical thiol-ene reaction, this option is straightforwardly realized by employing light and a photoinitiator for radical generation. This is not the case for the respective Michael addition. In an attempt to overcome this disadvantage several investigations have been conducted in order to obtain a thiol-Michael addition reaction that is triggered by light. It is clear that the actual Michael-type addition must remain unaltered as any deviations would surely deteriorate the overall reaction. Therefore, the only possibility to implement a light trigger is *via* photorelease or photodeprotection of a

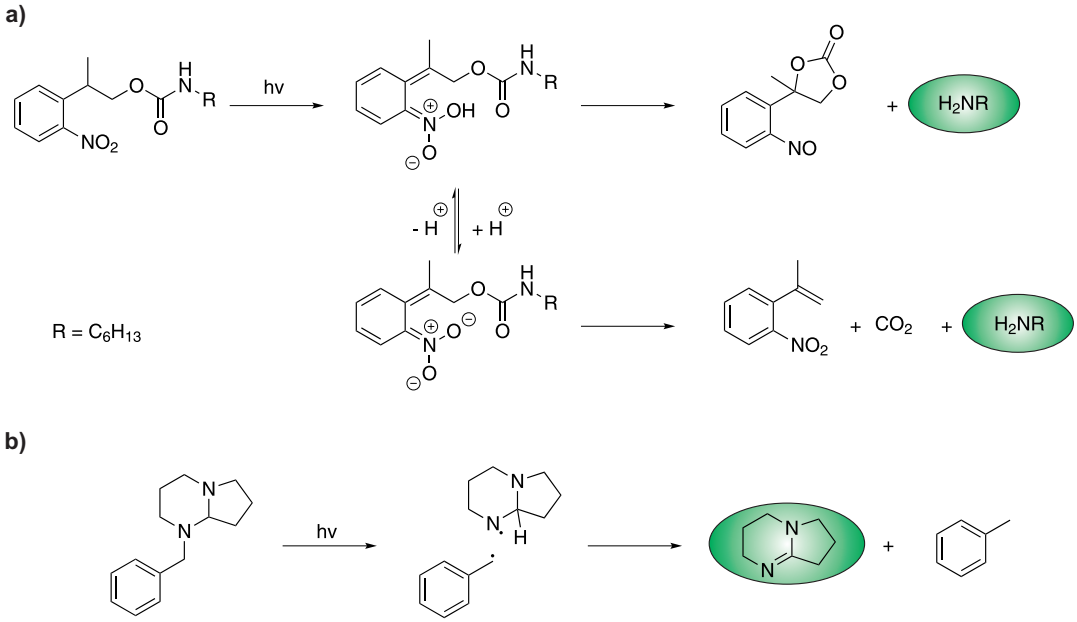

Figure 2.22: Photogeneration of different catalysts (highlighted in green) for the thiol-Michael addition reaction. a) Photo-release of a caged primary amine for nucleophilic initiation *via* hexylamine, and b) photo-activation of a photo-latent base for the generation of DBN as a basic initiator.

crucial reaction component, namely the catalyst, the thiol, or the double bond. In this context, different catalysts and catalyst precursor molecules were investigated. Specifically for the thiol-Michael addition reaction, a caged primary amine was implemented that releases hexylamine when irradiated with 320-390 nm light.[146] The released hexylamine efficiently initiates the thiol-Michael addition reaction *via* a nucleophilic initiation pathway. In a slightly different context regarding the reaction of thiolates for ring-opening of epoxides, a photolatent amine is employed that releases DBN upon light exposure which deprotonates a present thiol to the thiolate anion.[90] Potentially, this approach can be transferred to thiol-Michael addition reactions allowing for efficient thiolate anion generation by light activation of the photo-latent base. Next to photo-generation of the catalysts, the thiol can be provided in a light triggered step. As briefly described above, photo-labile protection groups for thiols are known and have been exploited in the literature.[142] This photo-release process has already been employed for facile and efficient bioconjugation.[147] Unfortunately, photo-induced thiol-Michael addition remains up to this day a subtopic which requires further in-depth investigation to increase the scope of application. This necessary task must be focused in order to take full advantage of the highly promising benefits.

2.4 Azide-Alkyne Cycloaddition

2.4.1 Copper-Catalyzed Azide-Alkyne Cycloaddition

Among the modular ligation techniques associated with *click* chemistry, the copper-catalyzed azide alkyne cycloaddition (CuAAC) has been labeled as the "cream of the crop" reaction,[17] stating that this reaction comes closest to the ideal *click* reaction. The CuAAC reaction is a copper-mediated version of the thermally induced 1,3-dipolar Huisgen cycloaddition between an azide and a terminal alkyne (see Figure 2.23) with a Cu(I)-complex as an active catalytic species. While the thermal reaction leads to a mixture of regioisomers as products, the copper-mediated reaction is highly regiospecific. In many cases the catalyst system consists of a copper(I) salt and an adequate ligand such as CuBr and N, N, N', N", N"-pentamethyldiethylenetriamine (PMDETA), respectively. However, such systems are prone to oxidation and therefore the reaction must be conducted under the exclusion of molecular oxygen. A convenient alternative is the usage of $CuSO_4$ and sodium ascorbate where the Cu(I) species is generated *in situ* by reduction of Cu(II).[148] In this fashion it is possible to conduct the reaction in the presence of oxygen. In a proposed mechanism, the Cu(I) species abstracts a hydrogen from the terminal alkyne under formation of a complex. Subsequently, cycloaddition with the azide occurs, followed by an exchange of the Cu(I) species with a hydrogen yielding the 1,2,3-triazole as the reaction product and thereby regenerating the catalyst.

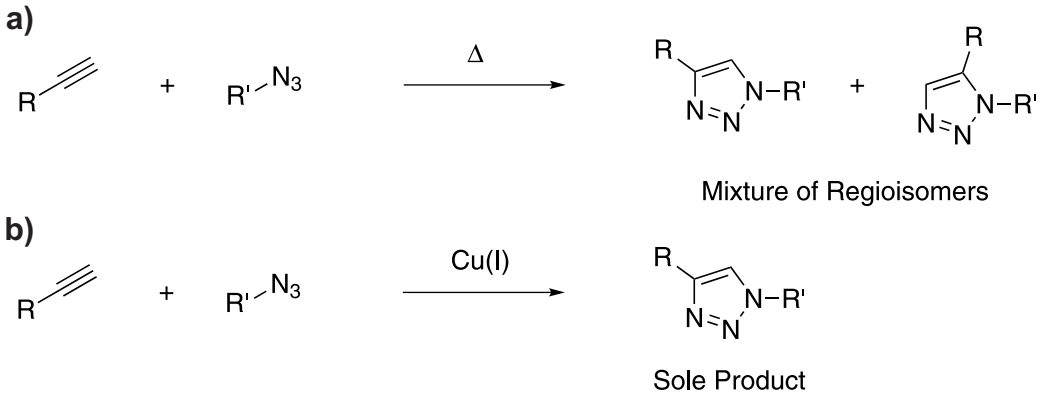

Figure 2.23: Product formation comparison of a) the conventional thermally induced 1,3-dipolar Huisgen cycloaddition and b) the copper-catalyzed version of the cycloaddition. While the conventional reaction yields a mixture of regioisomers, the CuAAC reaction yields the 1,4-substituted 1,2,3-triazole as the sole product.

In polymer science, the CuAAC reaction has been extensively employed for the formation of, dendrimers,[149] star polymers,[150] and hydrogels,[151] underlining the status of this reaction as being one of the best existent ligation methodologies. When placing this reaction into a lithographic context it becomes evident that spatial resolution *via* CuAAC is a challenging endeavor. Similar to the thiol-Michael addition or a Diels-Alder reaction, a possibility to achieve this task is the photoprovision of a crucial reaction component. Due to the large overall interest in this reaction, several approaches have been investigated that have either

been employed or show great potential for lithographic applications. The photo-induced reduction of Cu(II) to Cu(I) has proven to be one option to obtain spatial and temporal control of the CuAAC reaction.[152] In this approach reduction, occurs under participation of radicals generated from a photoinitiator under ambient conditions. The transiently formed Cu(I) can then undergo numerous reactions including a further radical-mediated reduction to Cu(0), disproportionation to Cu(II) and Cu(0), or oxidation with present oxygen. However, Cu(I) also participates in CuAAC reactions, a reaction pathway that can be exploited for synthesis of small molecules, as well as for patterning of materials. Next to photoreduction, adequate alkyne moieties can be provided in a light-induced manner. Cyclooctyne moieties can be prepared in an efficient decarboxylation reaction of corresponding cyclopropenones.[153] Interestingly, due to the distinct ring strain of the cyclooctyne, subsequent 1,3-dipolar cycloadditions with azides can be performed without catalytic Cu(I) at ambient temperature. In a multi-step approach, bifunctional surface modification has been performed *via* this reaction (see Figure 2.24).[154] In the said approach a photomask was employed in order to decarboxylate certain regions of the surface-attached precursor molecule that were reacted with an azide-containing dye. In a second step, the sample was globally irradiated, thereby decarboxylating hitherto unexposed regions in the presence of an azide-containing agent. Finally, in a particularly interesting approach, a precursor molecule containing a fluoroaryl azide and an alkyne moiety was immobilized in a PEG-based matrix *via* 2PA in a spatially resolved manner.[155] Immobilization was performed by a light-induced decomposition and nitrene insertion of the azide, resulting in the 3D spatially resolved presence of alkyne moieties. In a second step, an azide-containing dye was covalently immobilized throughout the alkyne-containing volume of the PEG matrix by conducting the CuAAC reaction. Analysis of the modified volume was investigated by LSM, revealing photografted 3D patterns with micrometer scale resolution.

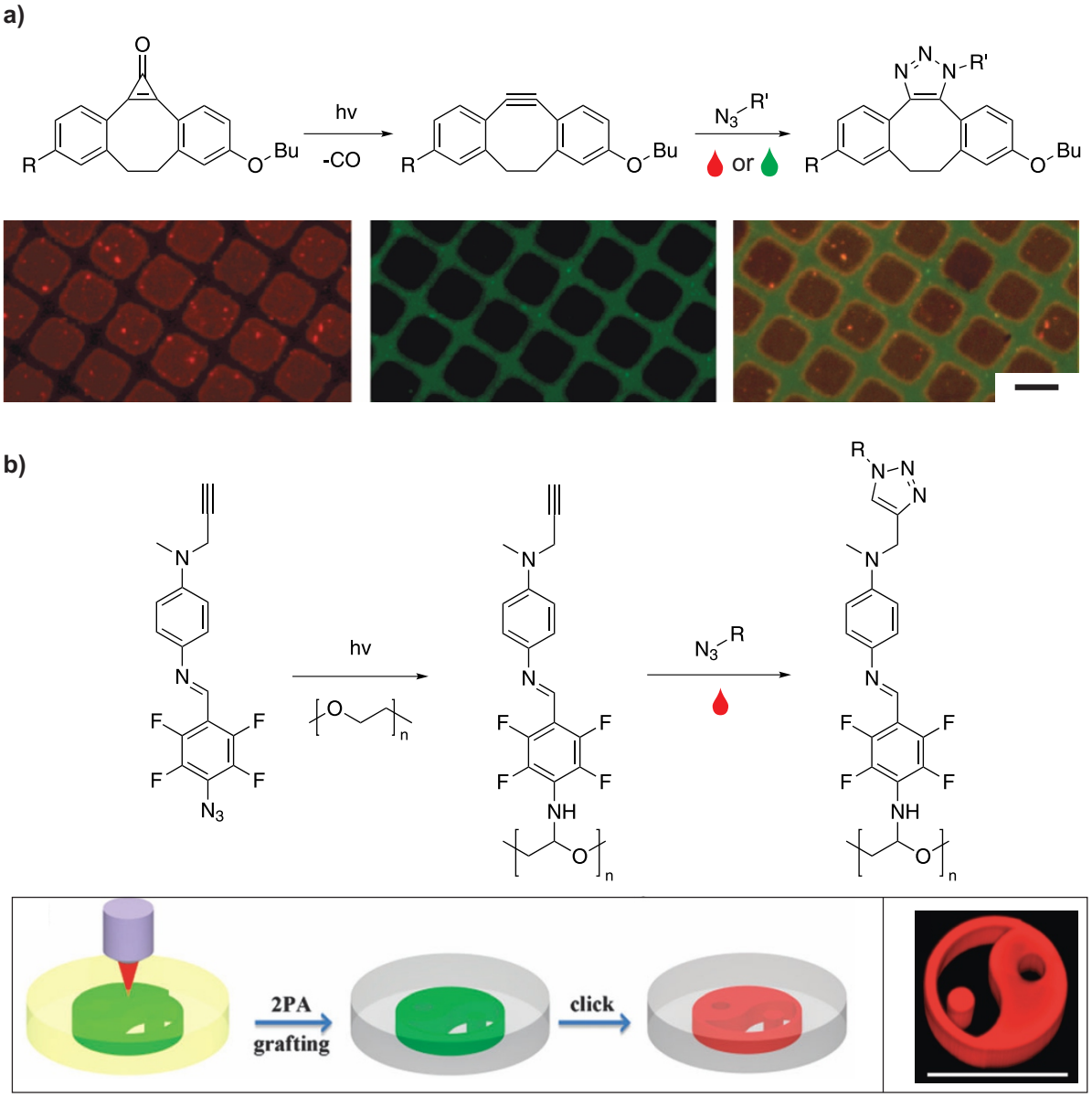

Figure 2.24: a) Photo-induced generation of a cyclooctyne compound (top) and application for spatially resolved surfaces employing two azide-containing fluorescent molecules (bottom). b) Two-photon induced immobilization of alkyne moieties and subsequent labeling *via* CuAAC in PEG hydrogels. The reaction scheme (top), the illustrated procedure (bottom, left), and an LSM image (bottom, right) are depicted. Scale bars are 10 and 100 µm for a) and b), respectively. Figure adapted from [153, 154] with permission from the Royal Society of Chemistry and the American Chemical Society.

2.5 Photoinduced Diels-Alder Chemistry

2.5.1 Brief Description of Classical Diels-Alder Chemistry

Since the first discovery in 1928[156] the Diels-Alder reaction has evolved to be an extremely important tool for carbon-carbon bond formation in synthetic chemistry.[157,158] This circumstance owes to several aspects of the reaction that are highly beneficial for complex molecular synthesis. In a typical reaction, feasible with a broad spectrum of readily available starting materials, rapid reaction rates are common and the reaction can be driven to high yields under a multitude of conditions. Further, no byproducts are formed during this [4+2] cycloaddition reaction, greatly simplifying work-up procedures. The Diels-Alder reaction also proceeds in an orthogonal manner towards many other functional groups. Due to the mentioned benefits several investigations have been conducted over the years to better understand the process and, consequently, tailor product formation.

Theories and rules concerning the Diels-Alder reaction have evolved, fundamentally increasing the general understanding and thereby enabling precise prediction of the product formation. One theory is the frontier molecular orbital theory,[159] stating that the highest occupied and the lowest unoccupied molecular orbitals of the respective components (HOMO and LUMO) determine the reaction. The energetic level of the HOMO-LUMO gap correlates with the overlap of the frontier orbitals. Thus, reactions that exhibit a small energetic gap are kinetically favored. In a conventional Diels-Alder reaction, small gaps exist between the HOMO of the diene and the LUMO of the dienophile. Common systems featuring this constellation are termed Diels-Alder reactions with “normal” electron demand. It should be noted that, albeit being uncommon, Diels-Alder reactions with “inverse” electron demand also exist where interaction between the HOMO of the dienophile with the LUMO of the diene takes place. A set of rules applicable for the Diels-Alder reaction but also for pericyclic reactions in general are the Woodward-Hoffmann rules.[160] Assuming that the orbital symmetry is maintained during reaction, these rules enable the prediction wether heat or light is the trigger for a pericyclic reaction. In this context, the Diels-Alder reaction can be classified, as mentioned above, as a [4+2] cycloaddition that proceeds in a thermal manner. With the aid of the Woodward-Hoffmann rules it became possible to precisely predict stereoinformation of the formed product,[161] a circumstance that is of particular value for total synthesis and methodologies in the context of bio-conjugations.[162]

As a result of the high number of beneficial features, the Diels-Alder reaction often fulfills the stringent criteria of the *click* chemistry paradigm and is often referred to – next to the CuAAC reaction – as a paramount *click* chemistry example. Naturally, the pronounced versatility has lead to the implementation of Diels-Alder chemistry in the majority of scientific fields that require efficient conjugation tools such as polymer or, to be more general, materials science.[163,164] Important reaction features such as the thermal reversibility or the usage of thiocarbonyl compounds as reaction components further extend this ligation method and amplify its extraordinary significance in this field. Reaction systems of the widely utilized furan-

maleimide pair, a hetero Diels-Alder system and a reversible surface anchoring application investigated in our group,[165] are depicted in Figure 2.25.

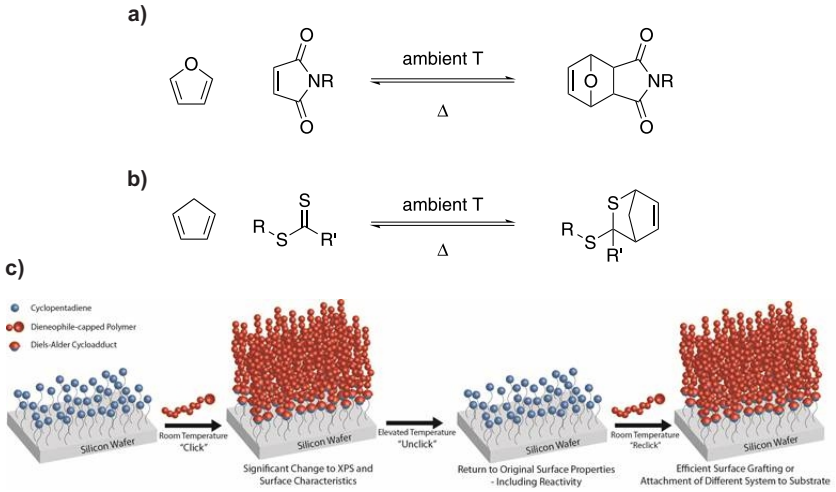

Figure 2.25: Depiction of widely utilized Diels-Alder reactions systems and an exemplified application. a) The furan-maleimide pair, b) a hetero Diels-Alder system employing a dithio carbonyl compound and cyclopentadiene, and c) an example for a Diels-Alder reaction exploited for the operation of an efficient, thermally reversible surface immobilization of dienophiles. c) Adapted from [165] with permission from Wiley-VCH.

2.5.2 Light-Triggered Diels-Alder Reactions

Apart from all the aforementioned benefits, the Diels-Alder reaction, similar to the already discussed thiol-Michael addition, is not directly triggered by light. As a matter of fact, the Woodward-Hoffmann rules explicitly state that the Diels-Alder reaction, being a [4+2] cycloaddition, must be thermally triggered. However, the usage of light as a reaction trigger is beneficial for a multitude of applications, especially when considering lithographic procedures. Consequently, light must be employed for the provision of an active component in order to achieve a light-induced Diels-Alder reaction. Therefore, two straightforward possibilities are available: the light-induced activation of either the dienophile or the diene. An advantage for numerous Diels-Alder systems is their rapid progression at ambient temperatures, greatly facilitating photochemical approaches as the photo-generated component promptly reacts in the [4+2] cycloaddition.

Both the photogeneration of the dienophile and the diene have been investigated (see Figure 2.26). One possibility for the light-induced provision of a diene is employing *o*-naphtoquinone-methide chemistry.[166] In a specific example, when exposing 3-hydroxy-2-naphtalenemethanol to UV light, a highly reactive *o*-naphtoquinone-methide species is generated that can be trapped with suitable dienophiles in a Diels-Alder reaction. However, it should be noted that, being an electron deficient diene, the *o*-naphtoquinone-methide features an “inverse”

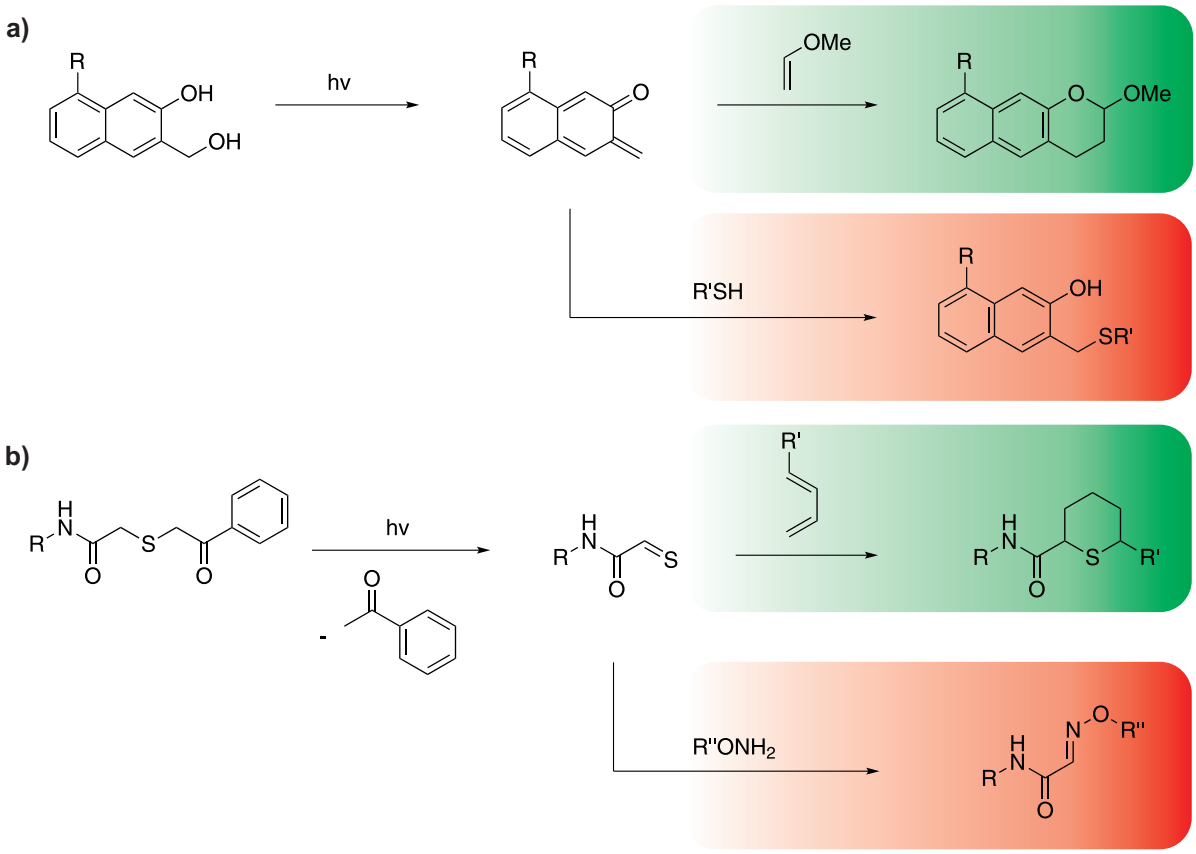

Figure 2.26: Exemplified depiction of light-induced Diels-Alder reactions by: a) the *o*-naphtoquinone-methide approach and b) the phenacyl sulfide approach. Diels-Alder reactions of each reactive intermediate species is highlighted in green while competitive reactions occurring with thiols or hydroxylamines are highlighted in red.

electron-demand Diels-Alder reaction. As a consequence, the reaction is restricted to electron rich dienophiles such as vinyl ethers. Nevertheless, *o*-naphtoquinone-methide chemistry has been employed in a spatially resolved grafting approach with vinyl ethers as dienophiles.[167] Besides the *o*-naphtoquinone-methide chemistry that allocates dienes, it is also possible to generate suitable dienophiles in a light-induced fashion. For this purpose, phenacyl sulfide functionalities can be employed which serve as an efficient source for the generation of reactive thioaldehyde species when exposed to UV light *via* a photofragmentation mechanism. The *in situ* produced thioaldehyde is a potent dienophile that can undergo a "normal" electron-demand Diels-Alder reaction with suitable dienes.[168] It must be noted that both the thioaldehyde and the *o*-naphtoquinone-methide are reactive intermediates that also undergo reactions with other functional groups. While it has been shown that *o*-naphtoquinone-methides can participate in Michael addition reactions,[169] thioaldehydes undergo efficient and rapid trapping reactions with different nucleophiles.[170] Although the mentioned reactions can in many cases be avoided, the criterion of orthogonality is clearly violated, leading to a loss of the *click* status

for these photoinduced cycloadditions. There is, however, a third possibility for photoinduced Diels-Alder chemistry that does not violate the orthogonality condition. *Via* a process termed photoenolization, the efficient generation of a reactive diene species is possible which can be trapped in Diels-Alder reactions. This reaction will be described in more detail within the following section.

2.5.3 Photoenolization

Photoenolization is a light driven tautomerization process leading to the formation of an enol species[16] – so-called photoenols – *via* the irradiation of *o*-alkylphenylketones and -aldehydes. Discovery of the mentioned process originated from the photo-reduction of benzophenone to benzopinakol under addition of diphenylmethanol. Thereby it was observed that benzopinakol formation was inhibited when an alkyl moiety was present in *ortho* position of the benzophenone derivative.[171] After several investigations concerning photoenolization, a reaction mechanism was proposed based upon transient absorptions gained from flash photolysis experiments on 2,4-dimethylbenzophenone in cyclohexane (see Figure 2.27).[172] In this mechanism, the ground

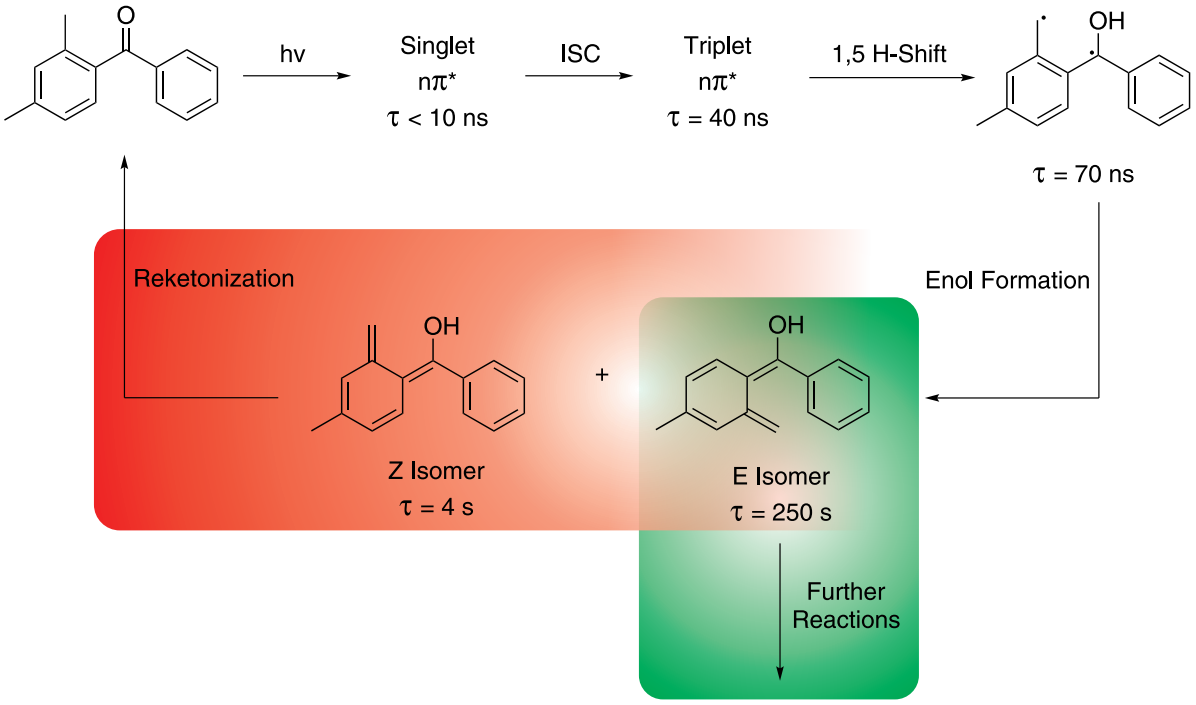

Figure 2.27: Depiction of the photoenolization mechanism exemplified with 2,4-dimethylbenzophenone in cyclohexane. Excitation of the starting molecule leads to formation of the excited singlet species followed by a rapid decay to the excited triplet state. After an internal 1,5 hydrogen shift, a bisradical species is formed prior to formation of both enol isomers (E / Z). Both isomers can undergo reketonization (highlighted in red) yielding the starting molecule, yet the E isomer can also participate in further reactions (highlighted in green).

state of the molecule undergoes excitation to the singlet state *via* the absorption of a photon. Having a lifetime of about 10 ns, excited molecules can undergo intersystem crossing to arrive at the triplet state which exhibits a lifetime of about 40 ns. Due to an internal 1,5 hydrogen transfer under participation of the *ortho* methyl group, a diradical species with a lifetime of about 70 ns is formed. Following a recombination of the radicals with the delocalized π-electrons of the aromatic ring, the enol species is formed in both diastereomeric configurations. Both enol isomers exhibit much longer lifetimes compared to the previous excited or radical species. However, the lifetime of each diastereomer is distinctly different. In the case of 2,4-dimethylbenzophenone, the Z isomer ($\tau = 4\,s$) has a much shorter lifetime than the E isomer ($\tau = 250\,s$). A plausible reasoning for this observation is the favored hydrogen reversion (*via* a 1,5 hydrogen rearrangement) of the Z isomer back to the starting molecule, also termed reketonization.[k] Moreover, lifetimes of a specific enol species are strongly dependent upon the employed solvent and also upon the oxygen concentration (see Table 2.1). Additionally it has also been shown that photoisomerization between both enol isomers is possible.[173,174]

Environment	**Z Isomer**	**E Isomer**
Cyclohexane	4 s	250 s
Cyclohexane / O_2	9.5 ms	20 ms
Ethanol	1.7 s	1.9 s
Ethanol / O_2	0.3 s	0.3 s

Table 2.1: Lifetimes of corresponding enol isomers (Z and E) for the photoenolization process of 2,4-dimethylbenzophenone conducted with different solvents, with or without oxygen. Values taken from [16].

2.5.4 Reactions of *o*-Quinodimethanes

With lifetimes in the order of seconds the enol species is able to participate as a component in reactions other than reketonization, so-called trapping reactions. Especially for the long-lived isomer, such *in situ* reactions become more likely. In contrast, the short-lived isomer reacts in a reketonization manner. Additional studies have shown that the short-lived isomer does not participate in any other specific trapping reactions, contrary to its long-lived counterpart.[175] Generated photoenol species belong to the chemical class of *o*-quinodimethanes.[176] Being a highly reactive functional group, *o*-quinodimethanes can undergo several reactions including the electrocyclic ringclosure to benzocyclobutene derivatives or a [4+4] cycloaddition yielding dibenzocyclooctadienes under appropriate conditions (see Figure 2.28). The already mentioned reketonization is only one of many possible reactions. Nevertheless, it often plays an important part as will be seen throughout this thesis. The most prominent reaction, however, is the Diels-Alder reaction. In this case the *o*-quinodimethane occupies the role of a diene for a "normal" electron demand reaction. A remarkable and very beneficial feature of the *o*-quinodimethane

[k] To be precise, the term "reketonization" is inaccurate as the precursor molecule may also be an aldehyde. However, the term stems from the historical discovery of the concept (with a ketone as molecule) and remains to be widespread in the literature.

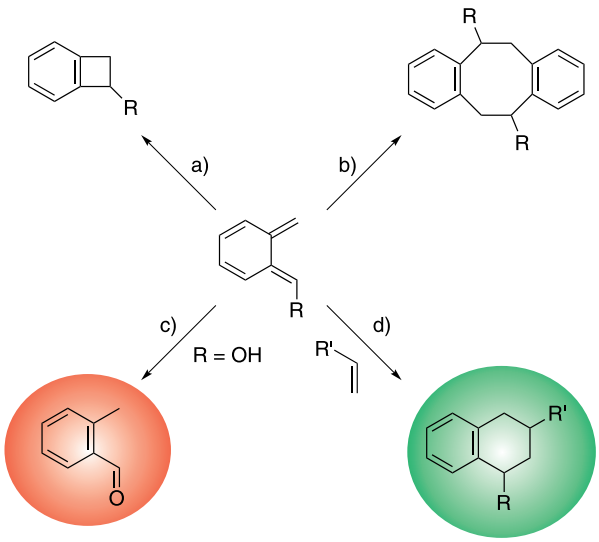

Figure 2.28: Potential reaction paths for an exemplified intermediate *o*-quinodimethane. Electrocyclic ringclosure is depicted in a) while the [4+4] cycloaddition of two intermediates is depicted in b). Reketonization (highlighted in red) and Diels-Alder cycloaddition (highlighted in green) are depicted in c) and d), respectively.

when undergoing Diels-Alder reaction is the interplay between the cycloaddition reaction and reketonization in the case of photoenols. Once the reactive *o*-quinodimethane is formed only two fates dominate further reaction, either the consumption in a Diels-Alder reaction or the reketonization to the precursor molecule. Potential side reactions including the aforementioned possibilities require special treatment and therefore do not commonly occur. Hence, even when undergoing reketonization, the molecule can participate in a Diels-Alder reaction *via* a further excitation. Ultimately, the interplay strongly enhances formation of the desired product in a quantitative yield while no side products are formed. This procedure is contrary to the large majority of reactions where reactive intermediates undergo side reactions that irreversibly alter the reaction path, lead to the formation of undesired side products, and ultimately limit obtainable yields.

o-Quinodimethanes in general have been extensively employed as reagents for Diels-Alder reactions throughout different fields. Natural product synthesis has exploited photoactivated *o*-quinodimethanes *inter alia* for the synthesis of 9-α-hydroxyestrone methyl ether.[177] Further, thermoreactive benzocyclobutene moieties have been employed for the synthesis of benzoperhydroindanes. In the case of benzocyclobutenes, thermally stimulated formation of the *o*-quinodimethane species proceeds *via* a reversible conrotatory opening of the cyclobutene ring. In fact, the described thermal accessibility of *o*-quinodimethanes is an important route in materials chemistry and has been exploited for the covalent functionalization of fullerenes *via* thermal provision from different molecules such as benzocyclobutenes or isochromanones (see Figure 2.29).[178,179] For the generation of *o*-quinodimethanes from isochromanones the formation and segregation of carbon dioxide is the driving force of the reaction. In polymer chemistry, thermal step growth polymerizations have been performed utilizing AB monomers

containing a benzocyclobutene moiety and additionally a potential dienophile moiety such as a stilbene[180] or maleimide.[181] Besides thermal applications, the light-induced provision of photoenols, *i.e.*, *o*-quinodimethanes from phenylaldehyde and -ketone species equipped with an alkyl moiety in *ortho* position, have been explored as an efficient ligation tool for conjugation in polymer science.

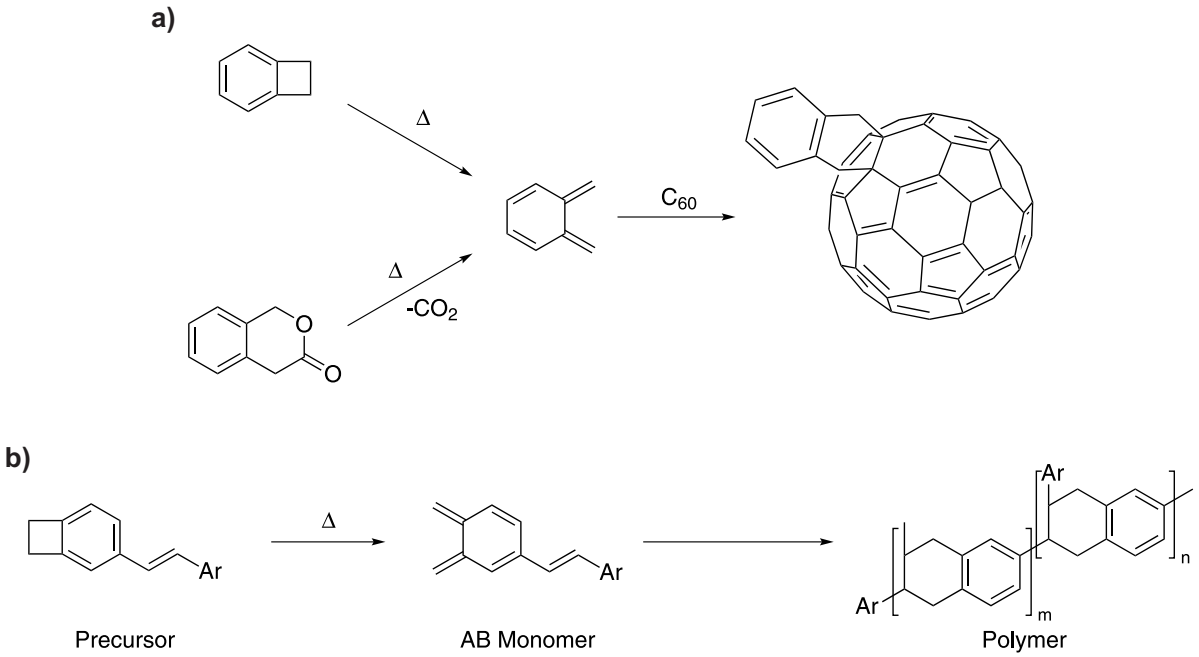

Figure 2.29: Applications of thermally induced *o*-quinodimethanes in materials and polymer science. Thermal generation of the intermediate species starting from benzocyclobutene or isochromanone and subsequent Diels-Alder reaction with a C_{60} fullerene is depicted in a). Step growth polymerization performed with thermally produced diene-dienophile AB monomers is depicted in b).

Within this context, quantitative endgroup modifications of ATRP polymers, prepared with a maleimide-containing initiator, were conducted.[182] Moreover, in this study a hydroxy-containing photoenol species was employed for ring-opening polymerization of ε-caprolactone. The resulting polymer was subsequently reacted with the maleimide-containing ATRP polymer to yield an AB block copolymer, once again emphasizing the *click* status of the technique (see Figure 2.30). Expansion of photoenol ligation towards other controlled radical polymerization protocols was demonstrated by utilizing the carbon-sulfur double bond as a reactive dienophile moiety in conventional RAFT polymers.[183] Again, demonstration of efficient endgroup modification of RAFT polymers with a small molecule preceded block copolymer formation between a RAFT polymer and a photoenol-bearing poly-ε-caprolactone. Remarkably, photoenol ligation is so powerful that it has been employed in the highly demanding field of sequential polymerization for the artificial generation of monodisperce macromolecules.[184] Additionally, photoenol chemistry has been utilized for the covalent decoration of various

surfaces with polymers, including grafting of RAFT polymers to microparticles,[185] grafting of peptides onto biosurfaces,[186,187] and, in combination with a catechol-inspired approach,[188] various surfaces such as gold, graphite, and polyethylene terephtalate. Apart from microparticle functionalization, spatially resolved patterning of the respective flat surface is easy to conduct *via* a photomask and has been performed within the mentioned applications. Photoenol chemistry has also been employed for the spatially resolved 3D surface functionalization of DLW-written designer petridishes for cell studies in a multistep approach.[80] Therein, a photoresist (Ormocer) was employed for fabrication of structures with pending hydroxygroups. In a second reaction step the structures were globally functionalized by silanization of a photoenol-containing tris-alkyloxysilane. Subsequently, selected structure parts were irradiated with a focused laser beam invoking multiphoton absorption and thereby attaching target molecules in a covalent manner.

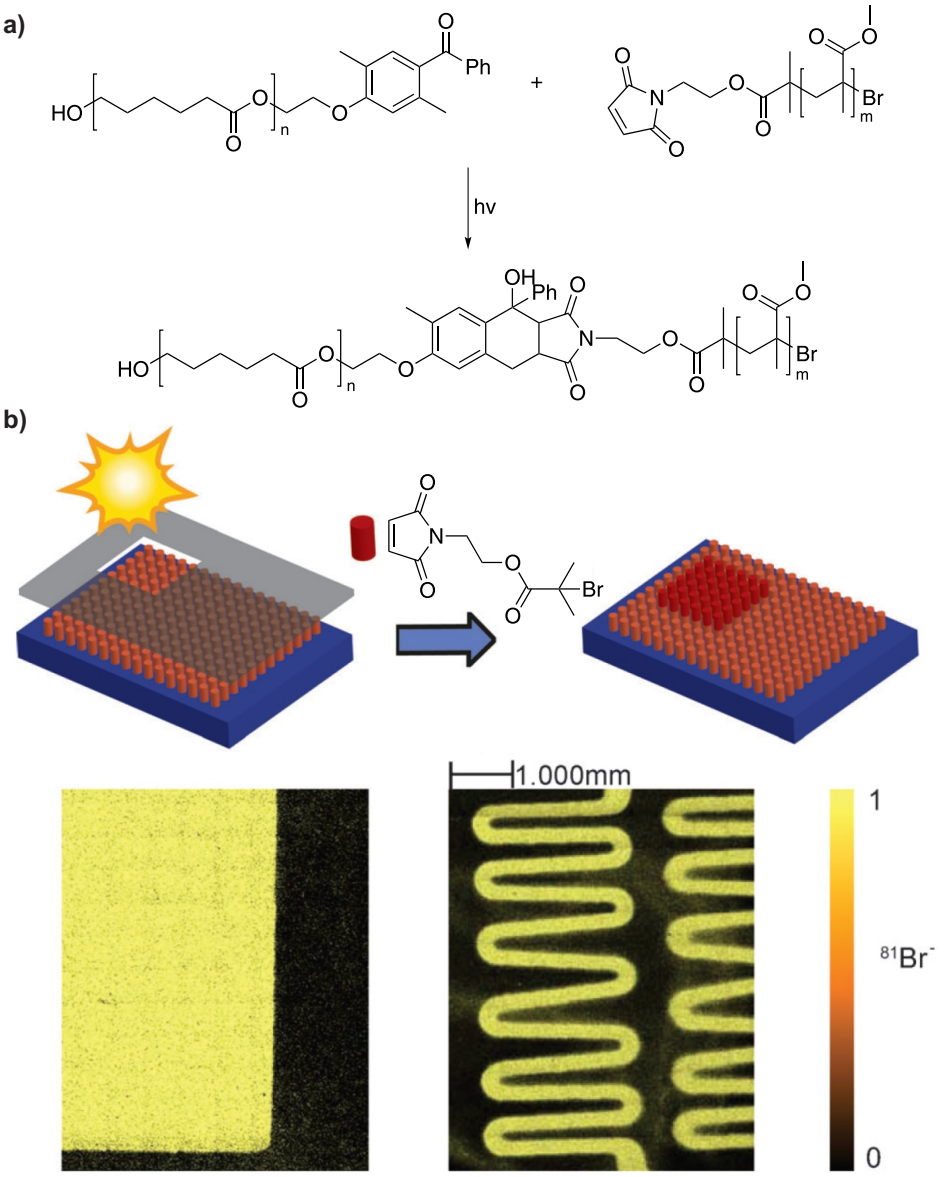

Figure 2.30: Applications of photoinduced Diels-Alder ligation in polymer science and materials chemistry. a) Efficient blockcopolymer formation of an ATRP generated PMMA with a dienophile-containing initiator and a photoenol-containing poly-ε-caprolactone. b) Spatially resolved immobilization of a bromine-containing dienophile (red) on a photoenol containing surface (light red) using photomasks (top). Different bromine patterns were acquired from different photomasks and analyzed *via* ToF-SIMS (bottom). b) adapted from [186] with permission from Wiley-VCH.

2.5.5 Photorelease and Photodeprotection Processes *via* Photoenols

Moving away from Diels-Alder chemistry, *o*-alkylphenacyl-containing molecules have also been investigated as photoremovable protection groups in chemistry and biology.[189] Similar to the mentioned photoenol systems, *o*-alkylphenacyl-containing molecules undergo photoenolization readily. From the *o*-quinodimethane state of these molecules, a suitable leaving group can be released (see Figure 2.31), with the overall process being termed a photorelease reaction. Released molecules can be halogen acids, yet also carboxylic acids, phosphates, sulfonic acids, alcohols, or amines have been reported.[190–193] In some cases, the quantum yield of the photorelease can be significantly increased by an adequate choice of solvent. In the case of extruded HCl, when going from benzene to methanol as solvent, the quantum yield increases from 11% to 76% with the hydrogen donor function of methanol supposedly being responsible for the large increase in quantum yield.[194] Moreover, adequate *o*-alkylphenacyl-containing molecules can also participate in photouncaging reactions where a functionality is produced *via* photoenolization in an intramolecular manner, not necessarily including any release. One example is the formation of a β-hydroxy-functionalized indanone following photoenolization, realized by a ring-opening process of a pending oxirane on the precursor molecule.[195]

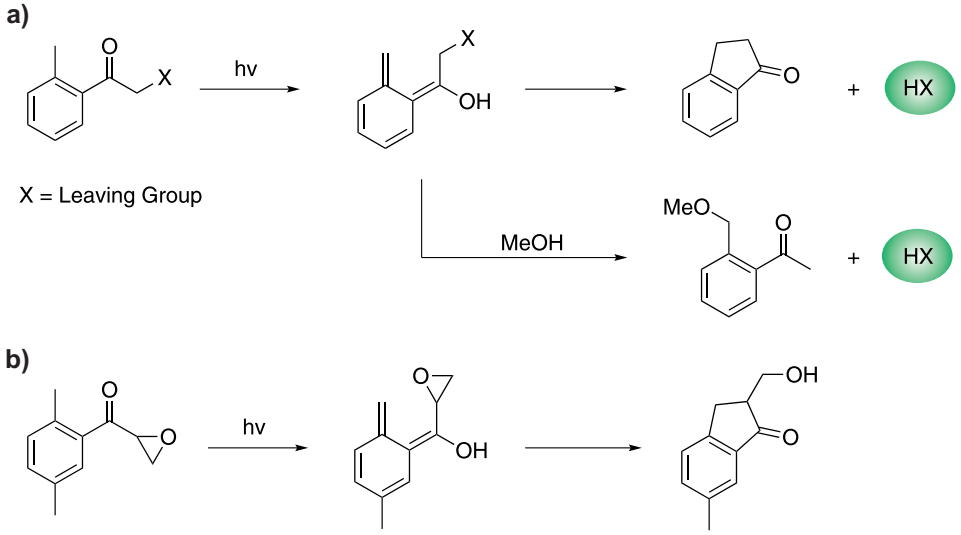

Figure 2.31: Photoenols as reagents in protective group chemistry. a) Photorelease for a range of leaving groups (highlighted in green) *via* the *o*-quinodimethane intermediate. The quantum yield of the release can be significantly increased when conducting the reaction in methanol. b) Photouncaging, exemplified by the generation of a β-hydroxy-containing indanone *via* a ring-opening reaction subsequent to *o*-quinodimethane formation.

In conclusion, reactions that play an important role in this thesis have been presented. Specifically, thiol-mediated reactions, especially the radical thiol-ene coupling, the radical thiol-yne coupling, and the thiol-Michael addition reaction, the CuAAC reaction, and photoinduced Diels-Alder chemistry of photoenols have been described. All reactions were introduced

in a general fashion and subsequently discussed in more detail regarding their respective suitability for application in 3D lithographic processes, including structure formation and post-modification. Selected applications were depicted in order give an impression of the usage of the presented chemistry in topics adjacent to 3D lithography, highlighting potential applicability. Throughout the following section, the results obtained during this thesis by combining the mentioned chemistry with DLW and direct covalent post-modification of resulting structures will be presented and discussed.

3

Thiol-Mediated Radical Coupling for Functional Three-Dimensional Microstructures

Throughout the last 15 years, DLW has become one of the most important tools for precision 3D micro- and nanostructuring. Steady refinement from an engineering – but also from a chemical point-of-view – have been key elements in the past that have largely contributed to this success. As previously described (see Section 2.2), chemical investigations have – up to this day – been mainly focused on the optimization and extension of traditional chain growth polymerization systems, namely FRP and cationic polymerization that were found to be suitable for DLW. From a polymer chemistry perspective, it is highly desirable to investigate polymerization protocols that differ from the mentioned traditional DLW systems. An important reasoning is the significantly increased chemical diversity that is obtained for DLW-produced structures. Concomitantly, additional options arise for both the fabrication procedure and the properties of the resulting structures. Originating from a physical / engineering perspective where the dimension and architecture of the 3D object was of prime importance, chemical systems were chosen to yield inert, stable networks. When having implementations of DLW into microfluidics, lab-on-a-chip systems and bioapplications in mind, the possibility for covalent alteration of generated structures is of high importance. Consequently, novel chemical approaches must be explored in order to meet these demands for further extension of DLW applicability into these fields. One potent option is the introduction of radical thiol mediated network formation into DLW which will be described in the following section.

3.1 Radical Thiol-Ene Mediated Direct Laser Writing

In this section, radical thiol-ene coupling will be introduced as a novel polymerization methodology featuring a fundamentally different polymerization mechanism compared to traditional DLW photoresists. While FRP and cationic polymerization proceed *via* a chain growth mechanism, polymerization occurring in a radical thiol-ene coupling manner exhibits a step growth nature. As explained in Section 2.1, in step growth polymerization every active species may

Parts of this chapter were reproduced from Quick, A.S.; Fischer, F.; Richter, B.; Pauloehrl, T.; Trouillet, V.; Wegener, M.; Barner-Kowollik, C. *Macromol. Rapid Commun.* **2013**, *34*, 335-340 and Quick, A.S.; de los Santos Pereira, A.; Bruns, M.; Bückmann, T.; Rodriguez-Emmenegger, C.; Wegener, M.; Barner-Kowollik, C. *Adv. Funct. Mater.* **2015**, DOI: 10.1002/adfm.201500683 with permission from Wiley-VCH.

react with one another and large molecular weights – and hence a stable, heavily crosslinked network for DLW – requires a high conversion. At first glance, such a polymerization behavior may seem adverse for 3D lithography, yet the resulting functions outweigh initial obstacles. Moreover, a high conversion results in the formation of uniform networks with very defined mechanical parameters. During a radical thiol-ene mediated polymerization, a single initiating radical invokes a multiplicity of consecutive thiol-ene reactions as the thiyl radical is sustained in the course of reaction (see Section 2.3.2). This behavior is very beneficial for obtaining high conversion, thus qualifying the radical thiol-ene reaction as a promising candidate for DLW curing.

3.1.1 Photoresist Design

For a negative-tone photoresist to be applicable in DLW, light-triggered curing must proceed rapidly and efficiently within the exposed region. The induced solubility change is thereby a permanent solidification in the cured volume, typically evoked by the formation of a densely crosslinked network. Polymer networks can be efficiently prepared *via* the radical thiol-ene reaction. A prerequisite thereby is a combined functionality of five or more olefin and thiol groups with each monomer component having a minimum functionality of two. For the synthesis of densely crosslinked networks, a system containing three or four functional groups on each monomer was proven to be well-suited.[13] As described in Section 2.3, the electron density of the employed olefin is important for the overall rate of the radical thiol-ene reaction. Due to the electrophilic nature of the thiyl radical, electron rich olefins ensure a fast reaction rate. A promising pair of functional groups that rapidly proceeds to a high conversion when exposed to light in the presence of a photoinitiator are alkyl thiols and allyl ethers.[101] Therefore, a tetrafunctional thiol (pentaerythritol tetra(3-mercaptoacetate), Tetrathiol 1 and a tetrafunctional allyl ether (pentaerythritol tetraallyl ether, PETE) in a 1:1 ratio were chosen as monomer components for a radical thiol-ene based photoresist. Both monomers are displayed in Figure 3.1. Exhibiting a total amount of eight functional groups, curing results in the formation of cross-linked, insoluble material. Apart from the monomers, additional components must

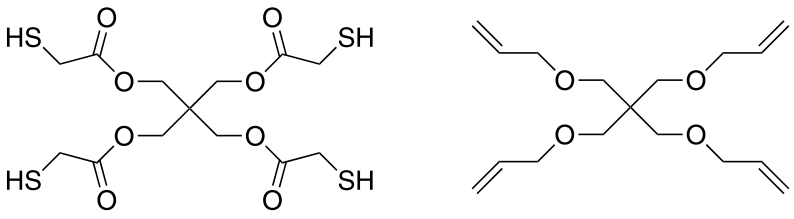

Tetrathiol 1 PETE

Figure 3.1: Depiction of the tetrafunctional thiol (Tetrathiol 1) and the tetrafunctional allyl ether (PETE) employed as monomers for the radical thiol-ene photoresist.

be present in the final resist. A photoinitiator was included for the provision of initiating radical fragments during exposure. For the resist, DETC was chosen as a photoinitiator that is known to effectively initiate acrylate polymerization *via* multiphoton absorption (for the

chemical structure of DETC, see Figure 2.7). Further, hydroquinone (HQ) was added as an inhibitor in order to avoid undesired polymerization during storage, thereby increasing the photoresist shelf-life. Finally, dimethyl acetamide (DMAC) was added as a solvent, as both monomer components are immiscible liquids to yield the final radical thiol-ene photoresist.

When designing a new photoresist it is important to select components that are readily available – a consideration that is not of scientific nature. One target of this thesis is the provision of chemical functionality in DLW. Many materials scientists working in 3D lithography do not have profound knowledge in the field of synthetic polymer chemistry. Therefore, a photoresist that requires multiple synthetic steps may not be applied, despite its beneficial features. Consequently, the preparation of the resist constituents must be kept as straightforward and facile as possible. Following this concept, all components of the radical thiol-ene photoresist are readily commercially available with the exception of PETE. While distributors exist that synthesize and sell PETE on demand, PETE has been synthesized in a convenient one step procedure in this thesis (see Figure 3.2).

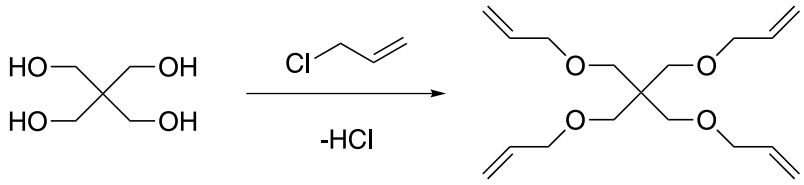

Figure 3.2: Depiction of the one step procedure for the synthesis of PETE from pentaerythritol and allyl chloride.

3.1.2 Direct Laser Writing System and General Sample Treatment

Employing the radical thiol-ene photoresist described in Section 3.1.1, DLW was performed in order to fabricate 3D microstructures. As a lithography setup, the commercially available Photonic Professional system (Nanoscribe GmbH, Karlsruhe) was utilized, equipped with a femtosecond pulsed laser at 780 nm center wavelength, an 100x oil-immersion objective (NA = 1.4) and a piezo stage for relative movement of the sample and the laser focus. A standard oil-immersion configuration was chosen for lithographic experiments with the radical thiol-ene photoresist. As substrates, glass cover slips with a thickness of 170 µm were employed. Prior to DLW exposure, a silanization reaction with 3-(trimethoxysilyl)propyl methacrylate was performed upon all substrates. In this fashion, an olefin moiety is covalently immobilized onto the glass substrate. The surface-bound olefin participates in the following polymerization reaction to a small extent, covalently anchoring the produced polymeric material to the surface. In this manner, the strength of attachment of fabricated microstructures to the substrate is strongly increased. Next to the silanization of substrates, undesired vaporization of volatile photoresist components must be minimized. A reason for such a precaution is the concomitant retention of sample reproducibility. Fabrication times for typical DLW procedures often possess a time frame of several hours and special experiments may take up to several days. Evaporation of a component, *e.g.*, the solvent leads to a distinct increase in monomer and

initiator concentration, inducing a change in threshold energy, and, ultimately leading to a time dependent alteration of optimum writing conditions. Therefore, samples are sealed during exposure, utilizing a polydimethylsiloxane (PDMS) ring and an additional glass cover slip (see Figure 3.3). After the lithographic experiment, uncured photoresist is typically removed in a development step. Thereby, the sample is immersed into acetone and subsequently rinsed with acetone, isopropanol and water.

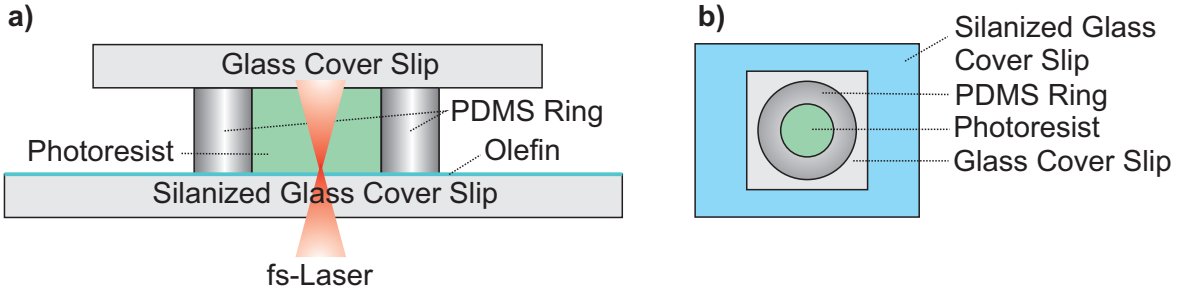

Figure 3.3: a) Side view and b) top view of a sealed sample for radical thiol-ene mediated DLW, preventing undesired evaporation of single photoresist components.

3.1.3 Simple Structure Fabrication

Figure 3.4: Schematic depiction of a DLW process employing the radical thiol-ene reaction as a polymerization method.

After having accomplished the above mentioned preparations, lithographic experiments were conducted *via* the radical thiol-ene photoresist, as schematically depicted in Figure 3.4. Unlike the connotation created by Figure 3.4, investigation of radical thiol-ene based lithography was not commenced by the generation of a complex 3D structure, but rather by the production of very simple standard objects. Structures with increased complexity were subsequently produced with the aid of information gained from the preceding experiments. Being the first novel DLW photoresist system described in this thesis, all standard lithographic experiments of radical thiol-ene mediated DLW will be discussed in detail below, giving the reader an impression of the general procedure of investigation.

To start, simple 2D lines were fabricated in order to investigate the performance of the photoresist and determine key parameters such as the dynamic range[a] and the threshold value at a given writing speed. A SEM image[b] of an exemplary "dosetest" for the radical thiol-ene photoresist is depicted in Figure 3.5.

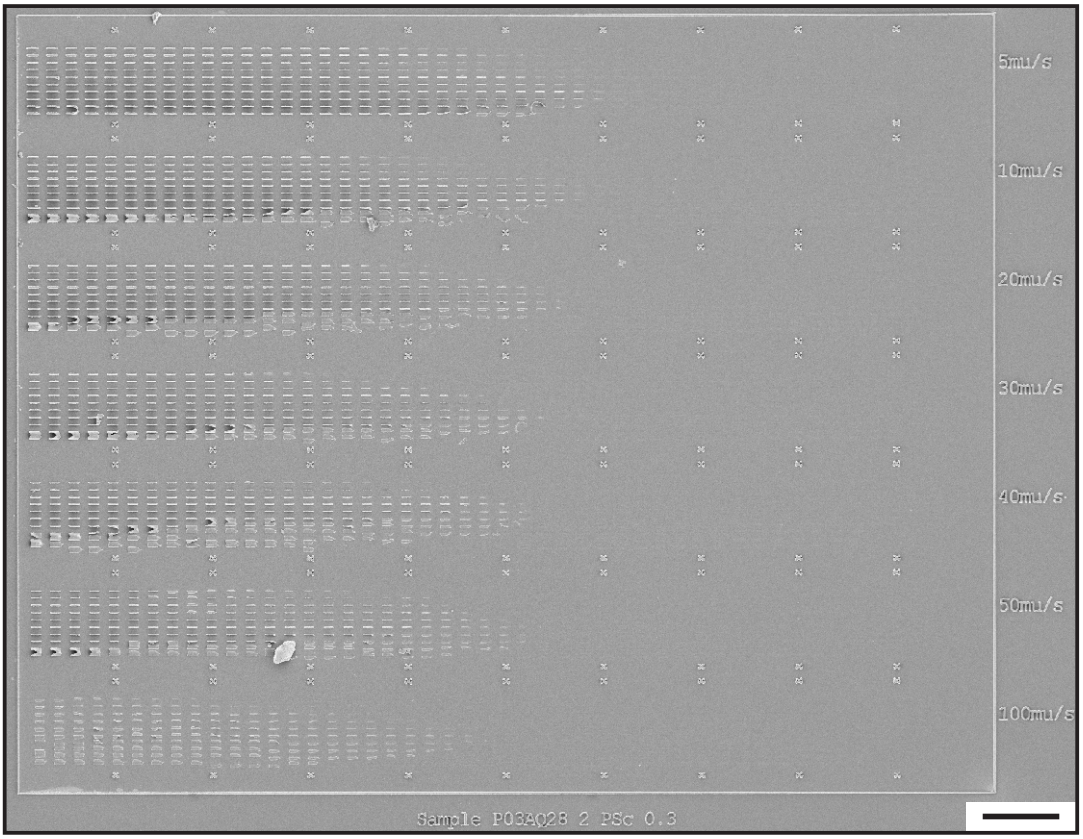

Figure 3.5: SEM image of a dosetest written with the radical thiol-ene photoresist. Test arrays for a writing speed ranging from 5 μm s^{-1} to 100 μm s^{-1} and a laser power between 0 mW and 6 mW are shown. The scale bar is 20 μm.

In such an experiment, arrays were fabricated under variation of the writing speed, ranging from 5 μm s^{-1} to 100 μm s^{-1}. Throughout each array, the laser power was linearly increased from 0 mW to 6 mW (from right to left) for the generation of dashed lines. Every line segment is attributed to a specific laser power and each array consists of ten dashed lines. From the top line to the bottom line of an array, the value of the vertical axis was increased with the result that the focal point position was located in the substrate for the topmost line and in the photoresist for the bottommost line. Threshold values for the respective writing speed were taken from the dashed line that produced segments in good quality at the lowest laser power of

[a]The term "dynamic range" describes the power range for a given writing speed wherein controlled structure fabrication is possible.

[b]SEM analysis in this section was performed by Johannes Kaschke.

the corresponding array and are displayed in Table 3.1. Apart from the determination of the threshold value, the simple experiment further reveals a large suitable power range for defined structure fabrication. It must be noted that for large exposure doses (above the dynamic range), uncontrolled polymerization behavior can occur, impeding controlled structure fabrication (not shown).

Writing Speed	**Threshold**
5 μm s^{-1}	2.40 mW
10 μm s^{-1}	2.64 mW
20 μm s^{-1}	2.76 mW
30 μm s^{-1}	2.88 mW
40 μm s^{-1}	3.00 mW
50 μm s^{-1}	3.00 mW
100 μm s^{-1}	3.48 mW

Table 3.1: Threshold values at a varying writing speed utilizing the radical thiol-ene photoresist.

Investigation of the produced segments revealed further lithographic details such as the line width for a written segment. A single segment stemming from the 100 μm s^{-1} array written at a laser power of 3.72 mW is depicted in Figure 3.6. The line width was measured to be close to 230 nm. Subsequent to the dose test fabrication and analysis, a more complicated pattern, the "macroarc" chemistry group logo, was generated. Thereby, a large benefit of DLW was demonstrated for the radical thiol-ene photoresist which is the facile production of arbitrary objects. Analysis of the pattern was carried out by SEM. The depicted image was taken from a stage angle of 45°. From the displayed image, a further characteristic feature can be deduced. All written structures are not entirely 2D, but rather exhibit a certain minimum height which is in agreement with the general concept of DLW photoresists.

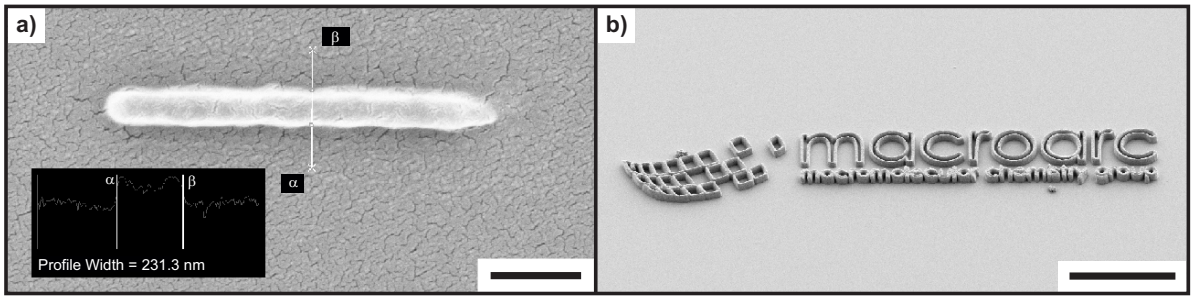

Figure 3.6: SEM analysis of a) a single segment of a fabricated dashed line (100 μm s^{-1} writing speed, 3.72 mW laser power) with a line width of approximately 230 nm and b) a produced "macroarc" logo featuring a minimum structure height. Scale bars are 600 nm and 20 μm for a) and b), respectively.

On the basis of the mentioned simple lithography experiments, structures were obtained from the radical thiol-ene photoresist and key writing parameters for the system have been

ascertained. In the following section, the gained knowledge will allow for the production of complex 3D resolved structures.

3.1.4 Complex 3D Structure Fabrication

In order to demonstrate the access to 3D microstructures *via* the radical thiol-ene photoresist, fully resolved 3D objects must be generated. In addition, the resolution limit for a given DLW system is a highly important parameter that must be determined. In the DLW community, the so-called "woodpile" (see Figure 3.4) has been established as a benchmark structure. The fabrication of such a periodic structure serves as an example for a highly complex 3D architecture. Furthermore, achievable 3D resolution of a given system can be determined *via* such an architecture due to the periodicity in both lateral and axial dimensions. Important parameters of a woodpile are the spacing between rods in one layer and the spacing between neighboring layers. Four neighboring layers (each layer being either rotated and / or shifted with respect to the other layers) form one period. An entire woodpile typically consists of several periods.

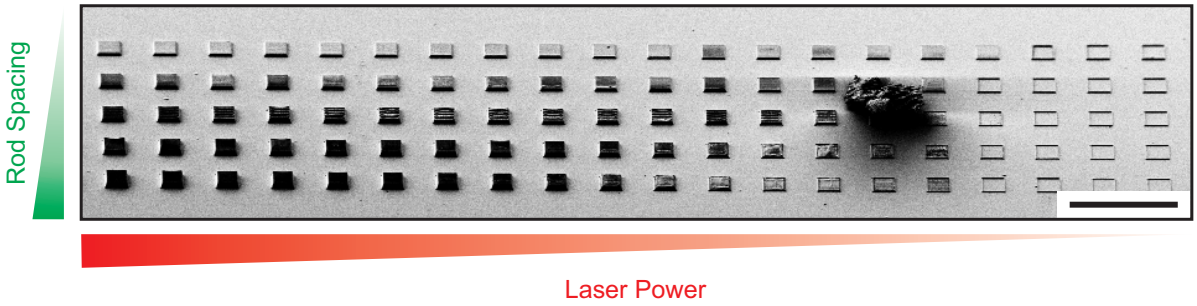

Figure 3.7: SEM overview of a specific parameter study of woodpiles with 22 layers fabricated at 100 µm s^{-1}. In the parameter study the laser power and the rod spacing was varied. An impurity originating from sample development is visible in the underexposed region. The scale bar is 100 µm.

In an effort to ascertain optimum fabrication conditions and hence optimum resolution for the woodpile structures, several parameter studies were performed employing the radical thiol-ene system. An overview SEM image of a specific parameter study with woodpiles exhibiting 22 layers and a footprint of 20×20 μm^2 is depicted in Figure 3.7. While keeping the writing speed constant (100 µm s^{-1}), the rod and layer spacing (increasing from top to bottom) as well as the laser power (increasing from right to left) were varied. From the presented overview, important exposure regions for radical thiol-ene mediated DLW can be categorized. For a low laser power and thus a low exposure dose (right, laser power = 0-2 mW), the writing threshold dose was not exceeded with the result that curing did not take place in this region. Visible squares were fabricated in a separate step (laser power = 5 mW) with the purpose of visualizing all exposed regions. With increasing laser power (middle, laser power = 2-6 mW), curing resulted in the formation of polymeric material in the exposed region. However, structures do not possess the envisaged geometry in the applied power region – a typical behavior in DLW

of structures fabricated in proximity to the threshold exposure dose. An explanation is the insufficient structure stability towards forces occurring during fabrication and development, leading to severe deformations. For high laser powers (left, laser power = 6-10 mW), generated structures exhibit less alteration. In-depth investigation of single structures in that region was therefore carried out in order to determine the 3D resolution of radical thiol-ene mediated DLW. For a detailed investigation, a woodpile structure with a designed footprint of $20\times20\ \mu m^2$

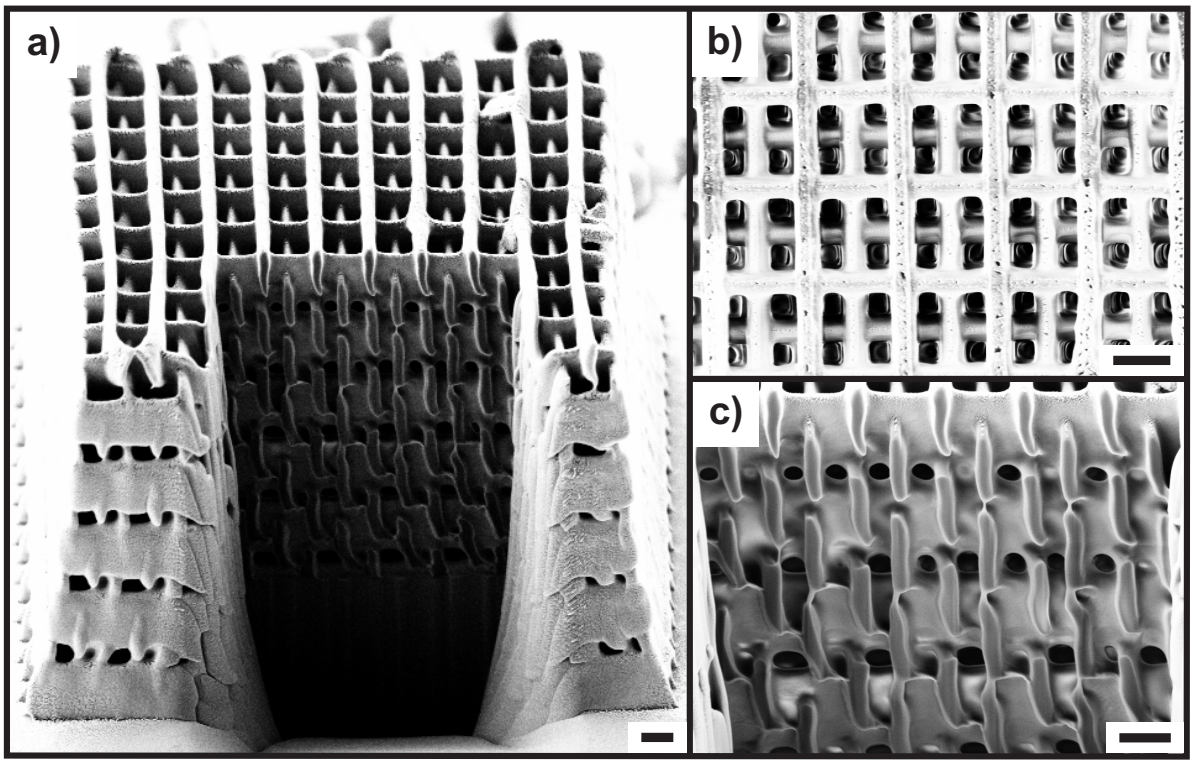

Figure 3.8: In-depth investigation of a fabricated woodpile structure employing the radical thiol-ene photoresist after FIB milling. The entire object is depicted in a), whereas detailed images of the top and the interior are depicted in b) and c), respectively. The scale bar for each image is 1 μm.

and a nominal height of 15.4 μm was fabricated. A writing speed of 100 μm s^{-1} and a laser power of 8 mW was employed. The woodpile structure consisted of 22 layers and exhibited a rod spacing of 2 μm and a layer spacing of close to 700 nm. After structure fabrication, FIB milling was performed,[c] thereby revealing the interior of the structure. SEM images of the overall structure as well as a detailed top and interior view after FIB milling are depicted in Figure 3.8, revealing the aspired geometry throughout the entire produced object. Furthermore, small deviations of the created architecture from the model structure can be identified. A slight difference of the anticipated structural height (15.4 μm) and the obtained experimental height of the generated object (12.8 μm) are visible. Two reasons mainly contribute to the observed height deviation. Firstly, radical thiol-ene mediated DLW experiments were carried

[c] All FIB milling procedures and corresponding SEM analysis in this thesis were performed by Patrice Brenner.

out in oil-immersion configuration. Thereby, defocus aberration stemming from the refractive index (RI) mismatch between the glass substrate and the photoresist or crosslinked polymer occurs, leading to slightly altered architectures. Secondly, deformation during polymerization and development – termed shrinkage – is typically observed for highly resolved DLW written scaffolds. Nevertheless, the depicted images clearly demonstrate the possibility for direct production of 3D structures with micrometer-scale resolution employing the radical thiol-ene photoresist. In comparison to *state-of-the-art* resolution obtained from FRP mediated DLW featuring woodpile structures with a rod spacing of down to 400 nm (see Section 2.2), radical thiol-ene mediated lithography features poorer resolution caused by the large aspect ratio of resulting architectures (see Figure 3.8). Most probably, the large aspect ratio stems from the insensitivity of the radical thiol-ene reaction to oxygen. While the oxygen insensitivity seems to be beneficial at first glance, recent investigations have attested oxygen induced termination in the peripheral voxel regions a crucial role for the obtainable resolution of acrylate based photoresists.[31]

The conducted SEM and FIB milling analysis does not give chemical information about the polymerization procedure. In order to verify the postulated pathway of the curing reaction during exposure, chemical analysis will be described in the following section.

3.1.5 Chemical Structure Characterization

After successful structure fabrication, it is important to investigate the polymerization process during DLW. Although radical thiol-ene chemistry was postulated as the polymerization reaction, verification of this hypothesis is mandatory. In a first step, any reaction that can occur between single resist components and lead to crosslinked structures had to be excluded. Therefore, a DLW dose test (ranging from 0 mW to 6 mW, as in Section 3.1.3) was performed with the original photoresist (**1**) and different resist compositions (**2**-**4**), each composition lacking one crucial component of the original system (see Table 3.2). Structure fabrication

Composition	Initiator	PETE	Tetrathiol 1	HQ	DMAC	DLW
1	+	+	+	+	+	+
2	-	+	+	+	+	-
3	+	-	+	+	+	-
4	+	+	-	+	+	-

Table 3.2: DLW experiments for different photoresist compositions with **1** being the original photoresist and all other photoresist compositions missing one important component (**2**-**4**). Curing is only possible when utilizing composition **1**.

was only possible with composition **1**, evidencing that all components must be present for the crosslinking reaction to occur. However, the simple experiment did not allow for any statement about the type of reaction occurring during crosslinking polymerization and therefore, further investigations had to be performed. A possibility for the investigation of fabricated structures and the photoresist is FTIR spectroscopy. For FTIR analysis, a solid cuboid structure with a footprint of $100 \times 100\ \mu m^2$ and a height of close to 25 µm was produced (writing speed =

100 µm s^{-1}, laser power = 8 mW) and examined. Moreover, a spectrum of the unexposed photoresist was recorded, allowing for the comparison of both spectra (see Figure 3.9). As described in Section 2.3.2, a progressing radical thiol-ene reaction features the consumption of thiols and olefins. Both thiols and double bonds exhibit distinct FTIR absorption peaks at approximately 2550-2600 cm^{-1} and 6100 cm^{-1}, respectively.[196] The particular signals correspond to the stretching vibration of the thiol and the olefin overtone vibration. In the spectrum of the photoresist, both the thiol and the olefin vibration were assigned to the absorption peaks at 2553 cm^{-1} and 6129 cm^{-1}, respectively. A comparison with the recorded spectrum of the cuboid structure revealed that no signal for the olefin overtone is visible anymore after curing. Furthermore, the thiol absorption peak is significantly decreased in the spectrum of the cured structure. These findings are in agreement with the consumption of both the thiol and the olefin functional groups during exposure. Therefore, the results clearly evidence the radical thiol-ene reaction being responsible for crosslinked, insoluble polymer formation during the photolithographic process.

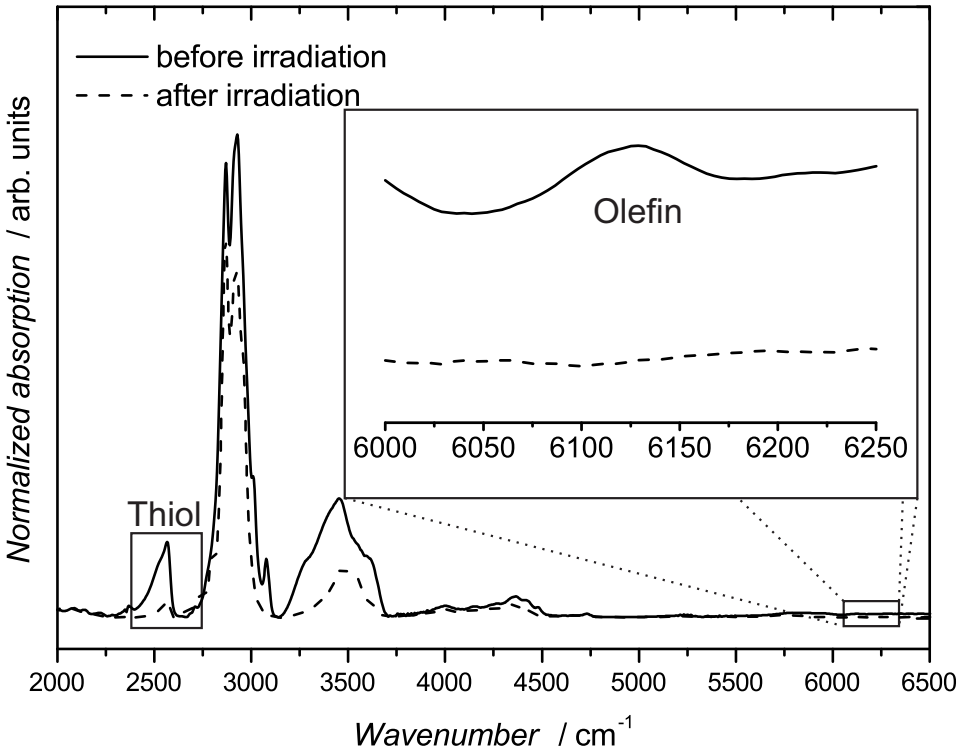

Figure 3.9: FTIR spectra of the photoresist (continuous line) and a fabricated cuboid structure (dashed line). Both the characteristic olefin (6129 cm^{-1}) and thiol (2553 cm^{-1}) absorption peak are visible in the spectrum of the photoresist. In the spectrum of the cured structure, the olefin signal is no longer detected and the signal of the thiol has decreased significantly, evidencing high conversion of the radical thiol-ene reaction during exposure.

The decrease of the olefin overtone indicates that polymerization has proceeded to high conversion throughout the exposed volume, a common behavior for multifunctional thiol-ene systems.[197] However, full conversion – as expected – was not obtained in the course of the curing process. Therefore, unreacted, residual functional moieties are present inside the cured polymer matrix of generated objects and on the structural surface.The spectrum shows no signal associated with the double bond. A possible explanation is the weak overtone signal which, combined with the high conversion allows no detection of small amounts of pending olefins. On the other hand, the signal stemming from the fundamental thiol vibration is far more pronounced. When comparing the thiol signal of both spectra, the decrease of the signal is evident for the DLW produced structure. However, the signal remains visible after fabrication, clearly revealing that residual thiol moieties are present throughout the generated architecture. Such thiols are highly potent functional groups which can be exploited for the covalent immobilization of organic molecules onto fabricated structures. In the following section, the mentioned immobilization procedure will be described.

3.1.6 Covalent Post-Modification

Accessible thiol moieties provided by the polymer structure can be exploited for functionalization, *e.g.*, *via* Michael-type conjugation chemistry. Thus, while the fabrication process is based on the radical thiol-ene reaction, the subsequent covalent immobilization can be performed by a thiol-Michael addition reaction (see Figure 3.10). In general, *click* reactions are well suited for such approaches as they combine an easy reaction procedure with a large versatility for different applications. Hence, it becomes possible to employ one modification methodology for the tuning of different properties. Potential modification targets a vast number of properties ranging from hydrophilicity alteration to pronounced luminescent behavior of the structures. To immobilize fluorescent molecules onto produced micro-objects, different structures were

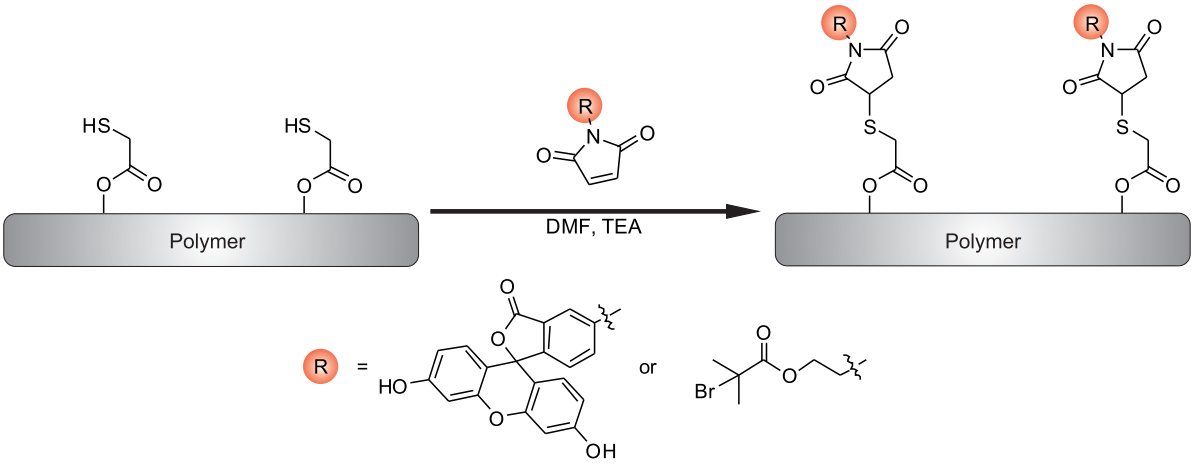

Figure 3.10: Schematic depiction of the thiol-Michael addition reaction as a covalent post-modification methodology for architectures produced *via* radical thiol-ene mediated DLW. Thereby, fluorescent or bromine containing molecules are attached to the micro-object.

immersed into a solution of fluorescein maleimide and triethyl amine with dimethyl formamide (DMF) as a solvent. In such a reaction, the thiol partakes as the Michael donor whereas the maleimide species serves as the Michael acceptor and triethyl amine functions as a catalyst. Resulting fluorescence images of a woodpile and the macroarc group logo, recorded by LSM,[d] are depicted in Figure 3.11. LSM samples were irradiated at 561 nm wavelength and emitted light was detected at a wavelength between 570 and 614 nm. The strong luminescence in the detected region clearly evidences the attachment of the fluorescein molecule onto the fabricated structures. Further, no fluorescence is detected in substrate regions where no polymer material is present, enabling the preparation of accurate and very defined fluorescent patterns on the substrate surface. It should, however, be noted here that the depicted patterns are not entirely two-dimensional. As already described in Figure 3.6 – due to the DLW concept – generated polymer architectures always exhibit a certain minimum height.

Figure 3.11: LSM images of structures fabricated by radical thiol-ene mediated DLW after subsequent immobilization of fluorescein maleimide *via* a thiol-Michael addition procedure. A woodpile structure is displayed in a) while the macroarc group logo is depicted in b). The scale bar for both images is 10 µm.

Although the provided result strongly evidences the attachment of fluorescein maleimide *via* the thiol-Michael addition, an important feature of the technique cannot be satisfactorily investigated by LSM analysis: The position of the attached molecules within the written scaffold. From an application-oriented point-of-view, a vital piece of information is the occurrence of surface functionalization. Therefore, an additional series of samples was prepared under identical conditions as for the previously described LSM analysis with one exception: Instead of a fluorescent moiety, the maleimide species expressed a bromine function (see Figure 3.10). Moreover, identical reaction conditions were performed utilizing a structure fabricated with an FRP acrylate-type photoresist. Surface-bound bromine moieties can be readily identified by X-ray photoelectron spectroscopy (XPS). Br 3d XPS spectra of different structures are depicted in Figure 3.12:[e] Objects generated by radical thiol-ene or FRP mediated DLW after thiol-Michael addition reaction as well as a pristine radical thiol-ene mediated scaffold. The presence of the Br 3d doublet signal with Br $3d_{5/2}$ at 70 eV after functionalization *via* the thiol-Michael

[d]LSM analysis in this thesis was performed by Dr. Benjamin Richter.
[e]XPS in this thesis was performed by Vanessa Trouillet.

addition of the radical thiol-ene mediated structure reveals the successful immobilization of the bromine-containing maleimide onto the surface.[165] For the polyacrylate surface, no Br 3d doublet signal is detected under identical grafting conditions. Naturally, the polyacrylate object does not exhibit any remaining thiol groups. A signal would therefore be attributed to non-covalent adhesion of the maleimide compound. As no signal is detected, non-covalent attachment can be excluded. Finally, it must be ruled out that the bromine signal stems from any contamination that is present on the radical thiol-ene mediated object prior to covalent post-modification. From the absence of a bromine signal for a pristine radical thiol-ene mediated scaffold, unintended bromine contamination can be excluded.

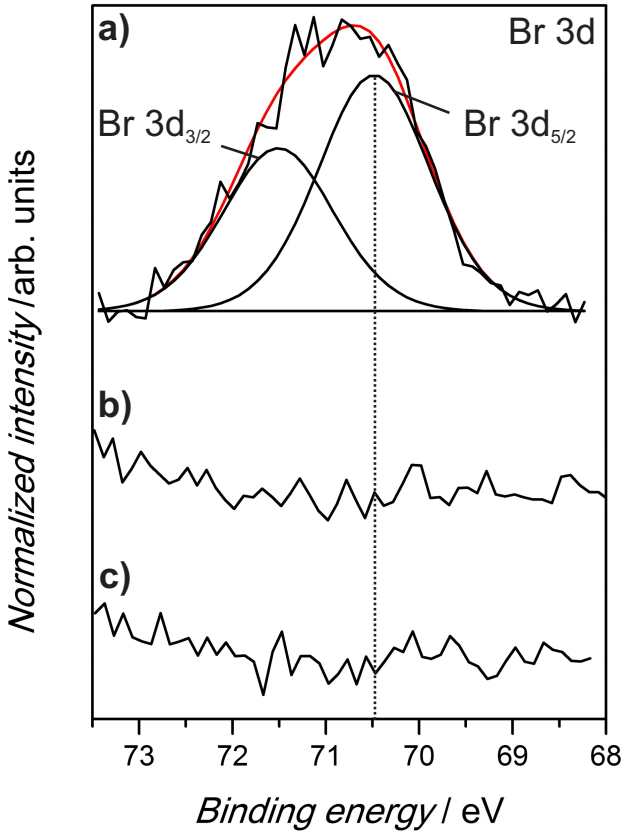

Figure 3.12: Br 3d XPS spectra of a) a thiol-ene and b) a polyacrylate surface after applying thiol-Michael addition conditions with a bromine-capped maleimide. c) Displays a pristine radical thiol-ene sample. The presence of bromine in a) and its absence in b) and c) evidence evidence successful covalent surface immobilization *via* thiol-Michael addition.

Apart from the XPS analysis verifying covalent surface modification, another important parameter is the grafting density that can be achieved by the thiol-Michael addition procedure. To determine the grafting density a calibration was derived from stock solutions of fluorescein maleimide with varying concentration employing the LSM setup. For each stock solution, single slice experiments at defined intervals from the glass-liquid interface were measured.

Concentration [mol L^{-1}]	**Measured Area** [μm^2]	**Average Gray Value (Interface)**
0.121	16232	584.04
0.109	15285	495.76
0.088	14556	287.85
0.061	12399	103.07

Table 3.3: Concentration, measured area, and average gray value at the glass-liquid interface of stock solutions of fluorescein maleimide.

The average gray value of a defined area was then evaluated from the obtained data using the software ImageJ. Plotting of the average gray value versus the distance from the interface (see Figure 6.2) allowed for calculation of the average gray value at the interface *via* a linear approximation (see Table 3.3). The integrated intensity was provided by multiplying the average gray value and the defined area. A value for the point spread function with FWHM in z-direction was measured to be 716 nm. Together with the defined area, the volume of the single slice experiments was accessible. In combination with the known concentration of the stock solution, the integrated intensity was assigned to a number of molecules in the final calibration (depicted in Figure 3.13).

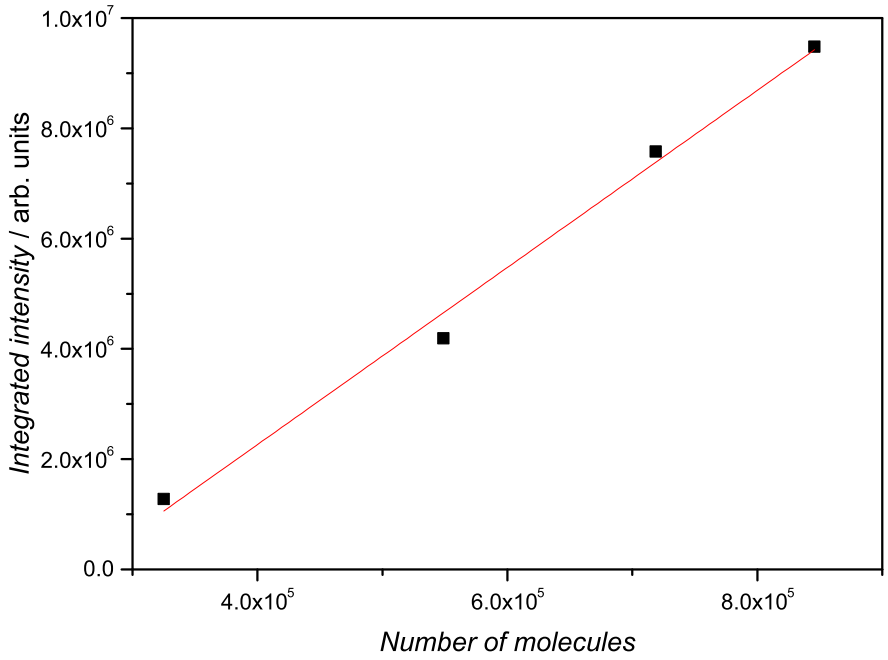

Figure 3.13: Depiction of the calibration for the grafting density estimation. The number of molecules is plotted versus the corresponding integrated intensity. The linear approximation (red line) is employed for the grafting density determination.

In order to determine the grafting density, polymer layers were fabricated with a footprint of $100 \times 100\ \mu m^2$ and a height of approximately 600 nm employing identical writing conditions as

for the woodpile structure depicted in Figure 3.8. Instead of DETC as a photoinitiator, DLW was performed with the non-fluorescent initiator Irgacure 819 (for the chemical formula of Irgacure 819, see Figure 2.7). Thereby, involuntary luminescence stemming from residual initiator molecules or fragments in the architecture is avoided (see Figure 3.14 for a comparison). The produced layer objects were grafted by the thiol-Michael addition reaction with fluorescein maleimide and subsequently analyzed by LSM. From the maximum projection images, average gray values from a defined area were taken for calculation. By multiplying the arithmetic average gray value with the defined area, the integrated intensity was provided. Comparison of the calculated intensity to the calibration curve revealed the number of fluorescing molecules in the measured area. Under the assumption of a perfectly flat surface and solely surface-expressed functionalization, calculation of the grafting density was possible (see Table 3.4). Arguments

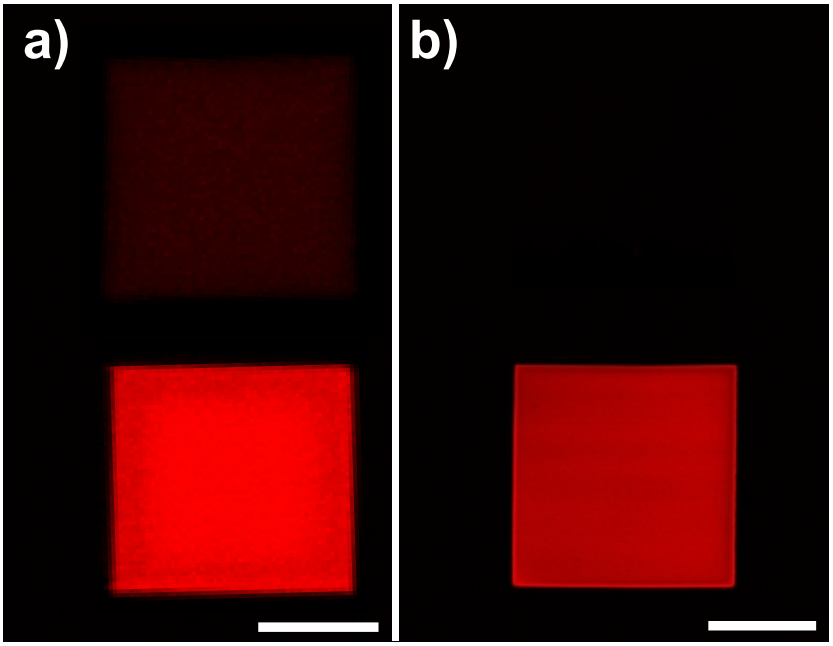

Figure 3.14: Maximum projection images of a) a woodpile structure fabricated with DETC and b) a layer structure generated with Irgacure 819 before (top) and after (bottom) fluorescent functionalization. The slight autofluorescence of the DETC produced object is not visible when changing the photoinitiator to Irgacure 819. Scale bars are 10 μm and 50 μm for a) and b), respectively.

that substantiate the last assumption are the high conversion during network formation and the presented XPS analysis. While the former argument antagonizes pronounced swelling behavior and hence renders internal thiols inaccessible for post-modification, the latter clearly evidences a successful surface reaction. The grafting density was determined to be close to 200 molecules μm^{-2}. Before the presented results are summarized, a short section will discuss an article that was published in parallel with the work derived from the current thesis and also addresses the radical thiol-ene reaction in lithography.

Arithmetic Average Gray Value	**Integrated Intensity** [arb. units]	**Number of Molecules**	**Grafting density** [molecules μm^{-2}]
2898	2.72×10^7	1.95×10^6	**208.1**

Table 3.4: Arithmetic average gray value (of 3 samples), integrated intensity, number of molecules, and grafting density as determined by the described evaluation of the LSM analysis.

3.1.7 Distinction from the Thiol-Ene Photofixation Approach

Simultaneously to the here presented research, another group employed the radical thiol-ene reaction for an alternative photofixation approach.[44] Therein, a combination of Diels-Alder chemistry and radical thiol-ene chemistry was utilized. The basic idea follows the organic-inorganic hybrid material approach described in Section 2.2. In such an attempt, a solid photoresist film is generated by mixing of a tetrafunctional furan molecule, a difunctional maleimide, a tetrafunctional thiol and a photoinitiator. Thereby, the furan moiety readily reacts with the maleimide, forming a network and solidifying the entire photoresist. Within the formed network, photoinitiator and tetrathiol molecules are still present. Further, oxynorbornene groups are formed as the product of the Diels-Alder reaction. Into the network a laser beam is focused, triggering a radical thiol-ene reaction between the thiols and the oxynorbornene groups. In a final step, the substrate is heated, thereby inducing the retro Diels-Alder reaction and resolidifying the network. However, in the exposed volume, the oxynorbornene moieties have already reacted and thus the network is fixated, resulting in the formation of insoluble structures. SEM images of fabricated structures are depicted in Figure 3.15.

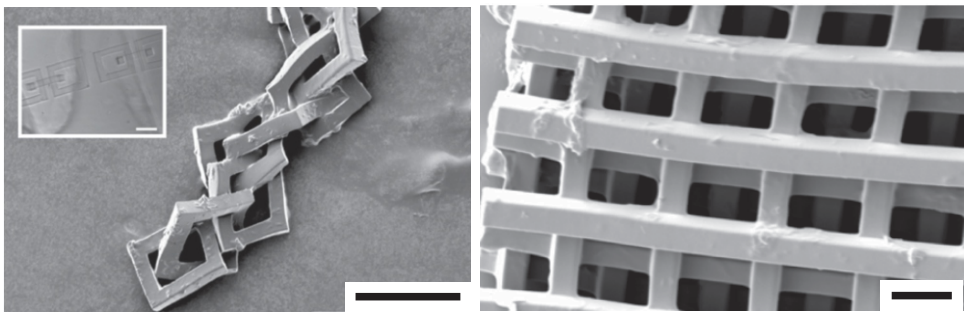

Figure 3.15: An interconnected chain (left) and a five layered woodpile structure (right), fabricated by photofixation of Diels-Alder networks. Scale bars are 200 µm and 40 µm for the left and right image, respectively. Figure adapted from [44] with permission from Wiley-VCH.

A comparison of the photofixation approach and the radical thiol-ene mediated DLW presented in this thesis reveals that, apart from the radical thiol-ene reaction being responsible for irreversible network formation during exposure, both approaches have little in common. While the photofixation focuses on the processing steps during fabrication, the radical thiol-ene approach concentrates upon the fabrication of resolved structures in the low micrometer region

and an efficient post-modification methodology. Neither the resolution, nor the functionalization has been performed in the photofixation study. To be more precise, the woodpile structures presented in Figure 3.8 and Figure 3.15 can be compared. The line width and the rod spacing of the photofixation scaffold can be estimated to be 20 µm and 50 µm, respectively. In the radical thiol-ene approach, the line width is close to 200 nm and the rod spacing for resolved architectures is 2 µm. Concerning the overall dimensions, the entire radical thiol-ene woodpile structure fits into a segment of a single line from the photofixation approach. As mentioned, no covalent post-modification – in contrast to the radical thiol-ene pathway – was conducted in the photofixation method. Covalent fine-tuning is, however, an important function for micro-objects that paves the way for numerous applications. Therefore, albeit sharing the same chemical reaction for permanent network formation, the compared approaches are very different and are hence both an enrichment for the materials science community.

3.1.8 Summary

Fabrication of microstructures has been successfully demonstrated by employing a radical thiol-ene based photoresist for DLW. Woodpile structures with a rod spacing of 2 µm have been produced and investigated by SEM and FIB milling. Confirmation of the radical thiol-ene reaction as the polymerization mechanism was achieved utilizing FTIR spectroscopy by investigation of the corresponding thiol and olefin signals. Residual thiols have been addressed in post-modification reactions *via* the thiol-Michael addition, adding luminescent behavior or bromine functionality to the structure. Covalent post-functionalization was evidenced by LSM and XPS. The grafting density for layered structures was calculated to be approximately 200 molecules μm^{-2}. By combining DLW and radical thiol-ene chemistry, a potent technique has been established that allows for the precise functionalization of the fabricated structures. The covalent post-modification ability *via* the thiol-Michael *click* reaction makes the thiol-ene structure a promising instrument for several applications, including the efficient attachment of cell signaling molecules in the frame of cell behavior studies and as functional scaffolds in microfluidics and lab-on-a-chip systems.

3.2 Radical Thiol-Yne mediated Direct Laser Writing

In the preceding chapter, radical thiol-ene chemistry was introduced to DLW as a novel polymerization method. A key benefit of such an approach was the possibility for facile covalent post-modification *via* a single *click* reaction. Further, the investigation of the described methodology (see Section 3.1) allowed for a large increase in experience concerning DLW in general as well as an accumulation of profound knowledge about the needs and demands of covalently alterable micro-objects within the community. Several important objectives were hereby identified for the post-modification of structures:

- The extension of covalent alteration to more than one chemical pathway,
- the implementation of multiple post-modification reactions on a single object,
- the possibility for spatially resolved functionalization within one structure.

In addition, drawbacks of the technique were revealed. Specific disadvantages of the employed system were the writing speed and the height limitation for structure fabrication, constraining the maximum size and the quantity of produced architectures. As mentioned in Section 2.2, the introduction of galvanometric mirrors and the Dip-in configuration have been researched and implemented to meet these drawbacks. However, especially for the Dip-in configuration, stringent requirements accompany the choice of the photoresist. Nevertheless, a successful merging of the mentioned DLW innovations and functional photoresists with the ability of covalent post-modification would be greatly beneficial, allowing for the rapid production of micro-resolved functional mesostructures. In the following section, radical thiol-yne mediated DLW will be described: A methodology that tackles the demands for chemical pathway extension and orthogonal multiple post-modification of the resulting structures. Moreover, it combines the functional photoresist with recent DLW innovations. Similar to its radical thiol-ene counterpart, radical thiol-yne coupling leads to polymer formation in a thiyl-sustaining step growth manner, facilitating a high conversion and thereby qualifying the reaction as a potent candidate for DLW curing.

3.2.1 Photoresist Design

In a radical thiol-yne reaction, coupling leads to the consumption of thiols and alkynes. For the formation of densely crosslinked polymer networks that are required for stable structure fabrication in DLW, multifunctional monomer molecules must be utilized. Therefore, a tetrafunctional alkyne (Tetraalkyne) and a tetrafunctional thiol (Tetrathiol 2) were selected as monomer components. Both the chemical structures and a schematic DLW process are depicted in Figure 3.16. Since both monomers are miscible liquids, solely a photoinitiator (DETC, see Section 2.2 for the chemical structure) was added in small quantity. Thiol and alkyne molecules were mixed in a ratio of 2:1, based on the molarity of the functional groups. The applied ratio was chosen to account for the reaction of vinyl sulfides – produced in the course of the reaction – with thiyl radicals. For similar systems it has been shown that the reaction of a thiol with a vinyl sulfide is faster than its thiol-alkyne counterpart.[122,123] Therefore, it can be assumed that,

for the given ratio, the majority of vinyl sulfides react in the course of the DLW exposure. The targeted outcome of the reaction is thus the bis-sulfide species, generated by the overall reaction of two thiols and one alkyne. Ease of preparation remained an important consideration for the resist formulation. Following this concept, both the photoinitiator and the tetrafunctional thiol are commercially available.

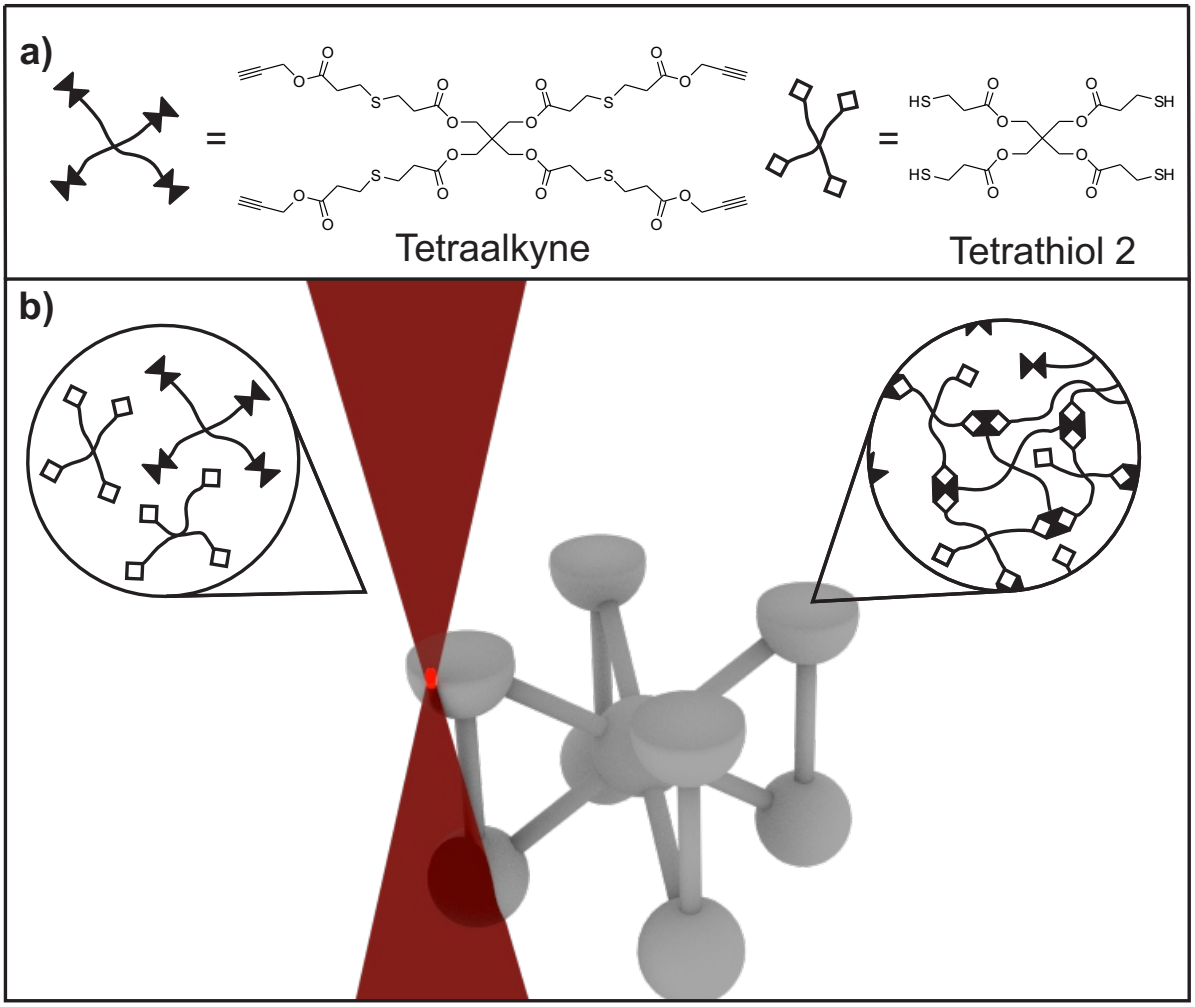

Figure 3.16: a) Schematic and chemical depiction of both monomer components of the radical thiol-yne photoresist: The tetrafunctional alkyne (Tetraalkyne) and the tetrafunctional thiol (Tetrathiol 2). b) Schematic depiction of the DLW process during structure fabrication with functional groups as lock-and-key models, differencing in uncured (left) and cured (right) regions. The double lock shape of the alkyne indicates the reaction of one alkyne and two thiols for bis-sulfide product formation.

Synthesis of the tetrafunctional alkyne can be readily performed in a one step procedure *via* a thiol-Michael addition reaction (see Figure 3.17). Therein, pentaerythritol tetrakis(3-mercaptopropionate) was reacted with an excess of propargyl acrylate in the presence of

hexylamine. Due to the *click* status of the thiol-Michael addition reaction, neither the use of a solvent nor a purification method was necessary. To obtain the final product, merely the residual catalyst and Michael acceptor were removed under reduced pressure.

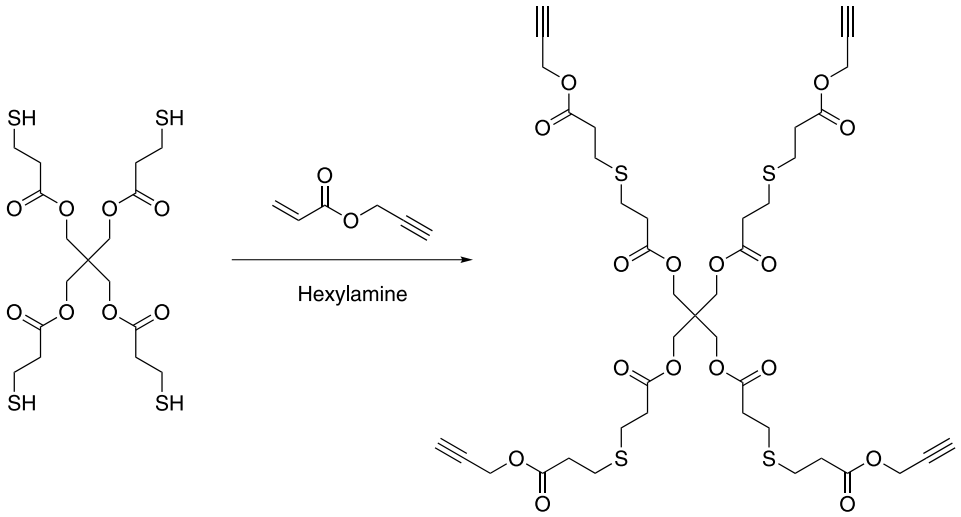

Figure 3.17: a) Depiction of the one step procedure for the synthesis of a sulfur containing tetrafunctional alkyne (Tetraalkyne) from pentaerythritol tetrakis(3-mercaptopropionate) (Tetrathiol 2), propargyl acrylate, and hexylamine. The employed reaction is a thiol-Michael addition.

Solvents, which are often needed in photoresist formulation in order to obtain homogeneous liquid resists, are not necessary for the presented radical thiol-yne photoresist, owing to the miscibility of both monomers and the solubility of the photoinitiator therein. Drawbacks attributed to solvent usage such as undesired evaporation, component precipitation, or even the complete desiccation of the sample leading to a time dependent threshold change or object destruction do not occur within the here presented photoresist. For convenient usage, a long shelf-life of the photoresist is desired, *e.g.*, for research that requires production of a large number of identical samples over a longer period of time. In the case of the here presented radical thiol-yne photoresist, no visible alteration of the performance was observed over a period of one month, whereupon the prepared batch was entirely consumed. In principle, a large variety of both thiols and alkynes can be considered as potential resist components, a fact that further increases the versatility of radical thiol-yne mediated DLW. However, the choice of components in this thesis served a specific purpose.

One of the main foci of radical thiol-yne mediated DLW was the combination of a novel polymerization process with a recent beneficial DLW innovation, namely the Dip-in configuration. Together with the usage of galvanometric mirrors, such a system allows for the rapid production of large architectures. As described in Section 2.2.7, a prerequisite for Dip-in DLW is a compatible RI between the photoresist and the employed objective lens. Therefore, the selection of monomers was influenced by the respective RI value of the resulting photoresist.

From the value of a commercially available immersion oil for the objective, the targeted RI for the photoresist is 1.52 (for 23°C and 589 nm). One possibility to tailor the RI of the photoresist is by adjusting the sulfur content.[130] A trivial option for RI increase of radical thiol-yne systems is by raising the thiol content. In the here presented case, however, this option cannot be conducted, since changing the molecular ratio would entail a drastically altered network formation, caused by the step growth nature of the polymerization. However, the sulfur content can also be modified by incorporation of additional sulfur atoms into the respective monomers. For the said reason, the utilized Tetraalkyne was selected to include four sulfur atoms. The resulting photoresist exhibits a RI of 1.52 (for 23°C and 589 nm), which is compatible with the employed objective lens. Hence, the here presented radical thiol-yne photoresist can conveniently be employed for DLW in Dip-in configuration, allowing for the fabrication of meso-type structures that feature 3D resolution on the low micrometer scale. The fabrication and characterization of such structures will be addressed in the following sections.

3.2.2 Microstructure Fabrication and Analysis

For the fabrication of radical thiol-yne mediated structures, the commercially available Photonic Professional GT system (Nanoscribe GmbH, Karlsruhe) was employed. Modifications of the new setup compared to the Photonic Professional system utilized in Section 3.1 are the usage of galvanometric mirrors and a different objective (63x oil-immersion objective, NA = 1.4). Production of objects in Dip-in configuration utilizing a fast writing speed is thereby enabled. Consequently, all scaffolds were generated with a writing speed of 1 cm s^{-1} (exceeding the writing speed in Section 3.1 by a factor of 100) employing Dip-in configuration in this section.

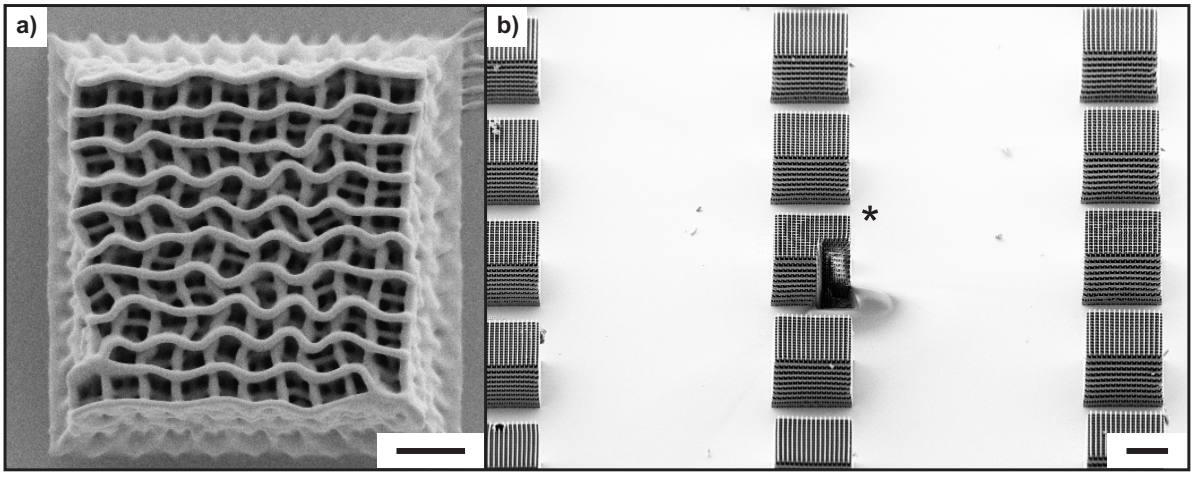

Figure 3.18: a) Top view of a deformed woodpile fabricated in a single exposure manner. b) A small section of an extensive parameter study (increasing laser power from top to bottom, increasing rod spacing from left to right) of multiple exposure (5x) woodpile photonic crystals. The interior of the marked woodpile has been revealed by FIB milling. An in-depth analysis of the marked woodpile can be viewed in Figure 3.19. Scale bars are 5 µm and 30 µm for a) and b), respectively.

In analogy to the radical thiol-ene photoresist (see Section 3.1), a most important parameter for every novel 3D lithographic system is the achievable 3D resolution. In order to investigate the attainable resolution, woodpile structures were fabricated and characterized concerning their structural integrity, yet also their performance as photonic crystals.[63] Very similar as

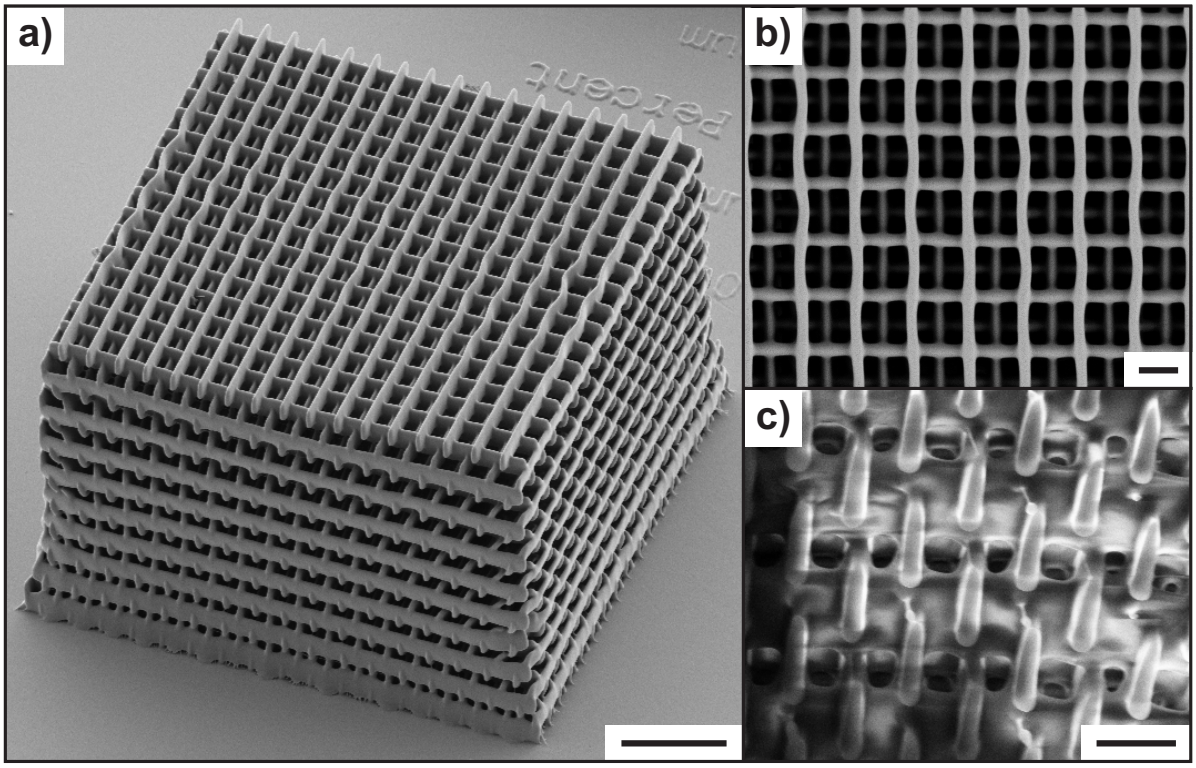

Figure 3.19: SEM micrograph of a) the side view and b) the top view of a woodpile photonic crystal fabricated by radical thiol-yne mediated DLW. c) Depicts the interior of the woodpile after FIB milling. Scale bars are 10 µm for a) and 2 µm for b) and c).

in Section 3.1, parameter studies were carried out where the rod- and layer spacing as well as the laser power were varied. Preliminary results indicated that woodpile photonic crystals generated with a laser power well above the threshold *via* a single exposure of every respective line typically yielded largely deformed structures after development (for an example, see Figure 3.18).[f] Such a pronounced deformation rendered the resulting structures useless and thus impeded accessible resolution on the low micrometer scale. A possible explanation for the detected deformation behavior was the insufficient conversion that is obtained for the radical thiol-yne photoresist during a single line exposure. An effective route to increase the conversion of obtained structures is to apply multiple exposures. A side effect of such a strategy is the slight decrease in resolution, caused by accumulated exposure dose in the peripheral voxel regions (following the argumentation of a "remembering" photoresist behavior in Section 2.2). Therefore, the parameter studies were augmented by multiple exposure structuring. Within these experiments, parameters were found that allow fabrication of woodpile photonic crystals

[f] SEM in this section was performed by Martin Schuhmann

with micrometer scale resolution. As an example, a SEM image of a specific woodpile featuring a footprint of 50×50 µm^2, a total number of 10 periods (40 layers), a rod spacing of 3 µm, and a layer spacing of 1.13 µm is depicted in Figure 3.19. The production laser power of the depicted woodpile was 19.44 mW. FIB milling was performed for in-depth investigation of the interior. Deformation stemming from development procedures has drastically been reduced and the image reveals a fully resolved 3D architecture. Besides the presented characterization, the structural integrity was also confirmed by analysis of features resulting from the periodic nature of the generated objects.

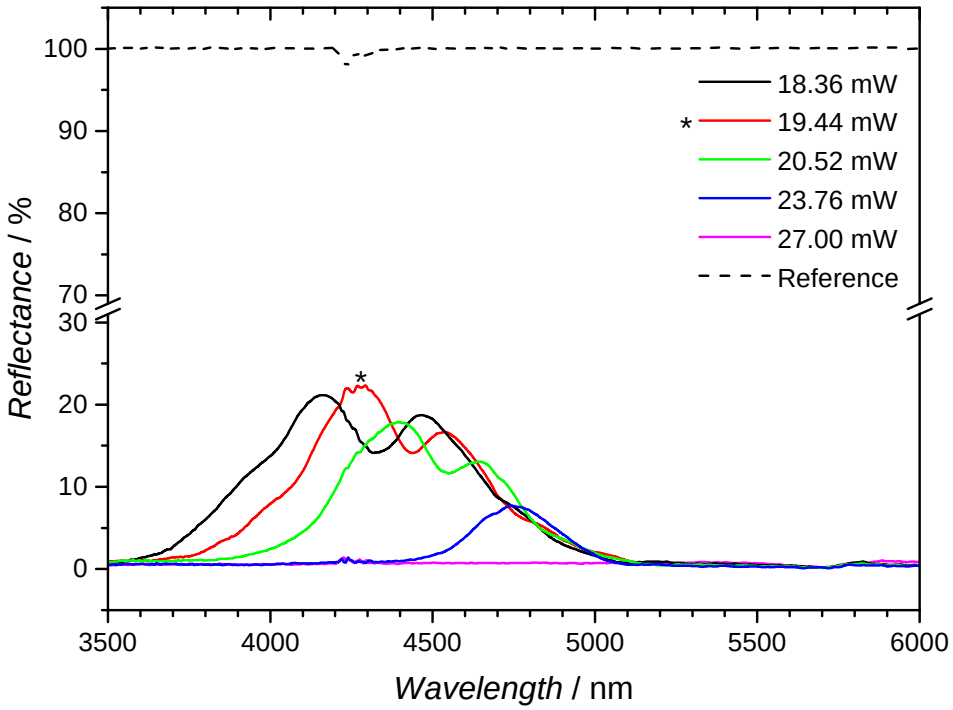

Figure 3.20: Reflectance spectroscopic measurements recorded for woodpile photonic crystals at different laser powers (rod spacing = 3 µm). With decreasing writing power the photonic stop band is shifted to a lower wavelength. The highest reflectance (23%) is observed for a writing power of 19.44 mW (marked spectrum, for SEM analysis of the corresponding structure, see Figure 3.19).

Within this section it has been mentioned that woodpile structures are photonic crystals, *i.e.*, they reflect light of a certain wavelength. The wavelength region of reflection is termed a photonic stop band. Apart from being useful for several applications, such a behavior can be exploited for a further, non-invasive investigation of structural quality. The said property is one of the main reasons why the woodpile has been established as a benchmark structure for resolution studies in 3D lithography. The spectral location of the stop band is dependent upon structural parameters such as the rod and layer spacing or the filling fraction. In general,

the wavelength of reflected light decreases for a reduced rod spacing and filling fraction. For a rod and layer spacing of 3 μm and 1.13 μm, respectively, the wavelength of reflected light lies in the infrared region. Reflectance IR measurements of a series of woodpile photonic crystals, fabricated utilizing the just mentioned spacing parameters at different writing powers, are depicted in Figure 3.20. As a reference, a silver mirror was employed for 100% reflectance. By comparison of the different collected spectra it becomes clear that for a high average laser power (27.00 mW) no photonic stop band is visible, indicating that the corresponding woodpile structure is not fully resolved. At 23.76 mW average laser power a photonic stop band can be assigned. For further reduced writing power, the filling fraction of the structure decreases, thereby shifting the corresponding stop bands to a lower wavelength. The highest quality structure, derived from the height of the stop band (23% reflectance, marked structure), was obtained for a laser power of 19.44 mW. In fact, the spectrum was collected from the exact same woodpile photonic crystal that is depicted in Figure 3.19.[g] Apart from reflection measurements, recorded transmission spectra are commonly investigated for stop band analysis. However, transmission spectra obtained for woodpile structures in the radical thiol-yne case are more complex. The stop band, visible as a decrease in transmittance in the corresponding region, is superimposed by signals stemming from different chemical vibrations of the structure (as will be presented in Section 3.2.4). For reasons of simplification, transmission spectra are thus not included in Figure 3.20. Following the successful demonstration of micro-resolved fabrication and characterization of woodpile photonic crystals, the production of meso-type scaffolds will be addressed in the following section, thereby taking full advantage of the employed DLW innovations.

3.2.3 Mesostructure Fabrication and Analysis

With both a rapid writing speed and Dip-in configuration at hand, the fabrication of micro-resolved structures with significantly increased overall dimensions was investigated in order to demonstrate the lithographic possibilities and performance of radical thiol-yne mediated DLW. For the said purpose, demanding parameters were selected. Again, a writing speed of 1 cm s^{-1} – the maximum specified writing speed of the Photonic Professional GT setup – was employed for experiments. Objects were generated in a layer-by-layer manner with a lateral and axial slicing distance of 400 nm and a writing power of 21 mW. Body-centered cubic unit cells were fabricated as proof-of-principle mesostructures (see Figure 3.21). While each period consisted of an array of 4×4 lateral unit cells, the number of periods in axial direction was varied. In that way, scaffolds with 1, 2, 4, 8, and 32 periods were subsequently produced in one single lithographic step. Every structure exhibited a nominal footprint of 132.5×132.5 μm^2 and the nominal height of each structure was set to be 42.5, 72.5, 132.5, 252.5 and 972.5 μm, respectively.

The tallest structure, consisting of 32 periods of unit cells, was investigated in more detail. In Figure 3.22, a SEM micrograph of the entire architecture as well as close-up views from the top and the side revealed a uniform, fully resolved object with a smooth surface and only

[g] Reflection FTIR measurements were performed prior to SEM analysis and FIB milling.

sparse deformation. From the SEM micrograph, the height of the structure was calculated to be approximately 970 µm (the angle of the SEM stage was set to 45°). The negligible difference between the nominal and the experimental height serves as supplemental proof for the high structural quality of the object.

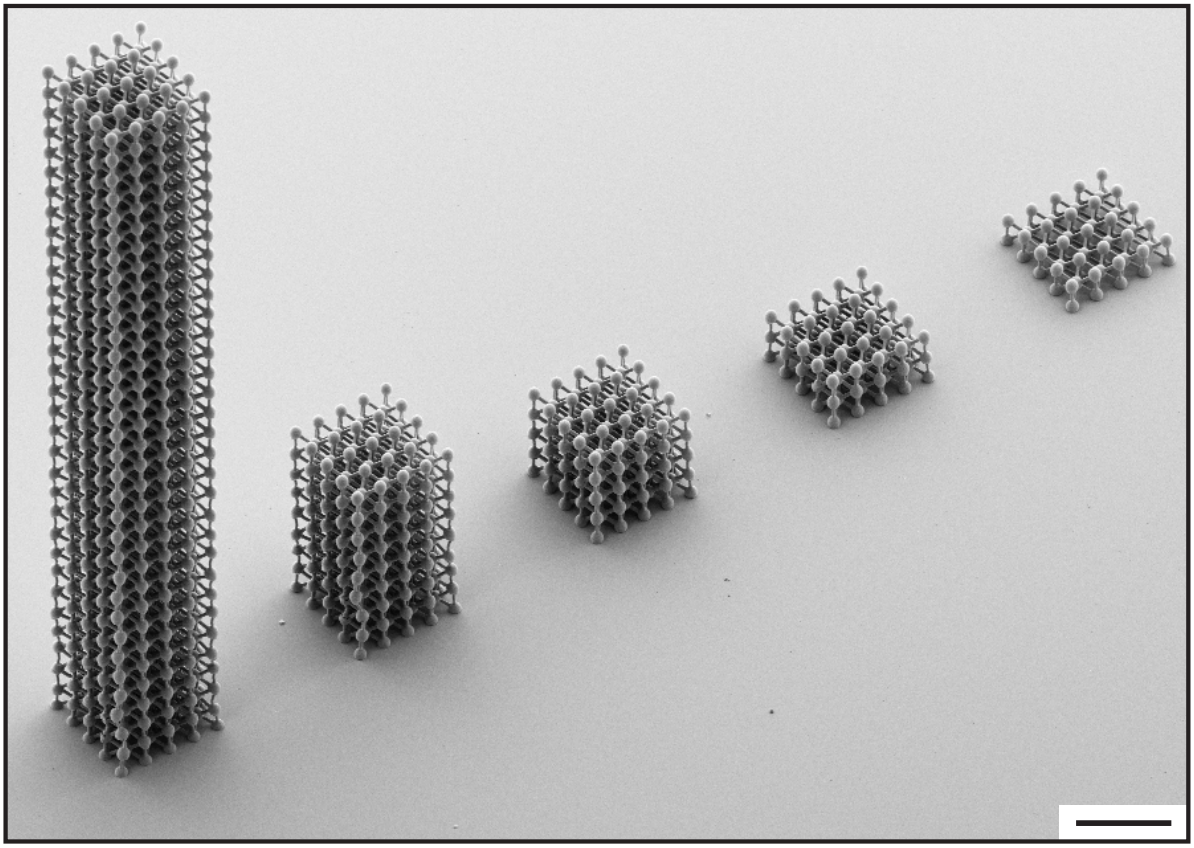

Figure 3.21: Overview SEM image of 1, 2, 4, 8, and 32 periods of 4×4 unit cell architectures (from right to left). The nominal height of each structure is 42.5, 72.5, 132.5, 252.5, and 972.5 µm, respectively. The scale bar is 100 µm.

Since the 32-period mesoscopic structure is easily visible to the naked eye, imaging *via* optical photography was possible.[h] In Figure 3.23, a camera image of the sample is depicted. The sample was placed in order to feature the 32-period structure in front. Careful observation allows for identification of the remaining scaffolds on the substrate that are aligned behind the front architecture (see also Figure 3.21). For comparison, a screw with a diameter of 2 mm (including the winding) was placed in the background. Moreover, as a novel characterization technique, ToF SIMS was implemented as an analysis tool for the fabricated structures.[i]

[h] Optical photography was performed by Tiemo Bückmann.
[i] ToF SIMS analysis in this section was conducted by Dr. Michael Bruns.

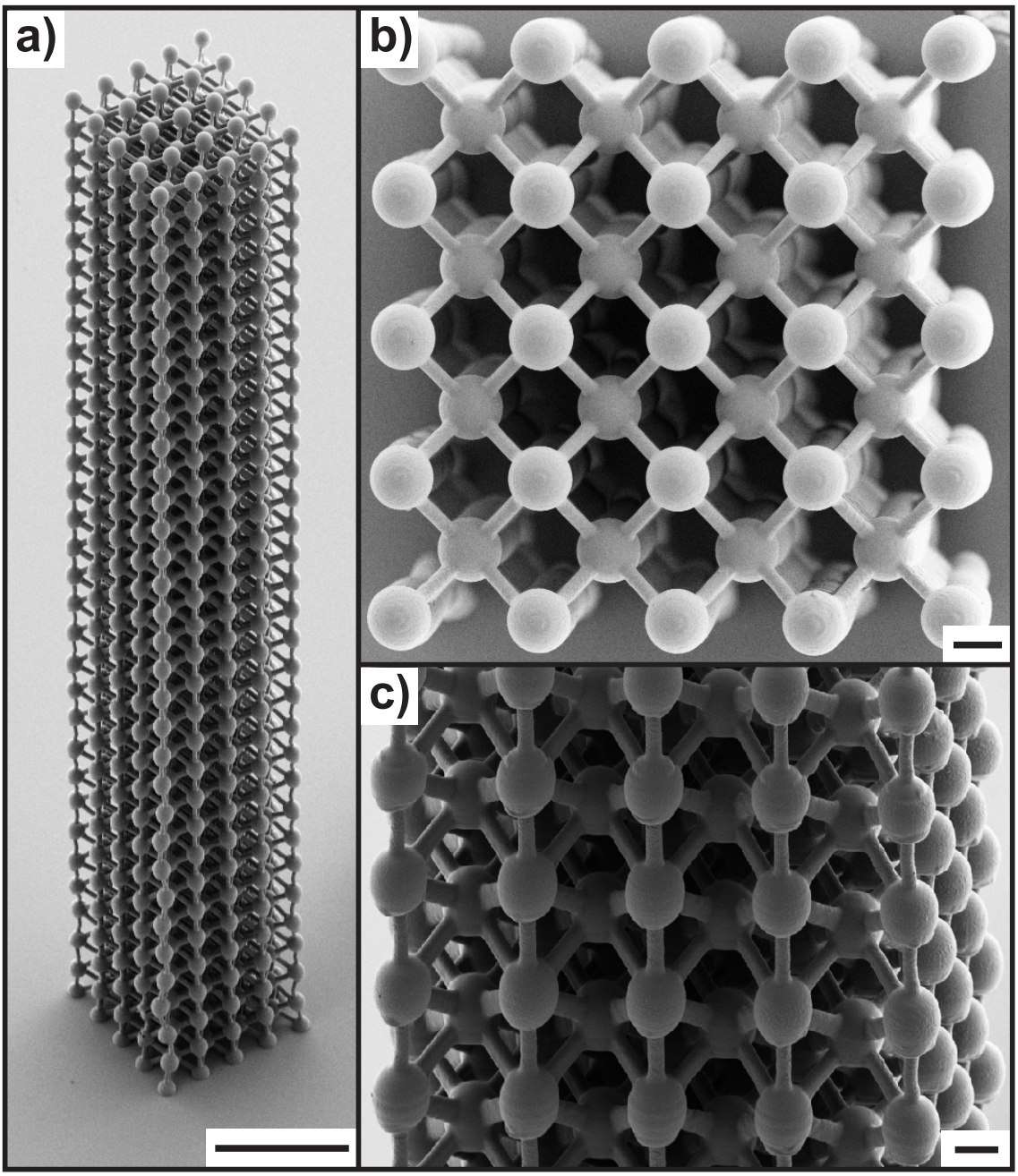

Figure 3.22: In-depth SEM analysis of the 32 period cubic unit cell structure. The entire architecture is depicted in a), while b) and c) are close-up views of the top and side of the object, respectively. Analysis reveals a uniform meso-object with micrometer feature size and a smooth surface. Scale bars are 100 μm for a) and 10 μm for b) and c).

ToF SIMS is a characterization technique that is widely used for the determination of surface bound chemical information of 2D samples. A beneficial feature of the technique is the possibility for spatially resolved sample characterization that allows for the investigation of,

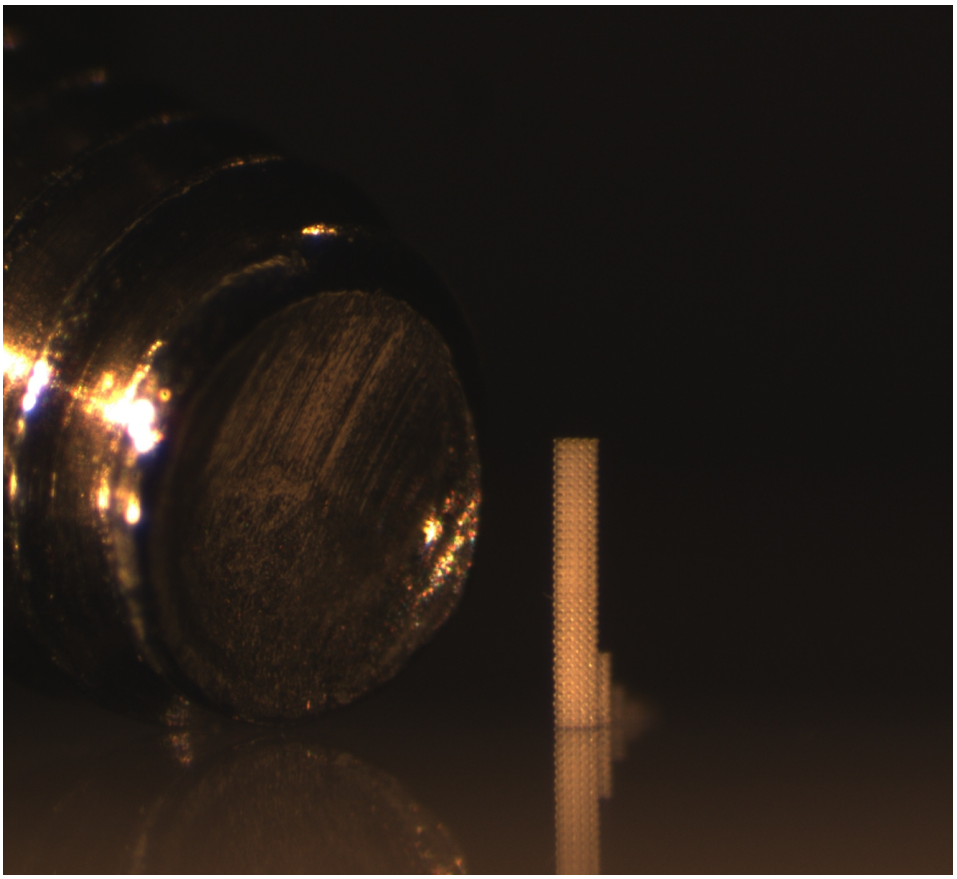

Figure 3.23: Optical photography image of the 32 period cubic unit cell structure (in front). Additional architectures are visible behind (compare to Figure 3.21). A 2 mm diameter screw is placed in the background for comparison.

e.g., photomask patterns apart from plain surface analysis.[198] Moreover, *via* sputter-depth profiling, ToF SIMS imaging has been extended for the analysis of layered 3D systems.[199] Such a characterization experiment alters the sample in a destructive way as layers must be removed in order to investigate subjacent regions. In an effort to establish a novel, non-destructive chemical characterization method for 3D DLW written objects, an adapted ToF SIMS imaging procedure was applied. Therein, the sample stage was slightly tilted, enabling non-destructive visualization of subjacent regions. For demonstration purposes, a gold sputtered (10 nm) scaffold (8 periods of a 3×3 cubic unit cell structure with additional horizontal bars throughout the object) was investigated by ToF SIMS analysis after conventional SEM imaging (see Figure 3.24). The depicted total ion count and Au^- images display the 3D architecture in a good quality and resolution. Efficient, mild and non-destructive 3D analysis is thereby clearly demonstrated, revealing ToF SIMS imaging as an excellent characterization method with the advantage of simultaneous achievement of chemical and structural information. For the analysis, the gold sputtered structure served as a proof-of-principle. From the Au^- image it becomes clear that in addition to the topmost layer, containing the majority of the deposited gold due to the sputtering technique, underlying gold exhibiting regions are detected and are

thus available for investigation. 3D ToF SIMS imaging was further utilized for detection of surface bound moieties of structures within Section 3.2.5.

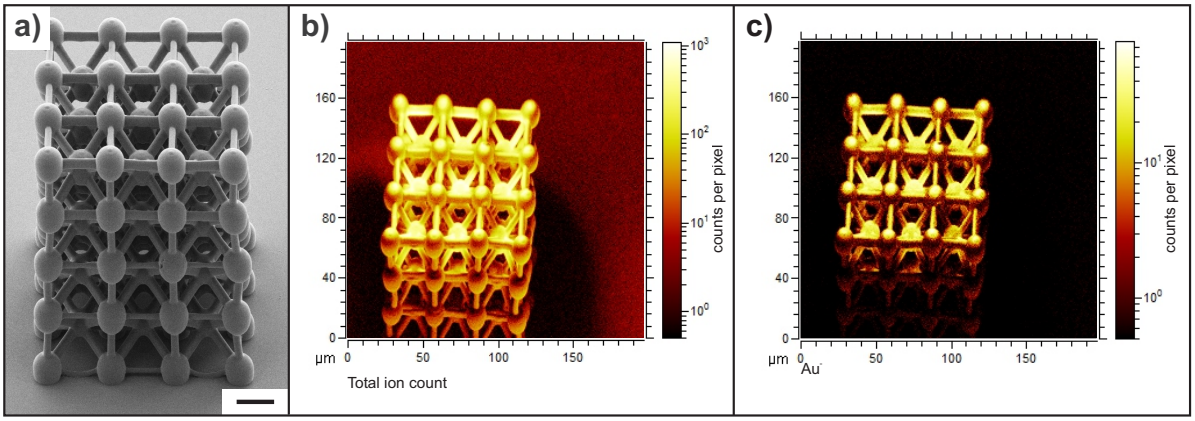

Figure 3.24: a) SEM micrograph of a gold coated 8 period cubic unit cell structure with horizontal bars. b) Subsequent total ion count and c) Au^- ToF SIMS imaging of the same object. The tilted sample stage allows for investigation of regions that are subjacent to the topmost period. The scale bar is 20 µm.

Together, the presented characterization methods clearly evidence the fabrication of both woodpile photonic crystals with micrometer resolution and meso-structures with an overall height of up to one millimeter *via* employment of the radical thiol-yne photoresist. As the next step, chemical analysis of the polymerization reaction during exposure is an important task for the verification of the postulated production mechanism. Such an investigation will be described in the following section.

3.2.4 Chemical Structure Characterization

Besides the production of objects, the verification of the postulated chemical reaction during the production process needed to be pursued. Evidence for the radical thiol-yne coupling being the dominant reaction during the generation of 3D scaffolds was obtained – as in Section 3.1 – by FTIR spectroscopy. As analysis scaffolds, solid cuboid structures with a footprint of $50 \times 50\ \mu m^2$ and a height of nominally 15 µm were produced. Thiols as well as alkynes possess characteristic vibrational bands, enabling to unequivocally prove their presence or absence.[196] Thiols – as already mentioned – exhibit a specific stretching vibration at a wavenumber of 2550-2600 cm^{-1}. Terminal alkynes display two characteristic stretching vibrations, one at 2100-2150 cm^{-1} and another at 3275-3325 cm^{-1} corresponding to the carbon-carbon triple bond and the carbon-hydrogen bond, respectively. FTIR spectra of each single photoresist component (excluding the photoinitiator), the mixed photoresist and a produced cuboid architecture are displayed in Figure 3.25. In the spectrum of Tetraalkyne, absorption bands are existent that correspond to stretching vibrations of different saturated alkane species at 2800-3000 cm^{-1}. In addition, characteristic signals are present at 2127 cm^{-1} and at 3277 cm^{-1} which can be assigned to the corresponding stretching vibration of the triple bond and the terminal carbon-hydrogen

bond, respectively. In the spectrum of Tetrathiol 2, a clear signal is detectable at 2567 cm^{-1} that can be assigned to the thiol stretching vibration. Apart from the photoinitiator, the photoresist is merely a mixture of the thiol and the alkyne monomer. Hence, the corresponding FTIR

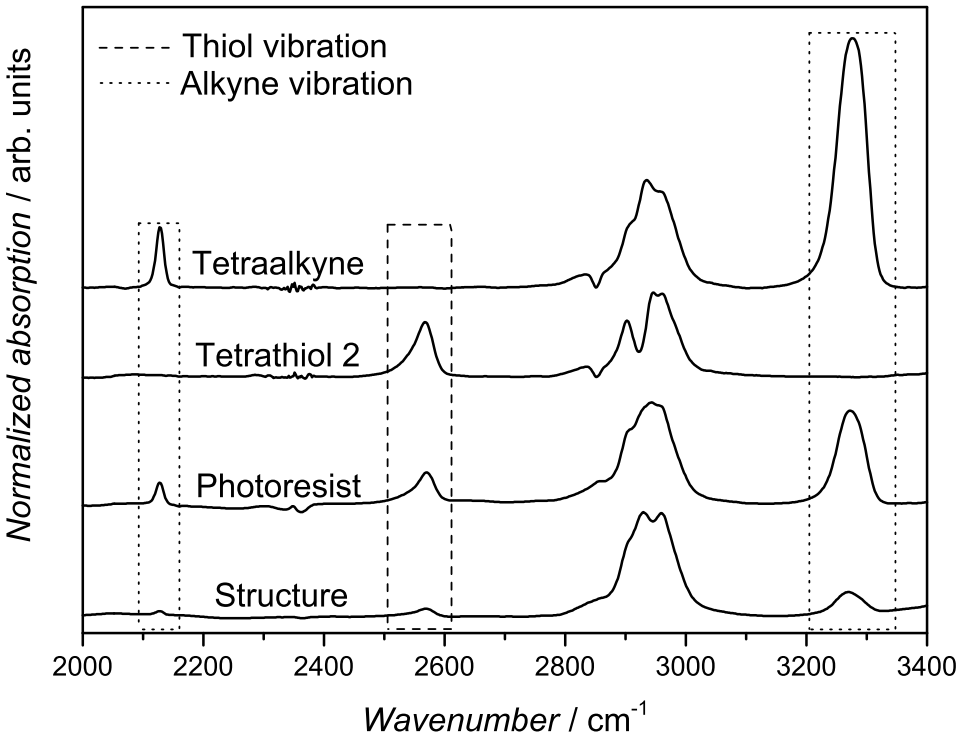

Figure 3.25: Comparison of recorded FTIR spectra: Tetraalkyne, Tetrathiol 2, the radical thiol-yne photoresist, and a fabricated cuboid structure (from top to bottom). Distinct signals are detected at 2127 cm^{-1} and 3277 cm^{-1} for the alkyne and at 2567 cm^{-1} for the thiol. The radical thiol-yne photoresist displays both the alkyne and the thiol vibration. After DLW, thiol and alkyne bands are clearly diminished, verifying the proposed curing mechanism. Further, the presence of residual functional groups after fabrication is shown. For better clarity, the spectra are normalized and shifted vertically.

spectrum contained – as expected – both the thiol and the alkyne signals. During the overall radical thiol-yne reaction, thiols and alkynes are consumed. Concomitantly, the corresponding absorption peaks are significantly diminished for a proceeding radical thiol-yne reaction. By comparison of the photoresist spectrum with the spectrum of the written structure, the significant decrease becomes evident. However, residual functional groups remain throughout the structure after fabrication, proven by the existence of small thiol and alkyne signals in the spectrum of the structure (similar to findings in Section 3.1). The expected occurrence can be explained by incomplete conversion during network formation: With increasing conversion, the mobility of the participating molecules decreases. At some point the decreased mobility of the functional groups prevents further reaction, leading to remaining chemical functionality within written architectures. A further indication for the postulated reaction is the absence of a signal

slightly above 3000 cm^{-1}, characteristic for unsaturated bonds such as the vinyl sulfide species. The mentioned finding underlines the assumption of an efficient reaction between two thiols and one alkyne towards the saturated bis-sulfide species. It should here be noted, that other, more unique signals for double bonds, *e.g.*, in the vicinity of 1600 cm^{-1} or in the fingerprint area can not be straightforwardly investigated with the here employed transmission FTIR, due to absorption of the glass cover slip. In principle, the utilization of silicon wafers as substrates allow for circumvention of said restriction. However, since the reaction pathway can readily be evidenced *via* the thiol and alkyne signals, such experiments have not been performed in this section.

All in all, the collected spectra clearly revealed that object formation during radical thiol-yne mediated DLW proceeds as hypothesized. The presence of pending thiols and alkynes throughout the fabricated scaffold deem radical thiol-yne mediated structures eminently suitable for post-modification procedures. Different from the presented radical thiol-ene mediated DLW (see Section 3.1), the here presented objects feature not merely one, but rather two highly eligible functional groups for reaction, namely a thiol and an alkyne. In the following section, covalent structure modification will be described employing these functionalities.

3.2.5 Covalent Post-Modification

During the verification of the proposed chemical pathway employing FTIR spectroscopy (see previous section), the presence of residual thiols and alkynes throughout written architectures became evident. Such functionalities can be exploited for post-modification strategies in highly effective reactions, thus enabling fine-tuning of material properties. In Section 3.1 covalent post-modification with residual thiols has been demonstrated by the thiol-Michael addition reaction. In radical thiol-yne prepared micro-objects, residual alkynes are present in addition to thiols. Therefore, next to the thiol-Michael addition reaction, chemical reactions with participating alkynes can be applied for covalent attachment. An adequate reaction is the copper(I) mediated 1,3 dipolar cycloaddition reaction between azides and alkynes (CuAAC, see Section 2.4), enabling the possibility for dual chemical modification (see Figure 3.26).

For a proof-of-concept investigation of dual functionalization, solid cuboid objects with identical structural parameters as in Section 3.2.4 were fabricated *via* radical thiol-yne mediated DLW. After production, residual thiols were addressed in a thiol-Michael addition reaction for the immobilization of a bromine-containing maleimide. In such a procedure, the cuboid samples were immersed in a solution containing the maleimide and triethyl amine for 24 hours. Subsequently, a development step was performed in order to remove non-covalently attached species. FTIR spectra of the cuboids were recorded before and after the thiol-Michael addition procedure (see Figure 3.27). In the course of the reaction, thiols are consumed and a saturated imide is formed. The successful reaction was clearly evidenced by the clear diminution of the corresponding thiol band in the collected spectrum after reaction. Furthermore, a signal stemming from the covalently immobilized saturated imide was assigned at 1776 cm^{-1}. The signal corresponds to one of two carbonyl stretching vibration bands. The second imide stretching signal located at approximately 1700 cm^{-1} could not be be taken as evidence for a

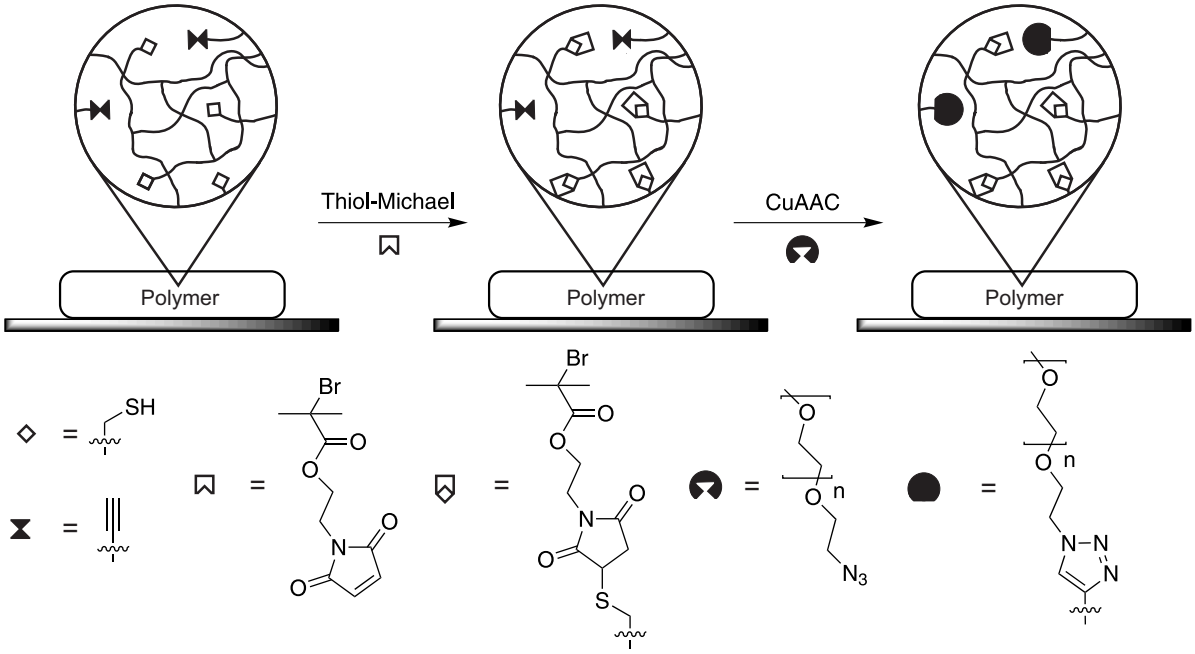

Figure 3.26: Schematic depiction of the dual covalent modification employing pending functional thiols and alkynes of produced objects. In a first reaction step, thiol-Michael addition was performed to immobilize a bromine moiety while the CuAAC reaction was employed for subsequent attachment of PEG.

successful functionalization due to the large overlap with other carbonyl signals. Orthogonality of the thiol-Michael addition reaction towards pending triple bonds was confirmed, indicated by the remaining absorption signals corresponding to the alkyne. Hence, subsequent to the thiol-Michael addition procedure, the residual alkynes were targeted for a further covalent modification, namely a CuAAC reaction. Thereby, the sample was immersed in an oxygen free solution containing α-azide poly(ethylene glycol) methyl ether (PEG-N_3, M_n = 2000 g mol^{-1}), PMDETA, and CuI for 48 hours to immobilize poly(ethylene glycol) moieties. In the case of a successful reaction, alkynes are consumed. The corresponding decrease in the FTIR spectrum revealed the success of the reaction, ultimately evidencing the targeted dual post-modification *via* sequential thiol-Michael addition and CuAAC. The missing azide signal at 2120-2160 cm^{-1} and the remaining imide signal further confirmed the absence of any physisorbed bromine or PEG moieties.

After evidencing the dual post-modification, it was important to investigate the location of the functional groups in detail. Although transmission FTIR spectroscopy clearly demonstrated the success of each reaction, no information about the location of the covalently bound molecules was obtained. A plausible speculation is the random distribution of functional groups within the 3D scaffold as neither the network formation nor the manner of fabrication channel the density of functional moieties into a specific region. Following this line of thought, a fraction of the residual functionalities should be located on, or in close proximity to, the structural surface.

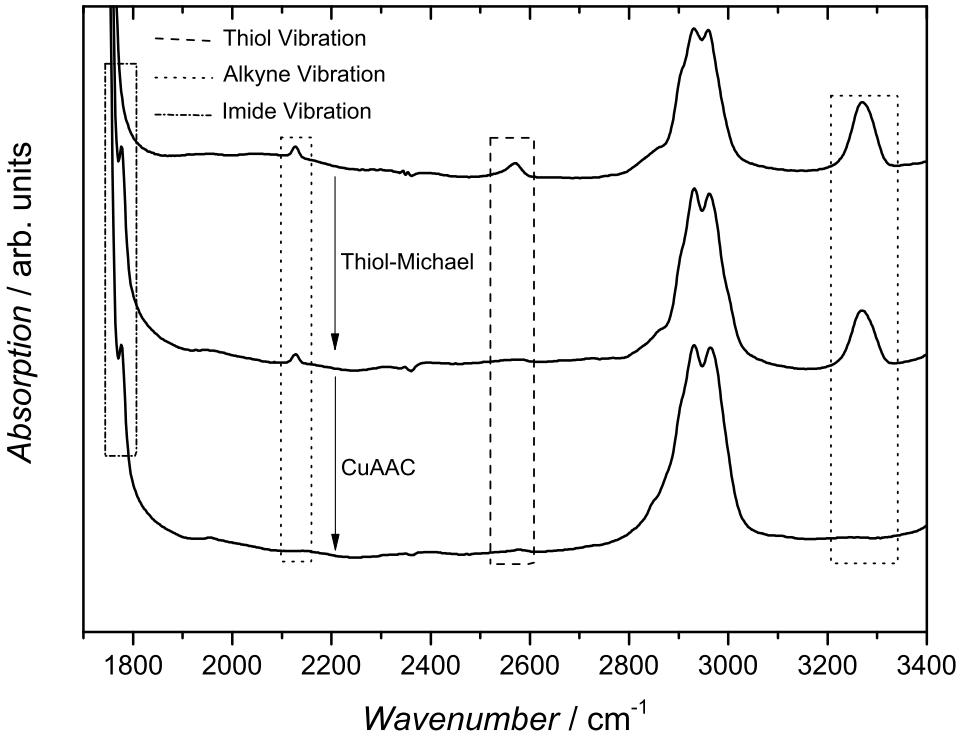

Figure 3.27: FTIR spectra of cuboid microstructures after fabrication, thiol-Michael addition, and CuAAC (from top to bottom). After the thiol-Michael addition, the thiol signal is strongly decreased and a saturated imide band is detected, confirming a successful reaction. The subsequent CuAAC reaction is evidenced by the diminution of the alkyne signals. For better clarity, the spectra are shifted vertically.

In order to identify surface bound moieties, the dual functionalized cuboid structures were subjected to ToF SIMS analysis (see Figure 3.28). The selection of molecules for covalent immobilization comprised the appearance of characteristic fragments for ToF SIMS imaging. Thus, a bromine and a PEG moiety was chosen for the thiol-Michael addition and the CuAAC, respectively. In the ToF SIMS analysis, a distinct signal stemming from both bromine isotopes ($^{79}Br^-$ and $^{81}Br^-$) was detected on the cuboid structures, revealing successful surface attachment *via* the thiol-Michael addition reaction. Furthermore, the viability of the attached bromine moiety for CuAAC reaction conditions is shown. Apart from bromine fragments, PEG fragments (C_2HO^-, $C_2H_3O^-$, $C_2H_2O_2^-$, $C_2H_3O_2^-$, and $C_2H_5O_2^-$) were revealed on the surface of the cuboids. In-depth analysis of the PEG fragments on the ToF SIMS image showed that small quantities of PEG are also present on the plain substrate surface, an effect that may stem from unspecific adsorption on the glass. Harsher development conditions or a change of the substrate might reduce the described undesired effect. Nevertheless, the combined results clearly show the covalent immobilization of PEG, thereby clarifying the presence of successful dual functionalization to the structural surface. Although the aim of investigation was a proof-of-concept, the attached molecules are, in principle, suitable for future scientific tasks. While the immobilized bromine moiety is a potent initiator for ATRP, PEG is a widely employed component for bioapplications. Naturally, dual functionalization is not restricted to

the here presented molecules. A significant advantage of the utilized *click* reactions is their compatibility with a vast number of molecules. As mentioned in Section 2.1.3, *click* reactions proceed rapidly in solution and, under correct conditions, reach full conversion within minutes or even seconds. In this section, the thiol-Michael addition and the CuAAC reaction were carried out for 24 hours and 48 hours, respectively. A shorter reaction time resulted in a less distinct alteration of the corresponding FTIR bands (not shown). This finding strongly indicates that the reaction rate of the *click* reactions is not the limiting factor in the approach. Therefore, a plausible speculation is that the overall rate of the bulk post-modification is limited by diffusion of the components throughout the structures.

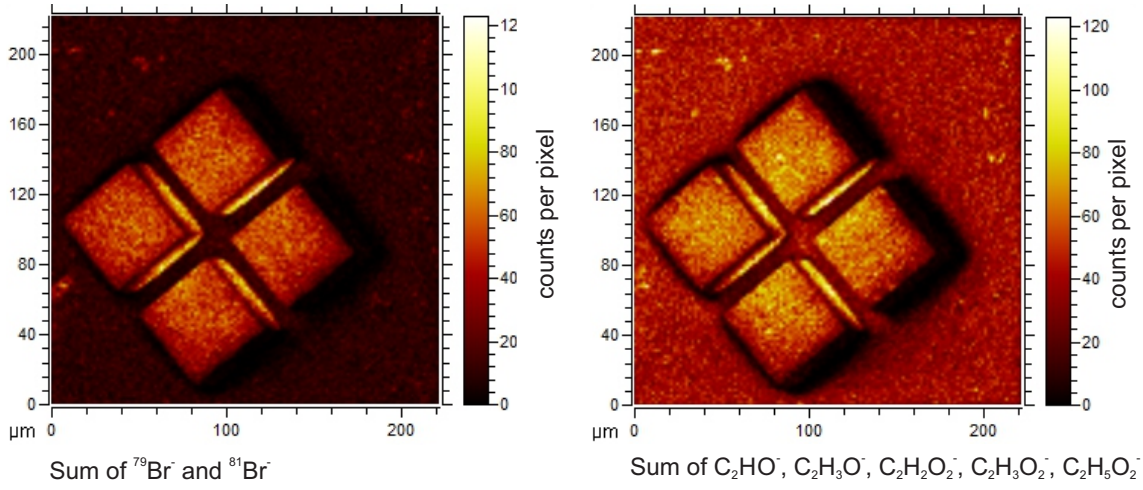

Figure 3.28: ToF SIMS analysis of cuboid structures after dual functionalization by thiol-Michael addition reaction and subsequent CuAAC. The presence of bromine (left) and PEG (right) on the structural surface is evidenced *via* the sum of corresponding characteristic fragments.

After revealing the possibility for covalent dual post-modification, the order of reaction sequence was investigated. In an alternative strategy, the order of post-modification reactions was inverted, now commencing with the CuAAC reaction. Thereby, a fabricated structure was immersed into a solution of CuCl, PMDETA, and a chloride-containing azide (2-azidoethyl 2-chloropropanoate). Comparison of the transmission FTIR spectra of the pre- and post-modified structure evidenced the consumption of pending triple bonds, thus confirming a successful CuAAC reaction (see Figure 3.29). Unfortunately, the thiol signal is also strongly diminished, indicating the consumption of thiols during CuAAC conditions and thereby impeding a subsequent thiol-Michael addition. A possible explanation is the usage of PMDETA. While serving as a copper (I) ligand in the CuAAC reaction, it also features the properties of a base and thus deprotonates thiols to activated thiolate anions. The activated thiolate species is a potent nucleophile that may undergo side reactions. A switching of the CuAAC conditions to a sodium ascorbate / copper(II) system was investigated, yet under these conditions covalent object modification *via* the CuAAC reaction was not successful (not shown). By comparing both sequential

post-modification pathways, the possibility for straightforward dual covalent modification is restricted to the first pathway where the CuAAC reaction follows the thiol-Michael addition reaction. The following section briefly summarizes the results for radical thiol-yne mediated DLW.

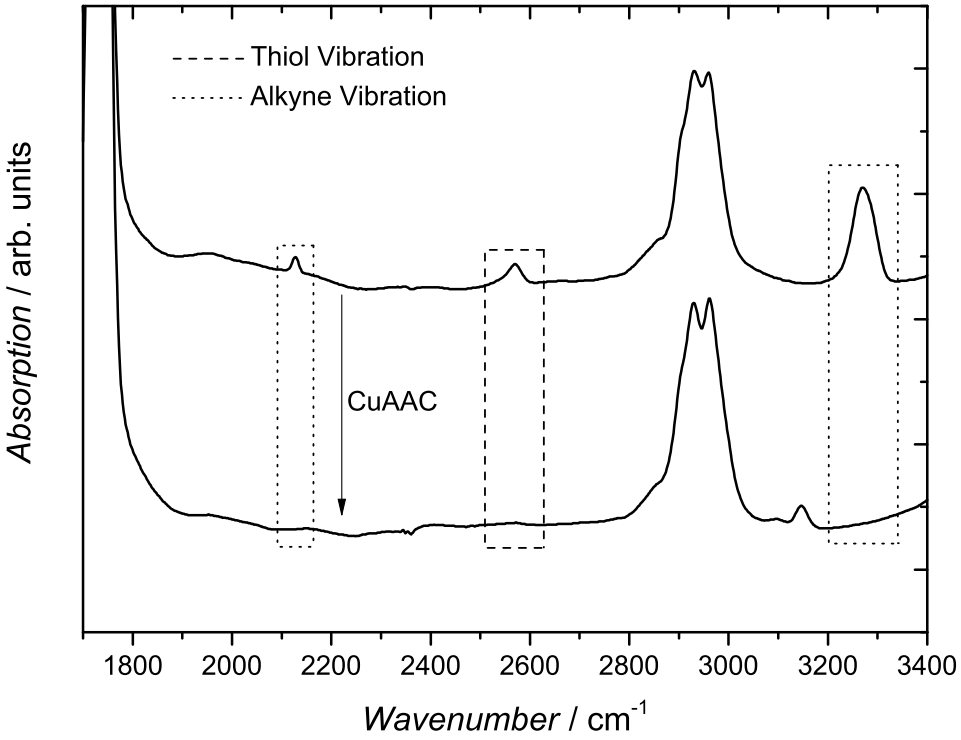

Figure 3.29: FTIR spectra of cuboid microstructures after fabrication and following CuAAC (from top to bottom). After the CuAAC reaction the alkyne signals are prominently decreased, confirming a successful reaction. Unfortunately, no thiols are present after the CuAAC reaction conditions, impeding straightforward dual functionalization.

3.2.6 Summary

Successful fabrication and post-modification of 3D micro- and mesostructures was demonstrated by radical thiol-yne mediated DLW. A novel photoresist, consisting of a tetrafunctional thiol, a tetrafunctional alkyne, and a photoinitiator was designed to feature a specific RI, enabling writing in Dip-in configuration. Combined with a fast writing speed, both woodpile photonic crystals with a rod spacing of 3 µm and cubic unit cell mesostructures with a height of up to 1 mm were rapidly produced. Characterization was performed *via* SEM, FIB milling, ToF SIMS, optical photography, and reflection spectroscopy. Moreover, FTIR spectroscopy was performed on photoresist components and generated cuboid structures, verifying the occurrence of the radical thiol-yne reaction during exposure. In these measurements, it was further shown that pending functional groups can be found throughout the produced scaffold

due to incomplete conversion during network formation. Consequently, the residual thiols and alkynes were addressed in a sequential covalent post-modification procedure consisting of a thiol-Michael addition and a subsequent CuAAC. Each sequential step was monitored and the success verified *via* FTIR spectroscopy, evidencing efficient dual functionalization. Due to the careful selection of attached molecules – a bromine during the thiol-Michael addition and a PEG during the CuAAC – ToF SIMS imaging furthermore confirmed the presence of both immobilized functions on the surface of the cuboids. The here presented radical thiol-yne mediated DLW combines thiol-yne chemistry with most recent DLW innovations, resulting in a simple to handle, rapid and powerful fabrication system. In combination with the option for dual covalent bulk and surface modification, the new system serves as a platform for a range of different applications, for instance, in lab-on-a-chip systems, microfluidics, and microreactors.

4

Photoenolization as a Versatile Concept for 3D Microlithography

In the previous chapter, thiol mediated radical coupling was employed as the key chemistry for the fabrication of 3D structures. During this research it became clear that step growth polymerization systems are well suited for DLW lithography. Moreover, an important finding was the existence of pending reactive groups for facile covalent post-modification. However, no straightforward, spatially resolved functionalization of the structure was demonstrated and the discussed systems were not applicable for diffraction unlimited lithography concepts. Therefore, a further chemical approach will be described in the following section: Photoenol mediated DLW.

4.1 Photoenol Mediated Direct Laser Writing

As described in Section 2.5, photoenolization combined with Diels-Alder trapping of *o*-quinodimethanes, termed photoenol chemistry, is a rapid and highly efficient ligation strategy. Consequently, the photoenol approach is a potent candidate for light-induced step growth polymerization procedures. The non-radical photoenol polymerization resembles classical step growth polymerization methodologies such as polyaddition rather than radical thiol coupling or chain growth procedures. In the latter polymerization methods only the generation of initiating fragments is light triggered. The following polymerization events, however, proceed independent of light irradiation. In the case of FRP, the active species is the propagating chain that remains active after incorporation of a monomer molecule, while in radical thiol coupling, a thiyl radical is formed in the reaction sequence, replacing the reacted thiyl molecule. Therefore, in both cases every propagation step sustains the active species. Within a liquid negative-tone photoresist, the associated active species can diffuse in an unobstructed manner. As a consequence, propagating species can exit the exposed volume and continue to polymerize, permanently solidifying unexposed areas and lowering the achievable resolution. For a non-radical step polymerization system utilizing photoenol chemistry the situation is

Parts of this chapter were reproduced from Quick, A.S.; Rothfuss, H.; Welle, A.; Richter, B.; Fischer, J.; Wegener, M.; Barner-Kowollik, C. *Adv. Funct. Mater.* **2014**, *24*, 3571-3580 with permission of Wiley-VCH and from Fischer, J.; Quick, A.S.; Richter, B.; Mueller, J.B.; Bastmeyer, M.; Barner-Kowollik, C.; Wegener, M. *Hochaufgelöste Photochemie Unterhalb des Beugungslimits Mittels Schaltbarer Photoenolisierung* **2015** with permission from the authors.

fundamentally different. While the generation of active species is also light-induced, active species are consumed, not sustained in the crosslinking reaction. Hence, each light-activated molecule only induces one single propagation step. In sharp contrast to the above described methodologies, active components may still diffuse out of the exposed volume, yet they do not continue to polymerize in the non-exposed region. Soluble oligomers therefore remain either idle in the non-exposed volume of the resist or reenter the currently irradiated reaction volume where they are readily incorporated into the ongoing network formation. Naturally, reaching a high conversion – a necessity for stable structure generation of step growth networks – is increasingly difficult for non-sustaining reactions. Therefore only the most rapid and efficient reactions, *i.e.*, *click* reactions, are promising candidates as modular building blocks in DLW.

Apart from the aspect of covalent functionalization it is important to increase the overall chemical toolbox of DLW photoresists. One motivation is the high reactivity of free radicals in FRP and thiol coupling DLW. While boosting the efficiency as polymerization species, various side reactions with organic molecules limit the incorporation of additives, a common strategy for the optimization of optical or mechanical properties of both the fabricated structure and the photoresist. Side reactions may alter the fabrication process parameters and resulting structural properties in an unforeseen way or, in the worst case, lead to failure of the entire curing step. The same holds true for cationic polymerization of epoxides in DLW. High reactivity due to the ring strain of the oxirane makes the monomer sensitive to additives containing, for example, nucleophiles. Self-evidently, a high reactivity is mandatory for a successful DLW process that always comes at the price of potential side reactions. However, with an increased arsenal of applicable chemical reactions, components that are problematic for free radical, cationic, or thiol mediated systems are often unproblematic in Diels-Alder reactions and *vice versa*. Therefore, the overall flexibility of photoresists is significantly increased by extending the chemical toolbox for structure fabrication.

4.1.1 Photoresist Design and Direct Laser Writing Setup

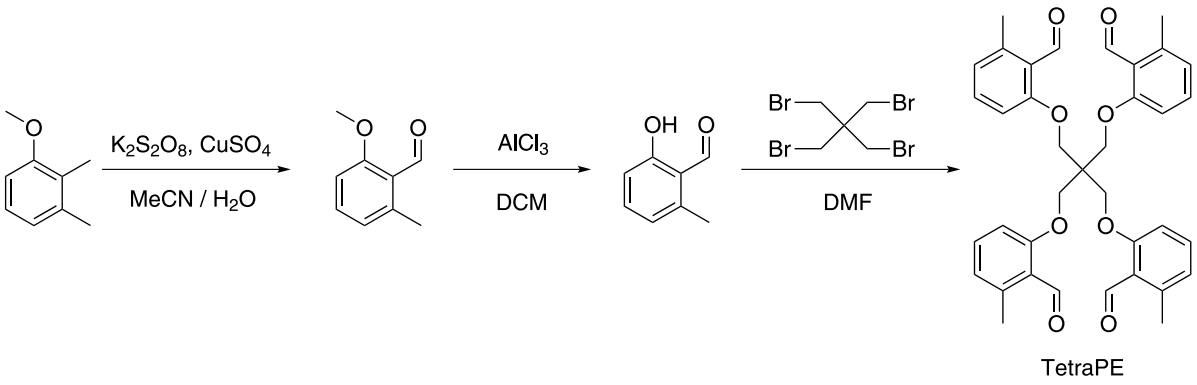

Figure 4.1: Synthetic pathway for the preparation of the tetrafunctional photoenol precursor molecule TetraPE. The synthesis pathway consists of an oxidation, followed by an ether cleavage and a subsequent nucleophilic substitution.

A mandatory prerequisite for a non-radical step growth polymerization methodology to function in DLW is – as mentioned above – a highly efficient, rapid, and stable covalent reaction between the monomer units. Certain Diels-Alder reactions fulfill these *click* criteria. In addition, either the reaction itself or the generation of a reactive species must be light triggered. As described in Section 2.5, according to the Woodward-Hoffmann rules, the Diels-Alder reaction – a [4+2] cycloaddition – is thermally induced. Thus, the generation of the reactive species must be light induced, a task that can be accomplished by photoenolization (see Section 2.5.3). Thereby, an *o*-quinodimethane – a potent diene for thermal Diels-Alder reactions – is formed that rapidly reacts with adequate dienophiles. For a working photoresist, a multifunctional photoenol precursor and a multifunctional dienophile must be provided. Unfortunately, neither component is readily available. Hence, the general resist policy of straightforward molecule availability was loosened and both components were synthesized in a respective multistep procedure. A tetrafunctional photoenol precursor molecule (TetraPE) was prepared in a three step procedure, consisting of a sequential oxidation, ether cleavage, and nucleophilic substitution (see Figure 4.1).

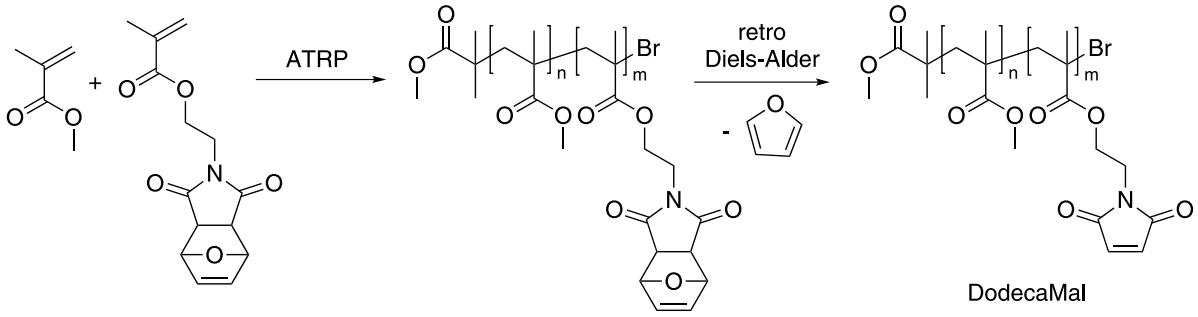

Figure 4.2: Synthetic pathway for the preparation of the dodecafunctional statistical copolymer (DodecaMal). The synthesis pathway consists of an ATRP copolymerization, followed by a retro Diels-Alder reaction for maleimide deprotection.

As a multifunctional dienophile counterpart, a statistical copolymer consisting of methyl methacrylate and a furan-protected maleimide methacrylate was generated *via* ATRP (see Figure 4.2). After a retro Diels-Alder deprotection, and hence provision of the maleimide species, the statistical copolymer (DodecaMal) featured a molecular weight of 10500 g mol^{-1} (calculated by usage of PMMA Mark-Houwink parameters), a dispersity of 1.2, and approximately 12 maleimide groups per polymer chain (derived from NMR analysis). A linear polymer component was chosen for photoenol mediated DLW as it readily allows for a large number of functional groups per macromolecule and lowers the necessary overall number of reactions during exposure for solid material generation. Together, the two components are dissolved in a solvent mixture in order to obtain the photoresist. A crucial process during photoenolization is the intramolecular hydrogen transfer (see Section 2.5.3). Therefore, the solvent mixture consists of only aprotic solvents. Moreover, selected solvents should feature low volatility to avoid photoresist performance alteration during sample exposure. The final photoresist exhibits a 1:1 ratio of photoenol and maleimide functional groups and consists of close to 10%wt

monomer components and 90%wt solvent (a mixture of γ-butyrolactone and acetophenone). A higher active molecule content was not achieved even though a vast selection of solvents and their corresponding mixtures was tested (not shown). With the obtained photoresist, DLW experiments were performed with a duration of up to six hours (see Section 4.1.2). Only minor evaporation-related shifts in the threshold power were observed.

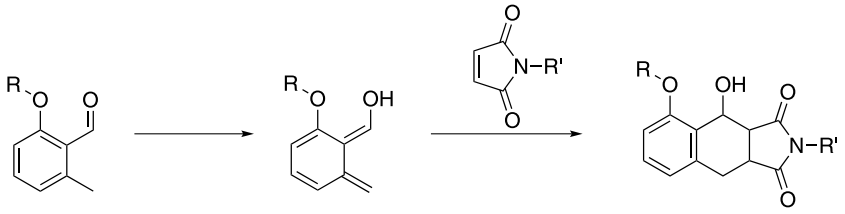

Figure 4.3: Depiction of the photoenolization process with subsequent Diels-Alder trapping. While the aromatic system is lost during the formation of the *o*-quinodimethane, it is restored by the trapping procedure.

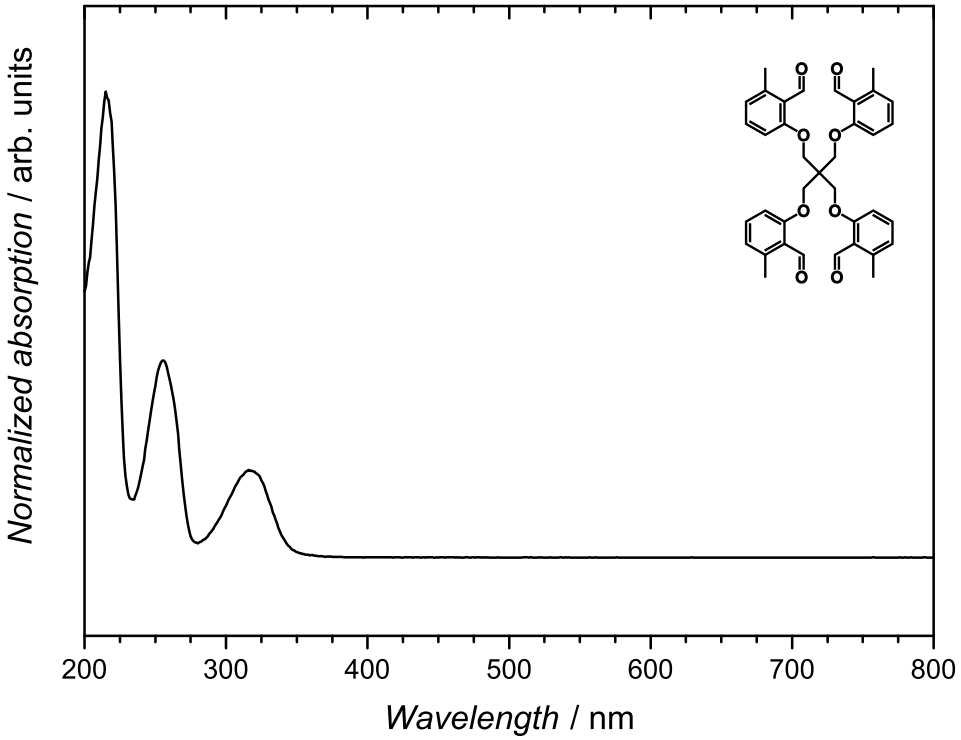

Figure 4.4: Recorded UV / VIS spectrum of TetraPE. Absorption of the molecule commences at approximately 350 nm.

During the formation of the *o*-quinodimethane, the aromatic system of the photoactive group is lost. After Diels-Alder trapping with a dienophile, the aromatic system is restored as depicted in Figure 4.3. The described rearomatization leads to two important features: Firstly, the

formation of an aromatic system further enhances the driving force of the reaction. Secondly, unintended retro Diels-Alder reaction is prevented from taking place during or after fabrication due to the additional energetic stabilization originating from the reformed aromatic system.

A UV / VIS spectrum of the photoactive TetraPE is depicted in Figure 4.4, showing absorption for a wavelength 350 nm and below. Commercial DLW setups that were utilized for radical thiol-ene and thiol-yne mediated curing (see Section 3.1 and 3.2) employ a laser with 780 nm center wavelength for targeted two-photon excitation and are thus not suited for irradiation of TetraPE. Therefore, a home-built DLW setup[a] was utilized for structure fabrication including a tunable Ti:sapphire laser oscillator.[200] The pulse picker described in the reference has been removed, resulting in a DLW system featuring femtosecond pulses, a tuned center wavelength of 700 nm, and a repetition rate of 80 MHz. The selected wavelength ensures efficient multiphoton absorption by TetraPE, a prerequisite for 3D structure formation that is described in the following section.

4.1.2 Microstructure Fabrication and Analysis

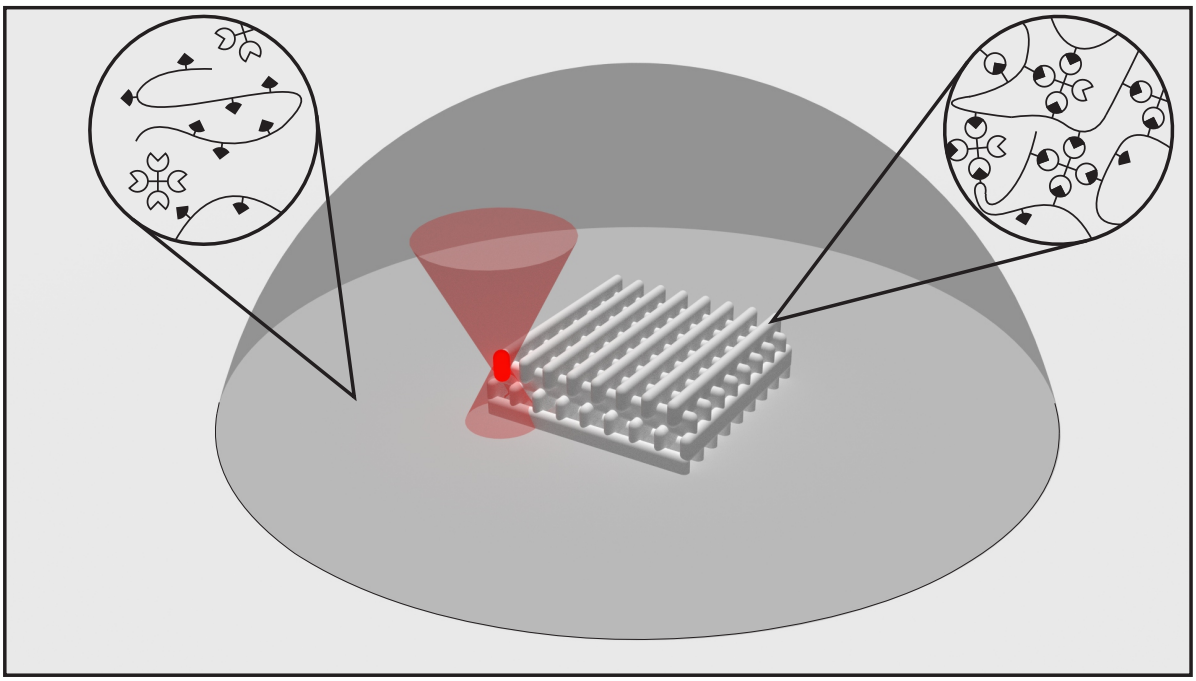

Figure 4.5: Schematic depiction of the photoenol mediated reaction for exposed and non-exposed regions during exposure in DLW as a lock-and-key model. The key component represents DodecaMal while the lock component illustrates TetraPE.

In order to determine the 3D resolution and facilitate comparison between different DLW systems, woodpile photonic crystals were fabricated as benchmark structures by photoenol mediated DLW. A schematic depiction of woodpile photonic crystal fabrication during the

[a]The home-built DLW setup was assembled by Dr. Joachim Fischer.

lithographic step is displayed in Figure 4.5. SEM images[b] of a woodpile photonic crystal featuring a footprint of $20\times20\ \mu m^2$, a total number of 20 layers (5 periods), a writing speed of $100\ \mu m\ s^{-1}$, a laser power of 4.3 mW, a nominal rod spacing of 700 nm, and a nominal layer spacing of 250 nm are displayed in Figure 4.6 before and after FIB milling. From the displayed analysis, a good uniformity of both the top peripheral region and the interior of the structure is revealed, clearly demonstrating the possibility to obtain highly resolved structures *via* the photoenol photoresist.

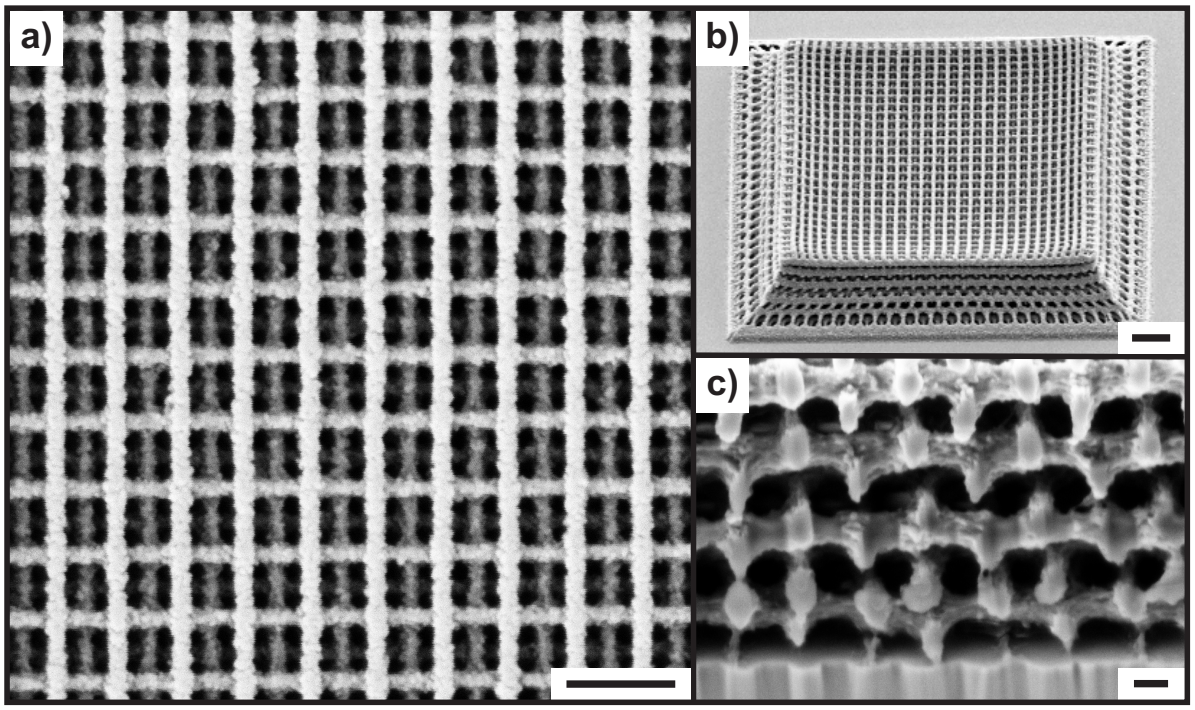

Figure 4.6: SEM images of a woodpile photonic crystal fabricated by photoenol mediated DLW with a lateral rod spacing of 700 nm. A close-up top view is displayed in a) while b) depicts the entire object. In c) the interior of the woodpile is revealed after FIB milling. Scale bars are 1 μm, 2 μm, and 200 nm for a), b), and c), respectively.

As previously mentioned (see Section 3.2), woodpile photonic crystals exhibit photonic stop bands.[63,201] The spectral location of the stop bands is dependent on structure parameters such as the rod and layer spacing. In order to investigate achievable resolution, parameter studies were conducted for woodpile structures with a footprint of $20\times20\ \mu m^2$, a total number of 20 layers (5 periods), and a writing speed of $100\ \mu m\ s^{-1}$. In these studies, the laser power and the rod (and corresponding layer) spacing were varied from 2.7 to 3.6 mW and 700 to 500 nm, respectively. Such an array enabled the determination of optimum fabrication conditions for structures with a certain rod spacing. For high quality woodpiles with a rod spacing of well below 1 μm, the corresponding stop band is located in the visible light region. Thus, stop bands

[b] SEM analysis in this chapter was performed by Johannes Kaschke.

of intact photonic crystals can be readily identified by transmission and reflection spectroscopy. The associated spectra of selected woodpile photonic crystals with a rod spacing of 700, 650, and 600 nm are displayed in Figure 4.7. For each rod spacing, a stop band in the visible region of light is identified. The photonic stop bands are – as expected – clearly shifted to a lower wavelength for decreased rod spacing.

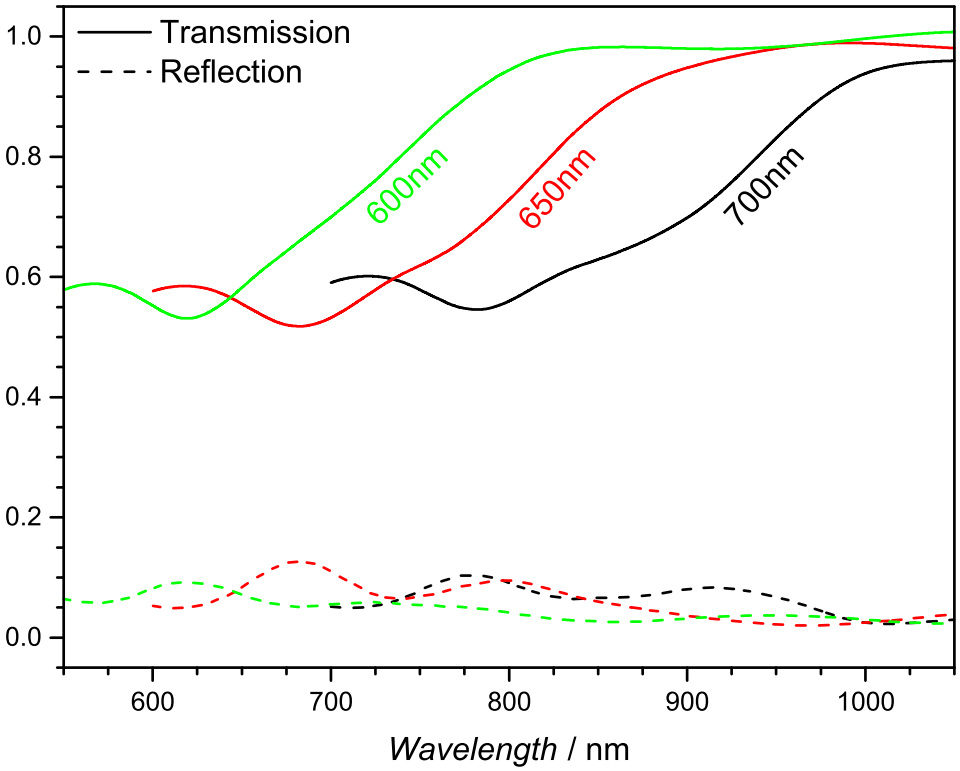

Figure 4.7: Transmission and reflection spectra of woodpile photonic crystals with a rod spacing varying from 700 nm to 600 nm. Both the photonic stop bands and the corresponding shift to a lower wavelength for a decreased rod spacing are clearly visible.

The visible light location of the stop band allows for further rapid and facile investigation of the structural quality by light microscope imaging. Figure 4.8 depicts a segment of the above mentioned parameter study, where woodpile structures with a rod spacing between 600 nm and 500 nm are displayed. The laser power for excitation increases from right to left. It becomes apparent that for a rod spacing of 600 nm and 550 nm a range of different excitation power yields intact photonic crystals of good quality while the power range for intact 500 nm woodpiles as well as the quality of the object is decreased considerably. Hence, the limit of achievable 3D resolution for the photoenol resist employed in this section was identified to be 500 nm rod spacing and approximately 175 nm layer spacing for woodpile structures.

A comparison with different resist systems for DLW such as cationic polymerization of SU8, FRP of multifunctional acrylates or radical thiol coupling presented in Section 3.1 and 3.2 reveals different behavior in several aspects. The effect of shrinkage during development of a sample usually becomes less pronounced for scaffolds that are produced far from the

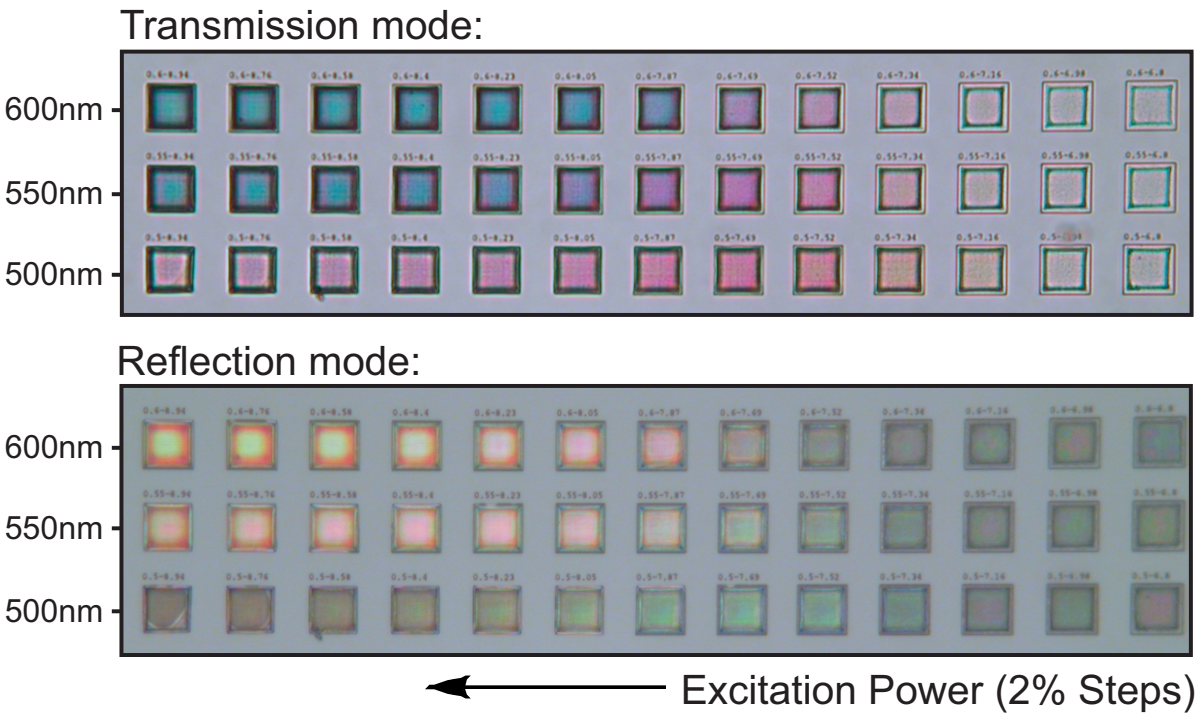

Figure 4.8: Light microscope images in transmission and reflection mode of woodpile photonic crystals written at varying laser power with the a rod spacing of 600 nm, 550 nm, and 500 nm.

resolution limit or the threshold power, *e.g.*, for multifunctional acrylate FRP. For the woodpile with 700 nm rod spacing presented in Figure 4.6, shrinkage is, however, still clearly visible. A possible explanation for the described behavior is the difference in crosslinking density that can be achieved in both systems. The employed DodecaMal is a statistical copolymer with a molecular weight of about 10000 Da and a total of 12 maleimide functional groups, entailing a maximum of 12 crosslinks per polymer chain. For comparison, an imaginary linear chain of the tetraacrylate PETTA with a molecular weight of 10000 Da would express close to 85 pending acrylate groups, allowing for a much higher crosslinking density. High crosslinking densities increase the stability of the network and thus impede distortion of the material after curing. Photoenol mediated structures also exhibit a certain surface roughness which may stem from the relatively low overall monomer content of the resist (roughly 10%wt for the photoenol resist compared to bulk FRP of multifunctional acrylates). Both shrinkage and surface roughness are adverse for the production of photonic crystals as they lead to disturbance of the required periodicity. Nevertheless, woodpiles with photonic stop bands for a rod spacing of down to 500 nm have been generated *via* photoenol mediated DLW. While conventional radical acrylate polymerization provides an even better resolution of down to 400 nm (see Section 2.2), the here achieved parameters are well below any woodpile photonic crystal fabricated by cationic polymerization of SU8 (minimum rod spacing of 650 nm)[201] or radical thiol coupling (rod spacing in the low micrometer range).

Up to this point, the polymerization mechanism for photoenol mediated production of architectures has not been proven. Therefore, chemical analysis of generated objects will be discussed in the following section.

4.1.3 Chemical Structure Characterization

Besides the determination of the resolution limit for the photoenol photoresist it is important to verify that the light-induced Diels-Alder reaction is actually responsible for the formation of insoluble network material during exposure. In theory, every component of the resist can undergo undesired side reactions. In order to exclude that the solubility change during DLW stems from reactions of a single active component with itself and / or the solvent mixture, several blind test were performed (see Table 4.1). The blind tests consisted of – next to the pristine photoresist – different test resists which were composed of up to one active compound (TetraPE or DodecaMal) and the solvent mixture. Each resist was cured in the DLW setup under identical conditions for simple line fabrication (not shown). As conditions, a writing speed of 100 $\mu m\,s^{-1}$ was chosen and the laser power was varied between 0 and 10 mW. For each test resist, no visible curing was observed, even at significantly larger average laser powers than the threshold value of the pristine photoresist (approximately 3 mW) which contained both active components. The blind tests revealed that the reaction which is responsible for the solubility change in the photoresist requires both TetraPE and DodecaMal. However, such a simple analysis provides no information about the nature of the crosslinking reaction.

	Original Photoresist	**Test Resist 1**	**Test Resist 2**	**Test Resist 3**
Solvent Mixture	+	+	+	+
TetraPE	+	+	-	-
DodecaMal	+	-	+	-
Curing	+	-	-	-

Table 4.1: Blind tests for the exclusion of single-component based side reactions. Curing is only possible if all components are present in the resist with a threshold of 3 mW (original photoresist).

In order to evidence the occurrence of the Diels-Alder reaction during exposure, FTIR spectra of TetraPE, DodecaMal, a stoichiometric mixture of TetraPE and DodecaMal (concerning functional groups), and a fabricated solid cuboid microstructure (footprint = $50\times50\ \mu m^2$, height = 10 µm) were recorded and compared (see Figure 4.9). TetraPE contains an aldehyde group with an absorption band clearly visible at 1680 cm^{-1} corresponding to the stretching vibration of the carbonyl group. Another specific absorption band of the aldehyde can be identified at 2780 cm^{-1}, originating from the Fermi-resonance of the C-H stretching vibration and the first overtone of the deformation vibration H-C=O. The second signal arising from the Fermi-resonance is located at approximately 2890 cm^{-1} and is not further considered as the weak signal overlaps with other absorption bands. DodecaMal contains two ester groups and an unsaturated imide within the polymer repeating units. The strong signal at 1700 cm^{-1} originates

from the stretching vibration of both ester groups and also contains one unsaturated imide absorption peak of the comonomer. The visible shoulder situated at 1730 cm^{-1} is assigned to a second imide signal of the comonomer as absorption bands corresponding to imides typically consist of two peaks.

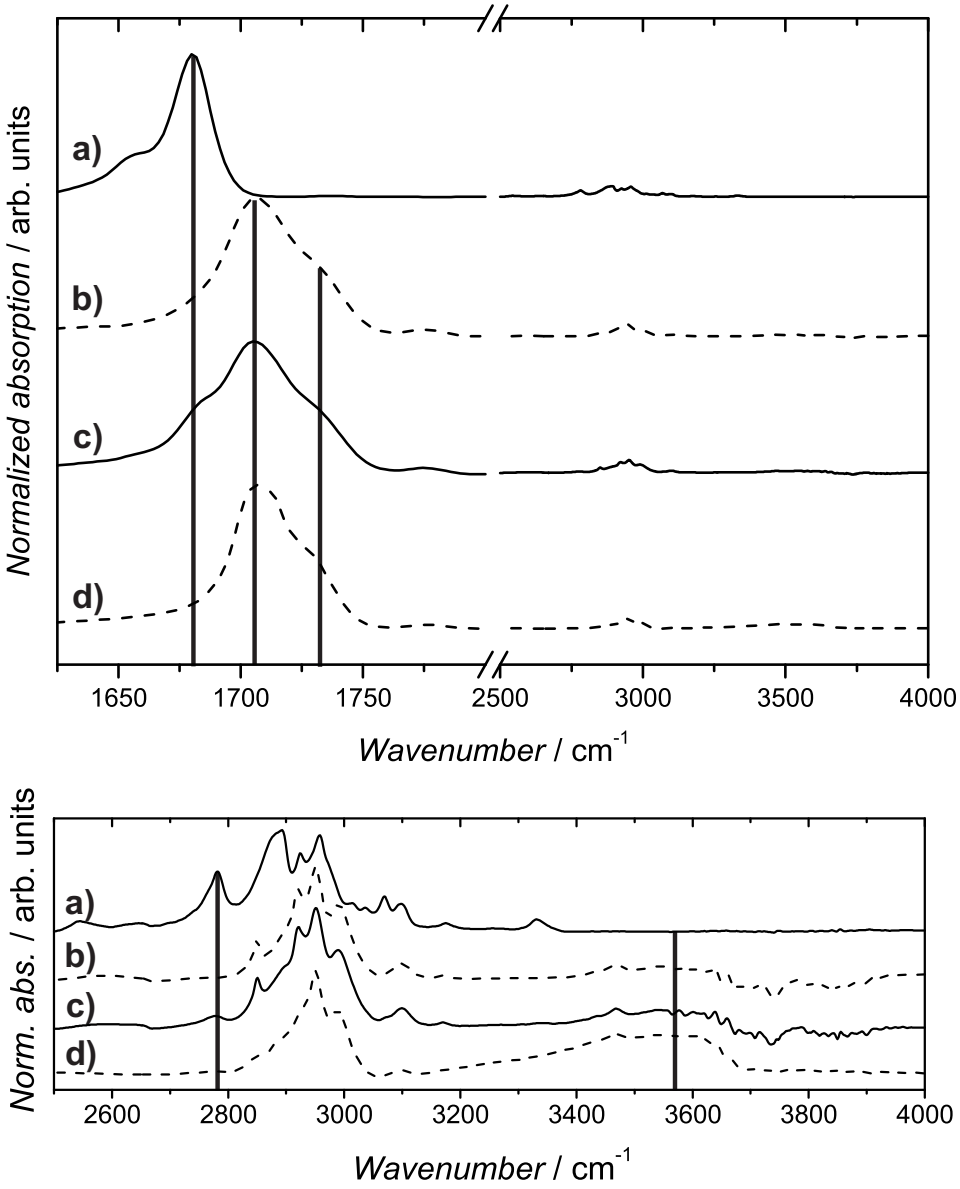

Figure 4.9: Top: FTIR spectra of a) TetraPE, b) DodecaMal, c) a stoichiometric mixture of TetraPE and DodecaMal, and d) a cuboid DLW microstructure. Bottom: enlarged depiction of the spectra in the range of 2500 to 4000 cm^{-1}. The spectra clearly display the disappearance of aldehyde- and occurrence of hydroxy signals during DLW exposure, evidencing the photo-induced Diels-Alder reaction. For better readability, the spectra are shifted vertically.

FTIR analysis of the stoichiometric mixture of both TetraPE and DodecaMal reveals that all assigned signals of the different carbonyl groups remain clearly visible in the spectrum. During the photoenolization process, the reactive *o*-quinodimethane is formed (see Section 2.5) which subsequently undergoes a Diels-Alder reaction with a provided maleimide. In the mentioned reaction, aldehyde groups are consumed and hydroxy groups are generated (see Figure 4.3). The postulated mechanism can be evidenced by the FTIR measurement of the microstructure. Absorption peaks corresponding to aldehyde group at 1680 cm^{-1} and 2780 cm^{-1} that are clearly visible in the stoichiometric mixture of TetraPE and DodecaMal are not present in the spectrum of the microstructure. All absorption peaks assigned to remaining carbonyl groups of the active compounds remain visible in the spectrum. The finding is expected, as, apart from the change in saturation of the imide which has no large influence on the energetic position of the absorption band, no other carbonyl group is altered during exposure. Furthermore, a broad signal in the range between 3200 and 3700 cm^{-1} appears in the microstructure spectrum that can be assigned to the formed hydroxyl group. The here discussed results unequivocally evidence that the photo-induced Diels-Alder reaction is responsible for the solubility change in the exposed volume of the photoresist, thereby also verifying that photoenolization can be efficiently triggered *via* multiphoton absorption.

As in Chapter 3, it can be assumed that conversion during exposure never reaches 100%. Thus, residual photoenol precursor moieties are present throughout the microstructure, enabling exploitation for covalent post-modification which will be described in the following section.

4.1.4 Spatially Resolved Covalent Post-Modification

After verifying the nature of the crosslinking reaction in the preceding section, the ability of covalent surface functionalization was investigated. As already mentioned, it can be assumed that pending functional groups are present on the 3D microstructures. In the case of the photoenol mediated objects in this section, such moieties include photoenol precursors. Contrary to a thiol-Michael addition or a CuAAC reaction (see Section 3.1 and 3.2), photo Diels-Alder post-modification requires a light trigger. Fulfilling the said prerequisite, accessible pending photoenols were addressed for the direct polymer surface modification of a developed sample. By immersing the structure in a solution of maleimide-containing functional molecules, the light-induced Diels-Alder reaction was performed. A benefit of the light activation is the facile confinement of the post-modification to certain regions. Under the assumption that the conditions for both the fabrication and the patterning are similar, the DLW fabrication setup was employed for post-fabrication patterning purposes. Schematically the general procedure is displayed in Figure 4.10. Such an approach allowed for the light-induced reaction to occur in a spatially resolved fashion of selected surface areas. Within the scanned areas, reactive *o*-quinodimethane moieties were generated from residual precursor molecules located on the structural surface that readily reacted with the provided maleimide in solution. A potential side reaction between the *o*-quinodimethane and pending maleimide located on the structure is impeded due to the low mobility of both species. In order to clearly verify successful surface attachment, a bromine containing maleimide was chosen for the reaction (see Figure 4.11). Consequently, in all regions where a successful surface reaction has occurred, bromine atoms

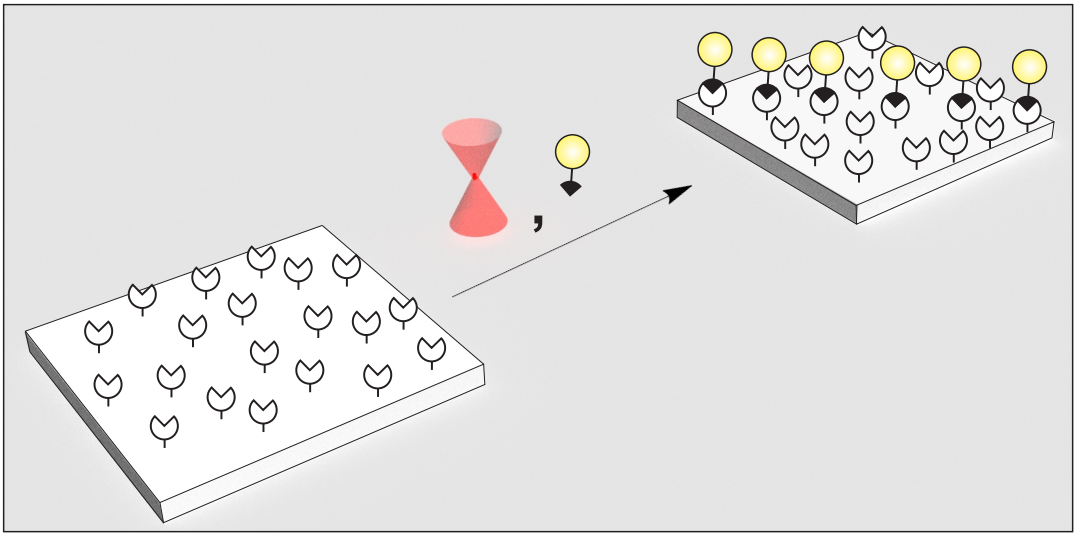

Figure 4.10: Schematic depiction of the post-modification procedure for light-induced Diels-Alder chemistry. Owing to the light activation of reactive molecules, the surface of the microstructures can be patterned in a spatially resolved manner employing the DLW setup.

are immobilized. As a structure, a solid polymer socket with a footprint of $90\times90\ \mu m^2$ and a height of close to 300 nm was produced. Onto the surface of such a structure, the Karlsruhe Institute of Technology logo with a total footprint of approximately $60\times40\ \mu m^2$ was patterned employing 5 mW average laser power and a writing speed of $100\ \mu m\ s^{-1}$.

ToF SIMS analysis[c] was performed with the surface modified sample (see Figure 4.12). Throughout the exposed area, the amount of bromine detected by signals corresponding to each isotope (79.16 u and 81.17 u) is drastically increased, providing strong evidence for the covalent attachment of the bromine containing maleimide to the targeted surface region. Close examination of the presented ToF SIMS images reveals that a small quantity of bromine is also present in the unexposed region of the socket. However, the occurring signal was not assigned to undesired covalent attachment or adhesion. It stems from the bromine end groups present in the DodecaMal compound (that was synthesized by ATRP), incorporated throughout the structure during the fabrication process. Being a proof-of-concept study, the bromine functionality was chosen in the course of the project due to the easy and distinct determination *via* ToF SIMS imaging. However, the spatially resolved surface patterning is not restricted to one compound. Essentially, any molecule that is inert to 700 nm light exposure and contains a reactive dienophile can be covalently bonded to exposed structural areas, making the introduced technique highly promising for future applications. Furthermore, it is emphasized that the presented technique allows for the fabrication and direct functional surface patterning of 3D microstructures utilizing a single lithographic setup and one single reaction. Apart from the possibility for covalent post-modification, photoenol mediated DLW features promising

[c]ToF SIMS analysis in this section was performed by Dr. Alexander Welle.

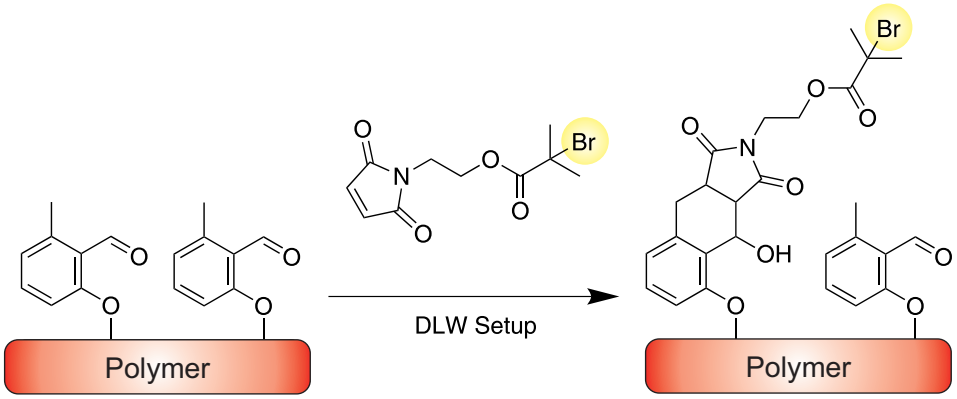

Figure 4.11: Light-induced Diels-Alder reaction between pending photoenol precursor molecules on the structural surface of micro-objects (red) and bromine containing maleimide molecules (yellow) in solution. Spatial resolution was obtained by employing the DLW setup.

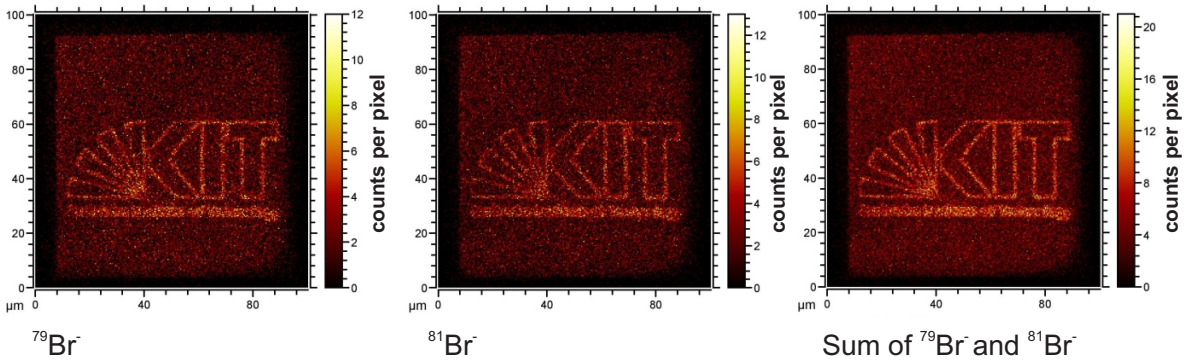

Figure 4.12: ToF SIMS images displaying each bromine isotope and the sum of isotopes (from left to right). The exposed area for post-modification is clearly visible as it contains an increased amount of covalently immobilized bromine.

characteristics for application in diffraction unlimited 3D lithography. First experiments and corresponding results will be described in the following section.

4.1.5 Photoenolization as a Diffraction Unlimited Approach in 3D Lithography

As described in Section 2.2, the conventional DLW process is fundamentally limited by diffraction. A possibility to circumvent the diffraction limitation is by employing the stimulated emission depletion (STED) concept derived from microscopy. In a designed DLW approach, a fluorescent initiator is employed for multiacrylate curing and the DLW setup is equipped with two lasers, each laser featuring a different wavelength (see Section 2.2.7). The “excitation” laser is chosen to populate the first excited singlet state of the initiator and thus eventually induce curing (as in conventional DLW) while the “depletion” laser is chosen to induce stim-

ulated emission. During stimulated emission, the excited singlet state is depopulated *via* the fluorescence channel to retrieve the ground singlet state. Ideally, in overlapping regions of both light sources, all excited singlet states are transferred to the ground state by stimulated emission. Therefore, while both laser beams are diffraction limited, the region of effective exposure dose is not, and can be designed to exhibit different shapes, depending on the overlap of both laser foci. As elucidated in Section 2.2, such a concept has been investigated and improved resolution has thereby been gained for a corresponding DLW system. However, due to several potential processes that may occur during the exposure,[202] the resolution is not as significantly increased as anticipated. Therefore, a pronounced interest persists for additional concepts that potentially allow for diffraction unlimited DLW.

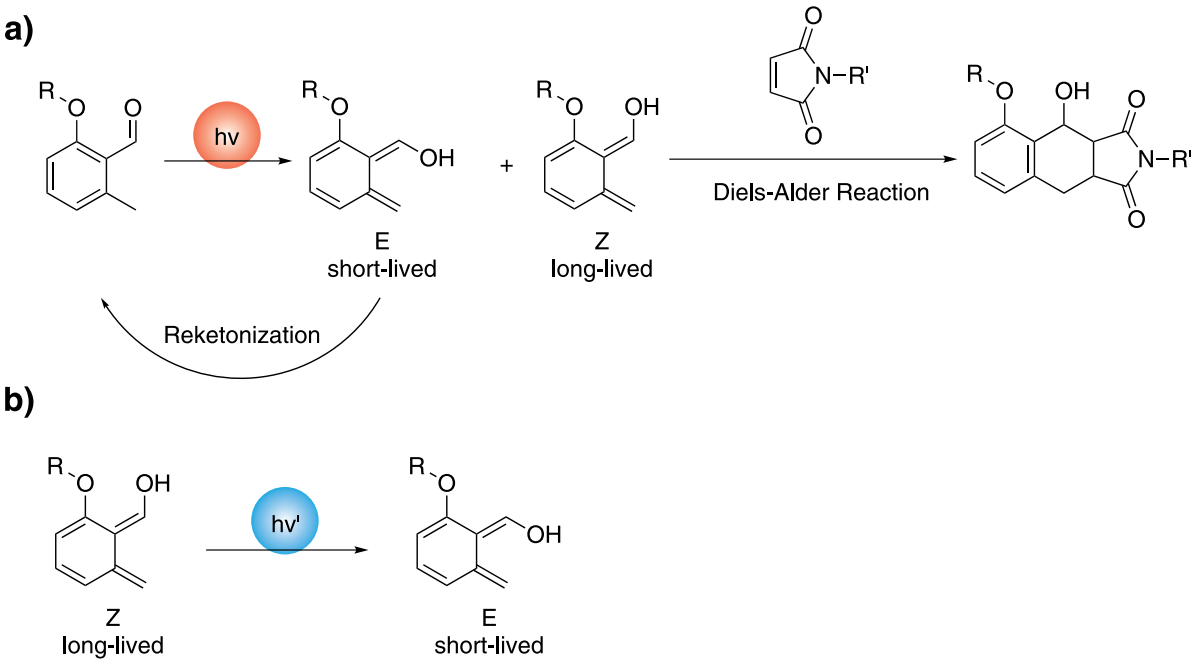

Figure 4.13: a) Photo-generation (700 nm, red) of both the short-lived and the long-lived isomer from the photoenol precursor molecule and the respective preferential reaction pathway. b) Photoisomerization (440 nm, blue), converting the long-lived isomer to the short-lived counterpart and hence impeding the Diels-Alder reaction.

All chemical species occurring during photoenolization (see Figure 2.27) have no pronounced luminescent behavior. Therefore, STED cannot be exploited for achieving diffraction unlimited resolution. On the other hand, the underlying general concept of reaction prohibition for diffraction unlimited resolution is not restricted to STED. In fact, any light-induced mechanism that prevents a curing reaction and ideally repatriates the targeted species to the incipient ground state is suitable. Admittedly, such systems are rare, wherefore the majority of past effort has been placed on the stimulated emission approach.

When having a close look at the photoenolization mechanism, it becomes apparent that two isomeric enol species (*o*-quinodimethanes) are formed. Typically, each respective isomer features a significantly different lifetime. While the choice of solvent determines the order of magnitude of the lifetime, it often has no effect upon the lifetime ratio of the isotopes. With no suitable reaction partner for the enol species (for example a dienophile), reketonization occurs *via* an 1,5 hydrogen reversion to the starting product. The mentioned fate does not change for the short-lived isomer when a suitable reaction partner is provided. Reketonization remains the dominant reaction path. For the long-lived isomer, the situation is fundamentally different. In the long-lived case, the provision of a potent reaction partner leads – at least to a certain degree – to a trapping reaction. In the case of photoenol mediated DLW, trapping was induced by the Diels-Alder reaction and ultimately led to curing of the photoresist. Following this line of thought, a plausible assumption is that, due to the rapid intramolecular reketonization, the concentration of the short-lived isomer is always zero. For a suitable "depletion" system, a

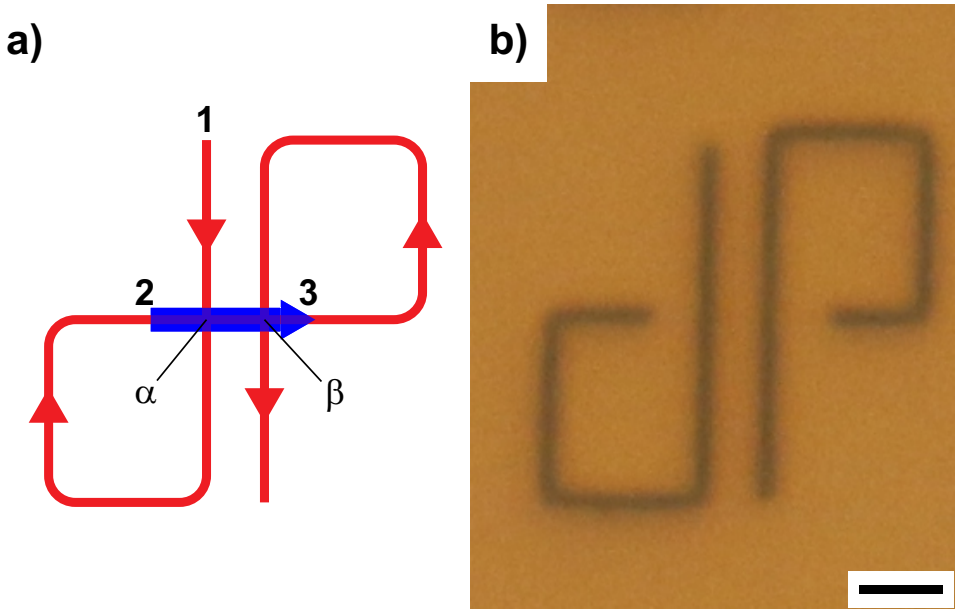

Figure 4.14: a) Model system of a proof-of-concept structure for photoenol depletion DLW. In red regions only the excitation laser is switched on while in blue regions both the excitation and the depletion laser are switched on. b) Light microscopy image of an experimentally obtained structure. In the region of the switched-on depletion laser, visible curing is suppressed. The scale bar is 2 µm.

light-induced reaction must be triggered that converts the long-lived isomer to its short-lived counterpart. Such a conversion can be induced by photoisomerization. The reaction pathway is illustrated in Figure 4.13 where – for this case – the Z isomer is long-lived and the E isomer is short-lived.[d] In the literature, photoisomerization has been conducted for isomers produced by

[d]Please note that the categorization into E and Z is derived from the Cahn-Ingold-Prelog priority rules. Therefore, there is no connection between the lifetime and the categorization into E or Z, a circumstance that can lead to confusion for non-chemists.

photoenolization. In one publication, the authors report a reaction from the long-lived to the short-lived isomer.[173] In a further report it is emphasized that photoisomerization can occur in both ways.[174] For both cases – under the assumption of rapid reketonization of the short-lived species – the concept should be applicable for lithography, as the long-lived isomer is converted and short-lived isomer is not present (and hence cannot be converted to the long-lived isomer).

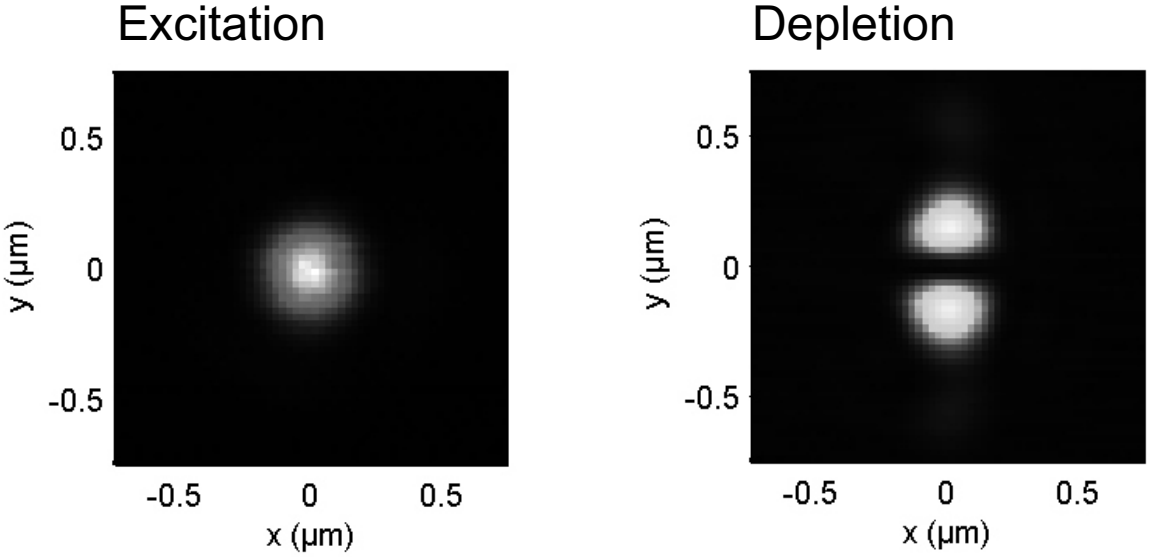

Figure 4.15: Focus shapes for photoenol depletion DLW experiments with increased lateral resolution in y-direction, stemming from the shape of the depletion focus.

In order to investigate the suitability of the photoenol system for curing suppression, a continuous-wave laser was added to the photoenol DLW setup with 440 nm center wavelength.[e] A beam alignment was performed in order to overlay the foci of both laser beams. In the described configuration, the 700 nm "excitation" laser induced photoenolization while the 440 nm "depletion" laser targeted the photoisomerization, *i.e.*, the conversion of long-lived isomer to short-lived isomer and hence prevention of the Diels-Alder reaction. A scheme of a model structure for the proof-of-concept of "photoenol depletion" as well as the result of a performed experiment employing the photoenol photoresist (see Section 4.1.1) are displayed in Figure 4.14. In the schematic depiction, the pathway of the overlying laser foci is shown. While the arrowheads indicate the direction of the movement, the color specifies which laser is switched on in which region. As a writing speed, 10 µm s^{-1} was chosen while the excitation and depletion laser power was set to be 3 mW and 2.5 mW, respectively. The experiment starts at the top right region (point **1**) with only the excitation laser (red) switched on. In this region, curing occurs due to Diels-Alder mediated reaction of the long-lived isomer, resulting in the formation of insoluble material. At point **2**, the depletion laser is additionally switched on. With an efficient photoisomerization taking place, the long-lived isomer ultimately reketonizes

[e] Additions to the experimental setup and experiments with simultaneous use of both lasers were carried out by Dr. Joachim Fischer.

to the starting product and thus does not participate in a Diels-Alder reaction. As a result, no curing takes place, even with the excitation laser switched on. At point **3**, the depletion laser is switched off again, curing now resumes. Two further regions are of particular importance. In the first region, indicated with α, the beam pathway (excitation and depletion) traverses an already cured region. Abnormalities in the pointed out region would indicate an undesired interaction of the cured structure with either the excitation or the depletion laser beam. In the second region, indicated with β, the beam pathway (excitation) traverses an already depleted region. Abnormalities in such a region would indicate incomplete reversion to the starting compound *via* the postulated depletion route. In the experimental result, regions where only the excitation laser was switched on feature a cured structure while regions where both the excitation and the depletion was turned on exhibit no visible curing. Moreover, no abnormalities are visible at both α and β position. These findings therefore strongly evidence the suitability of photoisomerization as an efficient depletion reaction in lithography.

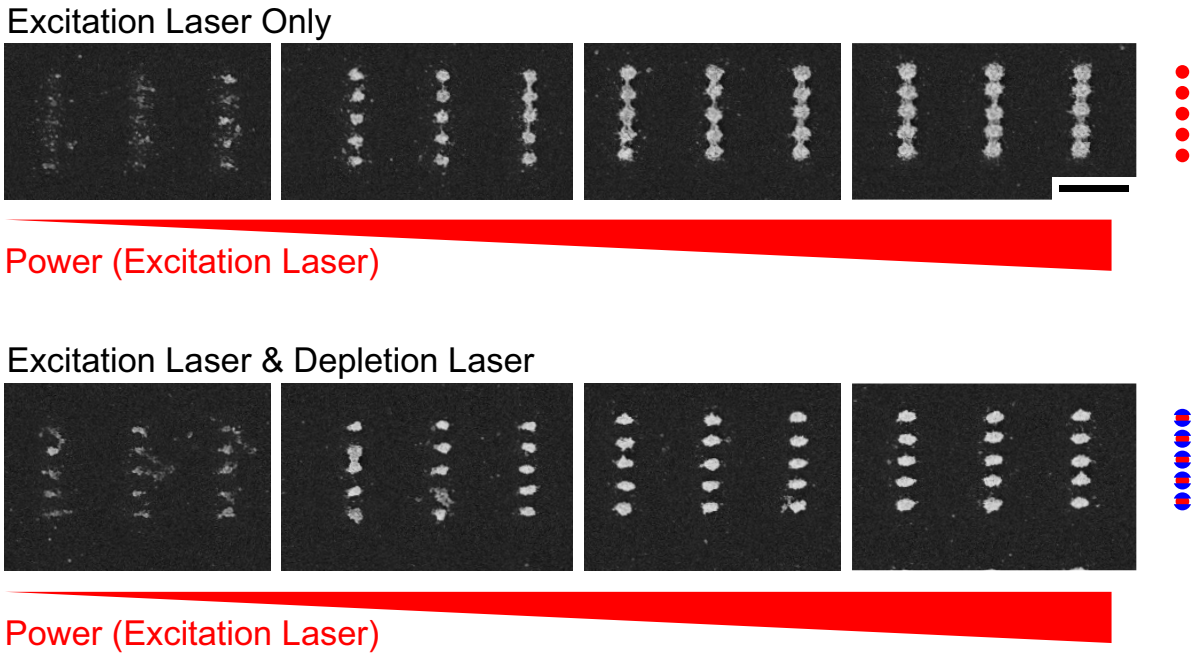

Figure 4.16: Comparison of point exposure experiments (300 nm point distance) without (top) and with (bottom) depletion laser exposure. While only a small excitation power range produced resolved structures for sole excitation exposure, additional depletion exposure increased both the range and the quality of resolved patterns. On the right, the shape and overlay of the respective foci is outlined. The scale bar is 1 µm.

In an attempt to verify improved resolution of depletion assisted photoenol DLW, the focus shape of the 440 nm laser was altered as depicted in Figure 4.15. With such a modified focus shape overlying the excitation focus, depletion and concomitant resolution improvement was targeted for the y-direction. Therefore, a series of point exposures in y-direction were conducted with either only the excitation laser switched on, or both the excitation and the depletion laser

switched on. In a series of experiments, the excitation laser power was varied in the range of 1.6-2.4 mW while the depletion laser power was chosen to be 7.5 mW. Furthermore, a fixed exposure time of 10 ms was applied. Sections of such experiments are displayed as SEM images for point distances of 300 nm (Figure 4.16) and 250 nm (Figure 4.17) in y-direction. For the 300 nm experiment with only the excitation laser switched on, a medium laser power led to the generation of separated point structures while for increasing laser power, the single exposed points blended into one structure, resulting in a non-resolved object. When additionally switching on the depletion laser, resulting point exposures are clearly resolved even at high excitation laser powers. For a point distance of 250 nm, no power region led to resolved structures for pure excitation laser exposure while additionally switching on the depletion laser lead to resolved point structures. A salient effect in the last SEM image is the existence of clearly resolved point structures next to seemingly connected points in one row. A close-up SEM investigation revealed that the "connected" points stem from the disc-like structure of the polymerized region due to the depletion focus shape. Such structures are not firmly anchored to the glass substrate and can therefore easily fall over during development, thereby mimicking a non-resolved object from top view.

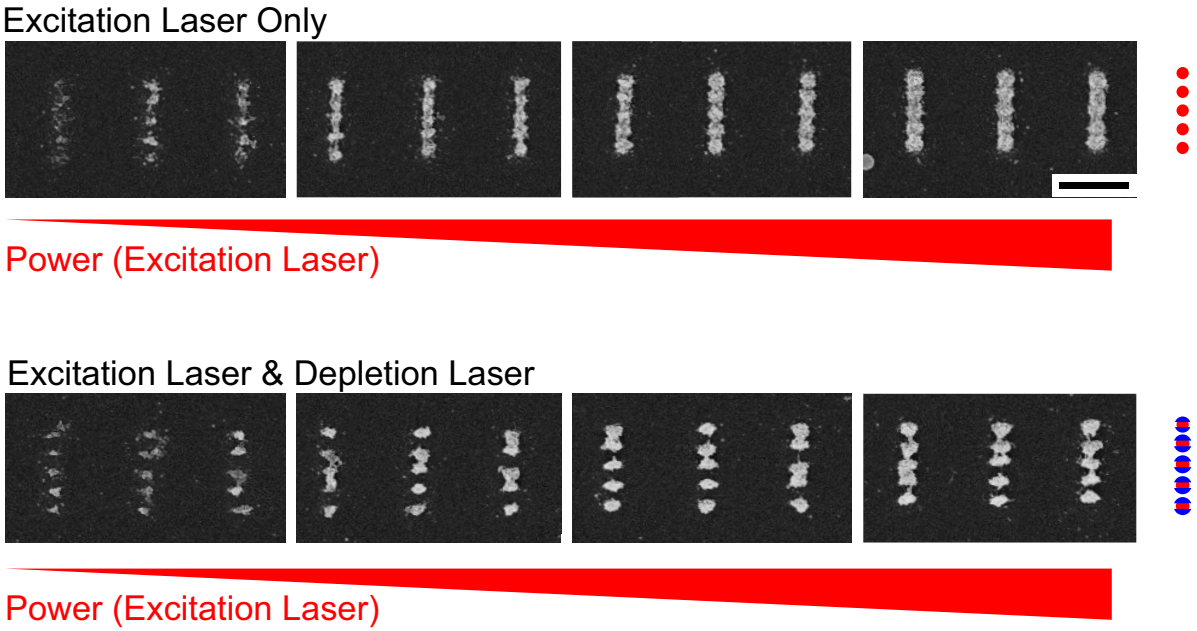

Figure 4.17: Comparison of point exposure experiments (250 nm point distance) without (top) and with (bottom) depletion laser exposure. While no excitation power produced resolved structures for sole excitation exposure, additional depletion exposure allowed for resolved structural patterning. On the right, the shape and overlay of the respective foci is outlined. The scale bar is 1 µm.

Unfortunately, the minimum diffraction limit (see Equation 2.8) for 700 nm has not been broken in the here presented experiment, even though the fundamental limitation can be overcome in the photoenol depletion approach. Possible explanations are the – to this date –

inferior quality of the produced photoenol mediated DLW material compared to other chemical systems such as acrylate DLW, thus impeding further resolution improvement. Nevertheless, the experiments impressively validate the improvement of lateral resolution by photoenol depletion, making the photoenol depletion concept highly promising for future investigations.

4.1.6 Summary

In summary, the photoenolization reaction has successfully been implemented into DLW lithography. By employing a tetrafunctional photoenol precursor molecule and a dodecafunctional maleimide polymer as monomers, woodpile photonic crystals with a rod spacing of down to 500 nm were produced and investigated by SEM, FIB milling, visible light spectroscopy, and light microscopy. Moreover, the chemical pathway for crosslinking during exposure was traced by FTIR spectroscopy and evidenced to be the postulated photoenol reaction. Pending photoenol precursor functional groups were addressed for light-induced covalent surface post-modification. By utilizing the DLW setup as exposure source, post-functionalization was carried out in a spatially resolved manner. The success of the patterned surface alteration was evidenced by ToF SIMS imaging. In addition, photoenol mediated DLW proved to be a suitable system for – in principle – diffraction unlimited DLW by exploiting the photoisomerization reaction. Both a proof-of-concept and an increased lateral resolution down to 250 nm were evidenced for photoenol depletion, revealing the described concept as highly promising for future investigations.

5

Concluding Remarks and Outlook

Within this thesis, three chemical systems, namely the radical thiol-ene, the radical thiol-yne and the photoenol system were implemented into direct laser writing 3D lithography. During resist preparation, the policy of readily available resist components and DLW systems was pursued. For both radical thiol coupling systems, the policy was maintained as the DLW setup is commercially available and all resist components are either commercially available or solely require a facile one step synthetic procedure. In the case of the photoenol system, the policy was not entirely maintained. Both monomeric components require a more complicated synthesis path and the DLW setup required a modified center wavelength of the laser.

For each system, the fabrication of complex 3D microstructures was successful. As benchmark structures, woodpile photonic crystals were produced and the achievable rod spacing was compared for the determination of obtainable 3D resolution. A resolution in the low micrometer range was obtained for both radical thiol-ene and radical thiol-yne mediated DLW whereas a rod spacing of down to 500 nm was achieved for the photoenol system. A standard writing speed of 100 $\mu m\ s^{-1}$ was employed for the radical thiol-ene and the photoenol system. For the radical thiol-yne photoresist a tuned RI value of 1.52 allowed for DLW without height restriction *via* Dip-in configuration. Combined with a writing speed of up to 1 $cm\ s^{-1}$, mesostructures with a height of up to 1 mm and retained micrometer resolution were obtained.

Apart from the structural performance, the postulated chemical pathway was investigated and verified for every chemical system. Moreover, the analysis revealed the existence of residual potent functional groups throughout the structure of each corresponding system, *i.e.*, thiols for radical thiol-ene mediated structures, thiols and alkynes for radical thiol-yne mediated objects, and photoenol precursor molecules for photoenol mediated architectures. Pending thiols of thiol-ene mediated scaffolds were addressed in a thiol-Michael addition reaction with different Michael acceptor molecules. Thereby, the covalent immobilization was evidenced on the structural surface and a corresponding grafting density of approximately 200 molecules μm^{-2} was calculated. In the case of radical thiol-yne mediated objects, residual thiols and alkynes were sequentially addressed in a thiol-Michael addition and a CuAAC reaction. Successful orthogonal, dual functionalization on a single structure was confirmed, further validating the attachment in bulk and on the surface of the target. For photoenol mediated structures, residual precursor molecules were activated *via* the DLW setup. In this manner, a spatially resolved surface patterning was achieved by triggering a light-induced Diels-Alder reaction.

Next to the possibility of covalent post-modification, photoenol mediated DLW features a non-destructive, light-triggered pathway for *in situ* deactivation of reactive species *via* photoisomerization. After having evidenced the suitability for curing suppression during structure formation by usage of a second laser, the technique was utilized for improvement of the obtainable lateral resolution in photoenol mediated DLW with the perspective of diffraction unlimited resolution.

In the general scope of DLW, the important issues of wide range applicability as well as high resolution have been successfully addressed and extended in the current thesis. All described systems are now well-investigated and therefore ready for application in materials science. The possibility for covalent post-modification enables access to a large range of applications. In this context, implementation of functional 3D microstructures into lab-on-a-chip systems and microfluidics appears highly potent, *e.g.*, for application as sensing devices or microreactors. In biological systems, the immobilization methodology can be exploited for targeted protein immobilization and in the frame of cell behavior studies. Considering the photenol DLW process in particular, continued investigation of the photoisomerization aspect is definitely of great importance. This route circumvents the diffraction limit, resulting in the theoretical accessibility of 3D architectures with below 10 nm resolution. The next scientific step is the improvement of the structural quality for photoenol DLW produced structures, which is the limiting factor of the concept at this point in time.

Finally, the ultimate destination for DLW or – to be more general – all production tools for 3D micro- and nanolithography can be categorized into two main targets. Accessibility of demanding structural parameters originates from a scientific point-of-view, paving the way for pioneering research. With certainty, molecular resolution for both 2D patterns and 3D objects would be a dream come true for physicists and material scientists alike. When regarding precise chemical functionality, biologists and chemists could mimic cascade reactions derived from nature in the smallest dimension, thereby bringing chemistry-driven microdevices to the next level. Another, more general perspective is the implementation of *state of the art* DLW technology for industrial purposes, maintaining the acquired precise control for mass production. In this fashion, both marvels of nature and artificial discoveries on the micro- and nanometer scale are within reach and can be exploited for astonishing, future-oriented everyday life devices.

6 Experimental Section

6.1 Thiol-Ene Mediated Direct Laser Writing

6.1.1 Materials

Acetone (99.5%, Roth), 2-propanol (99.5%, Roth), N,N-dimethyl||formamide (99.5%, Acros), N,N-dimethylacetamide (≥99.9%, Sigma Aldrich), ethyl acetate (≥99.5%, VWR), hexane (≥95%, VWR), toluene (≥99.5%, VWR), pentaerythritol tetrakis(mercaptoacetate) (90%, ABCR), sodium hydroxide (≥99.5%, Roth), pentaerythritol tetraacrylate (contains 350 ppm MEHQ as inhibitor, Sigma Aldrich), 7-diethylamino-3-thenoylcoumarine (Exciton), bis(2,4,6-trimethylbenzoyl)-phenylphosphineoxid (Ciba), sodium sulphate (≥99%, Roth), tetrabutylammonium bromide (≥99%, Acros), allyl chloride (98%, Acros), pentaerythritol (>97%, Fluka), triethylamine (99%, Acros) and 3-(trimethoxysilyl)propyl methacrylate (98%, Sigma Aldrich) were used as received without further treatment.

6.1.2 Synthesis

Pentaerythritol tetraallyl ether (PETE)

The synthesis was performed according to a modified literature procedure.[203] Caution, allyl chloride is toxic! To a 500 mL three-necked flask equipped with a dropping funnel and a reflux condenser, pentaerythritol (13.6 g, 0.1 mol, 1 eq), water (80 mL), NaOH (80.0 g, 2.0 mol, 20 eq), tetrabutylammonium bromide (400 mg, 1.2×10^{-3} mol, 0.012 eq) was added. To the heated reaction mixture (50°C), allyl chloride (162.8 g, 2.0 mol, 20 eq) was added in a dropwise fashion. The reaction mixture was left to stir for 24 hours at 50°C. During this time the organic phase turned yellow. The precipitate was filtered off and the phases were separated. The aqueous phase was extracted with 200 mL of toluene (3×). The solvent was removed from the combined organic phases under reduced pressure. The crude product was purified by column chromatography (hexane : ethyl acetate, 9 : 1) to yield a colorless oil (17.6 g, 60%). ^{1}H NMR ($CDCl_3$) δ / ppm = 3.45 (s, 8H), 3.95 (s, 8H), 5.12 (d, 4H), 5.24 (d, 4H), 5.87 (m, 4H) (see Figure 6.1).

Fluorescein Maleimide

N-(5-fluoresceinyl)maleimide was prepared according to a literature procedure.[204]

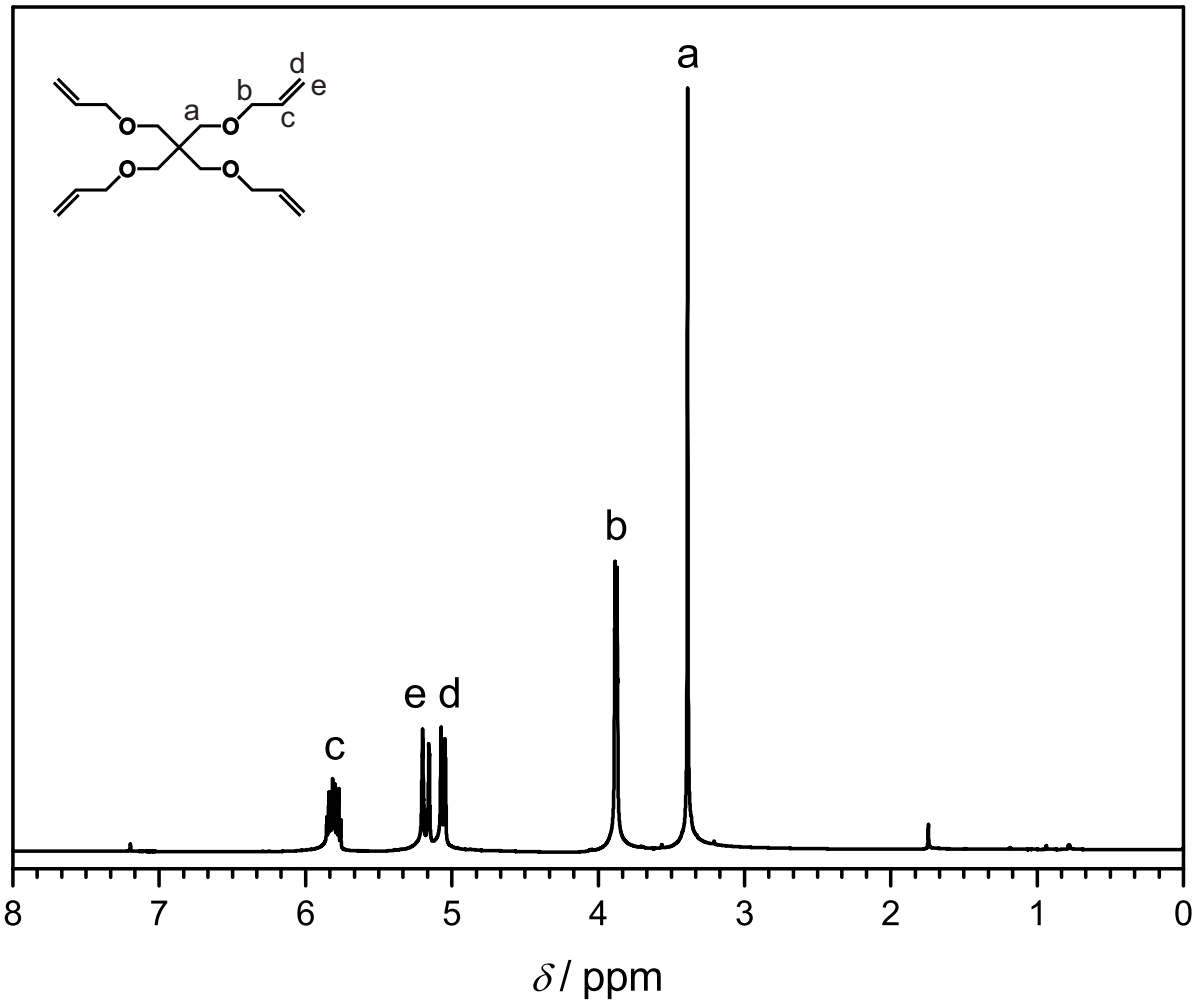

Figure 6.1: ^{1}H NMR of PETE in chloroform with assigned hydrogen signals. A signal originating from the chloroform solvent is visible.

Bromine Maleimide

2-Bromo-2-methyl propionic acid 2-(3,5-dioxo-10-oxa-4-azatricyclo[5.2.1.02,6]dec-8-en-4-yl) ethyl ester was prepared according to a literature procedure.[205]

6.1.3 Devices

Nuclear Magnetic Resonance

^{1}H NMR spectroscopy was performed using a Bruker AM 400 spectrometer at 400 MHz. The sample was dissolved in $CDCl_3$. The δ-scale is referenced to the internal standard tetramethylsilane (TMS, δ = 0.00 ppm).

Focused Ion Beam Milling

FIB milling was using a Zeiss Auriga equipped with a gallium ion source. The applied current was set to be 50 pA / 30 kV. All samples were coated with a 10 nm gold layer prior to measurements.

Scanning Electron Microscopy

SEM images were recorded using a Zeiss Supra 40VP. All samples were coated with a 10 nm gold layer prior to measurements.

X-ray Photoelectron Spectroscopy

XPS measurements were performed using a K-Alpha XPS spectrometer (ThermoFisher Scientific, East Grinstead, UK). Data acquisition and processing using the Thermo Avantage software is described elsewhere.[206] All samples were analyzed using a microfocused, monochromated Al Kα X-ray source (250 µm spot size). The K-Alpha charge compensation system was employed during analysis, using electrons of 8 eV energy, and low-energy argon ions to prevent any localized charge build-up. The spectra were fitted with one or more Voigt profiles (BE uncertainty: $\pm$0.2 eV) and Scofield sensitivity factors were applied for quantification.[207] All spectra were referenced to the C1s hydrocarbon (C-C) at 285.0 eV binding energy controlled by means of the well known photoelectron peaks of metallic Cu, Ag, and Au, respectively.

Fourier Transform Infrared Spectroscopy

FTIR measurements were performed on a Fourier-transform microscope spectrometer (Bruker Tensor 27 with Bruker Hyperion 1000). Liquid samples had a thickness of 40 µm and the thickness of the measured structures was close to 22.5 µm. Atmospheric compensation and baseline correction was performed upon the obtained spectra. The spectra were normalized *via* the ester absorption band at 1741 cm^{-1}.

Laser Scanning Microscopy

LSM measurements were performed using a Zeiss LSM 510 Meta. Samples were irradiated at a center wavelength of 561 nm. Emitted light was detected at a wavelength range between 570 and 614 nm. An oil-immersion lens (Zeiss Plan-Apochromat 63x/1.40 Oil) was employed. The pinhole was set to be 2.03 airy units.

Direct Laser Writing

DLW was performed using the "photonic professional" setup (Nanoscribe GmBH, Karlsruhe, Germany). The laser is a mode-locked and frequency-doubled Er-doped fiber oscillator emitting femtosecond pulses at 780 nm center wavelength. An oil-immersion lens (Zeiss Plan-Apochromat 100x/1.40 Oil) focuses the laser beam into the volume of the photoresist. Silanized glass cover slips of 170 µm thickness are used as substrates. The sample is moved relative to the laser focus using a 3D piezo stage (P-563.3CD, Physik Instrumente GmbH, Karlsruhe).

6.1.4 Direct Laser Writing Experiments

Cleaning and Preparation of Glass Substrates

All glass substrates were cleaned by ultrasonification for 15 min in acetone. Preactivation of the surfaces was achieved by separately placing the samples in small glass vials containing acidic piranha solution (sulfuric acid 95% : aqueous hydrogen peroxide 35%, 3:1, v/v) for 60 min at 100°C. Caution: piranha solution is an extremely strong oxidant and should be handled very carefully!

Silanization of Glass Substrates

Preactivated substrates were placed separately in small glass vials containing a solution of 3-(trimethoxysilyl)propyl methacrylate dissolved in toluene (1×10^{-3} mol L^{-1}) for 60 min at ambient temperature without stirring. The substrates were successively ultrasonicated in toluene (10 mL, 10 min) and acetone (10 mL, 5 min) to remove any physisorbed silane. The silanization process is performed in order to covalently bind the fabricated structures to the substrate surface during fabrication. The adhesive strength is increased thereby.

Radical Thiol-Ene Photoresist Preparation

The thiol-ene resist employed for DLW experiments consists of pentaerythritol tetrakis-(mercaptoacetate) (250 mg, 5.8×10^{-4} mol), PETE (171 mg, 5.8×10^{-4} mol), 7-diethylamino-3-thenoylcoumarine (10 mg, 3.05×10^{-5} mol), hydroquinone (1 mg, 9.08×10^{-6} mol) and N,N-dimethylacetamide (240 µL). For quantitative fluorescence measurements, 7-diethylamino-3-thenoylcoumarine was replaced by bis(2,4,6-trimethyl-benzoyl)-phenylphosphineoxid (14.7 mg, 3.05×10^{-5} mol).

Tetraacrylate Photoresist Preparation

The acrylate resist employed for DLW experiments consists of pentaerythritol tetraacrylate (10 g, 0.028 mol) and 7-diethylamino-3-thenoylcoumarine (23.2 mg, 7.1×10^{-5} mol). For quantitative fluorescence measurements, 7-diethylamino-3-thenoylcoumarine was replaced by bis(2,4,6 trimethylbenzoyl)-phenylphosphineoxid (29.7 mg, 7.1×10^{-5} mol).

Direct Laser Writing Sample Preparation

Silanized glass cover slips are equipped with a polydimethylsiloxane (PDMS) ring with a height of around 3 mm containing the photoresist. The top of the PDMS ring is covered with a second glass cover slip. This procedure prevents any evaporation of solvent during DLW (see Figure 3.3).

Direct Laser Writing Experiments for Woodpile Structures

Conditions for DLW fabrication of Woodpiles is described in Section 3.1.

Direct Laser Writing Experiments for FTIR Spectroscopy

A solid cuboid polymer block was fabricated from the thiol-ene resist with a footprint of $100 \times 100\ \mu m^2$ and a height of close to 25 μm for analysis. The laser power and the writing speed were set to be 8 mW and $100\ \mu m\ s^{-1}$, respectively.

Direct Laser Writing Experiments for XPS Analysis

Solid polymer blocks with a footprint of $280 \times 560\ \mu m^2$ and a height of about 1.4 μm were fabricated for analysis. The laser power and the writing speed were set to be 8 mW and $100\ \mu m\ s^{-1}$, respectively.

Direct Laser Writing Experiments for Quantitative Fluorescence Measurements

Solid polymer layers with an area of $100 \times 100\ \mu m^2$ were fabricated by writing an array of lines with a rod distance of 300 nm. The laser power and the writing speed were set to be 12 mW and $100\ \mu m\ s^{-1}$, respectively.

Development of Fabricated Structures

After DLW, the glass cover slips containing polymer structures were immersed into acetone (30 mL) for 20 min without stirring. Subsequently, the samples were rinsed first with acetone (5 mL), then with isopropanol (5 mL) and water (5 mL). Residual solvent was removed under reduced pressure.

6.1.5 Covalent Post-Modification

Functionalization *via* the thiol-Michael Addition

The developed polymer structures were immersed into a solution of N-(5-fluoresceinyl)-maleimide (2.3×10^{-6} mol, 0.7 mg) or 2-bromo-2-methyl propionic acid 2-(3,5-dioxo-10-oxa-4-azatricyclo[5.2.1.02,6]dec-8-en-4-yl) ethyl ester (2.3×10^{-6} mol, 1.0 mg) in DMF (3 mL) for 24 hours without stirring. The functionalized structure was subsequently immersed in DMF (10 mL) for 20 min. Afterwards, the samples were successively rinsed with DMF (5 mL) and acetone (5 mL). Residual solvent was removed under reduced pressure. When using N-(5-fluoresceinyl)maleimide, all reaction steps were performed under light exclusion to minimize any potential bleaching of the fluorophor.

6.1.6 Grafting Density Calculation

Laser Scanning Microscopy Settings

All LSM measurements for the calculation of the grafting density were performed under identical scanning conditions (detector gain, scan velocity, laser intensity and amplifier offset). Liquid samples were prepared by placing droplets of the solution onto a glass substrate that was further equipped with a PDMS ring. Onto solid samples (structures) droplets of DMF were

placed before measurement, ensuring identical chemical environment for the surface attached fluorescein molecules compared to molecules in DMF solution and therefore also ensuring identical fluorescence behavior.

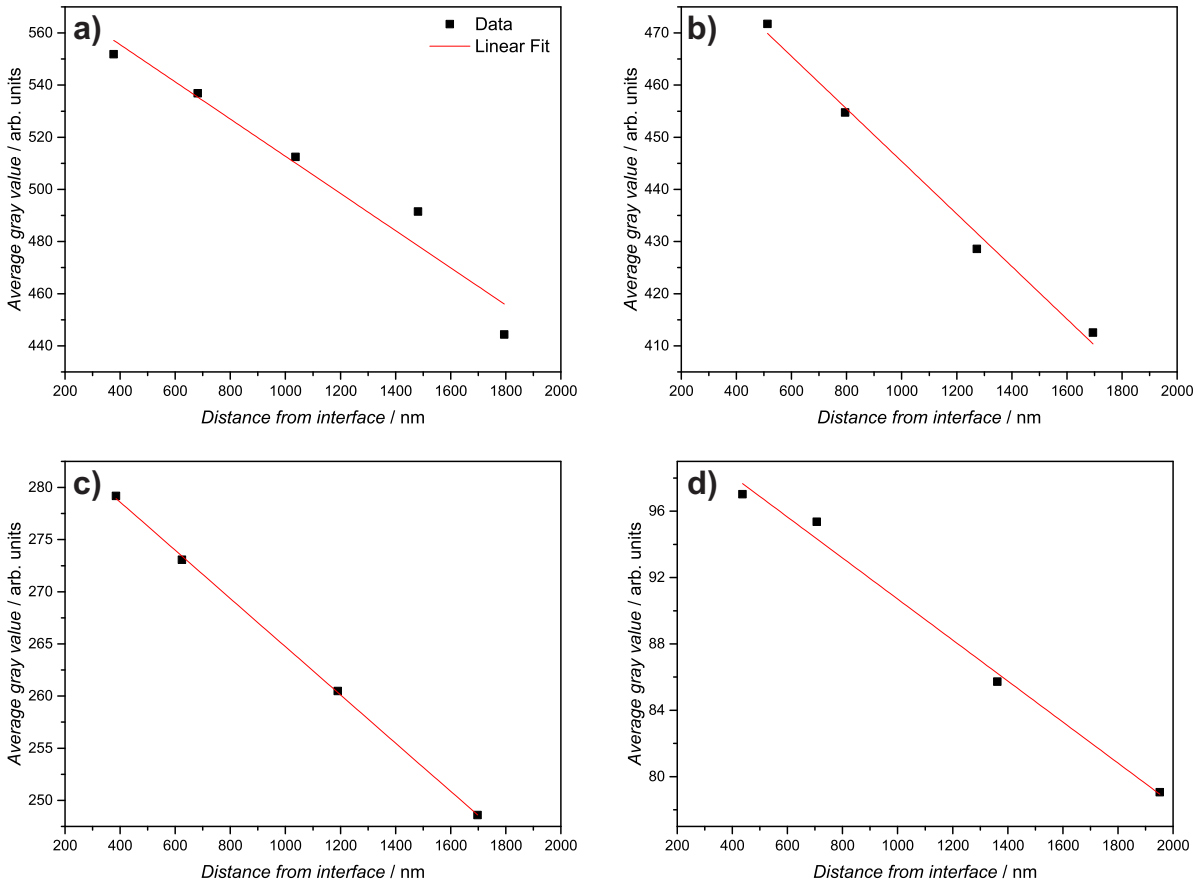

Figure 6.2: Determination of the interface gray value *via* linear approximation. a), b), c), and d) correspond to fluorescein maleimide stock solutions of 0.121, 0.109, 0.088, and 0.061 mol L^{-1} (compare to Table 3.3).

Derivation of the Calibration

Solutions of N-(5-fluoresceinyl)maleimide in DMF (for exact concentrations see Table 3.3) were measured in single slice experiments at different intervals from the glass-liquid interface. From the obtained data, the average gray value of a defined area was evaluated using the software ImageJ. By plotting the average gray value versus the distance from the interface, the linear approximation allows for calculation of the average gray value at the interface (see Figure 6.2). This value is used for further calculation. Multiplication of the average gray value with the defined area provides the integrated intensity. The point spread function was measured to be 716 nm at FWHM in z-direction. By employing the defined area and the point spread function, the volume of the exposed single slice was determined. In combination with the

concentration, the number of molecules in this volume can be calculated. A plot of the number of molecules versus the integrated intensity finally yields the calibration (Figure 3.13).

Determination of the Grafting Density

Maximal projection images of samples fabricated for quantitative fluorescence measurements were evaluated using the software ImageJ. Average gray values from a defined area (9385 μm^2) of functionalized structures were taken for calculation. Multiplication of the arithmetic average of gray values with the defined area provided the integrated intensity. Comparison of the calculated intensity to the calibration (see Figure 3.13) provided the amount of fluorescent molecules situated on the defined area. It was assumed that the fluorescent molecules are only situated on the surface of the structure. Furthermore, the surface of the structure was assumed to be flat, allowing for the calculation of the grafting density which is close to 200 molecules μm^{-2}.

6.2 Thiol-Yne Mediated Direct Laser Writing

6.2.1 Materials

Pentaerythritol tetrakis(3-mercaptopropionate) (>95%, Sigma Aldrich, Tetrathiol 2), propargyl acrylate (98%, Sigma Aldrich), hexylamine (99%, Sigma Aldrich), 7-diethylamino-3-thenoylcoumarine (DETC, Exciton), triethyl amine (99%, Acros Organics), acetone (99,5%, Roth), dimethylformamide (DMF, 99.5%, Acros Organics), dichloromethane (DCM, analytical grade, Fischer), copper(I) bromide (CuBr, 98%, Sigma Aldrich), copper(I) chloride (CuCl, 97%, Sigma Aldrich), PMDETA (99+%, Acros Organics), 3-(trimethoxysilyl)propyl methacrylate (98%, Sigma Aldrich) and methoxypolyethylene glycol azide (PEG-N_3, M_n = 2000 g mol^{-1}, Sigma Aldrich) were used as received without further purification.

6.2.2 Synthesis

Synthesis of Tetraalkyne

Tetrafunctional alkyne (Tetraalkyne) was synthesized employing a slightly modified literature procedure.[208] Pentaerythritol tetrakis(3-mercaptopropionate) (2.5 g, 5.12×10^{-3} mol, 1 eq, Tetrathiol 2) and 30 µL of hexylamine was added to a round bottom flask. Under stirring, propargyl acrylate (2.5 g, 22.7×10^{-3} mol, 1.1 eq) and was added over a period of 2 min. The mixture was stirred at ambient conditions for 1 hour. Subsequently, residual propargyl acrylate and hexylamine was removed under reduced pressure. ^{1}H NMR (400 MHz, $CDCl_3$, δ): 4.70 (d, J = 2 Hz, 8H, CH2), 4.16 (s, 8H, CH2), 2.80 (m, 16H, CH2), 2.65 (m, 16H, CH2), 2.49 (t, J = 2 Hz, 4H, CH) (see Figure 6.3).

Bromine Maleimide

2-Bromo-2-methyl propionic acid 2-(3,5-dioxo-10-oxa-4- azatricyclo[5.2.1.02,6]dec-8-en-4-yl) ethyl ester was synthesized employing a literature procedure.[205]

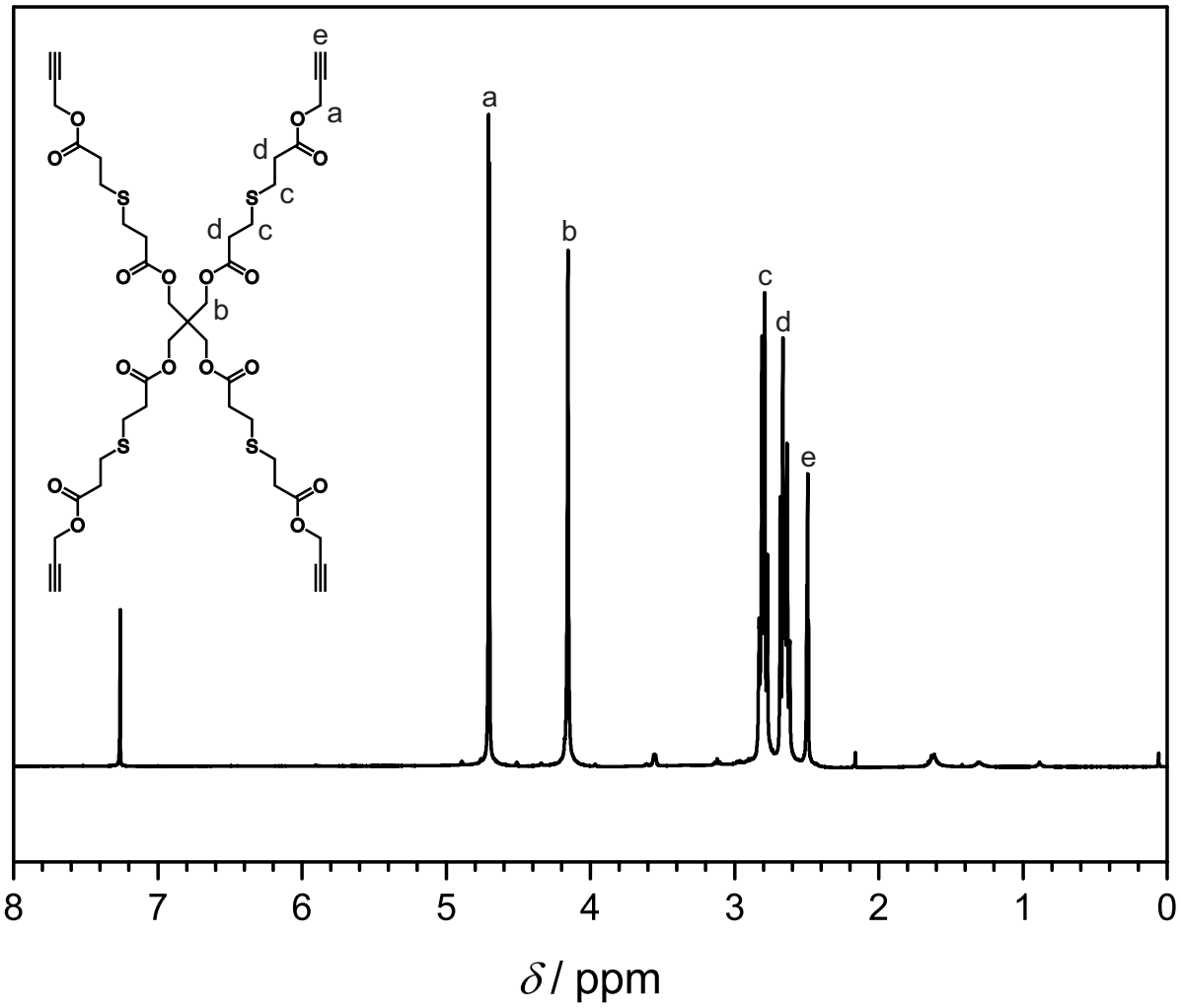

Figure 6.3: ^{1}H NMR of Tetraalkyne in chloroform with assigned hydrogen signals. A signal originating from the chloroform solvent is visible.

Chlorine Azide

2-Azidoethyl-2-chloropropanoate was synthesized employing a literature procedure.[209]

6.2.3 Devices

Nuclear Magnetic Resonance

^{1}H NMR spectroscopy was performed using a Bruker AM 400 spectrometer at 400 MHz. The δ-scale is referenced to the corresponding solvent signal.

Fourier Transform Infrared Spectroscopy

FTIR spectroscopy was performed using a Bruker Tensor 27 Fourier-transform microscope spectrometer equipped with Hyperion 1000 unit. Spectra of Tetrathiol 2, Tetraalkyne, and the

liquid photoresist were recorded employing attenuated total reflection infrared spectroscopy. Chemical analysis of the cuboid microstructures was performed *via* transmission IR spectroscopy using the Hyperion 1000 unit. Atmospheric compensation was performed upon the obtained spectra. Photonic stop band analysis of woodpile photonic crystals was performed *via* reflection IR spectroscopy using the Hyperion 1000 unit and a silver mirror as reference. The employed Cassegrain objective (Opticon 36x, NA = 0.5) illuminates the sample in an angular interval of 15°-30° from the optical axis. Spectra shown in Figure 3.25 were normalized *via* the highest peak in the region of 2900-2950 cm^{-1}.

Scanning Electron Microscopy

SEM imaging was performed using a Zeiss Supra 40VP. All samples were coated with a 7-10 nm gold layer prior to measurements.

Camera Imaging

Imaging was performed using a Sony GigE Vision XCG-500CR camera attached to a stereo microscope (Leica Mz 125 and a 0.5× adapter from Leica mount to C-mount).

Focused Ion Beam Milling

FIB milling was performed using a Zeiss Auriga equipped with a gallium ion source. The applied current was set to be 50 pA / 30 kV. The sample was coated with a 10 nm gold layer prior to measurement.

Time-of-Flight Secondary Ion Mass Spectrometry

ToF SIMS imaging was performed on a TOF.SIMS5 instrument (ION-TOF, Münster, Germany) equipped with a Bi liquid metal primary ion source and a nonlinear time-of-flight analyzer. For chemical surface characterization the Bi source was operated in the "bunched" mode, providing 0.7 ns Bi^+ ion pulses at 25 keV energy and a lateral resolution of approximately 4 µm. Negative polarity spectra were calibrated on the C^-, CH^-, and CH_2^- peaks. Primary ion doses for spectrometry were kept below 10^{11} ions cm^{-2} (static SIMS limit). After having established the chemical assignments from spectrometry data and the structures precisely aligned to the primary beam, high lateral resolution (3D) images were obtained applying the "burst alignment" mode of the primary ion source. This mode avoids chromatic aberration of the Bi primary ion beam and therefore provides a highly focused ion beam allowing for sub-µm lateral resolutions. Charge compensation was achieved by applying an electron flood gun providing electrons of 21 eV and tuning the secondary ion reflectron accordingly.

Direct Laser Writing

DLW experiments were performed using a commercially available DLW system (Photonic Professional GT, Nanoscribe GmbH, Germany) equipped with a frequency doubled Erbium fiber laser featuring a 780 nm center wavelength, a pulse duration of close to 90 fs, and a Zeiss

Plan-Apochromat 63x/1.4 Oil DIC objective. 3D patterning was performed by laser scanning *via* a set of galvanometric-mirrors and mechanical stages. All procedures were conducted in Dip-in configuration. Precise lithography parameters of presented structures can be found in Section 3.2.

6.2.4 Direct Laser Writing Experiments

Radical Thiol-Yne Photoresist Preparation

Tetraalkyne (1.00 g, 1.08×10^{-3} mol, 1 eq), Tetrathiol 2 (1.05 g, 2.16×10^{-3} mol, 2 eq) and DETC (5 mg, 0.25%wt) was added to a 5 mL brown glass vial equipped with a stir bar. The solution was stirred overnight at ambient (yellow light) conditions.

Glass Substrate Preparation

Glass substrates were reacted with 3-(trimethoxysilyl)propyl methacrylate prior to usage *via* the procedure described in Section 6.1.

Fabrication of Cuboid Structures

Silanized glass substrates with a dimension of $22\times22\times0.17$ mm were used. The photoresist was drop-casted onto the substrate. The scan raster was set to be 0.3 µm, laterally and 0.5 µm, axially. Development of the sample was conducted *via* the procedure described in Section 6.1.

Fabrication of Woodpile Photonic Crystals and Cubic Unit Cell Objects

Silanized DiLL glass substrates (Nanoscribe GmbH, Germany) with a $25\times25\times0.7$ mm^3 dimension were used. The photoresist was drop-casted onto the substrate. Development of the sample was conducted in acetone (30 min) followed by critical point drying in order to avoid capillary forces that occur during the conventional drying procedure. For cubic unit cells: The axial scan raster was chosen to be 0.5 µm. For high quality woodpiles: Each line was subsequently exposed five times in order to reduce structure deformation.

6.2.5 Covalent Post-Modification

Functionalization *via* the thiol-Michael Addition

To a glass vial, 2-bromo-2-methyl propionic acid 2-(3,5-dioxo-10-oxa-4-azatricyclo[5.2.1.02,6]-dec-8-en-4-yl) ethyl ester (5.8 mg, 2×10^{-5} mol), DCM (20 mL) and triethylamine (0.04 mL) was added. Into this solution, a substrate containing cuboid structures was immersed followed by a 24 hours period of slow shaking using a lab scale platform shaker. Afterwards, the substrate was subsequently developed in DCM (20 min), acetone (5 min), and water (5 min).

Functionalization *via* the Copper-Catalyzed Azide-Alkyne Cycloaddition

A glass vial was loaded with CuI (4.3 mg, 3×10^{-5} mol), DMF (30 mL), PMDETA (6.3 µL, 3×10^{-5} mol), PEG-N_3 (6 mg, 3×10^{-6} mol) and a 2 mm stir bar. Into this solution, a substrate containing cuboid structures was immersed followed by a 48 hours period of slow stirring (without the stir bar touching the substrate). Afterwards, the substrate was subsequently developed in DMF (20 min) and water (5 min). In order to prevent grease / oil contamination while ensuring absence of oxygen, the procedure (excluding the development steps) was performed under inert atmosphere in a glove-box. For post-modification using 2-azidoethyl-2-chloropropanoate, CuCl, PMDETA, and DMF were employed.

6.3 Photoenol Mediated Direct Laser Writing

6.3.1 Materials

GBL (≥99%, Sigma Aldrich), acetophenone (99%, Sigma Aldrich), pentaerythritol tetrabromide (96%, Sigma Aldrich), DMF (99.5%, Acros Organics), potassium carbonate (K_2CO_3, ≥99%, Roth), acetonitrile (anhydrous, Fischer), DCM (analytical grade, Fischer), hexane (analytical grade, Prolabo), ethyl acetate (analytical grade, Prolabo), basic alumina oxide (VWR), diethyl ether (Et_2O, analytical grade, Prolabo), isopropanol (≥99.5%, Roth), tetrahydrofuran (THF, GPC-grade, VWR), methyl α-bromoisobutyrate (≥99%, Sigma Aldrich), PMDETA (99+%, Acros Organics), copper(II) bromide (99%, Sigma Aldrich), methanol (MeOH, analytical grade, VWR) and toluene (analytical grade, Prolabo) were used without further treatment. Acetone (99.5%, Roth) employed for ATRP was dried over sodium sulfate prior to usage. Methyl methacrylate (99+%, Acros Organics) was deinhibited by percolating over a column of basic alumina oxide and stored at -19°C prior to usage. CuBr (98%, Sigma Aldrich) was successively washed with acetic acid and Et_2O and dried under vacuum.[210]

6.3.2 Synthesis

2-Hydroxy-6-methylbenzaldehyde

2-hydroxy-6-methylbenzaldehyde was synthesized employing a literature procedure.[186]

Photoenol Tetralinker (TetraPE)

2-Hydroxy-6-methylbenzaldehyde (1.30 g, 9.56×10^{-3} mol, 7 eq), pentaerythritol tetrabromide (0.53 g, 1.37×10^{-3} mol, 1 eq) and K_2CO_3 (2.83 g, 20.48×10^{-3} mol, 15 eq) was dissolved in 45 mL of DMF in a 100 mL round bottom flask, equipped with a stir bar and a reflux condenser. The reaction mixture was heated to 120°C and stirred for 3 days. The now black reaction solution was subsequently allowed to cool to ambient temperature. Thereafter, the solvent was removed under reduced pressure at 80°C. Then, silica gel (approximately 10 g) and 40 mL of acetonitrile/dichloromethane (7:3) was added to the black residue. After removing the solvent under reduced pressure, the crude product was further purified *via* column chromatography (hexane:ethyl acetate, 7:3, rf = 0.4) to give a yellow solid. The yellow solid was excessively

washed with Et_2O to yield the final product as an off-white powder that was dried in vacuo at 50°C. Yield: 0.41 g, 50%. ^{1}H NMR (400 MHz, $CDCl_3$, δ): 10.61 (s, 4H, CHO), 7.38 (t, J = 8.0 Hz, 4H, ArH), 6.89 (d, J = 8.4 Hz, 4H, ArH), 6.83 (d, J = 7.6 Hz, 4H, ArH), 4.50 (s, 8H, CH2), 2.54 (s, 12H, CH3); ^{13}C NMR (100 MHz, $CDCl_3$, δ): 190.9 (CHO), 161.4 (OCAr), 142.6 (CH3CAr), 135.0 (CAr), 125.0 (CAr), 123.5 (CHCAr), 110.2 (CAr), 67.0 (CH2), 45.8 (C(CH2O)4), 21.2 (CH3).

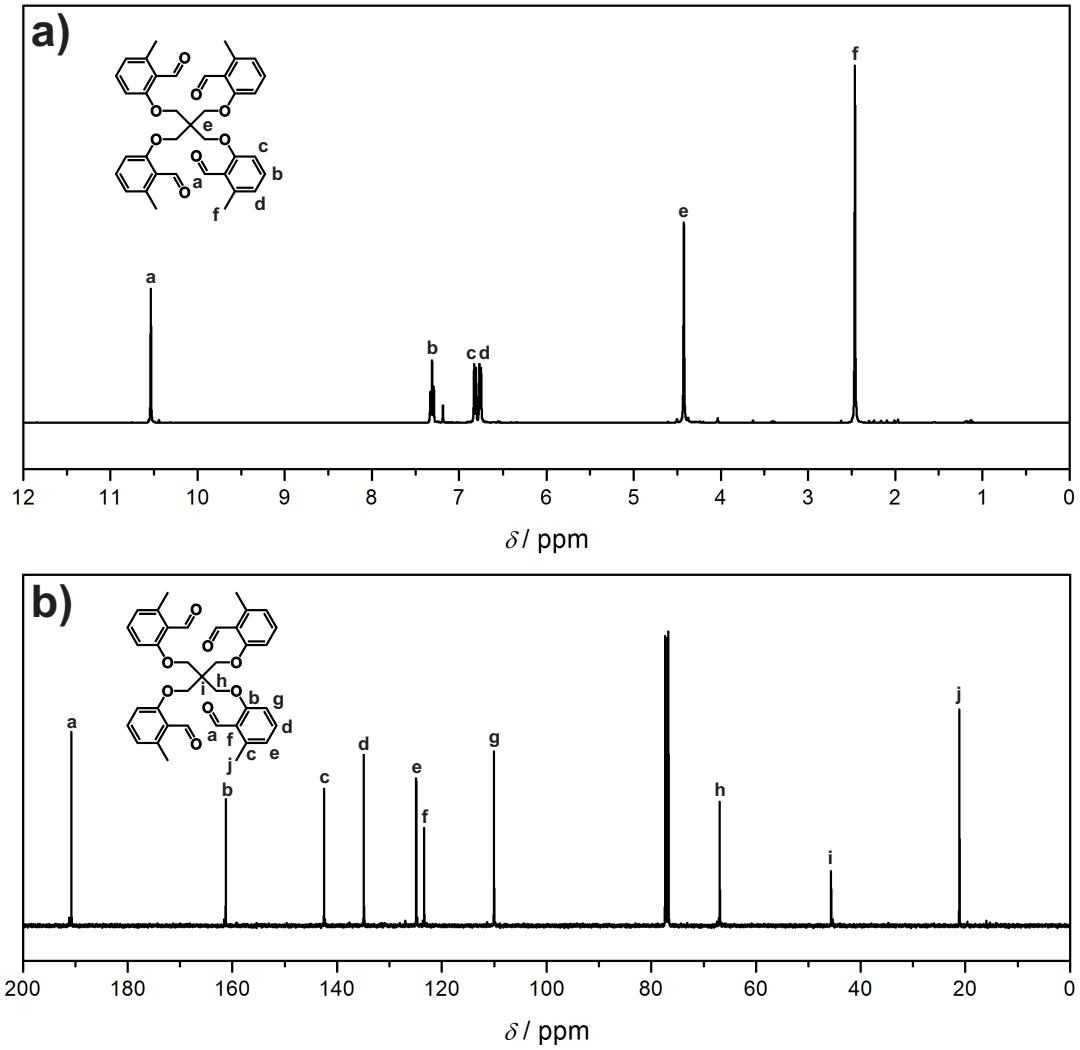

Figure 6.4: a) ^{1}H and b) ^{13}C NMR of TetraPE. A signal originating from the chloroform solvent is visible.

Maleimide Methacrylate

2-(1,3-dioxo-3a,4,7,7a-tetrahydro-1H-4,7-epoxyisoindol-2(3H)-yl)ethyl methacrylate (maleimide methacrylate) was synthesized employing a literature procedure.[211]

Dodecamaleimide Polymethacrylate (DodecaMal)

A 25 mL schlenk flask was equipped with methyl methacrylate (3.5 mL, 3.3 g, 32.9×10^{-3} mol, 4.1 eq), 2-(1,3-dioxo-3a,4,7,7a-tetrahydro-1H-4,7-epoxyisoindol-2(3H)-yl)ethyl methacrylate (2.2 g, 7.9×10^{-3} mol, 1.0 eq), methyl α-bromoisobutyrate (52.0 µL, 72.8 mg, 0.4×10^{-3} mol, 0.05 eq), PMDETA (52.0 µL, 43.2 mg, 0.25×10^{-3} mol, 0.03 eq), $CuBr_2$ (4.0 mg, 0.02×10^{-3} mol, 0.002 eq) 4 mL of acetone and a stir bar. Three consecutive freeze-pump-thaw cycles were performed. To the still frozen reaction mixture CuBr (16.0 mg, 0.11×10^{-3} mol, 0.014 eq) was added under reverse flow of nitrogen. After two additional consecutive freeze-pump-thaw cycles, the flask was rapidly heated to 50°C in a preheated oil bath and stirred for 7.5 hours. The reaction solution was subsequently exposed to air and passed through a short column of neutral alumina oxide. The generated polymer was precipitated in cold MeOH. The precipitated polymer was then dissolved in 15 mL of toluene in a 25 mL round bottom flask which was then connected to a condenser. The reaction mixture was then heated to reflux for 24 hours. Furan and solvent were removed under reduced pressure. The solid residue was dissolved in toluene and precipitated in cold MeOH. The Product was dried under reduced pressure at 50°C to yield a white solid (1.5 g). SEC: M_n = 10500 Da, PDI = 1.2; ^{1}H NMR (400 MHz, $CDCl_3$, δ): 6.80 (s, 2H; CH(C=O)N), 4.03 (s, 2H, H2CO), 3.80 (s, 2H, H2CN), 3.57 (s, 3H, H3CO), 2.03-1.66 (m, 2H, CCH2C), 1.05-0.66 (m, 3H, CH3C). For the calculation of the number of maleimide groups per polymer chain, the integrals of the ^{1}H NMR signals at 6.80 ppm and 3.57 ppm as well as the M_n of the SEC measurement where employed. The number of maleimide groups per polymer molecule was calculated to be close to 12.

Bromine Maleimide

2-Bromo-2-methyl propionic acid 2-(3,5-dioxo-10-oxa-4-azatricyclo[5.2.1.02,6]dec-8-en-4-yl) ethyl ester was synthesized employing a literature procedure.[205]

Acrylamide Silane

N-(3-(trimethoxysilyl)propyl) acrylamide was synthesized employing a literature procedure.[212]

6.3.3 Devices

Nuclear Magnetic Resonance

^{1}H and ^{13}C NMR spectroscopy was performed using a Bruker AM 400 spectrometer at 400 MHz. All samples were dissolved in $CDCl_3$. The δ-scale is referenced to the internal standard tetramethylsilane (TMS, δ = 0.00 ppm).

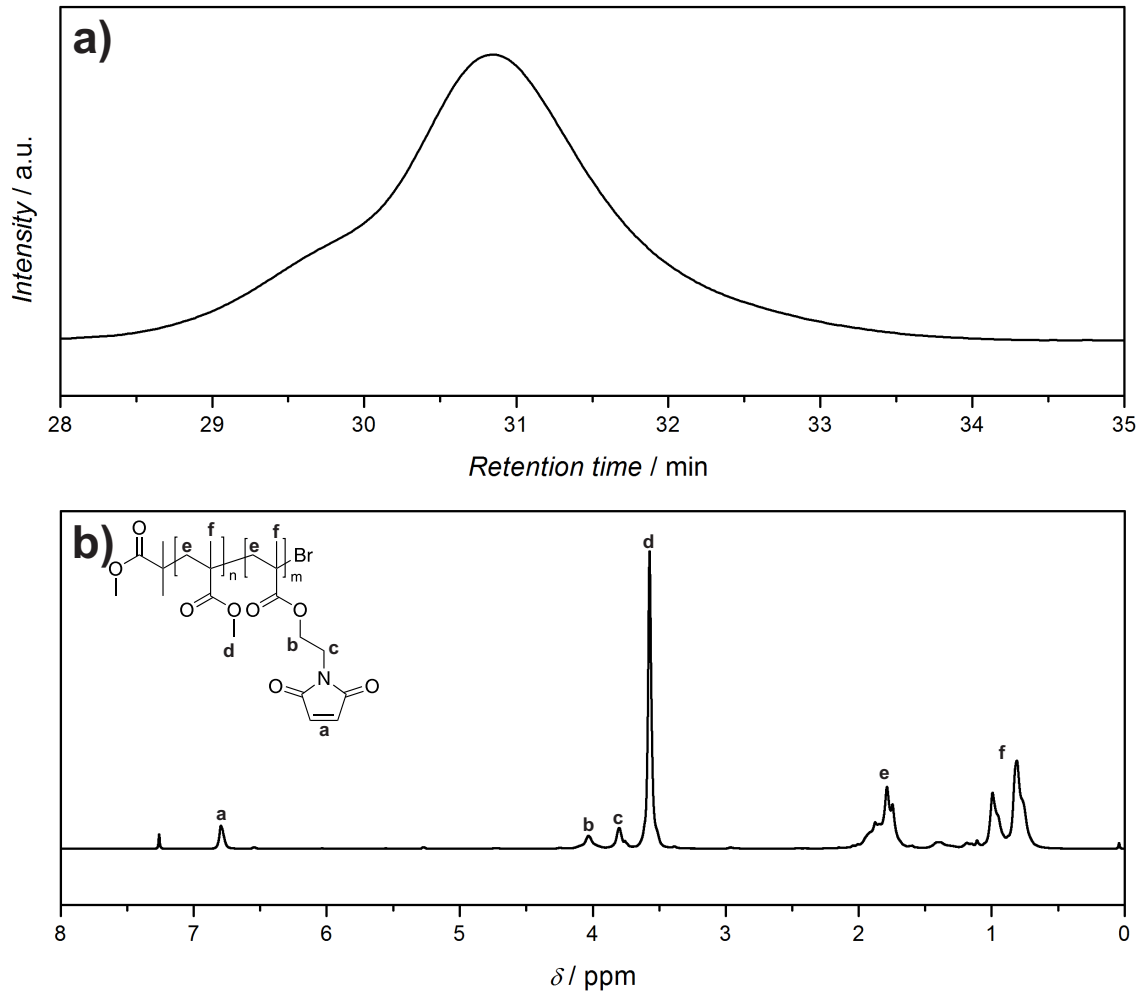

Figure 6.5: a) SEC trace and b) ^{1}H NMR of DodecaMal. A signal originating from the chloroform solvent is visible in the NMR.

Size Exclusion Chromatography

SEC was performed using a Polymer Laboratories PL-GPC 50 Plus system, comprised of an auto injector, a guard column (PLgel Mixed C, 50 × 75 mm) followed by three linear columns (PLger Mixed C, 300 × 7.5 mm, 5 µm bead size) and a differential refractive index detector, was employed. THF at 40°C at a flow rate of 1 mL min^{-1} was used as the eluent. The GPC system was calibrated using narrow poly(methyl methacrylate) standards ranging from 600 to 5195 g mol^{-1} (Polymer Standards Service (PSS), Mainz, Germany). The resulting molar mass distributions were determined by universal calibration using Mark-Houwink parameters for PMMA (K = 12.8 10^{-5} dL g^{-1}, α = 0.69). All M_n values were calculated using a PMMA calibration curve and the Mark-Houwink correction parameters, K and α.

UV-VIS Spectroscopy

UV-VIS measurements were recorded on a Varian Cary 300 Bio spectrophotometer.

Fourier Transform Infrared Spectroscopy

FTIR spectroscopy measurements were performed on a Fourier-transform microscope spectrometer (Bruker Tensor 27 with Hyperion 1000 unit). Spectra of TetraPE, DodecaMal and the stoichiometric mixture of TetraPE and DodecaMal were measured using attenuated total reflection infrared spectroscopy. The microstructure was characterized *via* transmission IR spectroscopy using the Hyperion 1000 unit. Atmospheric compensation and baseline correction was performed upon the obtained spectra. The spectra were normalized *via* the highest carbonyl absorption band at 1680-1710 cm^{-1}.

Scanning Electron Microscopy

SEM images were recorded using a Zeiss Supra 40VP. All samples were coated with a 10 nm gold layer prior to measurements.

Focused Ion Beam Milling

FIB milling was performed using a Zeiss Auriga equipped with a gallium ion source. The applied current was set to be 50 pA / 30 kV. All samples were coated with a 10 nm gold layer prior to measurements.

Optical Characterization of Photonic Crystals

Transmission and reflection spectra of the woodpile photonic crystals were taken using a commercial FTIR-spectrometer-microscope (Bruker Equinox 55). The Cassegrain objective (Opticon 36×, NA = 0.5) used illuminates the sample in the angular interval 15°-30° from the optical axis.

Time-of-Flight Secondary Ion Mass Spectrometry

ToF SIMS was performed on a TOF.SIMS5 instrument (ION-TOF GmbH, Münster, Germany), equipped with a Bi cluster primary ion source and a reflectron type time-of-flight analyzer. UHV base pressure was $< 5\times10^{-9}$ mbar. For high mass resolution the Bi source was operated in the "high current bunched" mode providing short Bi_1^+ or Bi_3^+ primary ion pulses at 25 keV energy and a lateral resolution of approx. 4 μm. The short pulse length of 1.1 ns allowed for high mass resolution. Spectra were calibrated on the omnipresent C^-,CH^-, CH_2^-, C_2^-, C_3^-, or on the C^+, CH^+, CH_2^+, and CH_3^+ peaks. ^{79}Br and ^{81}Br peaks were not accompanied by other strong peaks at identical nominal masses; therefore, for high lateral resolution imaging the primary ion source was operated in "burst alignment" mode. Here, only nominal mass resolution is obtained but the lateral resolution of the instrument is in the range of 150 nm. Images of 256×256 pixel were recorded, no filtering/averaging was performed.

Direct Laser Writing

DLW was conducted using a home-built setup that has been previously described in detail.[200] The pulse-picker described in the reference has been removed resulting in a repetition rate of 80 MHz and the laser has been tuned to 700 nm center wavelength. For photoenol depletion experiments, a second laser (Picoquant LDH-D-C-440) with a 440 nm center wavelength was incorporated into the home-built setup. The depletion laser was operated in continuous wave mode.

6.3.4 Direct Laser Writing Experiments

Photoresist Preparation

The resist employed for photoenol mediated DLW experiments consists of TetraPE (5 mg, 8.2 10^{-6} mol), DodecaMal (29.2 mg, 8.2 10^{-6} mol), 150 µL of GBL and 150 µL of acetophenone. After dissolving of the solid compounds, the resist was passed through a filter (Whatman, Spartan 13 / 0.2 RC) prior to usage.

Glass Substrate Preparation

All glass substrates were cleaned by ultrasonification for 15 min in acetone. Preactivation of the surfaces was achieved by exposure to air plasma for 10 min. Preactivated glass substrates were placed separately in small glass vials containing a solution of acrylamide silane dissolved in toluene (1 10^{-3} mol L^{-1}) for 60 min at ambient temperature without stirring. The substrates were successively ultrasonicated in toluene (10 mL, 10 min) and acetone (10 mL, 5 min) to remove any physisorbed silane. The silanization process is performed in order to covalently bind the fabricated structures to the substrate surface during fabrication. The adhesive strength is increased thereby.

Sample Preparation and Development

DLW samples were prepared and developed according to Section 6.1.

Fabrication of Woodpile Photonic Crystals

Woodpile photonic crystals with a rod spacing ranging from 700 nm to 500 nm were fabricated. The average laser power was varied between 2.7 mW and 4.3 mW. The writing speed was set to be 100 µm s^{-1}.

Fabrication of Samples for FTIR Spectroscopy

A solid cuboid polymer block was fabricated exhibiting a footprint of 50×50 µm^2 and a height of close to 10 µm for characterization *via* FTIR spectroscopy. The laser power and the writing speed were set to be 5 mW and 100 µm s^{-1}, respectively.

Fabrication of Samples for Spatially Resolved Surface Patterning

Solid polymer layers with base dimensions of 90×90 μm and a height of about 300 nm were fabricated. The fabrication parameters were set to be 5 mW average laser power and 100 μm s^{-1} writing speed.

6.3.5 Covalent Post-Modification

Spatially Resolved Surface Patterning

DLW fabricated structures were immersed into a solution of 2-bromo-2-methyl propionic acid 2-(3,5-dioxo-10-oxa-4-azatricyclo[5.2.1.02,6]dec-8-en-4-yl) ethyl ester in DMF (3 mg mL^{-1}) much similar to the preparation of a common DLW sample. Patterning was conducted using the DLW setup with fabrication parameters of 5 mW average laser power and 10 μm s^{-1} writing speed. Sample development was performed by immersing the sample into DMF (30 mL, 2 hours) and subsequent rinsing with acetone (5 mL), isopropanol (5 mL) and distilled water (5 mL). Residual solvent was removed under reduced pressure.

Bibliography

[1] F. Fleischhaker, R. Zentel, *Chem. unserer Zeit* **2007**, *41*, 38–44.

[2] K. Autumn, Y. A. Liang, S. T. Hsieh, W. Zesch, W. P. Chan, T. W. Kenny, R. Fearing, R. J. Full, *Nature* **2000**, *405*, 681–685.

[3] W. Barthlott, C. Neinhuis, *Planta* **1997**, *202*, 1–8.

[4] D. Dendukuri, D. C. Pregibon, J. Collins, T. A. Hatton, P. S. Doyle, *Nat. Mater.* **2006**, *5*, 365–369.

[5] M. Brust, M. Walker, D. Bethell, D. J. Schiffrin, R. Whyman, *J. Chem. Soc. Chem. Commun.* **1994**, 801–802.

[6] S. Y. Chou, P. R. Krauss, P. J. Renstrom, *J. Vac. Sci. Technol. B* **1996**, *14*, 4129–4133.

[7] C. N. LaFratta, J. T. Fourkas, T. Baldacchini, R. A. Farrer, *Angew. Chem. Int. Ed.* **2007**, *46*, 6238–6258.

[8] W.-H. Li, H. D. H. Stöver, *J. Polym. Sci. Part A: Polym. Chem.* **1998**, *36*, 1543–1551.

[9] L. Guo, P. R. Krauss, S. Y. Chou, *Appl. Phys. Lett.* **1997**, *71*, 1881–1883.

[10] C. M. Soukoulis, M. Wegener, *Nat. Photonics* **2011**, *5*, 523–530.

[11] S. Maruo, J. T. Fourkas, *Laser Photon. Rev.* **2008**, *2*, 100–111.

[12] C. E. Hoyle, T. Y. Lee, T. Roper, *J. Polym. Sci. Part A: Polym. Chem.* **2004**, *42*, 5301–5338.

[13] C. E. Hoyle, C. N. Bowman, *Angew. Chem. Int. Ed.* **2010**, *49*, 1540–1573.

[14] R. Hoogenboom, *Angew. Chem. Int. Ed.* **2010**, *49*, 3415–3417.

[15] J. Sauer, R. Sustmann, *Angew. Chem. Int. Ed.* **1980**, *19*, 779–807.

[16] P. G. Sammes, *Tetrahedron* **1976**, *32*, 405–422.

[17] H. C. Kolb, M. G. Finn, K. B. Sharpless, *Angew. Chem. Int. Ed.* **2001**, *40*, 2004–2021.

[18] C. Barner-Kowollik, F. E. Du Prez, P. Espeel, C. J. Hawker, T. Junkers, H. Schlaad, W. Van Camp, *Angew. Chem. Int. Ed.* **2011**, *50*, 60–62.

[19] S. Y. Chou, *MRS Bull.* **2001**, *26*, 512–517.

[20] M. Geissler, Y. Xia, *Adv. Mater.* **2004**, *16*, 1249–1269.

[21] D. S. Ginger, H. Zhang, C. A. Mirkin, *Angew. Chem. Int. Ed.* **2004**, *43*, 30–45.

[22] H. Trommsdorff, *Ann. Chem. Pharm.* **1834**, *11*, 190–207.

[23] A. Natarajan, C. K. Tsai, S. I. Khan, P. McCarren, K. N. Houk, M. A. Garcia-Garibay, *J. Am. Chem. Soc.* **2007**, *129*, 9846–9847.

[24] T. H. Maiman, *Nature* **1960**, *187*, 493–494.

[25] R. M. Osgood, H. H. Gilgen, *Annu. Rev. Mater. Sci.* **1985**, *15*, 549–576.

[26] H. Kodama, *Rev. Sci. Instrum.* **1981**, *52*, 1770–1773.

[27] K. Ikuta, K. Hirowatari in Proceedings of MEMS '93, IEEE, Fort Lauderdale, pp. 42–47.

[28] M. Göppert-Mayer, *Ann. Phys.* **1931**, *401*, 273–294.

[29] S. Maruo, H. Inoue, *Appl. Phys. Lett.* **2006**, *89*, 144101.

[30] K. Cicha, Z. Li, K. Stadlmann, A. Ovsianikov, R. Markut-Kohl, R. Liska, J. Stampfl, *J. Appl. Phys.* **2011**, *110*, 064911.

[31] J. B. Mueller, J. Fischer, F. Mayer, M. Kadic, M. Wegener, *Adv. Mater.* **2014**, *26*, 6566–6571.

[32] T. Bückmann, M. Thiel, M. Kadic, R. Schittny, M. Wegener, *Nat. Commun.* **2014**, *5*, 4130.

[33] M. Thiel, J. Fischer, G. von Freymann, M. Wegener, *Appl. Phys. Lett.* **2010**, *97*, 221102.

[34] P. Mueller, M. Thiel, M. Wegener, *Opt. Lett.* **2014**, *39*, 6847–6850.

[35] M. Malinauskas, M. Farsari, A. Piskarskas, S. Juodkazis, *Phys. Rep.* **2013**, *533*, 1–31.

[36] J. Serbin, A. Ovsianikov, B. Chichkov, *Opt. Express* **2004**, *12*, 5221–5228.

[37] M. Pawlicki, H. A. Collins, R. G. Denning, H. L. Anderson, *Angew. Chem. Int. Ed.* **2009**, *48*, 3244–3266.

[38] M. Albota, D. Beljonne, J.-L. Brédas, J. E. Ehrlich, J.-Y. Fu, A. A. Heikal, S. E. Hess, T. Kogej, M. D. Levin, S. R. Marder, D. McCord-Maughon, J. W. Perry, H. Röckel, M. Rumi, G. Subramaniam, W. W. Webb, X.-L. Wu, C. Xu, *Science* **1998**, *281*, 1653–1656.

[39] B. H. Cumpston, S. P. Ananthavel, S. Barlow, D. L. Dyer, J. E. Ehrlich, L. L. Erskine, A. A. Heikal, S. M. Kuebler, I. Y. S. Lee, D. McCord-Maughon, J. Qin, H. Röckel, M. Rumi, X.-L. Wu, S. R. Marder, J. W. Perry, *Nature* **1999**, *398*, 51–54.

[40] W. R. Zipfel, R. M. Williams, W. W. Webb, *Nat. Biotechnol.* **2003**, *21*, 1369–1377.

[41] E. Abbe, *Arch. f. Microskop. Anat.* **1873**, *9*, 413.

[42] J. Fischer, M. Wegener, *Laser Photon. Rev.* **2012**, 1–23.

[43] J. K. Gansel, M. Thiel, M. S. Rill, M. Decker, K. Bade, V. Saile, G. von Freymann, S. Linden, M. Wegener, *Science* **2009**, *325*, 1513–1515.

[44] B. J. Adzima, C. J. Kloxin, C. A. DeForest, K. S. Anseth, C. N. Bowman, *Macromol. Rapid Comm.* **2012**, *33*, 2092–2096.

[45] W. H. Teh, U. Dürig, G. Salis, R. Harbers, U. Drechsler, R. F. Mahrt, C. G. Smith, H.-J. Güntherodt, *Appl. Phys. Lett.* **2004**, *84*, 4095–4097.

[46] K. D. Belfield, K. J. Schafer, Y. Liu, J. Liu, X. Ren, E. W. V. Stryland, *J. Phys. Org. Chem.* **2000**, *13*, 837–849.

[47] Y. Murakami, C. A. Coenjarts, C. K. Ober, *J. Photopolym. Sci. Technol.* **2004**, *17*, 115–118.

[48] W. Zhou, S. M. Kuebler, K. L. Braun, T. Yu, J. K. Cammack, C. K. Ober, J. W. Perry, S. R. Marder, *Science* **2002**, *296*, 1106–1109.

[49] S. Maruo, K. Ikuta, H. Korogi, *J. Microelectromech. S.* **2003**, *12*, 533–539.

[50] K. J. Schafer, J. M. Hales, M. Balu, K. D. Belfield, E. W. V. Stryland, D. J. Hagan, *J. Photochem. Photobiol. A* **2004**, *162*, 497–502.

[51] P. J. Campagnola, D. M. Delguidice, G. A. Epling, K. D. Hoffacker, A. R. Howell, J. D. Pitts, S. L. Goodman, *Macromolecules* **2000**, *33*, 1511–1513.

[52] L. J. Jiang, Y. S. Zhou, W. Xiong, Y. Gao, X. Huang, L. Jiang, T. Baldacchini, J.-F. Silvain, Y. F. Lu, *Opt. Lett.* **2014**, *39*, 3034–3037.

[53] J. B. Mueller, J. Fischer, Y. J. Mange, T. Nann, M. Wegener, *Appl. Phys. Lett.* **2013**, *103*, 123107.

[54] T. Watanabe, M. Akiyama, K. Totani, S. M. Kuebler, F. Stellacci, W. Wenseleers, K. Braun, S. R. Marder, J. W. Perry, *Adv. Funct. Mater.* **2002**, *12*, 611–614.

[55] J. Serbin, A. Egbert, A. Ostendorf, B. N. Chichkov, R. Houbertz, G. Domann, J. Schulz, C. Cronauer, L. Fröhlich, M. Popall, *Opt. Lett.* **2003**, *28*, 301–303.

[56] A. Ovsianikov, J. Viertl, B. Chichkov, M. Oubaha, B. MacCraith, I. Sakellari, A. Giakoumaki, D. Gray, M. Vamvakaki, M. Farsari, C. Fotakis, *ACS Nano* **2008**, *2*, 2257–2262.

[57] M. Farsari, B. N. Chichkov, *Nat. Photonics* **2009**, *3*, 450–452.

[58] E. Kabouraki, A. N. Giakoumaki, P. Danilevicius, D. Gray, M. Vamvakaki, M. Farsari, *Nano Lett.* **2013**, *13*, 3831–3835.

[59] C. A. Coenjarts, C. K. Ober, *Chem. Mater.* **2004**, *16*, 5556–5558.

[60] S. Wong, M. Deubel, F. Pérez-Willard, S. John, G. A. Ozin, M. Wegener, G. von Freymann, *Adv. Mater.* **2006**, *18*, 265–269.

[61] A. M. Greiner, M. Jäckel, A. C. Scheiwe, D. R. Stamow, T. J. Autenrieth, J. Lahann, C. M. Franz, M. Bastmeyer, *Biomaterials* **2014**, *35*, 611–619.

[62] T. Bückmann, N. Stenger, M. Kadic, J. Kaschke, A. Frölich, T. Kennerknecht, C. Eberl, M. Thiel, M. Wegener, *Adv. Mater.* **2012**, *24*, 2710–2714.

[63] K. M. Ho, C. T. Chan, C. M. Soukoulis, R. Biswas, M. Sigalas, *Solid State Commun.* **1994**, *89*, 413–416.

[64] C. M. Sparrow, *Astro J.* **1916**, *44*, 76–86.

[65] J. Fischer, M. Wegener, *Opt. Mater. Express* **2011**, *1*, 614–624.

[66] S. W. Hell, *Nat. Methods* **2009**, *6*, 24–32.

[67] T. A. Klar, R. Wollhofen, J. Jacak, *Phys. Scripta* **2014**, *2014*, 014049.

[68] L. Li, R. R. Gattass, E. Gershgoren, H. Hwang, J. T. Fourkas, *Science* **2009**, *324*, 910–913.

[69] M. P. Stocker, L. Li, R. R. Gattass, J. T. Fourkas, *Nat. Chem.* **2011**, *3*, 223–227.

[70] T. F. Scott, B. A. Kowalski, A. C. Sullivan, C. N. Bowman, R. R. McLeod, *Science* **2009**, *324*, 913–917.

[71] S. Maruo, K. Ikuta, H. Korogi, *Appl. Phys. Lett.* **2003**, *82*, 133–135.

[72] S. Klein, A. Barsella, H. Leblond, H. Bulou, A. Fort, C. Andraud, G. Lemercier, J. C. Mulatier, K. Dorkenoo, *Appl. Phys. Lett.* **2005**, *86*, 211118.

[73] M. Schumann, T. Bückmann, N. Gruhler, M. Wegener, W. Pernice, *Light: Science & Applications* **2014**, *3*, e175.

[74] B.-B. Xu, Y.-L. Zhang, H. Xia, W.-F. Dong, H. Ding, H.-B. Sun, *Lab Chip* **2013**, *13*, 1677–1690.

[75] D. Wu, Q.-D. Chen, L.-G. Niu, J.-N. Wang, J. Wang, R. Wang, H. Xia, H.-B. Sun, *Lab Chip* **2009**, *9*, 2391–2394.

[76] J. Wang, Y. He, H. Xia, L.-G. Niu, R. Zhang, Q.-D. Chen, Y.-L. Zhang, Y.-F. Li, S.-J. Zeng, J.-H. Qin, B.-C. Lin, H.-B. Sun, *Lab Chip* **2010**, *10*, 1993–1996.

[77] Y. He, B.-L. Huang, D.-X. Lu, J. Zhao, B.-B. Xu, R. Zhang, X.-F. Lin, Q.-D. Chen, J. Wang, Y.-L. Zhang, H.-B. Sun, *Lab Chip* **2012**, *12*, 3866–3869.

[78] M. Thiel, H. Fischer, G. von Freymann, M. Wegener, *Opt. Lett.* **2010**, *35*, 166–168.

[79] J. Fischer, T. Ergin, M. Wegener, *Opt. Lett.* **2011**, *36*, 2059–2061.

[80] B. Richter, T. Pauloehrl, J. Kaschke, D. Fichtner, J. Fischer, A. M. Greiner, D. Wedlich, M. Wegener, G. Delaittre, C. Barner-Kowollik, M. Bastmeyer, *Adv. Mater.* **2013**, *25*, 6117–6122.

[81] H. Xia, J. Wang, Y. Tian, Q.-D. Chen, X.-B. Du, Y.-L. Zhang, Y. He, H.-B. Sun, *Adv. Mater.* **2010**, *22*, 3204–3207.

[82] L. D. Zarzar, B. S. Swartzentruber, J. C. Harper, D. R. Dunphy, C. J. Brinker, J. Aizenberg, B. Kaehr, *J. Am. Chem. Soc.* **2012**, *134*, 4007–4010.

[83] F. Klein, B. Richter, T. Striebel, C. M. Franz, G. von Freymann, M. Wegener, M. Bastmeyer, *Adv. Mater.* **2011**, *23*, 1341–1345.

[84] A. C. Scheiwe, S. C. Frank, T. J. Autenrieth, M. Bastmeyer, M. Wegener, *Biomaterials* **2015**, *44*, 186–194.

[85] M. Thiel, M. Decker, M. Deubel, M. Wegener, S. Linden, G. von Freymann, *Adv. Mater.* **2007**, *19*, 207–210.

[86] J. Kaschke, M. Blome, S. Burger, M. Wegener, *Opt. Express* **2014**, *22*, 19936–19946.

[87] M. Kaupp, A. S. Quick, C. Rodriguez-Emmenegger, A. Welle, V. Trouillet, O. Pop-Georgievski, M. Wegener, C. Barner-Kowollik, *Adv. Funct. Mater.* **2014**, *24*, 5649–5661.

[88] L. Stolzer, A. S. Quick, D. Abt, A. Welle, D. Naumenko, M. Lazzarino, M. Wegener, C. Barner-Kowollik, L. Fruk, *Chem. Commun.* **2015**, *51*, 3363–3366.

[89] P. J. Roth, C. Boyer, A. B. Lowe, T. P. Davis, *Macromol. Rapid Commun.* **2011**, *32*, 1123–1143.

[90] K. Dietliker, R. Hüsler, J. L. Birbaum, S. Ilg, S. Villeneuve, K. Studer, T. Jung, J. Benkhoff, H. Kura, A. Matsumoto, H. Oka, *Prog. Org. Coat.* **2007**, *58*, 146–157.

[91] F. Fringuelli, F. Pizzo, S. Tortoioli, L. Vaccaro, *Tetrahedron Lett.* **2003**, *44*, 6785–6787.

[92] J. L. Kice, *Acc. Chem. Res.* **1968**, *1*, 58–64.

[93] C. B. Anfinsen, E. Haber, *J. Biol. Chem.* **1961**, *236*, 1361–1363.

[94] J. C. Love, L. A. Estroff, J. K. Kriebel, R. G. Nuzzo, G. M. Whitesides, *Chem. Rev.* **2005**, *105*, 1103–1170.

[95] A. De los Santos Pereira, T. Riedel, E. Brynda, C. Rodriguez-Emmenegger, *Sens. Actuator B Chem.* **2014**, *202*, 1313–1321.

[96] D. P. O'Neal, L. R. Hirsch, N. J. Halas, J. D. Payne, J. L. West, *Cancer Lett.* **2004**, *209*, 171–176.

[97] A. Massi, D. Nanni, *Org. Biomol. Chem.* **2012**, *10*, 3791–3807.

[98] C. D. Hurd, L. L. Gershbein, *J. Am. Chem. Soc.* **1947**, *69*, 2328–2335.

[99] E. Dyer, J. F. Glenn, E. G. Lendrat, *J. Org. Chem.* **1961**, *26*, 2919–2925.

[100] C. R. Morgan, F. Magnotta, A. D. Ketley, *J. Polym. Sci. Part A: Polym. Chem.* **1977**, *15*, 627–645.

[101] N. B. Cramer, S. K. Reddy, A. K. O'Brien, C. N. Bowman, *Macromolecules* **2003**, *36*, 7964–7969.

[102] L. V. Natarajan, D. P. Brown, J. M. Wofford, V. P. Tondiglia, R. L. Sutherland, P. F. Lloyd, T. J. Bunning, *Polymer* **2006**, *47*, 4411–4420.

[103] A. F. Senyurt, C. E. Hoyle, *Eur. Polym. J.* **2006**, *42*, 3133–3139.

[104] N. B. Cramer, J. P. Scott, C. N. Bowman, *Macromolecules* **2002**, *35*, 5361–5365.

[105] N. B. Cramer, S. K. Reddy, M. Cole, C. Hoyle, C. N. Bowman, *J. Polym. Sci. Part A: Polym. Chem.* **2004**, *42*, 5817–5826.

[106] W. D. Cook, F. Chen, D. W. Pattison, P. Hopson, M. Beaujon, *Polym. Int.* **2007**, *56*, 1572–1579.

[107] Y. B. Kim, H. K. Kim, H. C. Choi, J. W. Hong, *J. Appl. Polym. Sci.* **2005**, *95*, 342–350.

[108] M. Black, J. W. Rawlins, *Eur. Polym. J.* **2009**, *45*, 1433–1441.

[109] Q. Fu, J. Liu, W. Shi, *Prog. Org. Coat.* **2008**, *63*, 100–109.

[110] N. Simpson, M. Takwa, K. Hult, M. Johansson, M. Martinelle, E. Malmström, *Macromolecules* **2008**, *41*, 3613–3619.

[111] A. K. O'Brien, N. B. Cramer, C. N. Bowman, *J. Polym. Sci. Part A: Polym. Chem.* **2006**, *44*, 2007–2014.

[112] M. Natali, S. Begolo, T. Carofiglio, G. Mistura, *Lab Chip* **2008**, *8*, 492–494.

[113] V. S. Khire, Y. Yi, N. A. Clark, C. N. Bowman, *Adv. Mater.* **2008**, *20*, 3308–3313.

[114] D. Kim, E. Kim, J. Kim, K. M. Park, K. Baek, M. Jung, Y. H. Ko, W. Sung, H. S. Kim, J. H. Suh, C. G. Park, O. S. Na, D. K. Lee, K. E. Lee, S. S. Han, K. Kim, *Angew. Chem. Int. Ed.* **2007**, *46*, 3471–3474.

[115] N. B. Cramer, S. K. Reddy, H. Lu, T. Cross, R. Raj, C. N. Bowman, *J. Polym. Sci. Part A: Polym. Chem.* **2004**, *42*, 1752–1757.

[116] Z. Hordyjewicz-Baran, L. You, B. Smarsly, R. Sigel, H. Schlaad, *Macromolecules* **2007**, *40*, 3901–3903.

[117] J. Justynska, Z. Hordyjewicz, H. Schlaad, *Polymer* **2005**, *46*, 12057–12064.

[118] C. Konak, V. Subr, L. Kostka, P. Stepanek, K. Ulbrich, H. Schlaad, *Langmuir* **2008**, *24*, 7092–7098.

[119] S. P. S. Koo, M. M. Stamenovic, R. A. Prasath, A. J. Inglis, F. E. Du Prez, C. Barner-Kowollik, W. Van Camp, T. Junkers, *J. Polym. Sci. Part A: Polym. Chem.* **2010**, *48*, 1699–1713.

[120] B. Yao, J. Sun, A. Qin, B. Tang, *Chinese Sci. Bull.* **2013**, *58*, 2711–2718.

[121] M. Minozzi, A. Monesi, D. Nanni, P. Spagnolo, N. Marchetti, A. Massi, *J. Org. Chem.* **2011**, *76*, 450–459.

[122] B. D. Fairbanks, T. F. Scott, C. J. Kloxin, K. S. Anseth, C. N. Bowman, *Macromolecules* **2008**, *42*, 211–217.

[123] B. D. Fairbanks, E. A. Sims, K. S. Anseth, C. N. Bowman, *Macromolecules* **2010**, *43*, 4113–4119.

[124] C. E. Hoyle, A. B. Lowe, C. N. Bowman, *Chem. Soc. Rev.* **2010**, *39*, 1355–1387.

[125] G. Chen, J. Kumar, A. Gregory, M. H. Stenzel, *Chem. Commun.* **2009**, 6291–6293.

[126] R. M. Hensarling, V. A. Doughty, J. W. Chan, D. L. Patton, *J. Am. Chem. Soc.* **2009**, *131*, 14673–14675.

[127] C. Wendeln, S. Rinnen, C. Schulz, H. F. Arlinghaus, B. J. Ravoo, *Langmuir* **2010**, *26*, 15966–15971.

[128] M. Lomba, L. Oriol, R. Alcala, C. Sanchez, M. Moros, V. Grazu, J. L. Serrano, J. M. De la Fuente, *Macromol. Biosci.* **2011**, *11*, 1505–1514.

[129] J. Kumar, A. Bousquet, M. H. Stenzel, *Macromol. Rapid Commun.* **2011**, *32*, 1620–1626.

[130] J. W. Chan, H. Zhou, C. E. Hoyle, A. B. Lowe, *Chem. Mater.* **2009**, *21*, 1579–1585.

[131] J. W. Chan, J. Shin, C. E. Hoyle, C. N. Bowman, A. B. Lowe, *Macromolecules* **2010**, *43*, 4937–4942.

[132] D. P. Nair, M. Podgorski, S. Chatani, T. Gong, W. Xi, C. R. Fenoli, C. N. Bowman, *Chem. Mater.* **2014**, *26*, 724–744.

[133] B. D. Mather, K. Viswanathan, K. M. Miller, T. E. Long, *Prog. Polym. Sci.* **2006**, *31*, 487–531.

[134] P. Carlqvist, M. Svedendahl, C. Branneby, K. Hult, T. Brinck, P. Berglund, *ChemBioChem* **2005**, *6*, 331–336.

[135] M. J. Stanford, A. P. Dove, *Macromolecules* **2009**, *42*, 141–147.

[136] H. Kakwere, S. Perrier, *J. Am. Chem. Soc.* **2009**, *131*, 1889–1895.

[137] A. Kamimura, N. Murakami, F. Kawahara, K. Yokota, Y. Omata, K. Matsuura, Y. Oishi, R. Morita, H. Mitsudera, H. Suzukawa, A. Kakehi, M. Shirai, H. Okamoto, *Tetrahedron* **2003**, *59*, 9537–9546.

[138] E. Emori, T. Arai, H. Sasai, M. Shibasaki, *J. Am. Chem. Soc.* **1998**, *120*, 4043–4044.

[139] K. A. McEwan, S. Slavin, E. Tunnah, D. M. Haddleton, *Polym. Chem.* **2013**, *4*, 2608–2614.

[140] J. W. Chan, B. Yu, C. E. Hoyle, A. B. Lowe, *Chem. Commun.* **2008**, 4959–4961.

[141] J. D. Flores, N. J. Treat, A. W. York, C. L. McCormick, *Polym. Chem.* **2011**, *2*, 1976–1985.

[142] T. Pauloehrl, G. Delaittre, M. Bastmeyer, C. Barner-Kowollik, *Polym. Chem.* **2012**, *3*, 1740–1749.

[143] K. C. Koehler, K. S. Anseth, C. N. Bowman, *Biomacromolecules* **2013**, *14*, 538–547.

[144] R. Tedja, A. H. Soeriyadi, M. R. Whittaker, M. Lim, C. Marquis, C. Boyer, T. P. Davis, R. Amal, *Polym. Chem.* **2012**, *3*, 2743–2751.

[145] C. O. Bounds, J. Upadhyay, N. Totaro, S. Thakuri, L. Garber, M. Vincent, Z. Huang, M. Hupert, J. A. Pojman, *ACS Appl. Mater. Interfaces* **2013**, *5*, 1643–1655.

[146] W. Xi, M. Krieger, C. J. Kloxin, C. N. Bowman, *Chem. Commun.* **2013**, *49*, 4504–4506.

[147] Z. Liu, T. Liu, Q. Lin, C. Bao, L. Zhu, *Chem. Commun.* **2014**, *50*, 1256–1258.

[148] B. H. M. Kuijpers, S. Groothuys, A. R. Keereweer, P. J. L. M. Quaedflieg, R. H. Blaauw, F. L. van Delft, F. P. J. T. Rutjes, *Org. Lett.* **2004**, *6*, 3123–3126.

[149] P. Wu, A. K. Feldman, A. K. Nugent, C. J. Hawker, A. Scheel, B. Voit, J. Pyun, J. M. J. Frechet, K. B. Sharpless, V. V. Fokin, *Angew. Chem. Int. Ed.* **2004**, *43*, 3928–3932.

[150] R. Hoogenboom, B. C. Moore, U. S. Schubert, *Chem. Commun.* **2006**, 4010–4012.

[151] M. Malkoch, R. Vestberg, N. Gupta, L. Mespouille, P. Dubois, A. F. Mason, J. L. Hedrick, Q. Liao, C. W. Frank, K. Kingsbury, C. J. Hawker, *Chem. Commun.* **2006**, 2774–2776.

[152] B. J. Adzima, Y. Tao, C. J. Kloxin, C. A. DeForest, K. S. Anseth, C. N. Bowman, *Nat. Chem.* **2011**, *3*, 256–259.

[153] C. D. McNitt, V. V. Popik, *Org. Biomol. Chem.* **2012**, *10*, 8200–8202.

[154] S. V. Orski, A. A. Poloukhtine, S. Arumugam, L. Mao, V. V. Popik, J. Locklin, *J. Am. Chem. Soc.* **2010**, *132*, 11024–11026.

[155] Z. Li, E. Stankevicius, A. Ajami, G. Raciukaitis, W. Husinsky, A. Ovsianikov, J. Stampfl, R. Liska, *Chem. Commun.* **2013**, *49*, 7635–7637.

[156] O. Diels, K. Alder, *Liebigs Ann.* **1928**, *460*, 98–122.

[157] K. C. Nicolaou, S. A. Snyder, T. Montagnon, G. Vassilikogiannakis, *Angew. Chem. Int. Ed.* **2002**, *41*, 1668–1698.

[158] C. O. Kappe, S. S. Murphree, A. Padwa, *Tetrahedron* **1997**, *53*, 14179–14233.

[159] K. Fukui, *Angew. Chem. Int. Ed.* **1982**, *21*, 801–809.

[160] R. B. Woodward, R. Hoffmann, *Angew. Chem. Int. Ed.* **1969**, *8*, 781–853.

[161] J. G. Martin, R. K. Hill, *Chem. Rev.* **1961**, *61*, 537–562.

[162] K. W. Hill, J. Taunton-Rigby, J. D. Carter, E. Kropp, K. Vagle, W. Pieken, D. P. C. McGee, G. M. Husar, M. Leuck, D. J. Anziano, D. P. Sebesta, *J. Org. Chem.* **2001**, *66*, 5352–5358.

[163] M. A. Tasdelen, *Polym. Chem.* **2011**, *2*, 2133–2145.

[164] J. Lahann, *Click Chemistry for Biotechnology and Materials Science*, John Wiley & Sons, Inc., Weinheim, **2009**.

[165] J. P. Blinco, V. Trouillet, M. Bruns, P. Gerstel, H. Gliemann, C. Barner-Kowollik, *Adv. Mater.* **2011**, *23*, 4435–4439.

[166] S. Arumugam, V. V. Popik, *J. Am. Chem. Soc.* **2009**, *131*, 11892–11899.

[167] S. Arumugam, V. V. Popik, *J. Am. Chem. Soc.* **2011**, *133*, 15730–15736.

[168] M. Glassner, K. K. Oehlenschlaeger, A. Welle, M. Bruns, C. Barner-Kowollik, *Chem. Commun.* **2013**, *49*, 633–635.

[169] S. Arumugam, V. V. Popik, *J. Am. Chem. Soc.* **2012**, *134*, 8408–8411.

[170] T. Pauloehrl, A. Welle, K. K. Oehlenschlaeger, C. Barner-Kowollik, *Chem. Sci.* **2013**, *4*, 3503–3507.

[171] N. C. Yang, C. Rivas, *J. Am. Chem. Soc.* **1961**, *83*, 2213–2213.

[172] G. Porter, M. F. Tchir, *J. Chem. Soc. D* **1970**, 1372–1373.

[173] J. C. Netto-Ferreira, J. C. Scaiano, *J. Am. Chem. Soc.* **1991**, *113*, 5800–5803.

[174] A. P. Pelliccioli, P. Klan, M. Zabadal, J. Wirz, *J. Am. Chem. Soc.* **2001**, *123*, 7931–7932.

[175] S. M. Mellows, P. G. Sammes, *J. Chem. Soc. D* **1971**, 21–22.

[176] J. L. Segura, N. Martin, *Chem. Rev.* **1999**, *99*, 3199–3246.

[177] G. Quinkert, *Chimia* **1977**, *31*, 225.

[178] T. Tago, T. Minowa, Y. Okada, J. Nishimura, *Tetrahedron Lett.* **1993**, *34*, 8461–8464.

[179] P. Belik, A. Gügel, A. Kraus, J. Spickermann, V. Enkelmann, G. Frank, K. Müllen, *Adv. Mater.* **1993**, *5*, 854–856.

[180] S. F. Hahn, S. J. Martin, M. L. McKelvy, *Macromolecules* **1992**, *25*, 1539–1545.

[181] L. S. Tan, F. E. Arnold, *Polym. Prepr.* **1986**, *27*, 453.

[182] T. Gruendling, K. K. Oehlenschlaeger, E. Frick, M. Glassner, C. Schmid, C. Barner-Kowollik, *Macromol. Rapid Commun.* **2011**, *32*, 807–812.

[183] K. K. Oehlenschlaeger, J. O. Mueller, N. B. Heine, M. Glassner, N. K. Guimard, G. Delaittre, F. G. Schmidt, C. Barner-Kowollik, *Angew. Chem. Int. Ed.* **2013**, *52*, 762–766.

[184] N. Zydziak, F. Feist, B. Huber, J. O. Mueller, C. Barner-Kowollik, *Chem. Commun.* **2015**, *51*, 1799–1802.

[185] M. Kaupp, T. Tischer, A. F. Hirschbiel, A. P. Vogt, U. Geckle, V. Trouillet, T. Hofe, M. H. Stenzel, C. Barner-Kowollik, *Macromolecules* **2013**, *46*, 6858–6872.

[186] T. Pauloehrl, G. Delaittre, V. Winkler, A. Welle, M. Bruns, H. G. Börner, A. M. Greiner, M. Bastmeyer, C. Barner-Kowollik, *Angew. Chem. Int. Ed.* **2012**, *51*, 1071–1074.

[187] T. Tischer, T. K. Claus, M. Bruns, V. Trouillet, K. Linkert, C. Rodriguez-Emmenegger, A. S. Goldmann, S. Perrier, H. G. Börner, C. Barner-Kowollik, *Biomacromolecules* **2013**, *14*, 4340–4350.

[188] C. M. Preuss, T. Tischer, C. Rodriguez-Emmenegger, M. M. Zieger, M. Bruns, A. S. Goldmann, C. Barner-Kowollik, *J. Mater. Chem. B* **2014**, *2*, 36–40.

[189] P. Klan, T. Solomek, C. G. Bochet, A. Blanc, R. Givens, M. Rubina, V. Popik, A. Kostikov, J. Wirz, *Chem. Rev.* **2013**, *113*, 119–191.

[190] M. Zabadal, A. P. Pelliccioli, P. Klan, J. Wirz, *J. Phys. Chem. A* **2001**, *105*, 10329–10333.

[191] P. Klan, A. P. Pelliccioli, T. Pospisil, J. Wirz, *Photochem. Photobio. S.* **2002**, *1*, 920–923.

[192] J. Literak, J. Wirz, P. Klan, *Photochem. Photobio. S.* **2005**, *4*, 43–46.

[193] L. Kammari, L. Plistil, J. Wirz, P. Klan, *Photochem. Photobio. S.* **2007**, *6*, 50–56.

[194] W. R. Bergmark, C. Barnes, J. Clark, S. Paparian, S. Marynowski, *J. Org. Chem.* **1985**, *50*, 5612–5615.

[195] T. Solomek, P. Stacko, A. T. Veetil, T. Pospisil, P. Klan, *J. Org. Chem.* **2010**, *75*, 7300–7309.

[196] M. Hesse, H. Meier, B. Zeeh, *Spectroscopic Methods in Organic Chemistry*, Thieme, Stuttgart, 2. Ed., **2007**.

[197] A. F. Jacobine, D. M. Glaser, P. J. Grabek, D. Mancini, M. Masterson, S. T. Nakos, M. A. Rakas, J. G. Woods, *J. Appl. Polym. Sci.* **1992**, *45*, 471–485.

[198] K. Fuchise, P. Lindemann, S. Heißler, H. Gliemann, V. Trouillet, A. Welle, J. Berson, S. Walheim, T. Schimmel, M. A. R. Meier, C. Barner-Kowollik, *Langmuir* **2015**, *31*, 3242–3253.

[199] J. Bailey, R. Havelund, A. G. Shard, I. S. Gilmore, M. R. Alexander, J. S. Sharp, D. J. Scurr, *ACS Appl. Mater. Interfaces* **2015**, *7*, 2654–2659.

[200] J. Fischer, J. B. Mueller, J. Kaschke, T. J. A. Wolf, A.-N. Unterreiner, M. Wegener, *Opt. Express* **2013**, *21*, 26244–26260.

[201] M. Deubel, G. von Freymann, M. Wegener, S. Pereira, K. Busch, C. M. Soukoulis, *Nat. Mater.* **2004**, *3*, 444–447.

[202] J. Fischer, J. B. Mueller, A. S. Quick, J. Kaschke, C. Barner-Kowollik, M. Wegener, *Adv. Opt. Mater.* **2015**, *3*, 221–232.

[203] A. Garcia-Bernabé, M. Krämer, B. Olah, R. Haag, *Chem. Eur. J.* **2004**, *10*, 2822–2830.

[204] P. Y. Reddy, S. Kondo, S. Fujita, T. Toru, *Synthesis* **1998**, *1998*, 999–1002.

[205] G. Mantovani, F. Lecolley, L. Tao, D. M. Haddleton, J. Clerx, J. J. L. M. Cornelissen, K. Velonia, *J. Am. Chem. Soc.* **2005**, *127*, 2966–2973.

[206] K. L. Parry, A. G. Shard, R. D. Short, R. G. White, J. D. Whittle, A. Wright, *Surf. Interface Anal.* **2006**, *38*, 1497–1504.

[207] J. H. Scofield, *J. Electron. Spectrosc. Relat. Phenom.* **1976**, *8*, 129–137.

[208] J. W. Chan, C. E. Hoyle, A. B. Lowe, *J. Am. Chem. Soc.* **2009**, *131*, 5751–5753.

[209] X. Tao, Z. Gao, T. Satoh, Y. Cui, T. Kakuchi, Q. Duan, *Polym. Chem.* **2011**, *2*, 2068–2073.

[210] R. N. Keller, H. D. Wrcoff, L. E. Marchi in *Inorganic Syntheses*, John Wiley & Sons, Inc., Weinheim, **2007**, pp. 1–4.

[211] F. G. Schmidt, S. Hilf, C. Barner-Kowollik, N. Guimard, K. K. Oehlenschlaeger, J. Mueller, *DE102012200235A1* **2013**.

[212] S. Varaprath, P. J. Varaprath, *US4861906* **1989**.

List of Figures

List of Tables

Abbreviations

2D	Two Dimensional
3D	Three Dimensional
DLW	Direct Laser Writing
FTIR	Fourier Transform Infrared
SEM	Scanning Electron Microscopy
FIB	Focused Ion Beam
CCD	Charge-Coupled Device
AOM	Acousto-Optic Modulator
EOM	Electro-Optic Modulator
1PA	One-Photon Absorption
2PA	Two-Photon Absorption
NA	Numerical Aperture
FRP	Free Radical Polymerization
STED	Stimulated Emission Depletion
PETTA	Pentaerythritol Tetraacrylate
PETA	Pentaerythritol Triacrylate
TPT	Trimethylolpropane Triacrylate
DPEPA	Dipentaerythritol Pentaacrylate
ITX	Isopropylthioxanthone
DIDMA	Diisopropyldimethylaniline
DETC	7-Diethylamino-3-thenoylcoumarin
DTT	Dithiothreitol
TCEP	Tris(2-carboxyethyl)phosphin
PEG	Polyethylene glycol
TEM	Transmission Electron Microscopy
AFM	Atomic Force Microscopy
HDA	Hetero Diels-Alder
RAFT	Reversible Addition Fragmentation Chain Transfer Polymerization
CuAAC	Copper-Catalyzed Azide-Alkyne Cycloaddition
ATRP	Atom Transfer Radical Polymerization
DBN	1,5-Diazabicyclo(4.3.0)non-5-ene
UV	Ultra Violet
PMMA	Poly(methyl methacrylate)
HCl	Hydrochloric acid
MEHQ	Methyl Ether Hydroquinone
HQ	Hydroquinone
NaOH	Sodium Hydroxide
NMR	Nuclear Magnetic Resonance
DMF	Dimethylformamide
DMAC	Dimethylacetamide

TMS	Tetramethylsilane
DCM	Dichloromethane
GBL	γ-Butyrolactone
THF	Tetrahydrofuran
MeOH	Methanol
CuBr	Copper Bromide
CuCl	Copper Chloride
SEC	Size Exclusion Chromatography
FWHM	Full Width Half Max

List of Publications

Publications Arising from this Thesis[a]

- **Thermally Responsive Core-Shell Microparticles and Cross-Linked Networks Based on Nitrone Chemistry**[§]
  Barner, L.; Quick, A.S.; Vogt, A.P.; Winkler, V.; Junkers, T.; Barner-Kowollik, C. *Polym. Chem.* **2012**, *3*, 2266-2276.

- **Facile Preparation of Reactive Three-Dimensional Microstructures via Direct Laser Writing and Thiol-Ene Chemistry**
  Quick, A.S.; Fischer, F.; Richter, B.; Pauloehrl, T.; Trouillet, V.; Wegener, M.; Barner-Kowollik, C. *Macromol. Rapid Commun.* **2013**, *34*, 335-340.

- **Fabrication and Spatially Resolved Functionalization of 3D Microstructures via Multiphoton-Induced Diels-Alder Chemistry**
  Quick, A.S.; Rothfuss, H.; Welle, A.; Richter, B.; Fischer, J.; Wegener, M.; Barner-Kowollik, C. *Adv. Funct. Mater.* **2014**, *24*, 3571-3580.

- **Photo-Induced Functionalization of Spherical and Planar Surfaces via Caged Thioaldehyde End-Functional Polymers**
  Kaupp, M.; Quick, A.S.; Rodriguez-Emmenegger, C.; Welle, A.; Trouillet, V.; Pop-Georgievski, O.; Wegener, M.; Barner-Kowollik, C. *Adv. Funct. Mater.* **2014**, *24*, 5649-5661.

- **Exploring the Mechanisms in STED-Enhanced Direct Laser Writing**
  Fischer, J.; Mueller, J.B.; Quick, A.S.; Kaschke, J.; Barner-Kowollik, C.; Wegener, M. *Adv. Opt. Mater.* **2015**, *3*, 221-232.

- **Photo-Induced Surface Encoding of Gold Nanoparticles**
  Stolzer, L.; Quick, A.S.; Abt, D.; Welle, A.; Naumenko, D.; Lazzarino, M.; Wegener, M.; Barner-Kowollik, C.; Fruk, L. *Chem. Commun.* **2015**, *51*, 3363-3366.

- **Rapid Thiol-Yne Mediated Fabrication and Dual Post-Functionalization of Micro-Resolved Mesostructures**
  Quick, A.S.; de los Santos Pereira, A.; Bruns, M.; Bückmann, T.; Rodriguez-Emmenegger, C.; Wegener, M.; Barner-Kowollik, C. *Adv. Funct. Mater.* **2015**, *25*, 3735-3744.

[a] Publications marked by a § were achieved during the diploma thesis of the author. All remaining publications originated during the course of the current thesis from projects where the author was involved.

- **Designing Molecular Printboards: A Photolithographic Platform for Recodeable Surfaces**
  Abt, D.; Schmidt, B.V.K.J.; Pop-Georgievski, O.; Quick, A.S.; Danilov, D.; Kostina, N.; Bruns, M.; Wenzel, W.; Wegener, M.; Rodriguez-Emmenegger, C.; Barner-Kowollik, C. **2015**, DOI: 10.1002/chem.201501707.

Patents Arising from this Thesis

- **Hochaufgelöste Photochemie Unterhalb des Beugungslimits Mittels Schaltbarer Photoenolisierung**
  Fischer, J.; Quick, A.S.; Richter, B.; Mueller, J.B.; Bastmeyer, M.; Barner-Kowollik, C.; Wegener, M. **2015**, EP-Number to be advised.